Sand Dunes on Mars and on Earth

Von der Fakultät Mathematik und Physik der Universität Stuttgart
zur Erlangung der Würde eines Doktors der
Naturwissenschaften (Dr. rer. nat.) genehmigte Abhandlung

vorgelegt von

Eric Josef Ribeiro Parteli

aus Recife/PE, Brasilien

Hauptberichter:	Prof. Dr. rer. nat. Hans Jürgen Herrmann
Mitberichter:	Prof. Dr. rer. nat. Günter Wunner
Tag der mündlichen Prüfung:	29. Januar 2007

Institut für Computerphysik der Universität Stuttgart

2007

Contents

List of publications related to this thesis.

1. E. J. R. Parteli and H. J. Herrmann, *A simple model for a transverse dune field*. **Physica A, 327, 554–562 (2003)**.
   Also in F. Mallamace and H. E. Stanley (Eds.), Proc. International School of Physics, "Enrico Fermi" 2003, ***The Physics of Complex Systems (New Advances and Perspectives)*, pp. 153–171, IOS Press (2004)**.

2. E. J. R. Parteli, *Das sich entziehende Land - Zur Physik der Düne und des Treibsands*. In J. Badura and S. Schmidt (Eds.), **"Niemandsland - Topographische Ausflüge zwischen Wissenschaft und Kunst", pp. 44 - 49, IZKT- Schriftenreihe Nr. 2, Stuttgart (2005)**.

3. J. H. Lee, A. O. Sousa, E. J. R. Parteli and H. J. Herrmann, *Modelling formation and evolution of transverse dune fields*.
   International Journal of Modern Physics C 12, No. 16, 1879–1892 (2005).

4. H. J. Herrmann, J. S. Andrade Jr., V. Schatz, G. Sauermann, E. J. R. Parteli, *Calculation of the separation streamlines of barchans and transverse dunes*.
   Proc. "PSIS 2004", Physica A 357, 44–49 (2005).

5. E. J. R. Parteli, V. Schwämmle, H. J. Herrmann, L. H. U. Monteiro and L. P. Maia, *Profile measurement and simulation of a transverse dune field in the Lençóis Maranhenses*.
   Geomorphology 81, 29–42 (2006).

6. H. J. Herrmann, E. J. R. Parteli, V. Schwämmle, L. H. U. Monteiro and L. P. Maia, *The coastal dunes of the Lençóis Maranhenses*.
   Proc. "ICS 2005", for Journal of Coastal Research.

7. E. J. R. Parteli, V. Schatz and H. J. Herrmann, *Barchan dunes on Mars and on Earth*. In R. Garcia-Rojo, H. J. Herrmann and S. McNamara (Eds.),
   Proc. "Powders and Grains 2005", Vol. 2, pp. 959–962, Balkema, Leiden (2005).

8. V. Schatz, H. Tsoar, K. S. Edgett, E. J. R. Parteli and H. J. Herrmann, *Evidence for indurated sand dunes in the Martian north polar region*.
   Journal of Geophysical Research 111(E4), E04006 (2006).

9. E. J. R. Parteli, O. Durán and H. J. Herrmann, *The Shape of the Barchan Dunes in the Arkhangelsky Crater on Mars*.
   Proc. "XXXVII Lunar and Planetary Science Conf.", #1827, 2006.

10. H. J. Herrmann, O. Durán, E. J. R. Parteli and V. Schatz, *Vegetation and induration as sand dunes stabilizators*. Proc. ICS 2005.
    Proc. "ICS 2005", Journal of Coastal Research (in press).

11. E. J. R. Parteli, O. Durán and H. J. Herrmann, *Minimal size of a barchan dune*.
    Physical Review E 75, 011301 (2007).

12. E. J. R. Parteli and H. J. Herrmann, *Saltation transport on Mars*.
    Physical Review Letters.

13. E. J. R. Parteli, O. Durán, V. Schwämmle, H. J. Herrmann and H. Tsoar, *Modelling seif dunes*.
    preprint.

Deutsche Zusammenfassung

Sanddünen treten in vielen Wüsten und Küstengebieten unseres Planeten auf, aber auch auf dem erdähnlichsten Planeten unseres Sonnensystems: dem Mars. Dünen sind ein Resultat des Wechselspieles zwischen dem turbulenten Fluid und dem Granulat und ergeben einen Beweis für das Vorliegen äolischer Kräfte.

Der für die Bildung von Dünen wichtige äolische Sandtransport findet durch *Saltation* statt (Bagnold 1941). Sobald die Windgeschindigkeit u_* einen minimalen Wert $u_{*\mathrm{t}}$ überschreitet, werden einzelne Körner mitgerissen, welche nach einer kurzen Flugstrecke wieder auf den Boden fallen. Dort stoßen sie auf ruhende Körner und lösen einige vom Boden, die ebenso vom Wind mitgetragen werden. So sammeln sich nach und nach immer mehr Sandkörner in der Saltationsschicht. Der Wind überträgt dabei Impuls an die Sandkörner (Owen 1964) und wird dadurch abgebremst (“feedback effect”). Somit reicht nach einiger Zeit die Geschwindigkeit des Windes nicht mehr aus, um weitere Sandkörner aufzunehmen, zumal die Dichte der in der Wolke transportierten Körner einen Grenzwert erreicht. Nach einer bestimmten Strecke, der sogenannten “Saturationslänge”, erreicht der Sandfluss einen maximalen Wert. Aus diesem Grund spielt die Saturationslänge eine für die Entstehung von Dünen entscheidende Rolle. Jeder Sandhügel, der kürzer als die Saturationslänge ist, wird vom Wind vollständig erodiert.

Es gibt in der Natur viele verschiedene Dünenformen, welche hauptsächlich von der Windrichtung und von der Verfügbarkeit von Sand auf dem Boden abhängig sind. Weht der Wind immer aus der selben Richtung, so entstehen bei geringer Sandmenge *Barchan Dünen*, die sogenannten “Wanderdünen”. Wenn mehr Sand vorhanden ist, entstehen in regelmässigen Abständen senkrecht zur Windrichtung *Transversaldünen*. Ändert sich die Windrichtung, dann entstehen bei ausreichend viel Sand *Longitudinaldünen*, die parallel zur resultierenden Windrichtung orientiert sind. Natürlich gibt es eine große Anzahl von verschiedenen Dünenformen, die bis heute, trotz der vielen Messungen der letzten Jahrzehnte, unerklärt sind.

Besonders interessant für Planetologen sind die Marsdünen, die oft ähnliche Formen haben wie die Dünen unseres Planeten. Seit der Entdeckung von Marsdünen im Jahr 1971, wurden diese zum Gegenstand intensiver Forschung. Hätten Marsdünen unter der heutigen dünnen Marsatmosphäre gebildet werden können? Marsdünen scheinen sich nicht zu bewegen. Unter den heutigen atmosphärischen Bedingungen wären nur Winde, die 10 mal so stark sind wie die Winde auf der Erde in der Lage, Sandkörner durch Saltation zu transportieren (Greeley et al. 1980). Solche Winde treten auf dem Mars nur selten auf (Sutton et al. 1978; Arvidson et al. 1983; Greeley et al. 1999; Sullivan et al. 2005). Aus diesem

Grund wurde voraussgesetzt, dass Marsdünen vor langer Zeit gebildet worden sind, als die Dichte der Marsatmosphäre höher war als heute (Breed et al. 1979). Der Zeitpunkt an dem die heutige atmosphärische Dichte $\rho_{\text{fluid}} \approx 0.016$ kg/m^3 (MGSRS 2006) erreicht wurde, ist allerdings unbekannt.

Erst kürzlich gelang es Kroy et al. (2002) eine mathematische Modellierung aufzustellen, welche die wesentlichen Teilprozesse der Physik der Dünen umfasst. Sie bezieht die mikroskopischen Mengen des Sandtransportes, die Luftbahnen der Sandkörner und die Rate ein, bei welcher Sandkörner in die sich bewegende Sandschicht mitgerissen werden (Sauermann et al. 2001; Kroy et al. 2002). Diese Modellierung besteht aus einem System von zweidimensionalen kontinuerlichen Gleichungen, welche an Wanderdünen ausgiebig geprüft wurden und an Feldmessungen quantitativ sehr erfolgreich bestätigt wurden (Sauermann et al. 2003). Das Modell reproduziert die beobachtete Abhängigkeit der Form einer Düne von deren Größe, sowie das Vorliegen einer minimalen Dünengröße.

Diese Arbeit befasst sich im folgenden mit dieser Modellierung, um zum einen die in der Natur am häufigsten beobachteten Dünenformen — Barchan-, Transversal- und Longitudinaldünen — als Funktion der Windrichtung und der Verfügbarkeit von Sand zu untersuchen, und zum anderen, um die Dünenbildung auf dem heutigen Mars zu berechnen. Hierbei stellt sich die Frage, ob deren Entstehung unter der dünnen Atmosphäre des roten Planeten möglich gewesen wäre.

Das eingesetzte Dünenmodell wird in Kapitel 1 präsentiert. Dabei werden die mit dem Sandtransport und der Dünenbildung wesentlichen Begriffe erläutert, welche wir benötigen, um die Herleitung des Modelles nachvollziehen zu können und um die Ergebnisse dieser Arbeit zu interpretieren. Wir diskutieren danach die Rolle der Windrichtungen und der zur Verfügung stehenden Sandmenge für die Entstehung unterschiedlicher Dünenformen, die wir in den nächsten Kapiteln untersuchen werden. Zuletzt werden die Gleichungen präsentiert, die wir für die Berechnung der Marsdünen verwenden werden. Mit Gleichungen (1.43), (1.50), (1.53) und (1.54) können die Parameter des Modelles für die Berechnung des Sandtransportes auf dem Mars gewonnen werden, die sonst nur aus Messungen vom Sandfluss ermittelt werden könnten, die bisher für den Mars nicht vorhanden sind.

Die Ergebnisse der in Kapitel 2 durchgeführten Berechnungen zeigen wesentliche Unterschiede zwischen Saltation auf dem Mars und auf der Erde. Während Sandkörner auf der Erde sich auf einer durchschnittlichen Höhe von etwa 15 cm dicht über dem Boden bewegen, saltieren die Marsteilchen bis über einer Höhe von 1.0 m (Tabelle 2.1). Darüber hinaus, erreichen diese eine durchschnittliche Geschwindigkeit von 15 m$/$s, etwa 10 Mal so hoch wie die Geschwindigkeit von irdischen Sandkörnern. Wie entscheidend dieser Unterschied für die Entstehung von Dünen auf dem Mars ist, werden wir in Kapitel 3 sehen.

Wir beginnen mit den am meisten studierten Dünen, den Barchan Dünen. Zuerst untersuchen wir wie die Form einer Barchan Düne von der Windgeschwindigkeit u_* und von dem Sandfluss zwischen den Dünen, q_{in}, abhängig ist. Kroy et al. (2005) stellten bereits fest, dass das Verhältnis zwischen der Höhe der Düne, H, und deren Länge L, mit der Windgeschwindigkeit u_* zunimmt. Jedoch konnten solche zweidimensionalen Simulationen die für die Stabilität der Barchan Dünen wichtigen Hörner nicht berücksichtigen. Hier präsentieren wir zum ersten Mal Ergebnisse von dreidimensionalen Berechungen, welche zeigen, dass Barchan Dünen höhere Werte von W/L mit zunehmender Windstärke aufweisen (Abb. 3.5), wobei W die Breite der Düne ist. Weiterhin entdecken wir, dass die minimale Größe einer Barchan Düne — unter deren die Düne keine Rutschhangseite ("slip face") aufweist — mit zunehmender Windgeschwindigkeit abnimmt, wobei das Verhältnis $L_{\mathrm{min}}/W_{\mathrm{min}}$ der kleinsten Barchan Düne mit zunehmendem q_{in} abnimmt. Diese Beobachtungen werden dann verwendet, um die Feldvariabeln q_{in} und u_* von Dünenfeldern auf dem Mars zu ermitteln.

Die minimale Größe einer Barchan Düne wird von der Saturationslänge ℓ_{s} (Gleichung (1.33)) bestimmt. Die Saturationslänge ist proportional zu der Größe $\ell_{\mathrm{drag}} = d\rho_{\mathrm{grain}}/\rho_{\mathrm{fluid}}$, wobei d die Korngröße und ρ_{grain} die Dichte der Sandkörner ist. Darüber hinaus ist die Saturationslänge eine nichtlineare Funktion der Windgeschwindigkeit, und ebenso ist sie umgekehrt proportional zu der Rate, mit der Körner in die Saltationswolke mitgerissen werden (Gleichung (1.11)). Diese "entrainment rate" ist in dem Parameter γ miteinbezogen. Sauermann et al. (2001) konnten $\gamma = 0.2$ für äolische Saltation auf der Erde finden, indem sie die Simulationsergebnisse mit Windkanaldaten der Saturationstransienten des Sandflusses verglichen haben, welche für den Mars allerdings nicht vorhanden sind. Darum berechnen wir Marsdünen vorerst mit dem irdischen $\gamma = 0.2$.

Wir untersuchen zuerst die riesigen Barchan Dünen, die in dem Arkhangelsky Krater auf dem Mars auftauchen. Aus dem Vergleich mit den Simulationsergebnissen wollen wir die Windgeschwindkeit u_* und den Sandfluss q_{in} finden, die für die beobachteten Dünenformen verantwortlich sind. Ausgangspunkt ist die Breite $W_{\mathrm{min}} \approx 200$ m der kleinsten Düne im Arkhangelsky Krater.

Wir finden ein überraschendes Ergebnis: Nehmen wir das irdische $\gamma = 0.2$ für den Mars, so wird die minimale Breite W_{min} nur mit einer Windgeschwindigkeit von etwa 6.0 m/s reproduziert. Dieser Wert ist viel zu hoch, um realistisch zu sein. Die höchsten Geschwindigkeiten von Marswinden befinden sich zwischen 2.2 und 4.0 m/s (Moore 1985; Sullivan et al. 2005). Um den richtigen Wert W_{min} mit realistischen Werten von u_* wiederzugeben, müssen wir γ um etwa eine Größenordnung erhöhen.

Warum ist die "entrainment rate" γ auf dem Mars höher als auf der Erde? Wir stellen eine Gleichung für γ auf, die gebraucht werden kann um die "entrainment rate" unter physikalischen Bedingungen zu berechnen, die anders sind als die auf der Erde (Gleichung (3.3)). Die Rate, bei welcher Teilchen in die Saltationswolke mitgerissen werden, wächst mit zunehmender Intensität der Teilchen-Sandboden Kollisionen ("splash") an, welche zu der Geschwindigkeit der saltierenden Körner proportional ist. Die höhere "entrainment rate" auf dem Mars ist ein Resultat aus der 10 Mal höheren Geschwindigkeit der Sandkörner. Wenn die Gleichung (3.3) in die Berechnungen miteinbezogen wird, dann kann die Form und die minimale Größe der Arkhangelsky Dünen wiedergegeben werden. Weiterhin können die Simulationen die Form von Dünen an anderen Stellen auf dem Mars, mit realistischen Werten von u_* wiedergeben. Überraschenderweise wird eine Windgeschwindigkeit gefunden, die etwa 3.0 m/s beträgt, unabhängig von den lokalen Bedingungen von Druck und Temperatur, welche den Minimalwert $u_{*\mathrm{t}}$ bestimmen. Die Berechnungen zeigen, dass Marsdünen sich unter derselben Bedingung von $u_*/u_{*\mathrm{t}}$ etwa 10 Mal schneller fortbewegen als Erddünen (Abbildung 2). Berücksichtigen wir aber die Häufigkeit, bei welcher sandbewegende Winde auf dem Mars auftreten, so erlangen wir eine Abschätzung der Zeit, die eine Barchan Düne auf dem Mars benötigt, um eine Strecke von 1.0 m zurüeckzulegen: 4000 Jahre (Kapitel 3).

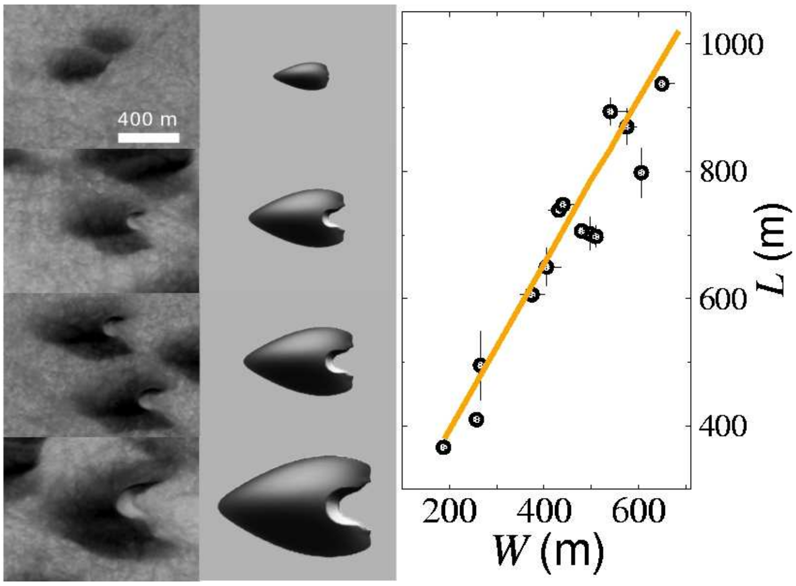

Abbildung 1: Barchan Dünen im Arkhangelsky Krater auf dem Mars. Links sehen wir Satellitenbilder, während die simulierten Dünen rechts gezeigt werden. Die Länge L der berechneten Dünen wird als Funktion deren Breite W aufgetragen (Linie), während die Kreise den echten Marsdünen entsprechen.

In Kapitel 4 untersuchen wir die *Transversaldünen*. Diese Dünen entstehen unter unidirektionalem Wind und wenn der Boden von Sand bedeckt ist. Sie treten am häufigsten in Küstengebieten auf, da dort die Verfügbarkeit von Sand und die Windgeschwindigkeit besonders hoch sind. Hier werden Ergebnisse dargestellt, die aus Messungen an einem Transversaldünenfeld — in den sogenannten “Lençóis Maranhenses” — im Nordosten Brasiliens ermittelt wurden (Abb. 4.5).

Die Ergebnisse der Messungen zeigen, dass Transversaldünen, die ungefähr dieselbe Höhe haben, einen variablen horizontalen Abstand zwischen ihrem Rande (“brink”) und ihrer Position von Maximalhöhe (“crest”) vorweisen. Dies ist im starken Gegensatz zu der Situation von Barchan Dünen, deren “crest-brink” Abstand mit wachsender Dünenhöhe regelmässig abnimmt. Des Weiteren zeigen die Ergebnisse unserer Feldmessungen, dass der durchschnittliche Abstand zweier Transversaldünen zwischen $2-4$ Mal so groß ist wie ihre Höhe. Allerdings ergeben Simulationen mit dem Dünenmodell viel höhere Abstände zwischen Transversaldünen, die etwa $6-8$ Mal deren Höhe betragen.

Unsere Messungen zeigen weiterhin, dass der Abstand zweier Transversaldünen stark von dem “crest-brink” Abstand abhängig ist. An dem Rand, wo die Gleitfläche ansetzt, entsteht eine scharfe Kante. Weht der Wind über eine solche Kante, so wird an ihr der Luftstrom aufgetrennt in eine obere Zone, in welcher der Wind relativ ungestört weitergeht, und in eine untere mit einem rückströmenden Wirbel. In dieser unteren Zone, der

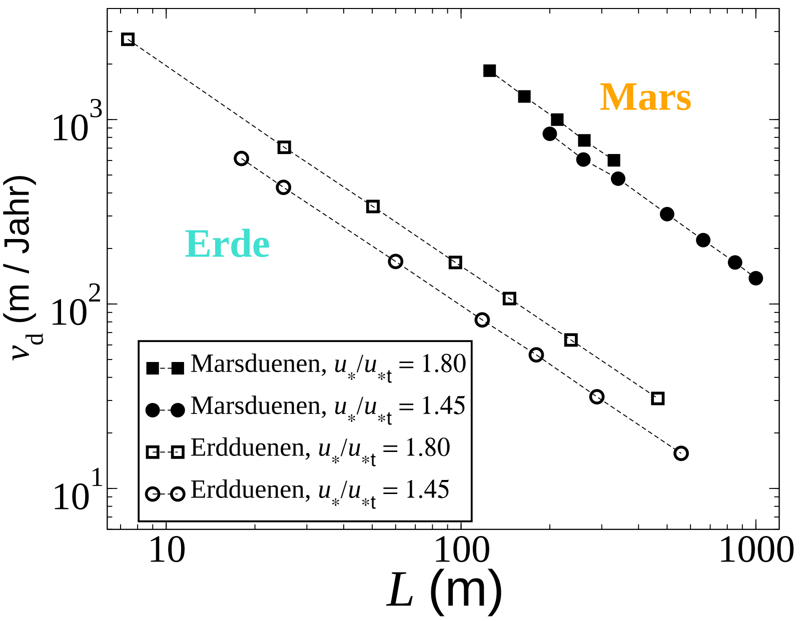

Abbildung 2: Dünengeschwindigkeit v_d als Funktion der Dünenlänge L. Wir sehen dass Marsdünen (gefüllte Bildzeichen) sich typischerweise 10 mal schneller fortbewegen als Erddünen (leere Bildzeichen) derselben L, wobei beide Mars- und Erddünen mit gleichen Werten von $u_*/u_{*\mathrm{t}}$ berechnet wurden.

so genannten Trennblase (“separation bubble”), kann der Sand aufgrund des schwachen Windfeldes nicht mehr transportiert werden. Die Trennblase wird durch ein Polynom dritter Ordnung modelliert (Gleichung (1.37)), welches die Dünenkante mit dem auf dem Boden liegenden “reattachment point” verbindet (Abb. 1.8). Hier stellen wir ein alternatives Modell für die Trennblase vor (Gleichung (4.3) und Abb. 4.13), welches die Berechnung von Transversaldünen mit geringeren Abständen, als die aus den bisherigen Simulationen (Schwämmle und Herrmann 2004) erlaubt. Die Gleichung (4.3) bezieht unsere Beobachtungen ein, dass die Länge der Trennblase größer ist für die Dünen mit koinzidierendem Maximum und Rutschhangkante (Abb. 4.11). Verwenden wir die neue Gleichung für die Trennblase, so geben die Simulationen die Form und Abstände der gemessenen Dünen wieder.

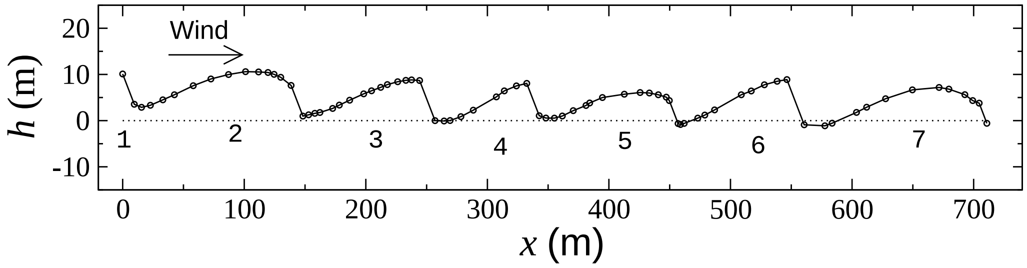

Abbildung 3: Das Höhenprofil des gemessenen Dünenfeldes in den Lençóis Maranhenses, Nordosten Brasiliens.

Aber wie entsteht ein Dünenfeld? In Kapitel 5 stellen wir ein einfaches Modell vor, um die Entwicklung eines Transversaldünenfeldes zu untersuchen. Das Modell besteht aus einem System von phänomenologischen Gleichungen (Gleichungen (5.1), (5.2) und (5.3)), welche die beobachteten Verhältnisse der Geschwindigkeit der Düne und des Sandflusses auf deren Kamm, als Funktion der Dünenhöhe, miteinbeziehen. In den Berechnungen werden unterschiedliche Anfangsbedingungen angesetzt (Abbildung 5.1), wobei sich die Frage stellt, ob die Entwicklung eines Dünenfeldes von der Anfangsverteilung der Höhen und Abstände zwischen den Dünen abhängig ist. Die Ergebnisse zeigen, dass die Dünen nach einer Übergangszeit eine charakteristische Höhe erreichen, welche zu dem am Anfang des Feldes angesetzten Sandfluss proportional ist. Dieses Ergebnis ist von den Anfangsbedingungen unabhängig (Abbildung 5.2). Darüber hinaus untersuchen wir die Auswirkung des Zusammenwachsens zweier Dünen auf die Entwicklung des Dünenfeldes. Hierbei wird angenommen, dass zwei Dünen, die sich zeitgleich an einer Position befinden, immer zusammenwachsen. Wie in Abbildung 5.5 zu sehen ist, nimmt die Anzahl von Dünen in einem Feld mit dem Logarithmus der Zeit ab, wie es kürzlich von Schwämmle und Herrmann (2004) in Simulationen von zweidimensionalen Dünenfeldern gefunden wurde.

Das in Kapitel 5 vorgestellte Modell wollen wir nun anwenden, um die Bildung von Dünenfelder wie sie in Baja California (Abbildung 1.3b) und in den Lençóis Maranhenses (Abbildung 4.5) auftreten. Dünen, die in Küstengebieten unseres Planeten auftreten, stammen aus dem Sand, der vom Meer am Strand abgelagert wird. Dabei bilden sich kleine Barchan- und Transversaldünen, welche mit systematisch zunehmenden Höhen auf den Kontinenten wandern, um in regelmässigen Abständen riesige Transversaldünen zu bilden. Wir beginnen mit einem leeren Boden. Auf diesem wandern kleine Dünen, welche am Strand (Position $x = 0$) gebildet werden, und eine Höhe von 1.0 m aufweisen. Hierbei wird das Verhältnis zwischen der Höhe der Düne und deren Breite berücksichtigt, welches in den Lençóis Maranhenses gemessen wurde. Darüber hinaus wird jeder Düne eine Trennblase zugeschrieben (Abbildung 5.8). Die Wechselwirkung zwischen zwei Dünen erfolgt nach den Gleichungen (5.6) und (5.7). Wenn die Dünen auf eine steinige Oberfläche (“bedrock”) auftreffen, dann ergeben die Berechnungen ein unrealistisches Muster: die kleinsten, schnellsten Dünen erscheinen am Ende des Feldes, wobei grosse Transversaldünen in kurzem Abstand vom Strand zu beobachten sind (Abbildung 5.9). Berücksichtigen wir nun ein Dünenfeld, das sich auf einem von Sand bedeckten Boden entwickelt, so muss die Saturationslänge in das Modell miteinbezogen werden. Da der Sandfluss innerhalb der Saturationslänge λ_{s} null ist, kann der Fuss einer in Windrichtung folgenden Transversaldüne nicht erodiert werden, wenn der Abstand zwischen dieser und der vorherigen Düne grösser als λ_{s} ist. Aus diesem Grund können Transversaldünen nur Abstände aufweisen, die dieselbe Grössenordnung der Saturationslänge haben (Abbildung 5.10). Berücksichtigen wir nun den Sandfluss in Windrichtung, so erhalten wir mit dem einfachen Modell das bekannte Muster eines Küstendünenfeldes: kleine Dünen erscheinen am Anfang des Feldes und erreichen, nach einigen Kilometern in Windrichtung, gleichmässige Abstände und Höhen (Abbildungen 5.14 und 5.15).

Des Weiteren untersuchen wir in Kapitel 5 die Entstehung eines Dünenfeldes mit dem komplexen Dünenmodell. Als Anfangsbedingung setzen wir einen linearen Rücken, welcher senkrecht zur Windrichtung orientiert ist, und ein Gaussförmiges Querprofil aufweist. Entscheidend für die Entstehung von Dünen ist, dass der Sandfluss, der am Anfang des Feldes in Windrichtung eingesetzt wird, gleich dem maximalen Fluss $q_{\rm s}$ ist. Wenn der saturierte Sandfluss in die Simulationen miteinbezogen wird, entstehen kontinuierlich Barchan- und Transversaldünen (Abbildung 5.16), deren Ursprung am Strand liegt, und deren Form von der Windgeschwindigkeit u_* abhängig ist. Die in Kapitel 5 durchgeführten Simulationen erläutern somit die Entstehung eines Dünenfeldes unter maximalem Sandfluss und unidirektionalem Wind, welche als typische Bedingungen in Küstengebieten vorzufinden sind.

In Kapitel 6 untersuchen wir zum ersten Mal mit dem Dünenmodell die Dünenformen, die unter zweidirektionalem Wind entstehen. Hierbei oszilliert die Windrichtung zwischen zwei Richtungen, welche einen Winkel $\theta_{\rm w}$ einschließen. Der Wind verweilt in jeder der zwei Richtungen eine charakteristische Zeit $T_{\rm w}$.

Die Ergebnisse der Simulationen zeigen die Bedingungen für die Entstehung von *Longitudinaldünen*. Die wichtige Größe ist der Winkel zwischen den Windrichtungen, $\theta_{\rm w}$. Longitudinaldünen bilden sich nur wenn $\theta_{\rm w} > 90^\circ$ ist. Weiterhin zeigen unsere Berechnungen, dass Longitudinaldünen instabil sind und zusammen mit Barchan Dünen auftreten, wenn $\theta_{\rm w}$ zwischen 90° und $\approx 120^\circ$ liegt. Nähert sich $\theta_{\rm w}$ dem Wert 180°, so entstehen die “reversing dunes”, welche hier nicht untersucht werden.

Die Berechnungen geben die charakteristische “verwickelte” Form der Longitudinaldünen wieder. Allerdings nimmt der Mäander der Dünen mit abnehmenden Werten von $T_{\rm w}$ ab. Wenn $T_{\rm w}$ zu groß wird, entstehen Lawinen nur auf einer Seite der Longitudinaldüne, die nun einer Transversaldüne ähnelt.

Viele exotische Dünenformen, die bislang unerklärt sind, werden noch auf der Oberfläche des roten Planeten beobachtet. Dünen, wie sie in Abbildung 4 dargestellt sind, können nicht unter unidirektionalem Wind entstehen, da dieser zu Barchan Dünen und Transversaldünen führt. Unsere Simulationen zeigen, dass diese Dünen sich unter *zweidirektionalem* Wind bilden. Wir berechnen die unterschiedlichen Dünenformen, die sich auf steinigem Untergrund bilden, als Funktion von $\theta_{\rm w}$ und $T_{\rm w}$. Danach berechnen wir die Werte von $T_{\rm w}$ und $\theta_{\rm w}$, welche zu den unterschiedlichen Dünenformen führen, die in Abbildung 4 dargestellt sind. Dabei wird eine Windgeschwindigkeit von 3.0 m/s eingesetzt, welche aus den Berechnungen von Barchan Dünen auf dem Mars gefunden wurde (Kapitel 3).

Interessanterweise finden wir, dass die Dünenformen in Abb. 4 mit $\theta_{\rm w}$ zwischen 100° und 140° reproduziert werden können, was eine exzellente Übereinstimmung mit $\theta_{\rm w}$ der Longitudinaldünen ergibt. Des Weiteren ergeben die Simulationen Werte von $T_{\rm w}$ zwischen $1 - 5$ Tagen auf dem Mars. Dies ist ein überraschendes Ergebnis, da vorausgesetzt wurde, dass die Winde auf dem roten Planeten im Wesentlichen unidirektional sind (Lee und Thomas 1995). Jedoch müssen unsere Ergebnisse anhand der *eigentlichen* Zeit $T_{\rm real}$ interpretiert werden, die viel größer ist als $T_{\rm w}$, da u_* meist unterhalb von $u_{*{\rm t}}$ liegt. Wie von Arvidson et al. (1983) bereits festgestellt wurde, findet Saltation auf dem Mars nur 40 Sekunden lang alle 5 Jahre statt. Aus diesem Grund liegt die aus den Simulationen ermittelte charakteristische Zeit der Oszillation der Windrichtung auf dem Mars zwischen 10800 und 54000 Jahren. Diese Zeitskala ist dieselbe Größenordnung wie eine halbe “Präzessionsperiode” des roten Planeten, welche für Änderungen der Windrichtungen um mehr als 90° verantwortlich ist (Arvidson et al. 1979). Schliesslich ergeben die Berechnungen der Marsdünen, die sich unter bidirektionalem Wind bilden, einen indirekten Beweis, dass die heutige Atmosphäre des roten Planeten fähig ist, Sand zu transportieren und Dünen zu bilden.

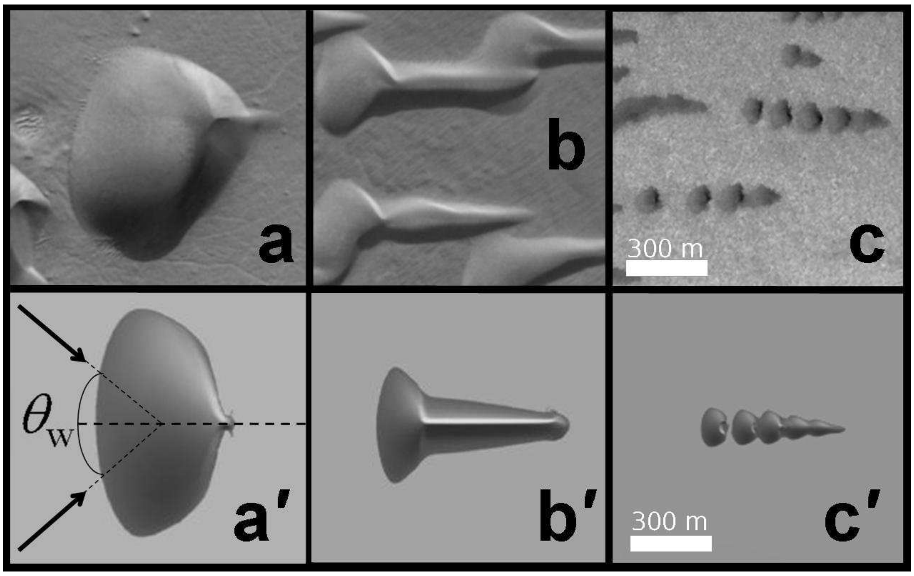

Abbildung 4: Exotische Dünenformen auf dem Mars. **a**, **b** und **c** sind Satellitenbilder, während wir in **a**′, **b**′ und **c**′ mit zweidirektionalem Wind berechnete Dünen darstellen. Die Dünenform in **a**′ lässt sich mit $\theta_w = 100°$ und $T_w = 2.9$ Tagen generieren; die in **b**′ mit $\theta_w = 120°$ und $T_w = 5.8$ Tagen. Um das in Abb. **c** beobachtete Muster zu reproduzieren, müssen wir eine sich ändernde Windrichtung einsetzen. Setzen wir erst $\theta_w = 140°$ und $T_w = 0.7$ Tage, so entsteht eine Longitudinaldüne, welche der in der Abb. **b**′ dargestellten Düne ähnelt. Lassen wir nun θ_w auf $80°$ sinken, entsteht aus der Longitudinaldüne ein komplexes Muster, das aus einer Reihe von kleinen Barchan Dünen besteht.

Introduction

Sand dunes are beautiful sand patterns formed by the wind. They appear on many coastal areas and deserts of our planet, as we see in fig. 1, and they are evidence of the existence of aeolian forces. Dunes appear when there is enough loose sand and when the wind has sufficient *strength* to mobilize the grains. Bagnold (1941) first noticed that the sand of dunes is transported by the wind through saltation, which consists of grains travelling close to the ground in a sequence of ballistic trajectories. Since then, saltation transport has been subject of systematic theoretical and experimental investigation (Owen 1964; Ungar and Haff 1987; Anderson and Haff 1988; McEwan and Willetts 1991; White and Mounla 1991; Butterfield 1993; Nalpanis et al. 1993; Rasmussen et al. 1996; Iversen and Rasmussen 1999; Andreotti 2004; Almeida et al. 2006).

Understanding the formation of dunes and predicting rate of dune motion is of extreme importance. In many areas, dunes represent enormous hazard for the population, which must spend large amount of money to protect cities and roads threatened by saltating sand (Sauermann 2001). Indeed, there is a high variety of dune shapes that could not be explained so far in spite of the many field studies performed in the last decades (Bagnold 1941; Finkel 1959; Long and Sharp 1964; Hastenrath 1967; Besler 1975; Fryberger and Dean 1979; Ash and Wasson 1983; Lancaster 1983; Tsoar 1989; Embabi and Ashour 1993; Hesp and Hastings 1998; Jimenez et al. 1999; Tsoar and Blumberg 2002; Gonçalves et al. 2003; Barbosa and Dominguez 2004; Elbelrhiti et al. 2005).

There are sand dunes also on the most earthlike of the planets in the solar system: Mars. The “red planet” is smaller than Earth, with only 10% of the terrestrial volume and mass, and its gravity $g = 3.71$ m/s^2 is nearly $1/3$ of the Earth’s gravity. On the other hand, the days of Mars (called *sols*), are essentially of the same duration of the Earth’s days, and the Martian temperatures, though normally much lower, can reach values as high as 20°C. However, Mars has an almost negligible atmospheric density, if we compare with the Earth, and the pressure of the Martian air is in average less than 6 mbar — almost thousand times lower than the Earth’s atmospheric pressure (~ 1.0 bar). Nevertheless, there is a surprising variety of aeolian features on the surface of Mars, which has become “*a natural laboratory for testing our understanding of the physics of aeolian processes in an environment different from that of Earth*” (Sullivan et al. 2005).

What we see in fig. 2 are images of some of the most typical aeolian features observed on Mars. These images have been taken by the Mars Orbiter Camera (MOC) (fig. 2*a*), which is on board of the Mars Global Surveyor (MGS) (fig. 2b) — the most successful Mars mission, orbiting Mars since 1997. In fig. 2*c*, we see an example of big *dust*

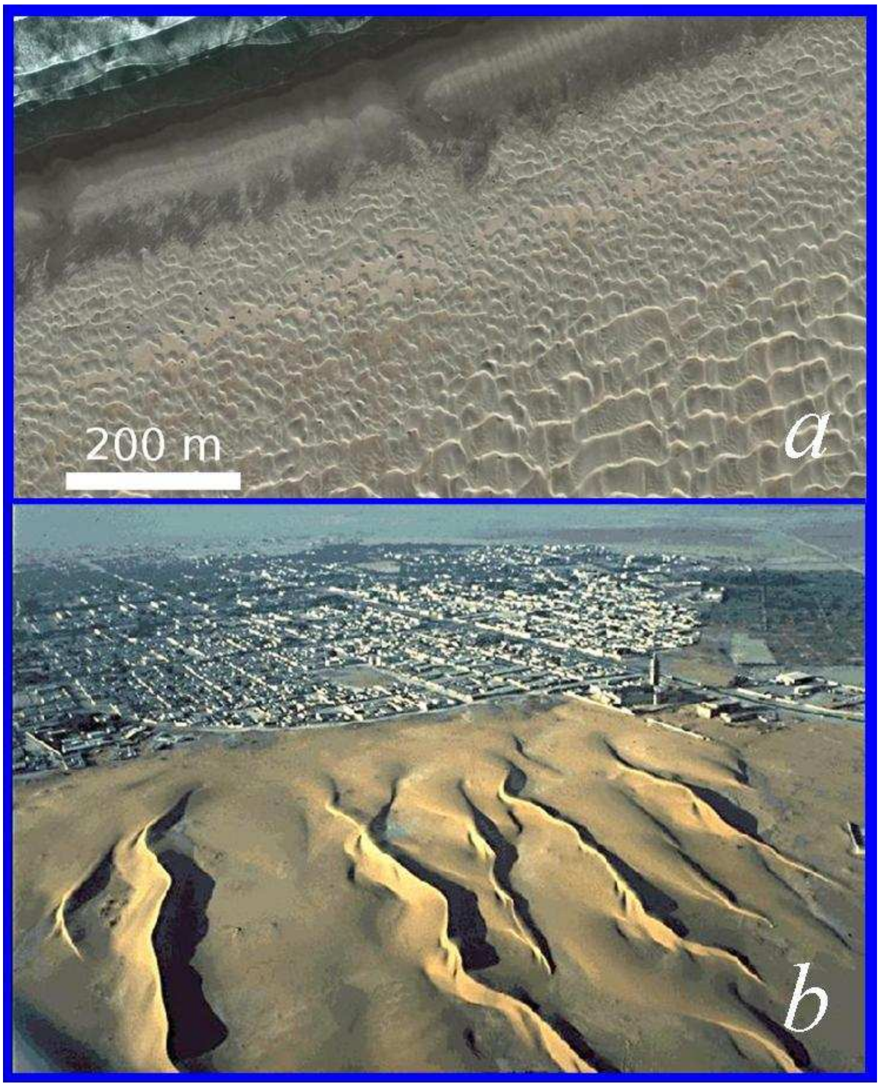

Figure 1: Sand dunes on Earth. **a.** Coastal dunes at Baja California. Very small *barchans* emerge from the sandy beach when the wind is essentially unimodal. We see that barchans join at their horns forming *transverse dunes*. **b.** *Seif* dunes close to Nouackchot (image credit: NASA). These dunes emerge from bimodal winds, elongate and move in the direction of the resultant wind.

storms, which are known to be typical on Mars for more than a century (Sheehan 1996). It is not known, however, which processes compete to nucleate such enormous storms, which can maintain clouds of particles having a few microns of diameter suspended in the atmosphere for several weeks. In fig. 2*d* we see Martian *yardangs*, which are erosional features that appear on the ground due to persistent impact of sand grains mobilized by strong surface winds. The dark streaks shown in fig. 2*e* are tracks left by *dust devils*. These streaks are ephemeral features that change within timescales of a few weeks. In contrast, the *bright streaks* (fig. 2*f*) that appear at the lee of several Martian craters may remain unmodified for several years, and have been observed to change orientation just after extreme dust storms (Sullivan et al. 2005).

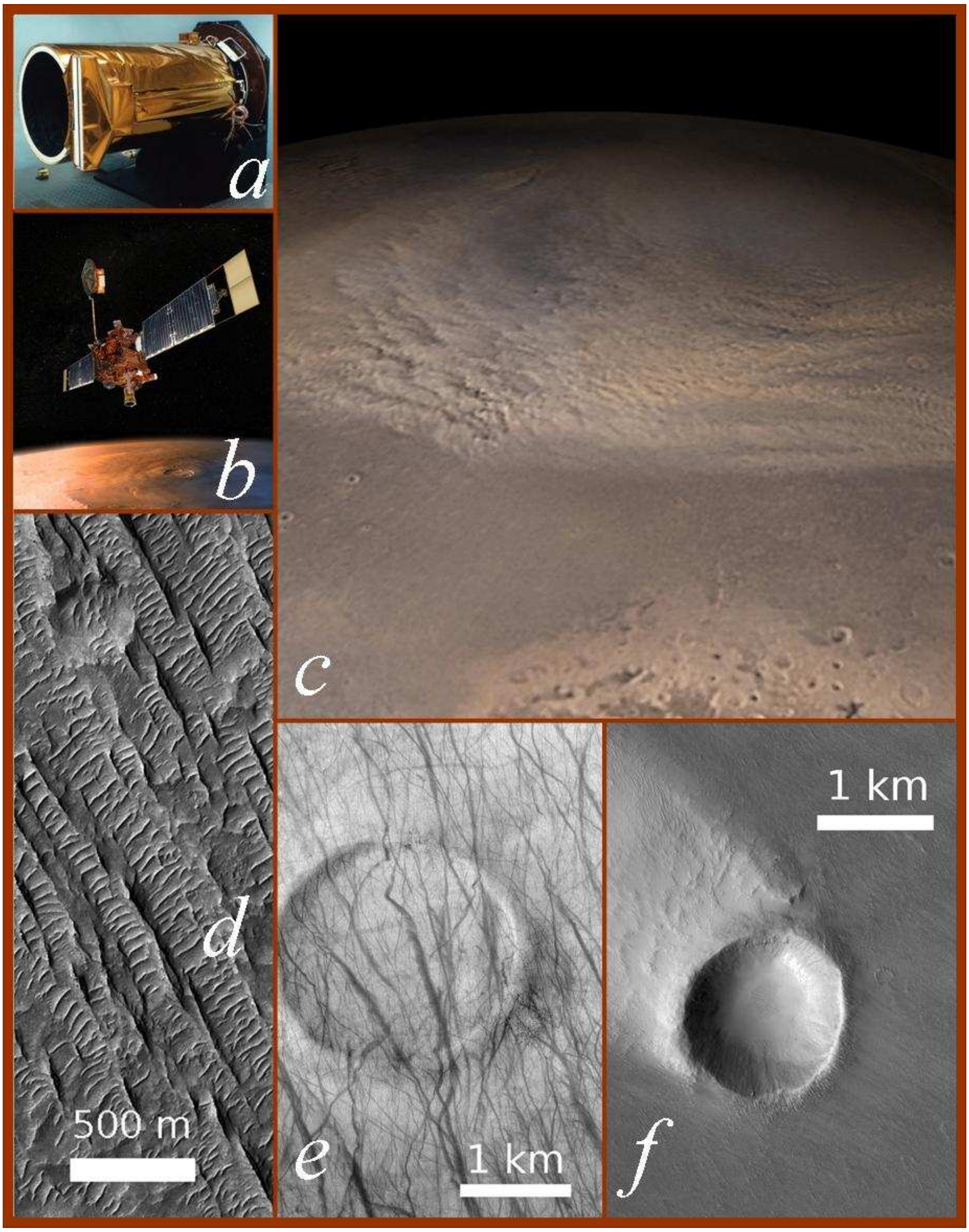

Figure 2: Aeolian transport on Mars: images by the Mars Orbiter Camera (MOC) (**a.**) on board of the Mars Global Surveyor (MGS) (**b.**). **c.** A large *dust storm* begins to form on the northern plains of Mars. **d.** *Yardangs* and bright *ripples* near $0.9°$ N, $212.5°$ W. **e.** *Dust devils* create ephemeral dark streaks by removing or disrupting thin coatings of fine, bright, dust on the surface. The circular feature is a Martian crater near $57.4°$S, $234.0°$W. **f.** Bright *wind streak* at the lee of a crater located at $6.7°$S, $141.4°$W. Image credits: MSSS, NASA/JPL.

But the most intriguing features are certainly the enormous Martian dark sand dunes. Figure 3 shows MOC images of dunes at different locations on Mars. We see that Martian dunes may have different shapes, and they look dark because their sand is made of grains of basalt (Fenton et al. 2003), while terrestrial dunes are mostly constituted of quartz grains (Bagnold 1941). Moreover, studies of thermal properties of the dunes revealed that the sand of Martian dunes is coarser than the terrestrial dune sand. While the average grain diameter of Earth's dunes is around 250 μm (Bagnold 1941), the particles that constitute Martian dunes have a mean diameter $d = 500\mu$m (Edgett and Christensen 1991). It appears surprising that the scarce atmosphere of Mars could put such large basaltic grains into saltation and form the enormous dunes observed in the images. Indeed, Martian dunes do not appear to have been moving in the last Martian years, which means winds have not been strong enough to transport grains or dunes move at a rate too low to be detected by the orbiters.

In fact, it is interesting that Martian dunes are subject of much scientific investigation. The reason is that any information about their origin, the time they have been formed, whether they move or could move in the future, can be valuable to understand the climatic and atmospheric history of the red planet. The young Mars was effectively very different than what it appears now, with high atmospheric temperatures and abundant liquid water on the surface billions of years ago. Probably, Mars had also a much denser atmosphere than now. However, the atmospheric density has been decreasing with time, mainly because of the constant meteorite bombardment (Melosh and Vickery 1989). Owing to its low gravity, the small red planet has been easily losing large amounts of its atmospheric particles after collisions of meteorites. This provides the first constraint to estimate the age of Martian dunes: if there were craters on the dunes, they must have been formed at the time of meteorite bombardment. As can be seen in the images, impact craters are not found on the surface of dunes, which have been formed, thus, *after* the epoch of meteorite bombardment (Marchenko and Pronin 1995).

But under the present atmospheric conditions of Mars, only winds 10 times stronger than on Earth are able to transport grains through saltation (Greeley et al. 1980). Such winds seldom occur on Mars (Sutton et al. 1978; Arvidson et al. 1983; Greeley et al. 1999; Sullivan et al. 2005). It has been therefore hypothesized that Martian dunes must have been formed in the past when the atmospheric density of Mars was still larger than in the present (Breed et al. 1979), whereas the time at which the present atmospheric density $\rho_{\mathrm{fluid}} \approx 0.016$ kg/m^3 (MGSRS 2006) has been reached is not known.

There is furthermore an important constraint that is related to the *size* of Martian dunes. The scale of Martian dunes appears inconsistent with an atmosphere 100 times lower density than the Earth's. In addition to the grain diameter d, there appears another length scale that is related to the motion of the grains and determines the physics of dunes. When grains travelling with an average saltation length ℓ impact on the bed, they eject further grains, thus increasing the amount of grains in the air. After a characteristic distance called *saturation length*, the amount of grains in the air is so high that the air is not able anymore to carry more sand and to erode the surface. Therefore, the saturation length of the flux, λ_{s}, is the relevant length scale of dunes: any sand dune that is smaller than the saturation length will disappear because of erosion. On the other hand, it has been suggested that λ_{s} is itself constant and proportional to $d\rho_{\mathrm{grain}}/\rho_{\mathrm{fluid}}$ (Hersen et al. 2002),

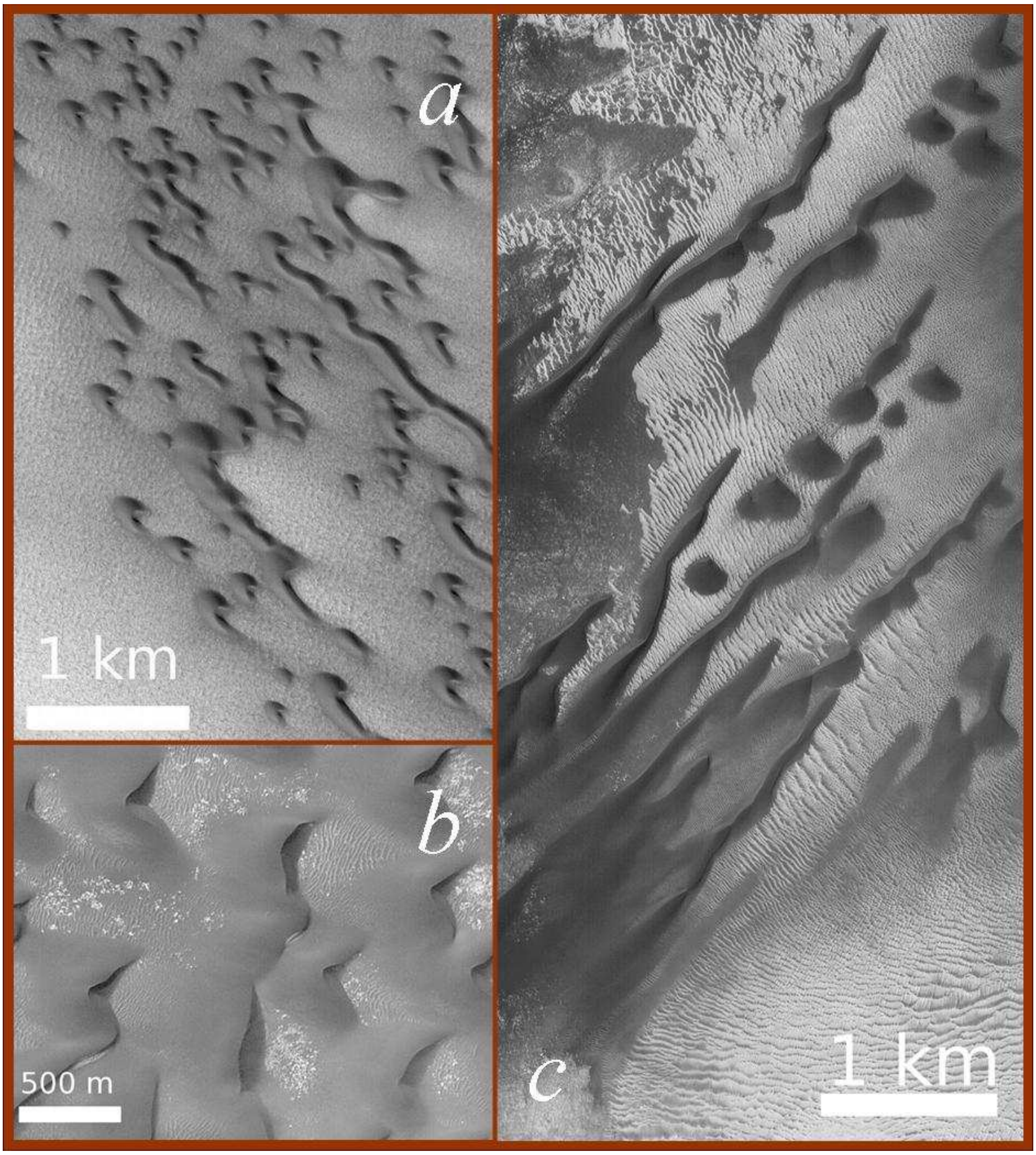

Figure 3: Sand dunes on Mars: **a.** Dunes near the north pole, at $77.6°$N, $103.6°$W. **b.** Dunes on the floor of Kaiser crater, near $46.5°$S, $340.7°$W. **c.** Dunes at a crater in Noachis Terra, near $46.0°$S, $323.6°$W.

and that sand dunes must have width larger than $20\, d\rho_{\mathrm{grain}}/\rho_{\mathrm{fluid}}$. This scaling relation implies that the smallest dunes on Mars should have width of 2 km, since $\rho_{\mathrm{grain}} = 3200$ kg$/$m^3 and $d = 500\mu$m, but on Mars there appear dunes of width of a few hundred meters in width. Only if the density of Mars were much higher, could dunes of the observed size be formed. Alternatively, Claudin and Andreotti (2006) speculated that the grain size of Martian dunes should be much smaller, thus challenging previous estimates of the grain diameter from thermal methods (Edgett and Christensen 1991; Fenton et al. 2003). On the other hand, Kroy et al. (2005) proposed that still unknown microscopic quantities of the Martian saltation must be unveiled and taken into account to correctly predict the minimal dune size on Mars.

Several wind tunnel simulations have been carried out to investigate saltation under atmospheric conditions of Mars (White et al. 1976; White 1979; Greeley and Iversen 1985; Marshall et al. 1998). Still only the average saltation trajectories, grain velocities and sand flux could be investigated from such experiments, while the saturation transient of the flux could not be measured. It has been as well not possible to measure saltation transport through the Mars missions, which never landed on dune fields. Thus, the question whether Martian dunes might be active or not, remains far from being answered.

Recently, much understanding has been gained through dune modellization, which encompasses the main ingredients of the physics of dunes and accounts for the microscopic quantities of sand transport, the trajectories of the grains and the rate at which particles enter saltation (Sauermann et al. 2001; Kroy et al. 2002). The dune model reproduces quantitatively the shape of terrestrial dunes, the sand flux and wind profile, the velocity of real dunes on Earth, and also the scale dependence of the dune shape and the observation of a minimal dune size (Kroy et al. 2002; Sauermann et al. 2003). Furthermore, the model has been applied to calculate interaction of dunes in a field and unveiled the physical mechanisms behind the apparent solitary wave behaviour of dunes (Schwämmle and Herrmann 2003; Durán et al. 2005). Recently, the model equations have been extended to calculate the behaviour of sand dunes in the presence of vegetation (Durán and Herrmann 2006b), which is ubiquitous in coastal and humid areas of our planet and may stabilize the dunes (Tsoar and Blumberg 2002). The model could reproduce the shape of vegetated dunes, and the conditions for their stabilization. Indeed, it is also possible to calculate the evolution of dune fields of some few kilometers in length and width, to investigate the interaction between dunes and between dunes and obstacles or vegetation. The dune model is, therefore, not only a valuable tool in the investigation of dune shapes, but it can be certainly very helpful in coastal management and to improve our ability to control desert dune movement.

In this Thesis, we apply the dune model to calculate the formation of sand dunes on the *present* Mars. Our aim is to see whether Martian dunes could appear under the thin atmosphere of the red planet.

This is the first time that the dune model is extended to calculate sand transport in an environment different from the Earth. The dune model has parameters related to the atmosphere, sand and wind, which we must adapt to the Martian conditions. In fact, as we will see, many of the model parameters are known, while others must be estimated from the dune shape. One of our purposes is to obtain the wind strength that formed the dunes observed in the images of Mars.

One very common type of dunes on Mars are *barchans*, dunes that appear under unidirectional winds and occur mainly in craters on Mars (Bourke et al. 2004). As the model reproduces the shape of barchans which excellent quantitative agreement with measurements (Sauermann et al. 2003), we start calculating barchan dunes on Mars. On the other hand, there are also many dune shapes on Mars that were clearly formed by winds of complex regimes. In contrast to barchans, longitudinal dunes as those in fig. 3*c* are formed by winds of two main directions, and elongate in the direction of the resultant wind. Moreover, many exotic Martian dune shapes, which can be also seen in fig. 3*c*, appear on bedrock. Such dunes must have been also formed by a bimodal wind regime, since barchans should occur if the wind direction were constant. Therefore, to understand dune formation on Mars, it also appears fundamental to reproduce the shape of bimodal dunes.

However, first we must understand how longitudinal dunes appear. Which angles do the wind directions have to define to form them? At which rate must the wind change its direction in order to form bimodal dunes? In this manner, we begin applying the dune model to study first the appearance of different dune shapes observed on *Earth*. We want to investigate how the *wind regimes* and the *sand availability* on the ground — which are the relevant field quantities for the dune shape (Wasson and Hyde 1983; Bourke et al. 2004) — determine the shape (i) of barchans and transverse dunes (fig. 1*a*) and (ii) of the bimodal, linear dunes. Then, we extend the model to *Mars*, where we first concentrate on the simplest dunes, the barchan dunes. Next, we will compare with the shape of Martian bimodal dunes to obtain the timescale of wind changes on Mars.

Overview

This Thesis is organized as follows.

In Chapter 1 we will give a brief presentation of the dune model. We will examine fundamental concepts related to sand transport and formation of dunes which we need to understand the derivation of the model and to interpret the results of this Thesis. We will discuss the role of the wind regimes and sand availability for the appearance of different dune forms, which are studied in later chapters. Finally, we present equations that will be used to calculate the quantities governing saltation transport on Mars.

Chapter 2 is dedicated to the aeolian transport of sand on Mars. We present data obtained from Mars orbiters and landers, including wind velocity, roughness of the surface and grain diameter, which are used in the calculations of Martian dunes. We also show that evidences for saltation transport on the present Mars could be uncovered from combined data of satellite images and *in situ* measurements. Next, we apply the model equations to calculate saltation transport on Mars. We estimate the quantities that control the saltation trajectories and calculate the sand flux at different places on Mars.

We then study the different shapes of sand dunes on Mars and on Earth in chapters 3−6, as function of the wind regime and of the sand availability. In Chapter 3, we begin with the simplest dunes, the *barchan dunes*, with which we also start our exploration of Martian dunes. First, we examine the factors controlling the shape of barchan dunes on Earth and use our results to explain the shape of barchan dunes on Mars. From the shape of dunes, we also find a microscopic feature of the Martian saltation which is the missing link to understand the scale of Martian dunes. We find an equation for the rate at which grains enter saltation, which can be used in the calculations of dunes under different atmospheric conditions. We then estimate the wind velocity on Mars and predict the velocity of Martian barchans.

In chapter 4 we investigate the shape of *transverse dunes*. These dunes also appear under unidirectional winds, but when there is larger amounts of sand available for transport. Transverse dunes are very common in coastal areas of our planet, because of the high littoral drift due to the accumulation of sand on the beach (fig. 1a). Here we present field measurements of a transverse dune field in the Lençóis Maranhenses, a coastal dune field in northeastern Brazil. We show how the shape of transverse dunes depends on the dune size. Then, we calculate the inter-dune spacing and adapt the dune model to reproduce the height profile of the measured dunes.

In Chapter 5 we study the formation of dune fields. We introduce a simple model to study the evolution of a transverse dune field, and then we adapt this model to calculate the formation of coastal dune fields. The simple model consists of a set of phenomenological equations that include the results of our field observations in the Lençóis Maranhenses. We show that transverse dunes formed on sand sheets must behave differently from those on bedrock. We then use the complex dune model to calculate the formation of coastal fields starting with a sandy beach and an unidirectional wind of constant strength $u_{*}/u_{*\mathrm{t}}$.

In chapter 6, we study, for the first time using the dune model, the shape of dunes that appear under bimodal wind regimes. The wind direction oscillates between two directions, which define an angle θ_{w}, whereas the wind lasts at each direction for a characteristic time T_{w}. We investigate the conditions for the formation of *longitudinal dunes*. We also find different dune forms developing on bedrock depending on θ_{w} and T_{w}. Finally, we use our results to calculate dunes formed by bimodal winds on Mars, and obtain the corresponding values of Martian θ_{w} and T_{w}. We also estimate the timescale of changes in wind regimes on Mars from the shape of Martian dunes.

In Chapter 7 we present a summary of our results, and notice the implications of our findings for the formation and evolution of dunes on Mars. Finally, we conclude giving a quick estimation of rates of sand transport and dune sizes on Venus and Titan, using the equation for sand entrainment found from the shape of dunes on Mars.

Chapter 1

Physics of aeolian sand and sand dunes

Winds are the sources of energy for the mobilization of sand and the formation of dunes. Indeed, each particular type of dunes is a result of a certain wind regime, i.e. wind strength and direction. In this chapter, the physics of wind-blown sand and formation of dunes is discussed. We present the equations of the model for sand dunes, which will be used in the present work to calculate dunes on Mars and on Earth. This model incorporates the main mechanisms of the formation, propagation, and evolution of dunes, from the sand transport at a "microscopic" level to the development of dune avalanches and dune fields. Finally, we present the equations that will be used to obtain the values of the model parameters for Mars.

1.1 Wind-blown sand

Sand transport takes place near the surface, in the turbulent boundary layer of the atmosphere (Pye and Tsoar 1990). In this turbulent layer, the wind velocity $u(z)$ at a height z may be written as:

$$u(z) = \frac{u_*}{\kappa} \ln \frac{z}{z_0}, \tag{1.1}$$

where $\kappa = 0.4$ is the von Kármán constant, u_* is the wind shear velocity, which is used, together with the fluid density ρ_{fluid}, to define the shear stress $\tau = \rho_{\text{fluid}} u_*^2$, and z_0 is the aerodynamic roughness. u_* and z_0 are two independent variables which may be determined experimentally. One way to obtain them is to measure the wind velocity at different heights z, and to plot the data as a linear-log curve $u(z) \times \log z$. The inclination of the straight line of the fit is the shear velocity u_*, and the value of z for which $u(z) = 0$ is the roughness z_0. This method has been applied for instance to determine the wind profile, shear velocity and surface roughness at the Pathfinder landing site on Mars (Sullivan et al. 2000), as we will see in chapter 2.

The aerodynamic roughness z_0 is distinguished from the roughness z_0^{sand} which is of the order of a few tens of microns, and which is due to the microscopic fluctuations of the sand bed when the grains are at rest. z_0 means the "apparent" roughness which is a consequence of the motion of saltating grains. Bagnold (1941) already observed that z_0 must be larger than z_0^{sand}, and increases if there are pebbles or rocks.

1.1.1 Threshold wind strength for entrainment

There is a minimum wind velocity for particles to be transported. A turbulent wind exerts two types of forces on particles when blowing over a sand bed. The first is called the *drag force* F_{d}, which acts horizontally in the direction of the flow. This force may be written as $F_{\mathrm{d}} = \beta u_*^2[\rho_{\mathrm{grain}}\pi d^2/4]$, where d is the diameter of the particle, ρ_{grain} its density, and β contains information about the packing. The second force is the *lift force* $F_{\mathrm{l}} = \Delta p[\rho_{\mathrm{grain}}\pi d^2/4]$, which appears due to the static pressure difference Δp between the bottom and the top of the grain, caused by the strong velocity gradient of the air near the ground. Chepil (1958) showed that $F_{\mathrm{l}} = cF_{\mathrm{drag}}$, where $c \approx 0.85$. However, gravity g counteracts the lift force. The grain's weight may be written as $F_{\mathrm{g}} = (\rho_{\mathrm{grain}} - \rho_{\mathrm{fluid}})g[\pi d^3/6]$. F_{d}, F_{l} and F_{g} are depicted in fig. 1.1.

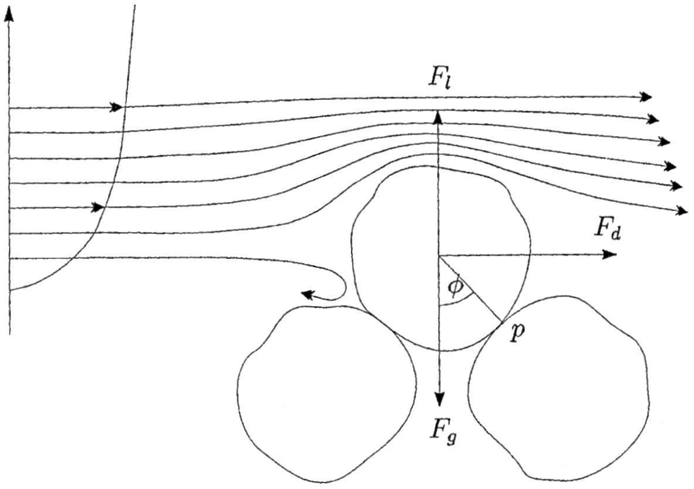

Figure 1.1: The lift force F_{l}, the drag force F_{d}, and the weight of the grain, F_{g} determine the threshold for particle entrainment. This is defined by the momentum balance with respect to the pivot point p. After Sauermann (2001).

Particles within the uppermost layer of the bed are entrained into flow when the aerodynamic forces overcome the gravitational force. The particle is about to rotate around its pivot point p (fig. 1.1) when the balance between the forces is achieved:

$$F_{\mathrm{d}}\frac{d}{2}\cos\phi = (F_{\mathrm{g}} - F_{\mathrm{l}})\frac{d}{2}\sin\phi. \tag{1.2}$$

Equation (1.2) defines a minimal shear velocity u_* for particle entrainment, which we call *fluid threshold velocity* $u_{*\mathrm{ft}}$, or threshold wind friction speed for aerodynamic entrainment. We solve eq. (1.2) for the threshold aerodynamic shear stress $\tau_{\mathrm{ft}} = \rho_{\mathrm{fluid}}u_{*\mathrm{ft}}^2$:

$$\frac{\tau_{\mathrm{ft}}}{(\rho_{\mathrm{grain}} - \rho_{\mathrm{fluid}})gd} = \frac{2}{3\beta}\left(\frac{\sin\phi}{\cos\phi + c\sin\phi}\right). \tag{1.3}$$

The angle ϕ and the parameter β, which appear on the right-hand side of eq. (1.3) reflect the characteristics of the packing of the grains, their shape and sorting. Shields (1936) introduced a dimensionless coefficient Θ to express the ratio of the applied tangential force to the resisting grain movement: $\Theta = \tau_{\text{ft}}/(\rho_{\text{grain}} - \rho_{\text{fluid}})gd$ gives the term at the right-hand side of eq. (1.3). In this manner, the threshold shear velocity for aerodynamic entrainment is given by the equation

$$u_{*\text{ft}} = A\sqrt{\frac{(\rho_{\text{grain}} - \rho_{\text{fluid}})gd}{\rho_{\text{fluid}}}}, \tag{1.4}$$

where $A = \sqrt{\Theta}$ is called the Shields parameter and has value around 0.11. In this manner, the threshold wind velocity increases with gravity and with the size and the density of the grains, and decreases with the atmospheric density ρ_{fluid}.

Once a particle is lifted from the bed, it can be transported in different manners: suspension, saltation, reptation and creep. Suspension refers to very small particles (also called “fines”). On Earth, particles with diameter between 40 and $60\,\mu$m may remain suspended in air travelling long distances in irregular trajectories before reaching the ground again. Suspension becomes more difficult with increasing particle size, since in this case the fluctuations of the vertical component of the wind velocity become insignificant compared to the weight of the particle (Tsoar and Pye 1987). Particles of diameter between 170 and $350\,\mu$m enter *saltation*, which is the movement of sand grains in ballistic trajectories close to the ground (Bagnold 1941; Pye and Tsoar 1990). The term “reptation” refers to saltating grains that transfer a too low amount of momentum at the collision with the bed, and thus cannot eject further grains (Andreotti 2004). Finally, particles that are too large to enter saltation may just “creep” on the bed. Evidences for basically all aeolian transport modes observed on Earth have been uncovered on Mars (Sagan et al. 1972; Arvidson et al. 1983; Greeley et al. 2000; Sullivan et al. 2005). Aeolian transport of particles on Mars will be discussed in the next chapter.

1.1.2 Saltation

As first noticed by Bagnold (1941), the sand of dunes is transported through saltation. In fact, grain size histograms of particle size of dunes appear sharply distributed around diameter $d = 250\,\mu$m (Pye and Tsoar 1990). Therefore, saltation will be the aeolian transport mode considered in the present work.

The grains that form terrestrial dunes are mainly grains of quartz, whose density is $\rho_{\text{grain}} = 2650$ kg$/$m^3 (Bagnold 1941). Using the values $g = 9.81$ m$/$s^2 and $\rho_{\text{fluid}} = 1.225$ kg$/$m^3, we find that the threshold shear velocity for entrainment (eq. 1.4) of saltating grains is $u_{*\text{ft}} \approx 0.28$ m$/$s. Once the wind velocity achieves a value larger than $u_{*\text{ft}}$, some grains are lifted from the sand bed and are next accelerated downwind. The relevant forces acting on saltating grains are the gravitational and drag forces, whereas the lift force is only important to start saltation. Since gravity dominates the vertical motion, it follows that grains saltate in ballistic trajectories (fig. 1.2).

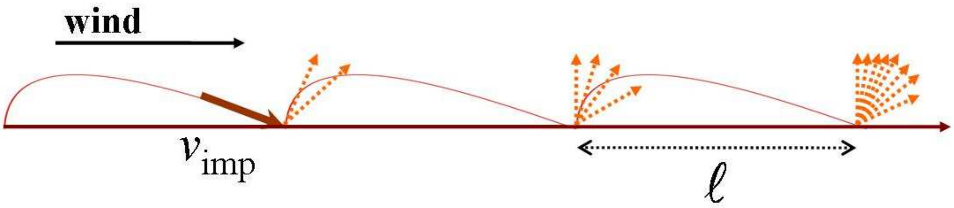

Figure 1.2: Schematic diagram with the main elements of *saltation*. The number of ejected grains (indicated by the arrows) is proportional to the velocity of the impacting grain, v_{imp} (Anderson and Haff 1988). The mean saltation length of the grains is defined as ℓ.

Saltating grains impact back onto the ground after being accelerated downwind. The interaction of the impacting grains with the bed is usually called *splash*. After splash, other grains may be ejected from the sand bed, depending on the velocity (momentum) of the impacting grains. Anderson and Haff (1988) have shown that the number of ejected particles increases linearly with the grain velocity v_{imp} at the grain-bed collision. The splashed particles are ejected with different velocities and at different angles, and in this manner only a part of the ejected grains enter saltation (Andreotti 2004), the other fraction remaining close to the bed (in reptation or creep). The stochastic process of the splash has been studied by many authors, and still it remains poorly understood (Anderson and Haff 1988; Anderson and Haff 1991; Rioual et al. 2000).

The splash is the main mechanism of sand entrainment during saltation. The wind velocity may even decrease to values lower than $u_{*\text{ft}}$, and still saltation can be sustained, once initiated. However, the wind strength cannot be lower than the *impact threshold velocity* $u_{*\text{t}}$, which is around 80% $u_{*\text{ft}}$. Saltation ceases if $u_* < u_{*\text{t}}$, and therefore the impact threshold velocity is an essential parameter for aeolian sand transport.

Once saltation starts, the number of saltating grains first increases exponentially due to the multiplicative process inherent in the splash events (fig. 1.2). However, because of Newton's second law, the wind loses more momentum with increasing number of entrained particles until a saturation is reached (Owen 1964; Anderson and Haff 1988; McEwan and Willetts 1991; Butterfield 1993). The presence of saltating grains reduces the wind strength and thus modifies the profile of the wind velocity above the ground. The height at which the reduction is maximum nearly coincides with the height at which the probability to find saltating particles is maximum (Almeida et al. 2006). When the number of grains has increased to a maximum value, the wind strength is not enough anymore to lift further grains from the bed. The maximum number of grains a wind of given strength can carry through a unit area per unit time defines the saturated flux of sand q_{s}.

A consequence of saltation transport is the erosion and deposition of sand and the formation of sand dunes. For sand dunes to appear, however, there must be an amount of sand distributed on the ground over a distance larger than the *saturation length* of the flux. This is because any sand surface is eroded at all positions where the flux increases. If there is enough sand on the ground, many different types of dunes may appear, as described in the next section.

1.2 Factors determining dune types

The different shapes of dunes observed in nature are consequence of the *wind regime* and of the *sand availability*, i.e. the amount of mobile sand on the ground.

When the wind direction is nearly constant over the year, *crescent* dunes are formed. *Barchan dunes* are crescent dunes that develop on bedrock, when there is not enough sand to cover the ground (fig. 1.3a). As the sand availability increases, *transverse dunes* appear (fig. 1.3b). The windward side of barchans and transverse dunes has a gentle average slope, typically around $10°$ (Hesp and Hastings 1998; Parteli et al. 2006c). Saltating grains are transported downwind through the windward side of these dunes and are deposited at the lee side through avalanches, which occur wherever the downwind slope of the dune reaches the angle of repose, $\theta_{\rm r} \approx 34°$ (Bagnold 1941). Barchans and transverse dunes occur frequently in coastal areas of high-energy, unimodal winds, but they are also common in many desert areas of Africa and Asia.

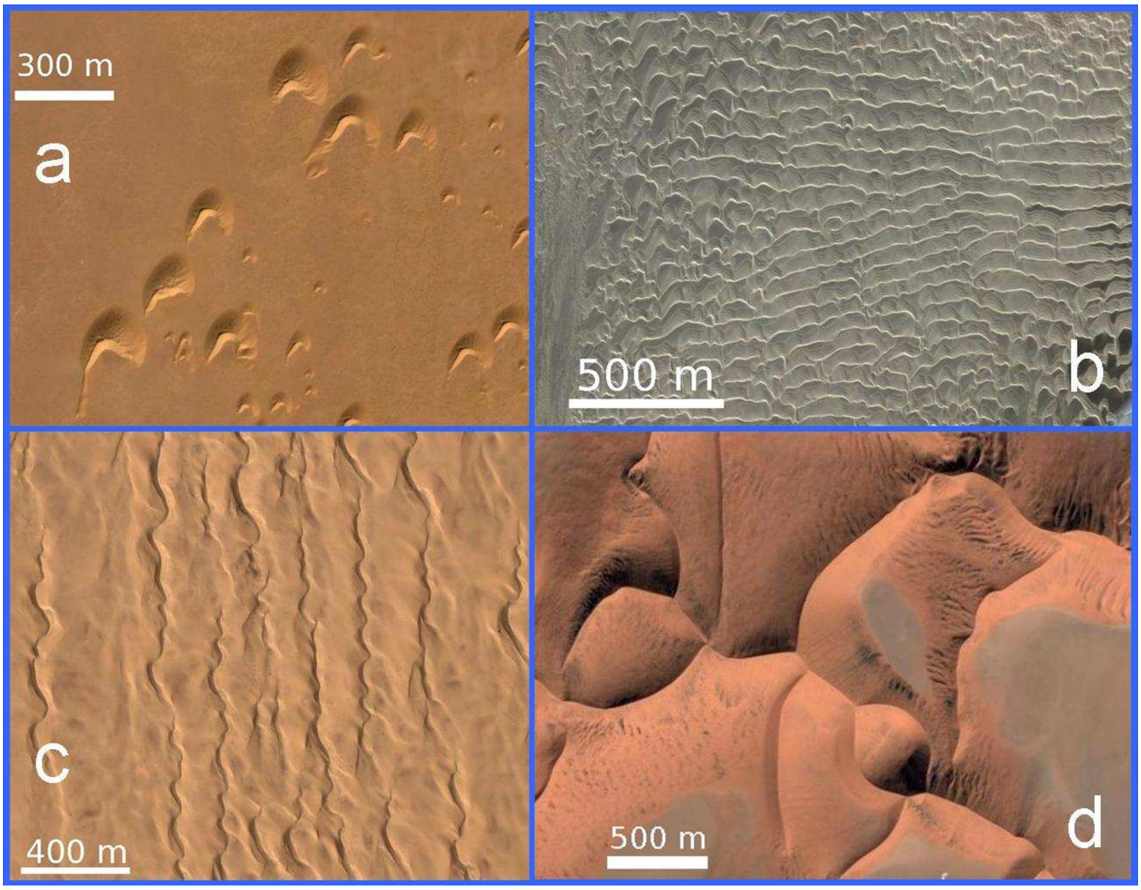

Figure 1.3: Sand dunes on Earth. **a.** *Barchan dunes* in Westsahara, near $26.51°$N, $13.21°$W. **b.** *Transverse dunes* in Baja California, near $28.06°$N, $114.05°$W. **c.** *Linear dunes* in Namibia, near $24.55°$S, $14.57°$E. **d.** *Star dunes* in Namibia, near $24.46°$S, $15.25°$E. Images from Google Earth.

Indeed, nearly $3/4$ of the terrestrial sand seas is covered with dunes that appear under complex wind regimes. *Longitudinal dunes*, also called *seif* or *linear* dunes (fig. 1.3c), appear when the wind has two prevailing components which define a resultant direction in which net transport of sand occurs. Normally, the wind alternates between its two directions, and the shape of linear dunes depends on the period of the oscillation and also on the angle between the wind directions. Multimodal wind regimes form more complex dune types, called *star dunes* (fig. 1.3d).

Fryberger and Dean (1979) classify the different types of dunes according to the shape of the corresponding *sand roses* (fig. 1.4). A sand rose is a circular histogram that gives the potential sand drift from the 16 directions of the compass. Each arm of the sand rose indicates the direction from which the wind blows (as in the case of the wind rose), and the length of each arm is proportional to the potential rate of sand transport from the direction indicated by the arm (Fryberger and Dean 1979).

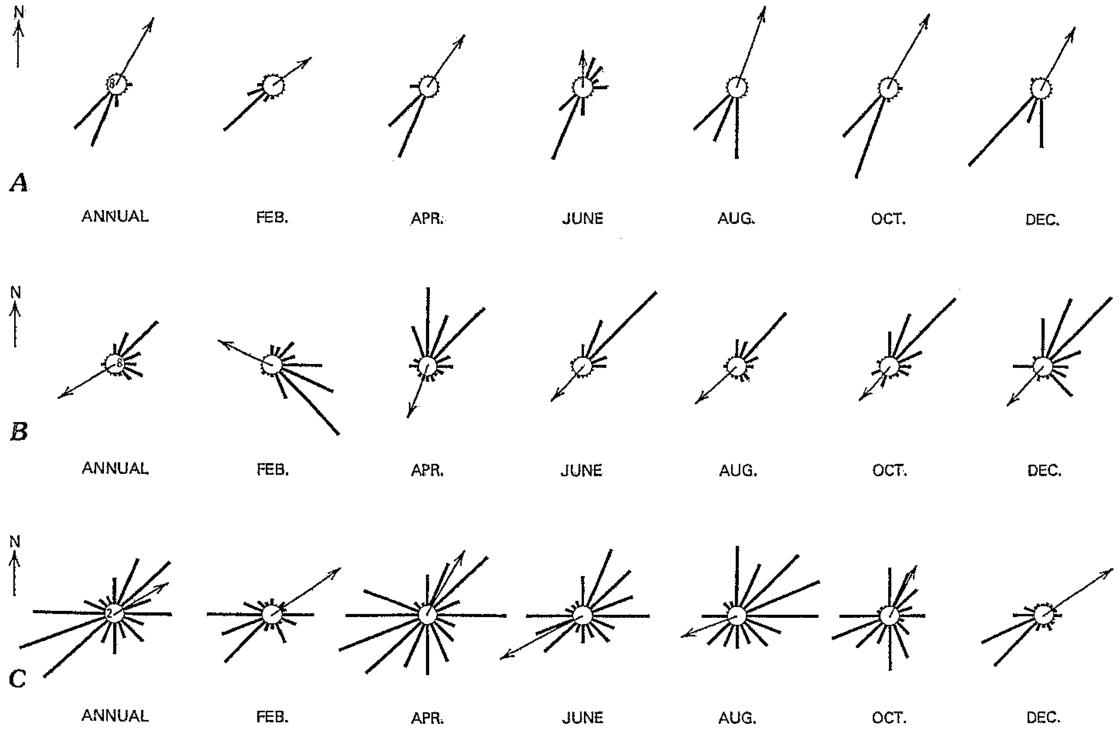

Figure 1.4: Annual and bimonthly sand roses of three basic dune types (after Fryberger and Dean (1979)). A. Narrow unimodal; barchanoid dunes near Pelican Point, South-West Africa. B. Bimodal; linear dunes near Fort-Gourard, Mauritania. C. Complex; star dunes near Ghudamis, Libya. Arrows indicate resultant drift direction.

In fig. 1.4, we see annual sand roses which depict the distribution of the winds in areas of different types of dunes. The simplest sand rose in this figure is the one of a barchan dune field in South Africa (A). The sand rose in (B) corresponds to the field of linear dunes near Fort-Gouraud, Mauritania. The sand rose in (C) is the most complex one of fig. 1.4. It is the sand rose of a field of *star dunes* near Ghudamis, Libya. Such dunes have three or more arms (horns) and also more than one avalanche or slip face (fig. 1.3d). They are among the largest dunes on Earth, and develop in areas of large accumulation of sand resulting from the multimodal wind regimes. As a consequence, star dunes have negligible rate of motion compared to barchan dunes.

Summarizing, in fig. 1.5 we see how the shape of dunes depends on the wind regime and on the sand availability.

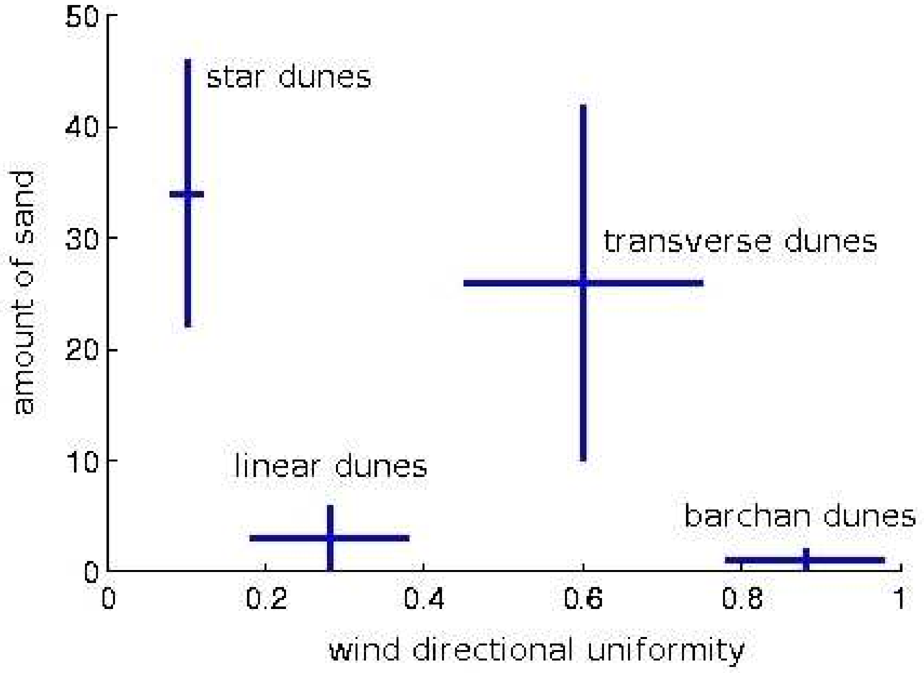

Figure 1.5: The shape of dunes depends on the amount of sand on the ground and on the wind variability (0: greatest; 1: least). The amount of sand in the dunes is expressed as equivalent spread-out sand depth in meters. After Wasson and Hyde (1989).

Dunes on Mars

In fig. 1.6, we see that the same types of dunes shown in fig. 1.3 occur on Mars. Figure 1.6 shows MOC images of barchans (a), transverse dunes (b), linear dunes (c) and star dunes (d) in different places on Mars. We see that sand dunes may help significantly investigation of climatic conditions of Mars. From the dune shapes, it is possible to infer which are the wind regimes associated with different areas on Mars. Barchans and transverse dunes are the most common dune forms on Mars, and appear mainly in craters and in the north polar region (Breed et al. 1979; Tsoar et al. 1979; Bourke et al. 2004). On the other hand, longitudinal and star dunes seldom occur, which led several authors to conclude that wind regimes on Mars are in general narrow unimodal (Edgett and Christensen 1994; Lee and Thomas 1995).

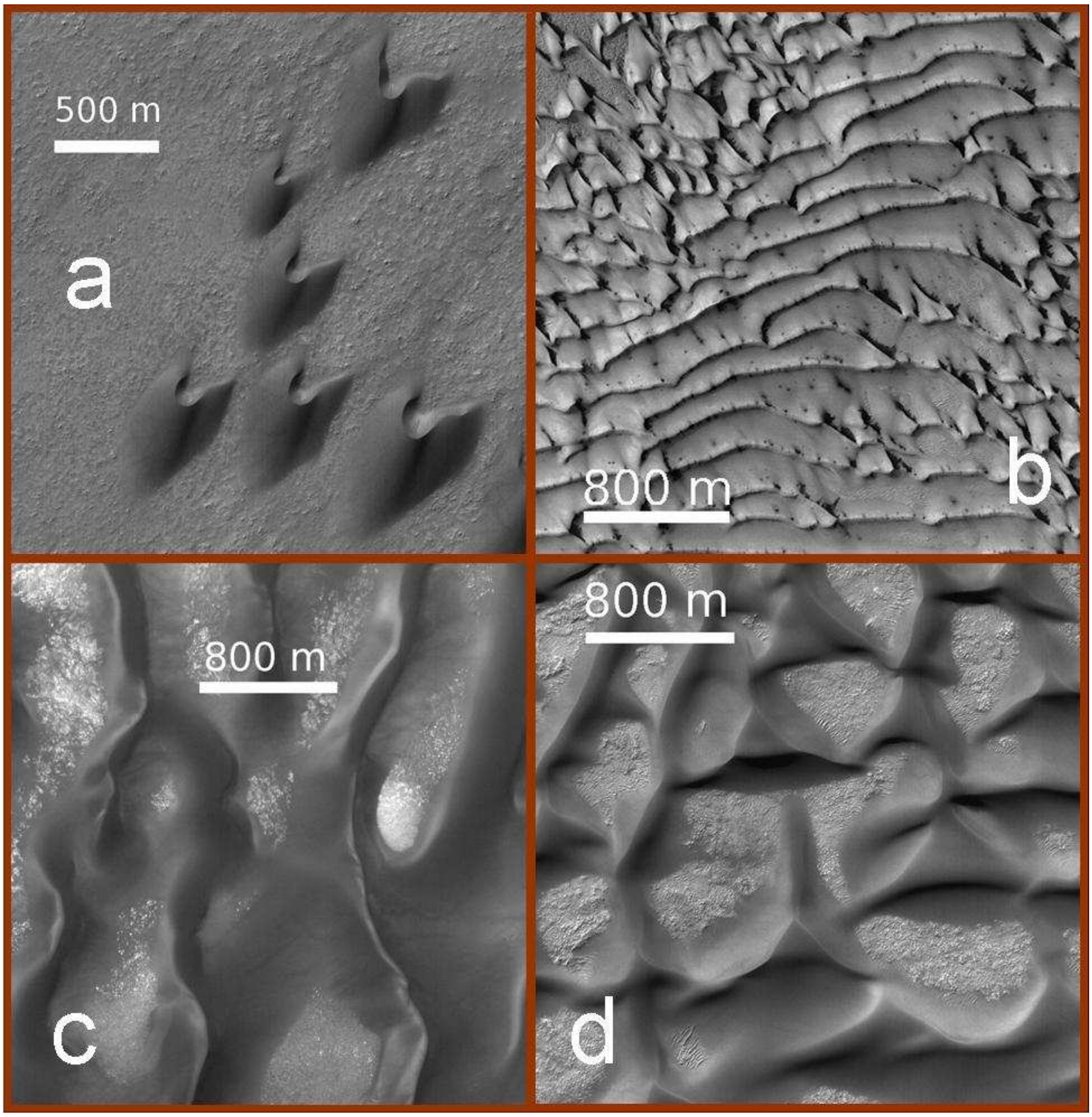

Figure 1.6: Mars Global Surveyor MOC images of sand dunes on Mars. **a.** Barchan dunes in the Arkhangelsky Crater, near $41.2°$S, $25.0°$W. **b.** Frost-covered transverse dunes in the north polar region, near $80.0°$N, $114.6°$W. **c.** Linear dunes on the floor of a crater in Noachis Terra, located near $45.4°$S, $331.2°$W. **d.** Star dunes on the floor of Bunge crater, located near $33.8°$S, $48.9°$W.

There are also other factors which determine the shape of dunes. For example, in many terrestrial dune fields, the shape of dunes is modified by the presence of vegetation, which transforms barchan dunes into "U" shaped parabolic dunes (Tsoar and Blumberg 2002; Durán and Herrmann 2006b). Moreover, inter-dune lagoons in coastal dune fields also influence the dune shape, while the movement of dunes in the north polar region of Mars competes with the seasonal caps of CO_2 frost. In the present work, we will not concentrate on such factors. We will study the shape of dunes on Earth and on Mars resulting from the conditions of wind and from the amount of sand that can be transported by the wind.

1.3 Model for sand dunes

After 60 years of research on aeolian transport and dune formation since Bagnold's pioneer works, a complete but minimal, theoretical model which couples the equations of wind and sand transport and reproduces the evolution of dunes could be finally achieved (Sauermann et al. 2001; Kroy et al. 2002; Schwämmle and Herrmann 2005; Durán and Herrmann 2006a). The fundamental idea of the model is to consider the bed-load as a thin fluid-like granular layer on top of an immobile sand bed. The dune model combines an analytical description of the turbulent wind velocity field above the dune with a continuum saltation model. One of the most important novelties of this modellization has been the inclusion of saturation transients in the calculation of the sand flux, which allowed reproduction of the minimal dune scale and the breakdown of the scale invariance of dunes.

1.3.1 Wind shear stress

According to eq. (1.1), the wind velocity over a flat surface increases logarithmically with the height above the ground. A dune or a smooth hill can be considered as a perturbation of the surface that causes a perturbation of the air flow onto the hill. In the dune model, the shear stress perturbation is calculated in the two dimensional Fourier space using the algorithm of Weng et al. (1991) for the components τ_x and τ_y, which are, respectively, the components parallel and perpendicular to the wind direction. The procedure has been presented in details by Kroy et al. (2002) and Schwämmle and Herrmann (2005). The following expressions hold for the shear stress perturbation components $\hat{\tau}_x$ and $\hat{\tau}_y$:

$$\hat{\tau}_x(k_x, k_y) = \frac{2\,h(k_x, k_y)k_x^2}{|k|\,U^2(l)} \cdot \left(1 + \frac{2\ln(\mathcal{L}|k_x|) + 4\epsilon + 1 + \mathrm{i}\,\mathrm{sign}(k_x)\pi}{\ln\left(l/z_0\right)}\right), \tag{1.5}$$

and

$$\hat{\tau}_y(k_x, k_y) = \frac{2\,h(k_x, k_y)k_x k_y}{|k|\,U^2(l)}, \tag{1.6}$$

where the axis $x(y)$ points parallel (perpendicular) to the wind direction, k_x and k_y are wave numbers, $|k| = \sqrt{k_x^2 + k_y^2}$, $\epsilon = 0.577216$ (Euler's constant) and $\mathcal{L}$ is the characteristic length of a hill (Hunt et al. 1988). It is defined as the horizontal distance between the crest, which is the position of maximum height H_{max}, and the position of the windward side where the height is $H_{\mathrm{max}}/2$. The variable $\mathcal{L}$ is computed iteratively, i.e. it is not a constant parameter but depends on the size of the hill at each iteration. $U(l) = u(l)/u(h_{\mathrm{m}})$ is the undisturbed logarithmic profile (1.1) calculated at height l, which is given by

$$l = \frac{2\kappa^2\mathcal{L}}{\ln l/z_0}, \tag{1.7}$$

and normalized by the velocity at the reference height $h_{\mathrm{m}} = \mathcal{L}/\sqrt{\log \mathcal{L}/z_0}$, which separates the middle and upper flow layers (Hunt et al. 1988). The shear stress in the direction i ($i = x, y$) is then given by:

$$\vec{\tau}_i = \hat{i}\left[\tau_0(1 + \hat{\tau}_i)\right], \tag{1.8}$$

where τ_0 is the undisturbed air shear stress over the flat ground. From the shear stress, the sand flux is calculated according to the continuum saltation model (Sauermann et al. 2001).

In what follows, we give a brief presentation of the sand transport equations and refer to Sauermann et al. (2001) and Schwämmle and Herrmann (2005) for the extensive derivation of the saltation model.

1.3.2 Continuum saltation model

The saltation model is derived from the mass and momentum conservation in presence of erosion and external forces. The sand bed represents an open system which can exchange grains with the saltation layer, for which the erosion rate $\Gamma(x, y, t)$ at any position (x, y) represents a source term:

$$\frac{\partial \rho}{\partial t} + \vec{\nabla} \cdot (\rho \vec{v}) = \Gamma. \tag{1.9}$$

where $\rho(x, y, t)$ is the density of grains in the saltation layer, and $\vec{v}(x, y, t)$ is the characteristic velocity of the saltating grains.

Erosion rate

The erosion rate Γ is defined as the difference between the vertical flux of grains leaving the bed and the rate ϕ at which grains impact onto the bed:

$$\Gamma = \phi(n - 1), \tag{1.10}$$

where n is the average number of splashed grains. The flux of saltating grains reduces the air born shear stress (“feedback effect”). At saturation, the number of ejecta nearly compensates the number of impacting grains ($n = 1$), and the air shear stress at the bed, τ_{a}, is just large enough to sustain saltation, i.e. τ_{a} is close to the threshold $\tau_{\mathrm{t}} = \rho_{\mathrm{fluid}} u_{*\mathrm{t}}^2$ (Owen 1964). In this manner, we write n as a function $n(\tau_{\mathrm{a}}/\tau_{\mathrm{t}})$ with $n(1) = 1$. Expansion of n into a Taylor series up to the first order term at the threshold yields

$$n = 1 + \tilde{\gamma}\left(\frac{\tau_{\mathrm{a}}}{\tau_{\mathrm{t}}} - 1\right), \tag{1.11}$$

where

$$\tilde{\gamma} = \frac{\mathrm{d}n}{\mathrm{d}(\tau_{\mathrm{a}}/\tau_{\mathrm{t}})} \tag{1.12}$$

is the *entrainment rate* of grains into saltation, and determines how fast the system reaches saturation (Sauermann et al. 2001). The parameter $\tilde{\gamma}$ depends on microscopic quantities of the grain-bed and wind-grains interactions, which are not available within the scope of the model. Therefore, $\tilde{\gamma}$ must be determined from comparison with measurements or microscopic simulations.

The rate ϕ at which the grains impact onto the bed is defined as $\phi = \rho|\vec{v}|/\ell$, where ℓ is the average saltation length. Substituting this expression for ϕ and eq. (1.11) into eq. (1.10), the balance eq. (1.9) yields

$$\frac{\partial \rho}{\partial t} + \vec{\nabla} \cdot (\rho \vec{v}) = \frac{\rho|\vec{v}|}{\ell}\tilde{\gamma}\left(\frac{\tau_{\rm a}}{\tau_{\rm t}} - 1\right). \tag{1.13}$$

But $\tau_{\rm a} = \tau - \tau_{\rm g}$, where $\tau_{\rm g}$ is the contribution of the grains to the total shear stress at the ground (Sauermann et al. 2001). In this manner we rewrite the right-hand-side of the above expression in terms of $\tau_{\rm g}$:

$$\frac{\rho|\vec{v}|}{\ell}\tilde{\gamma}\left(\frac{\tau - \tau_{\rm g}}{\tau_{\rm t}} - 1\right) = \frac{\rho|\vec{v}|}{\ell}\tilde{\gamma}\left(\frac{\tau - \tau_{\rm t}}{\tau_{\rm t}} - \frac{\tau_{\rm g}}{\tau_{\rm t}}\right) = \frac{\rho|\vec{v}|}{\ell}\tilde{\gamma}\frac{\tau - \tau_{\rm t}}{\tau_{\rm t}}\left(1 - \frac{\tau_{\rm g}}{\tau - \tau_{\rm t}}\right). \tag{1.14}$$

The grain born shear stress is defined as $\tau_{\rm g} = \phi \Delta v_{\rm hor} = \Delta v_{\rm hor}\rho|\vec{v}|/\ell$, where $\Delta v_{\rm hor} = v_{\rm hor}^{\rm imp} - v_{\rm hor}^{\rm eje}$ gives the difference between the horizontal velocities (in the direction of flow) of the grains at the moment of impact, $v_{\rm hor}^{\rm imp}$ and at the moment of ejection, $v_{\rm hor}^{\rm eje}$. Therefore, eq. (1.14) may be written as

$$\frac{\partial \rho}{\partial t} + \vec{\nabla} \cdot (\rho \vec{v}) = \frac{\rho|\vec{v}|}{\ell}\tilde{\gamma}\frac{\tau - \tau_{\rm t}}{\tau_{\rm t}}\left(1 - \rho|\vec{v}|\frac{\Delta v_{\rm hor}/\ell}{\tau - \tau_{\rm t}}\right), \tag{1.15}$$

which is differential equation for the density ρ of grains in the saltation layer. The mean saltation length ℓ, the average grain velocity $\vec{v}$ and $\Delta v_{\rm hor}$ are calculated as below.

Average saltation trajectory and grain velocity

The mean saltation length ℓ is defined as the length of a ballistic trajectory (Sauermann et al. 2001): $\ell = v_z^{\rm eje}(2|\vec{v}|/g)$, where $v_z^{\rm eje}$ is the initial vertical velocity, g is gravity and $\vec{v}$ is the average grain velocity. Further, $v_z^{\rm eje}$ is related to the gain in horizontal velocity of the grains, $\Delta v_{\rm hor}$, through an effective restitution coefficient for the grain-bed interaction, α (Sauermann et al. 2001), which is defined as

$$\alpha = \frac{v_z^{\rm eje}}{\Delta v_{\rm hor}} = \frac{v_z^{\rm eje}}{v_{\rm hor}^{\rm imp} - v_{\rm hor}^{\rm eje}}. \tag{1.16}$$

In this manner, the mean saltation length is written as

$$\ell = v_z^{\rm eje}\frac{2|\vec{v}|}{g} = \frac{\alpha}{\Delta v_{\rm hor}}\frac{2|\vec{v}|}{g} = \frac{1}{r}\left[\frac{2|\vec{v}|^2\alpha}{g}\right], \tag{1.17}$$

where $r \equiv |\vec{v}|/\Delta v_{\rm hor}$ is the constant of proportionality between the average grain velocity $|\vec{v}|$ and the difference between impact and eject velocity of the grains, $\Delta v_{\rm hor}$.

The mean velocity of the saltating grains, $\vec{v}$, is determined from the balance between three forces: (i) the drag force acting on the grains; (ii) the bed friction which yields the loss of momentum when the grains impact onto the ground, and (iii) the downhill force.

(i) The drag force acting on a single grain in the saltation layer which has velocity $\vec{v}_{\rm grain}$ and experiences a wind velocity $\vec{u}_{\rm fluid}$ is the Newton drag force on a spherical particle of diameter d,

$$\vec{F}_{\rm drag} = \frac{1}{2}\rho_{\rm fluid} C_{\rm d} \frac{\pi d^2}{4}(\vec{u}_{\rm fluid} - \vec{v}_{\rm grain})|\vec{u}_{\rm fluid} - \vec{v}_{\rm grain}|, \tag{1.18}$$

where $C_{\rm d}$ is the drag coefficient. We multiply $\vec{F}_{\rm drag}$ with the density ρ of the saltation layer and divide it by the mass $m = (4/3)\pi(d/2)^3\rho_{\rm grain}$ of a grain to obtain the drag force acting on a volume element of the saltation layer:

$$\vec{f}_{\rm drag} = \rho \frac{3}{4} C_{\rm d} \frac{\rho_{\rm fluid}}{\rho_{\rm grain}} \frac{1}{d}(\vec{u}_{\rm eff} - \vec{v})|\vec{u}_{\rm eff} - \vec{v}|, \tag{1.19}$$

where the velocity $\vec{u}_{\rm eff}$ is called *effective wind velocity*, which is a representative wind velocity value $\vec{u}_{\rm fluid}$ for the drag force on the grains in the saltation layer, and is calculated at a height z_1 above the ground. However, here we cannot use the undisturbed wind profile, eq. (1.1), to compute $\vec{u}_{\rm eff} = \vec{u}_{\rm fluid}(z_1)$, because the saltating grains modify the wind profile close to the ground ("feedback effect").

The total shear stress τ at any height z above the ground is constant, and given by $\tau_{\rm fluid}(z) + \tau_{\rm grains}(z)$, where $\tau_{\rm fluid}(z)$ and $\tau_{\rm grains}(z)$ are the air born shear stress and the grain born shear stress at height z, respectively. At the ground, $\tau_{\rm grains}(z=0) \equiv \tau_{\rm g}$ and $\tau_{\rm fluid}(z=0) \equiv \tau_{\rm a}$, while the shear velocity $u_{*{\rm fluid}}(z) \equiv \sqrt{\tau_{\rm fluid}(z)/\rho_{\rm fluid}}$ is varying with the height z. As shown by Anderson and Haff (1991), the profile $\tau_{\rm grains}(z)$ is nearly exponential. Thus, we can write $\tau_{\rm grains}(z) = \tau_{\rm g} e^{-z/z_{\rm m}}$, where $z_{\rm m}$ is called *mean saltation height*. In this manner, the modified wind profile $\vec{u}_{\rm fluid}$ follows the equation

$$\frac{\partial \vec{u}_{\rm fluid}}{\partial z} = \frac{\vec{u}_{*{\rm fluid}}(z)}{\kappa z} = \frac{\vec{u}_*}{\kappa z}\sqrt{1 - \frac{\tau_{\rm grains}(z)}{\tau}} = \frac{\vec{u}_*}{\kappa z}\sqrt{1 - \frac{\tau_{\rm g} e^{-z/z_{\rm m}}}{\tau}}. \tag{1.20}$$

To obtain the modified wind profile, we integrate eq. (1.20) from $z_0^{\rm sand}$ to the height z after linearizing the exponential function. The value of $\vec{u}_{\rm fluid}$ at the reference height z_1 gives the effective wind velocity $\vec{u}_{\rm eff}$. For values of z_1 which follow the condition $z_0^{\rm sand} < z_1 \ll z_{\rm m}$, the following expression is obtained for $\vec{u}_{\rm eff}$ (Sauermann et al. 2001):

$$\vec{u}_{\rm eff} = \frac{u_*}{\kappa}\sqrt{1 - \frac{\tau_{\rm g}}{\tau}}\left[2\sqrt{1 + \frac{z_1}{z_{\rm m}}\frac{\tau_{\rm g}}{\tau - \tau_{\rm g}}} - 2 + \ln\frac{z_1}{z_0^{\rm sand}}\right]\frac{\vec{u}_*}{|\vec{u}_*|}, \tag{1.21}$$

where the grain born shear stress at the ground can be written using the result of eq. (1.17):

$$\tau_{\rm g} = \frac{\Delta v_{\rm hor}\rho|\vec{v}|}{\ell} = \frac{\rho g}{2\alpha}. \tag{1.22}$$

Inserting eq. (1.21) into eq. (1.19) gives the drag force of the wind on a volume element of the saltation layer.

(ii) Saltating grains give part of their momentum to the ground when they impact onto it. This results in a deceleration of the grains. The friction force of the bed on the grains, $f_{\rm bed}$, must exactly compensate the grain born shear stress at the ground, $\tau_{\rm g}$. Therefore, we have

$$\vec{f}_{\rm bed} = -\tau_{\rm g}\frac{\vec{v}}{|\vec{v}|} = -\frac{\rho g}{2\alpha}\frac{\vec{v}}{|\vec{v}|}. \tag{1.23}$$

(iii) Besides the aeolian drag force and the bed friction, an additional force — the gravitational force, $\vec{f}_{\mathrm{grav}}$ — acts on the saltation layer in the presence of bed slopes. The gravitational force is written as

$$\vec{f}_{\mathrm{grav}} = -\rho g \vec{\nabla} h. \tag{1.24}$$

This force is negligible for the downwind motion of the saltation layer for instance on the windward side of a barchan or transverse dune. However, $\vec{f}_{\mathrm{grav}}$ plays an important role for the *lateral sand transport*. For instance, the slope of barchan dunes in lateral directions reaches 20° (Hesp and Hastings 1998; Sauermann et al. 2000). Since the cross profile of barchans has a parabolic shape (Sauermann et al. 2000), the magnitude of the gravitational force increases linearly from the center to the sides of the dune.

The balance $\partial\vec{v}/\partial t + (\vec{v}\cdot\vec{\nabla})\cdot\vec{v} = (\vec{f}_{\mathrm{drag}} + \vec{f}_{\mathrm{bed}} + \vec{f}_{\mathrm{grav}})/\rho$ leads to an equation for the average velocity $\vec{v}$ of the grains in the saltation layer:

$$\frac{\partial\vec{v}}{\partial t} + (\vec{v}\cdot\vec{\nabla})\cdot\vec{v} = \frac{3}{4}\frac{\rho_{\mathrm{fluid}}}{\rho_{\mathrm{grain}}}\frac{C_{\mathrm{d}}}{d}(\vec{u}_{\mathrm{eff}} - \vec{v})|\vec{u}_{\mathrm{eff}} - \vec{v}| - \frac{g\vec{v}}{2\alpha|\vec{v}|} - g\vec{\nabla}h. \tag{1.25}$$

Sand flux

The closed model of saltation transport consists in substituting the grain velocity obtained from eq. (1.25), using the effective wind speed $\vec{u}_{\mathrm{eff}}$ (eq. (1.21)), into eq. (1.15). However, some considerable simplifications are employed to solve the equations.

First simplification — To solve eqs. (1.15) and (1.25), we use the *stationary* condition $\partial/\partial t = 0$, since the time scale of the surface evolution of a dune is several orders of magnitude larger than the typical values of transient time of the saltation flux (some seconds). We can thus rewrite eq. (1.15) in the following manner:

$$\vec{\nabla}\cdot(\rho\vec{v}) = \frac{\rho|\vec{v}|}{\ell}\tilde{\gamma}\frac{\tau - \tau_{\mathrm{t}}}{\tau_{\mathrm{t}}}\left(1 - \rho|\vec{v}|\frac{\Delta v_{\mathrm{hor}}/\ell}{\tau - \tau_{\mathrm{t}}}\right), \tag{1.26}$$

where we can identify two important physical quantities: the *saturation length*, $\ell_{\mathrm{s}} = [\ell/\tilde{\gamma}]\tau_{\mathrm{t}}/(\tau - \tau_{\mathrm{t}})$, and the *saturated density* of grains in the saltation layer,

$$\rho_{\mathrm{s}} = (\tau - \tau_{\mathrm{t}})\ell/\Delta v_{\mathrm{hor}} = (\tau - \tau_{\mathrm{t}})2\alpha/g. \tag{1.27}$$

Second simplification — The convective term $(\vec{v}\cdot\vec{\nabla})\cdot\vec{v}$ in eq. (1.25) is only important at places where large velocity gradients occur. In the case of dunes, such abrupt changes occur only in the wake region behind the brink, where the wind velocity decreases drastically to zero. In the model, as discussed later, the wind and grain velocites after the dune brink are simply considered to be zero. Outside the wake regions, on the other hand, we can *neglect* the convective term. From the first and second simplifications, the following equation is obtained for the grain velocity, which must be solved numerically:

$$\frac{3}{4}\frac{\rho_{\mathrm{fluid}}}{\rho_{\mathrm{grain}}}\frac{C_{\mathrm{d}}}{d}(\vec{u}_{\mathrm{eff}} - \vec{v})|\vec{u}_{\mathrm{eff}} - \vec{v}| - \frac{g\vec{v}}{2\alpha|\vec{v}|} - g\vec{\nabla}h = 0. \tag{1.28}$$

Third simplification — One major difficulty to solve eq. (1.26) is that the grain velocity $\vec{v}$ still depends on the density ρ of grains in the saltation layer, since $\vec{u}_{\mathrm{eff}}$ (eq. (1.21)) is function of $\tau_{\mathrm{g}} = \rho g/2\alpha$. To decouple $\vec{v}$ from ρ we can make use of an useful approximation which is valid when the shear velocity u_* is not much larger than $u_{*\mathrm{t}}$, and which leads to only a negligible error (Sauermann et al. 2001).

In geomorphological applications, the sand flux is nearly everywhere saturated, with exception of those places where external variables change discontinuously, as for instance at a flow-separation, which occurs at the dune brink, or at a phase boundary bedrock/sand which occurs at the windward foot of a barchan dune. Therefore, in eq. (1.21), we can replace the density ρ which appears in the expression for τ_{g} (eq. (1.22)) by the saturated density ρ_{s} (eq. (1.27)). In this manner, the effective velocity of the wind in the saltation layer, $\vec{u}_{\mathrm{eff}}$, is written as

$$\vec{u}_{\mathrm{eff}} = \frac{u_{*\mathrm{t}}}{\kappa}\left\{\ln\frac{z_1}{z_0^{\mathrm{sand}}} + 2\left[\sqrt{1+\frac{z_1}{z_{\mathrm{m}}}\left(\frac{u_*^2}{u_{*\mathrm{t}}^2}-1\right)}-1\right]\right\}\frac{\vec{u}_*}{|\vec{u}_*|}, \tag{1.29}$$

and represents now the wind velocity in the *equilibrium*, where the grain born shear stress, τ_{g}, achieved the maximum value $\rho_{\mathrm{s}} g/2\alpha$, and the air born shear stress τ_{a} has been reduced to τ_{t}. The average grain velocity obtained from the numerical solution of eq. (1.28) using eq. (1.29) is, therefore, the *average grain velocity in the equilibrium*, $\vec{v}_{\mathrm{s}}$. This velocity is substituted into eq. (1.26), which we can write in terms of the *sand flux*,

$$\vec{q} = \rho\vec{v}_{\mathrm{s}}, \tag{1.30}$$

and the *saturated sand flux*,

$$q_{\mathrm{s}} = \rho_{\mathrm{s}}|\vec{v}_{\mathrm{s}}| = \frac{2\alpha|\vec{v}_{\mathrm{s}}|}{g}(\tau-\tau_{\mathrm{t}}) = \frac{2\alpha|\vec{v}_{\mathrm{s}}|}{g}u_{*\mathrm{t}}^2\left[(u_*/u_{*\mathrm{t}})^2-1\right]. \tag{1.31}$$

Furthermore, the grain velocity also appears in the computation of the mean saltation length ℓ (eq. (1.17)), which is now calculated using $|\vec{v}_{\mathrm{s}}|$. The resulting equation for the sand flux is a differential equation that contains the saturated flux q_{s} at the steady state,

$$\vec{\nabla}\cdot\vec{q} = \frac{1}{\ell_{\mathrm{s}}}|\vec{q}|\left(1-\frac{|\vec{q}|}{q_{\mathrm{s}}}\right), \tag{1.32}$$

where $\ell_{\mathrm{s}} = [\ell/\tilde{\gamma}]\tau_{\mathrm{t}}/(\tau-\tau_{\mathrm{t}})$ is the saturation length, which contains the information of the saturation transient of the sand flux. Using eq. (1.17), ℓ_{s} may be written as

$$\ell_{\mathrm{s}} = \frac{\ell}{\tilde{\gamma}}\left[\frac{\tau_{\mathrm{t}}}{\tau-\tau_{\mathrm{t}}}\right] = \frac{1}{\tilde{\gamma}}\left[\frac{\ell}{(u_*/u_{*\mathrm{t}})^2-1}\right] = \frac{1}{\gamma}\left[\frac{2|\vec{v}_{\mathrm{s}}|^2\alpha/g}{(u_*/u_{*\mathrm{t}})^2-1}\right], \tag{1.33}$$

where we defined $\gamma \equiv r\tilde{\gamma}$, with $r = |\vec{v}_{\mathrm{s}}|/\Delta v_{\mathrm{hor}}$. Furthermore, using eq. (1.16), r may be written as

$$r = \frac{|\vec{v}_{\mathrm{s}}|}{\Delta v_{\mathrm{hor}}} = \alpha\frac{|\vec{v}_{\mathrm{s}}|}{v_z^{\mathrm{eje}}}. \tag{1.34}$$

In this manner, γ may be written as

$$\gamma = r\tilde{\gamma} = \alpha\frac{|\vec{v}_{\mathrm{s}}|}{v_z^{\mathrm{eje}}}\left[\frac{\mathrm{d}n}{\mathrm{d}(\tau_{\mathrm{a}}/\tau_{\mathrm{t}})}\right]. \tag{1.35}$$

1.3.3 Surface evolution

The surface is eroded wherever the sand flux increases in the direction of wind flow, and sand deposition takes place if the flux decreases. The time evolution of the topography $h(x, y, t)$ is given by the mass conservation equation:

$$\frac{\partial h}{\partial t} = -\frac{1}{\rho_{\rm sand}} \vec{\nabla} \cdot \vec{q}, \tag{1.36}$$

where $\rho_{\rm sand} = 0.62\rho_{\rm grain}$ is the mean density of the immobile sand which constitutes the sand bed (Sauermann et al. 2001). If sand deposition leads to slopes that locally exceed the angle of repose $\theta_{\rm r} \approx 34^\circ$, the unstable surface relaxes through avalanches in the direction of the steepest descent. Avalanches are assumed to be instantaneous since their time scale is negligible in comparison with the time scale of the dune motion.

Separation bubble

For a dune with slip face, flow separation occurs at the brink, which represents a discontinuity of the surface. The flow is divided into two parts by streamlines connecting the brink with the ground. These streamlines define the separation bubble, inside which eddies occur (fig. 1.7).

In the model, the dune is divided into slices parallel to wind direction, and for each slice, the separation streamline is identified (fig. 1.8). Each streamline is fitted by a third order polynomial

$$s(x) = a_3 x^3 + a_2 x^2 + a_1 x + a_0 \tag{1.37}$$

connecting the brink with the ground at the reattachment point as described by Kroy et al. (2002). At the brink ($x = 0$) the separating streamline has height $s(0) = h_0$, while $s'(0) = h_0'$. Therefore, we have

$$a_0 = h_0, \quad a_1 = h_0'. \tag{1.38}$$

In the same manner, at the reattachment point ($x = L_{\rm r}$), we have $s(L_{\rm r}) = 0$ and $s'(L_{\rm r}) = 0$. Therefore, we obtain

$$a_2 = (3h_0 + 2h_0' L_{\rm r}) L_{\rm r}^{-2}, \quad a_3 = (2h_0 + h_0' L_{\rm r}) L_{\rm r}^{-3}. \tag{1.39}$$

To determine the reattachment point, we note that the laminar flow above the separating streamline descends never steeper than a maximum angle $\theta_{\rm l}$. The maximal slope of the separation streamline occurs at the turning point $x_{\rm t} = -a_2/3a_3$, where $s''(x_{\rm t}) = 0$. The slope $s'(-a_2/a3)$ is, thus, given by $-\tan\theta_{\rm l} = -C$, which then yields an equation for $L_{\rm r}$:

$$L_{\rm r} = -3h_0 \frac{C - h_0' - \sqrt{C(C + h_0')}}{h_0'(h_0' - 3C)} \approx \frac{3h_0}{2C}\left[1 + \frac{1}{4}\frac{h_0'}{C} + \frac{1}{8}\left(\frac{h_0'}{C}\right)^2\right], \tag{1.40}$$

where we have given the second-order approximation of the expression for $L_{\rm r}$. Kroy et al. (2002) fixed the slope $C = 0.25 \approx \tan 14^\circ$, while we use a slightly smaller value,

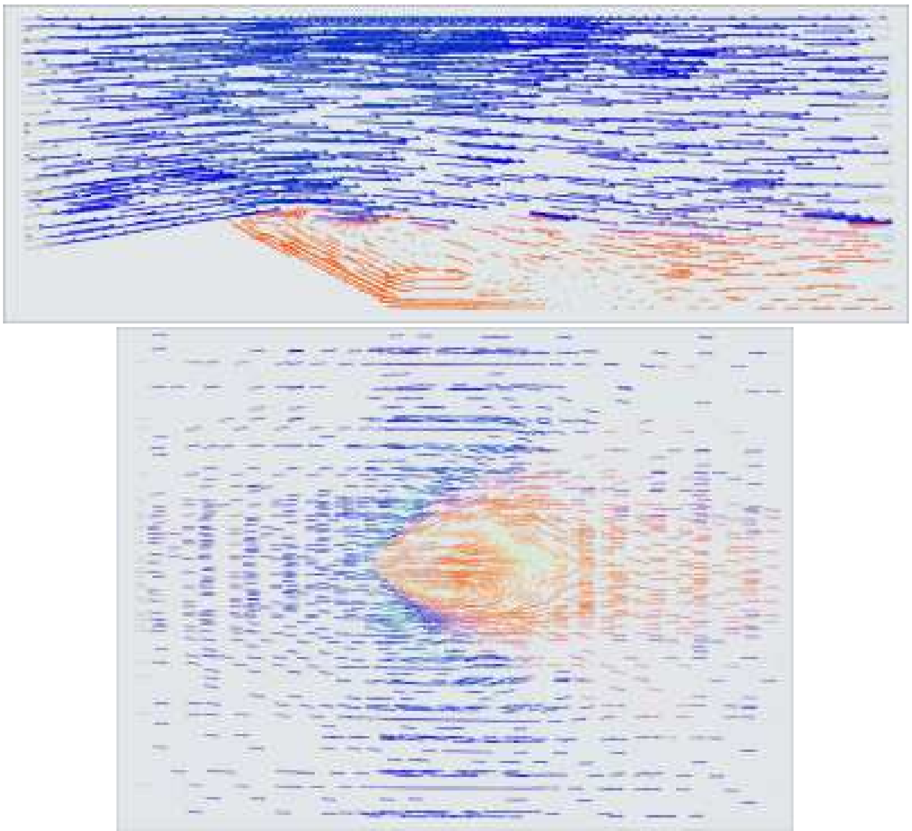

Figure 1.7: Calculation of the wind flow over a barchan dune. On top: cut along the symmetry plane, the central slice of the dune. The depicted velocity vectors clearly show the separation of flow at the brink and a large eddy that forms in the wake of the dune. Bottom: the projection of the dune on the $x-y$ plane and the depicted velocity vectors reveal the three-dimensional structure of the large wake eddy. Calculations performed with FLUENT (Herrmann et al. 2005).

$C = 0.20 \approx \tan 11.5^\circ$, since this is the value that was used in Durán and Herrmann (2006a) to fit the shape of a barchan dune in Morocco using expressions derived in that work for the model parameters (sec. 1.3.4).

In this manner, each separation streamline is given by eq. (1.37), where the coefficients are obtained from expressions (1.38) and (1.39), and the reattachment point L_r follows eq. (1.40). Inside the separation bubble, the wind shear stress and sand flux are set to zero.

The simulation steps may be summarized as follows:

1. the shear stress over the surface is calculated using the algorithm of Weng et al. (1991), eqs. (1.5), (1.6) and (1.8);
2. from the shear stress, the sand flux is calculated using eq. (1.32), where the saturation length ℓ_s and the saturated sand flux q_s are calculated from expressions (1.33) and (1.31), respectively;

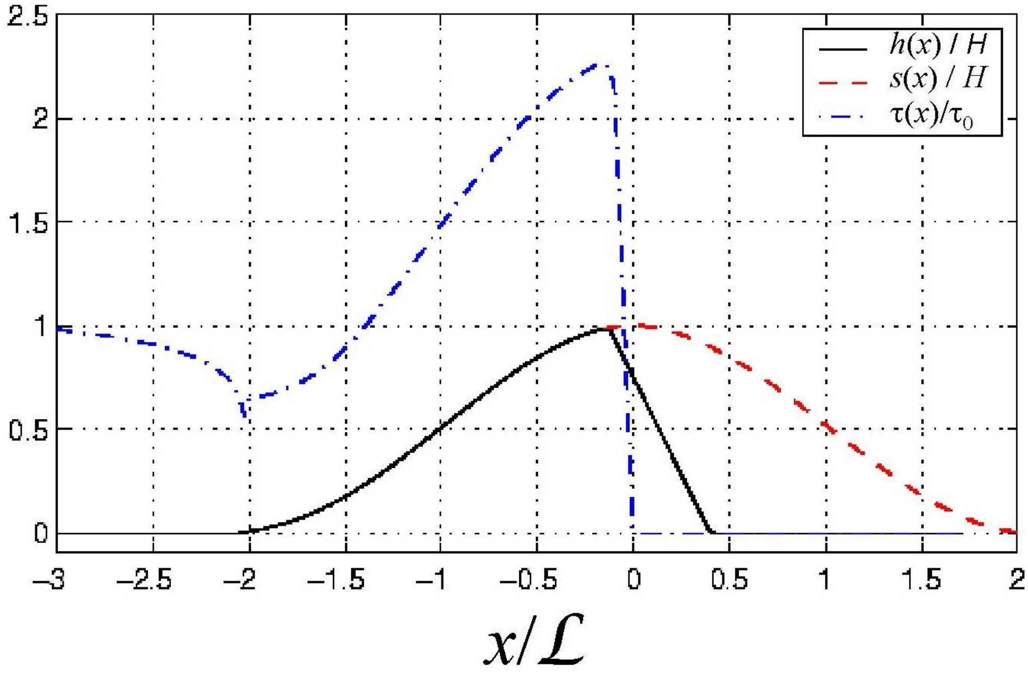

Figure 1.8: This figure shows the central slice of a barchan dune, $h(x)$, and the separation bubble $s(x)$ at the lee of the dune normalized by the dune height H. The shear stress $\tau(x)$ over the dune is normalized by the undisturbed shear stress τ_0, and the horizontal distance x is normalized by $\mathcal{L}$, which is the half length of the windward side of the dune. After Kroy et al. (2002).

3. the change in the surface height is computed from mass conservation (eq. (1.36)) using the calculated sand flux; and
4. avalanches occur wherever the inclination exceeds $34°$, then the slip face is formed and the separation streamlines are introduced.

Calculations consist of the iterative computation of steps $1-4$.

Two-dimensional equation for the grain velocity — In the simple case of the two-dimensional flow over a sand bed, $\vec{u}_{\mathrm{eff}} = u_{\mathrm{eff}}\hat{x}$, $\vec{v}_{\mathrm{s}} = v_{\mathrm{s}}\hat{x}$, and we can disregard the gravitational term, such that eq. (1.28) can be solved analytically:

$$v_{\mathrm{s}} = u_{\mathrm{eff}} - v_{\mathrm{f}}/\sqrt{2\alpha}, \tag{1.41}$$

where v_{f} is the settling or "falling" velocity of a saltating grain. Defining $s \equiv \rho_{\mathrm{grain}}/\rho_{\mathrm{fluid}}$, the falling velocity v_{f} is written as

$$v_{\mathrm{f}} = \sqrt{\frac{4}{3C_{\mathrm{d}}}(s-1)gd} \approx \sqrt{\frac{4}{3C_{\mathrm{d}}}sgd}, \tag{1.42}$$

where we considered $s - 1 \approx s$, which is a good approximation for aeolian transport in which $\rho_{\mathrm{grain}} \gg \rho_{\mathrm{fluid}}$, but not for the motion of grains in water, since in this case the Archimedes force due to the fluid cannot be neglected.

1.3.4 Model parameters

The saltation model has the following parameters: the gravity, g; the average grain diameter, d, and the density of the grains, ρ_{grain}; the density of the fluid, ρ_{fluid}; the drag coefficient C_{d}, the roughness of sand bed, z_0^{sand}, in the absence of saltation transport; the threshold wind friction speed $u_{*\mathrm{t}}$; the wind shear velocity, u_*, and the aerodynamic roughness, z_0. Besides, to solve the equations, we need the values of the phenomenological parameters: the effective restitution coefficient of the grain-bed interaction, α, the heights z_{m} and z_1, and the entrainment rate of grains into saltation, γ.

Sauermann et al. (2001) used typical values encountered in the literature (Owen 1964; Pye and Tsoar 1990; Anderson and Haff 1991): $d = 250$ μm, $\rho_{\mathrm{grain}} = 2650$ kg/m^3, $\rho_{\mathrm{fluid}} = 1.225$ kg/m^3 and $u_{*\mathrm{t}}$ around 0.25 m/s. Typical values of u_* used in previous calculations of dunes (Sauermann et al. 2003; Schwämmle and Herrmann 2003; Schwämmle and Herrmann 2004; Schwämmle and Herrmann 2005) are between 0.3 and 0.5 m/s, while z_0 has been usually set around 1.0 mm, which reproduced the wind profile over a barchan dune in Jericoacoara with a wind velocity of 0.36 m/s (Sauermann et al. 2003).

Moreover, the values of the model parameters could be estimated for saltation on Earth from comparison with measurements of sand flux and saturation transients. Sauermann et al. (2001) determined $\alpha = 0.35$, $z_{\mathrm{m}} = 0.04$ m and $z_1 = 0.005$ m by fitting eq. (1.31) to flux data measured in a wind tunnel by White and Mounla (1991). On the other hand, Sauermann et al. (2001) found $\gamma = 0.2$ from comparison with reported measurements of saturation transient and microscopic simulations of saltation (Anderson and Haff 1991; McEwan and Willetts 1991; Butterfield 1993).

However, the phenomenological parameters of the saltation model have been determined from comparison with experiments and simulations which are not available for Mars. How determine such parameters for Mars? The equations presented below allow calculate many of the quantities controlling saltation under diverse atmospheric conditions. Thus, they will be used in the present work to obtain the model parameters for saltation on Mars.

Threshold wind shear velocity for saltation

The threshold wind shear velocity $u_{*\mathrm{ft}}$ for aerodynamic entrainment may be written as

$$u_{*\mathrm{ft}} = A\sqrt{(s-1)gd}, \tag{1.43}$$

where $s \equiv \rho_{\mathrm{grain}}/\rho_{\mathrm{fluid}}$ and A is called the *Shields parameter*, which depends on the shape and sorting of the grains and on the angle of internal friction (Shields 1936). While the Shields parameter for terrestrial sand has a value around 0.01 for Reynolds numbers larger than 10, it has been shown that for atmospheric pressures different from the Earth's, A presents a complex dependence also on the grain diameter. Iversen and White (1982) proposed the following equation for the Shields Parameter A:

$$A = 0.129\left[\frac{\left(1 + 6.0\times10^{-7}/\rho_{\mathrm{grain}}gd^{2.5}\right)^{0.5}}{\left(1.928\mathrm{Re}_{*\mathrm{ft}}^{0.092} - 1\right)^{0.5}}\right] \tag{1.44}$$

for $0.03 \leq \mathrm{Re}_{*\mathrm{t}} \leq 10$ and

$$A = 0.129\big(1 + 6.0 \times 10^{-7}/\rho_{\mathrm{grain}} g d^{2.5}\big)^{0.5} \cdot \{1 - 0.0858 \exp\left[-0.0617(\mathrm{Re}_{*\mathrm{ft}} - 10)\right]\} \tag{1.45}$$

for $\mathrm{Re}_{*\mathrm{ft}} \geq 10$, where $\mathrm{Re}_{*\mathrm{ft}}$ is the friction Reynolds number $\mathrm{Re}_{*\mathrm{ft}} \equiv u_{*\mathrm{ft}} d/\nu$, and the constant 6.0×10^{-7} has units of kg·m$^{0.5}$·s^{-2}, while all other numbers are dimensionless. The kinematic viscosity ν is defined as $\eta/\rho_{\mathrm{fluid}}$, where η is the dynamic viscosity. We notice that in contrast to ν, η depends only on the atmospheric temperature and composition. For the Earth's atmosphere, η is typically 1.8×10^{-5} kg/s·m. We calculate the threshold velocity for aerodynamic entrainment with eqs. (1.43) and (1.44) or (1.45), and obtain the impact threshold velocity $u_{*\mathrm{t}}$ using the relation:

$$u_{*\mathrm{t}} = 0.8\, u_{*\mathrm{ft}}. \tag{1.46}$$

For $d = 250$ μm we obtain $u_{*\mathrm{t}} \approx 0.217$ m/s for saltation on Earth.

Drag coefficient

The drag coefficient is a function of the Reynolds number. This dependence must be taken into account in calculations of dunes using other physical conditions different from the terrestrial atmosphere.

Jiménez and Madsen (2003) calculated the drag coefficient C_{d} of a particle falling with settling velocity v_{f}. From the balance between the gravitational force and the drag resistance of the fluid, they obtained an expression for C_{d} which depends on the Reynolds number. To adapt the formula by Jiménez and Madsen (2003) to grain saltation, we consider the balance between the fluid drag f_{drag} on the grains in the saltation layer and the bed friction that compensates the grain-born shear stress at the surface: $f_{\mathrm{drag}} = \tau_{\mathrm{g}}$. The drag coefficient is then written as

$$C_{\mathrm{d}} = \frac{4}{3}\left(A_{\mathrm{d}} + \frac{B_{\mathrm{d}}}{S}\right)^2, \tag{1.47}$$

where

$$S = \frac{d}{4\nu}\sqrt{\frac{(s-1)gd}{2\alpha}} \tag{1.48}$$

is called the fluid-sediment parameter, $s = \rho_{\mathrm{grain}}/\rho_{\mathrm{fluid}}$, and A_{d} and B_{d} are constants that contain information about the sediment shape factor and roundness. Jiménez and Madsen (2003) suggested to use $A_{\mathrm{d}} = 0.95$ and $B_{\mathrm{d}} = 5.12$ for typical applications when particle's shape and roundness are not known.

Saltation model parameters

As mentioned above, the model parameters $\alpha = 0.35$, $z_1 = 0.005$ m and $z_{\mathrm{m}} = 0.04$ m have been determined by Sauermann et al. (2001) from comparison with sand flux data obtained with tunnel experiments. However, since such data are not available for Mars, these parameters cannot be determined in a similar manner as for saltation on Earth.

Recently, Durán and Herrmann (2006a) found expressions for the model parameters α, z_1, $z_{\rm m}$ and for the surface roughness $z_0^{\rm sand}$ as function of the sand and atmospheric properties. Therefore, their relations can be applied for saltation in any environment where the physics of saltation is the same as on Earth. The procedure of Durán and Herrmann (2006a) to obtain the expressions can be summarized in the following manner.

First, Durán and Herrmann (2006a) proposed one equation for the aerodynamic roughness z_0, which depends on $z_{\rm m}$ and $z_0^{\rm sand}$ and is a function of the ratio $u_*/u_{*{\rm t}}$. The expression was used to fit wind tunnel data by Rasmussen et al. (1996) of the aerodynamic roughness z_0 as a function of u_* for different values of the grain diameter d, which led to a scaling $z_{\rm m} \propto \sqrt{d}$ (Durán and Herrmann 2006a). However, from dimensional analysis, the fluid viscosity and the gravity must be also included in the scaling. In this manner, the timescale

$$t_\nu \equiv \left(\nu/g^2\right)^{1/3} \tag{1.49}$$

was incorporated to the scaling of $z_{\rm m}$, which led to the following expression (Durán and Herrmann 2006a):

$$z_{\rm m} = 14 u_{*{\rm t}} t_\nu. \tag{1.50}$$

On the other hand, $z_0^{\rm sand}$ was identified as the minimum of z_0 obtained in the wind tunnel experiments by Rasmussen et al. (1996) for different values of d. Thus, $z_0^{\rm sand}$ follows the expression

$$z_0^{\rm sand} = d/20, \tag{1.51}$$

which gives intermediate values between $d/30$ (Bagnold 1941) and $d/8$ (Andreotti 2004).

Next, z_1 and α have been determined from the best fit of eq. (1.31) to experimental data by Iversen and Rasmussen (1999) of the saturated sand flux $q_{\rm s}$ as function of u_* for different values of d.

Durán and Herrmann (2006a) found that $z_1 \approx 3.5$ mm does not depend on d and, from dimensional analysis, must be therefore written in terms of another lengthscale, ℓ_ν. This lengthscale can be defined from the Reynolds number $Re = \left(d/\ell_\nu\right)^{1/3}$. From the definition of $Re = u_{*{\rm t}} d/\nu$, where $u_{*{\rm t}} = A\sqrt{dg(s-1)}$, it follows that

$$\ell_\nu \equiv \left[\frac{\nu^2}{A^2 g(s-1)}\right]^{1/3}. \tag{1.52}$$

Using parameters for Earth, a value about 100 μm is obtained for ℓ_ν. Comparing with $z_1 = 3.5$ mm, the following expression follows (Durán and Herrmann 2006a):

$$z_1 = 35\ell_\nu. \tag{1.53}$$

Finally, from the best fit of α to the sand flux data for different grain diameters, Durán and Herrmann (2006a) found the following expression:

$$\alpha = 0.17 d/\ell_\nu. \tag{1.54}$$

Summary — To calculate saltation on Earth, we use $g = 9.81$ m/s^2, $d = 250\,\mu$m, $\rho_{\rm grains} = 2650$ kg/m^3, $\rho_{\rm fluid} = 1.225$ kg/m^3 and $\eta = 1.8$ kg/m·s. Next, from the expressions presented in this section, we obtain $u_{*{\rm t}} = 0.217$ m/s, $C_{\rm d} = 2.75$, $z_{\rm m} = 0.016$ m, $z_1 = 0.004$ m and $\alpha = 0.43$. Finally, we use $\gamma = 0.2$ as obtained by Sauermann et al. (2001) from comparison with measurements.

We note that the values of z_1, $z_{\rm m}$ and α calculated from the equations above for Earth are similar to the values obtained by Sauermann et al. (2001) from the best fit to the flux data by White and Mounla (1991). Indeed, eqs. (1.50), (1.53) and (1.54) can be used to calculate sand transport on Mars. Saltation on Mars will be calculated in the next chapter.

1.3.5 Sand dunes

In spite of the apparent complexity of its equations, the dune model is so far the simplest method to calculate the formation and the evolution of sand dunes. In particular for barchan dunes, the model has been extensively tested and its results have been found to be quantitatively in good agreement with field measurements (Sauermann et al. 2003).

Barchan dunes are calculated using a Gaussian hill as initial condition (fig. 1.9). A constant upwind shear velocity u_* is set at the inlet of the simulation, as well as a small upwind sand flux $q_{\rm in}$. The sand influx represents the rate of sand transport in the area between dunes, and plays an important role for the shape of barchans, as we will see in chapter 3. In fig. 1.9 we see that the Gaussian heap evolves in time until the characteristic horns and slip face of a barchan dune appear downwind in the direction of propagation. To calculate transverse dunes, on the other hand, a dense sand bed is used, on which the dunes appear and increase in size (Schwämmle and Herrmann 2004).

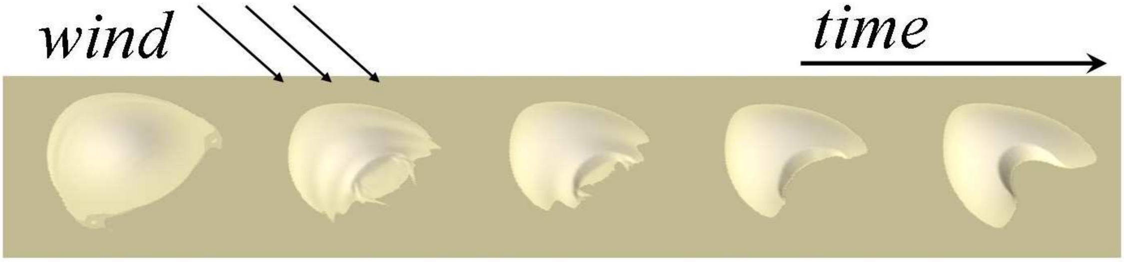

Figure 1.9: Time evolution of a Gaussian hill into a barchan dune under an unidirectional wind. Time increases from the left to the right.

Indeed, the shape of dunes depends on the dune size. This happens because there is a characteristic distance — the saturation length — that is large enough to break the scale invariance of the dunes. In fig. 1.10a we see the evolution of the sand flux q, as function of distance x, calculated over a flat sand bed for different values of wind strength $u_*/u_{*{\rm t}}$. A constant influx $q_{\rm in} = 10\%$ of $q_{\rm s}$ has been used. We see that the sand flux q increases from $0.1q_{\rm s}$ until it reaches the saturated value $q_{\rm s}$. We define $\lambda_{\rm s}$ the distance after which the flux has achieved 99% of $q_{\rm s}$. A sand hill that is shorter than $\lambda_{\rm s}$ will be systematically eroded until disappear. Therefore, the saturation length introduces a minimal size for a hill to evolve into a dune (Kroy et al. 2005). We will see in chapter 3 that, as a consequence of the saturation length, the sand hill (or dome) must have, furthermore, a minimal size to develop slip face and horns.

In fig. 1.10a we indicate for each value of $u_*/u_{*\mathrm{t}}$ the characteristic distance of flux saturation, ℓ_s, calculated with eq. (1.33). It is this distance that determines the saturation length, i.e. λ_s is proportional to ℓ_s, as we see in the main plot of fig. 1.10b. In the inset of this figure, we see that ℓ_s decreases with $u_*/u_{*\mathrm{t}}$, and that the dependence of ℓ_s on the wind strength is significant for low values of u_*. Because realistic winds are in the range of 1.0 to $2.0u_{*\mathrm{t}}$ (Fryberger and Dean 1979), we see that the strength of the wind plays a relevant role for the dune size. On the other hand, as we will see in chapter 3, the breakdown of shape invariance of dunes is relevant for the smallest dunes. As the dune volume increases, the influence of the saturation length becomes less significant (Sauermann et al. 2000; Sauermann 2001).

The migration velocity of the dune also depends on the dune size. The dune velocity of a barchan or transverse dune can be calculated from the flux q at the brink and the height h at the brink, as sketched in fig. 1.11. The sand is deposited on the slip face and transported downhill by avalanches which maintain the angle of repose (Bagnold 1941). Therefore, the dune advances with velocity $v_\mathrm{d} = [1/\rho_\mathrm{sand}]q/h$. However, this relation is valid only for dunes that propagate shape invariantly. In reality, the shape of barchan dunes depends on the dune size, and the dune velocity scales with the inverse of the dune length L (Kroy et al. 2002), i.e.

$$v_\mathrm{d} \propto \frac{1}{L}. \tag{1.55}$$

The dune velocity may be written in this case as $v_\mathrm{d} = [1/\rho_\mathrm{sand}]q/(C_0 + h)$, where C_0 is a constant that decreases with the shear velocity (Sauermann 2001). Therefore, the migration velocity of a dune approaches the relation for shape invariant dunes as the dune height increases and/or as the shear velocity increases.

The fact that smaller dunes move faster than larger ones have a crucial implication for the evolution of dune fields. The dune model has been applied to calculate interactions of barchan dunes in a field, and revealed that dunes may interact in different ways, depending on their sizes. As we see in fig. 1.12, faster moving small barchans may easily “collide” with larger, slower wandering ones during their downwind motion in a field. It has been shown that very small dunes in this case may be “swallowed up” by larger dunes downwind. But if the size difference between the interacting dunes is not too large, then the smaller dune upwind gains sand from the larger one, which then becomes smaller and may wander away (fig. 1.12). Effectively, it is like if the smaller dune were crossing over the larger one (Schwämmle and Herrmann 2003), as proposed recently by Besler (1997).

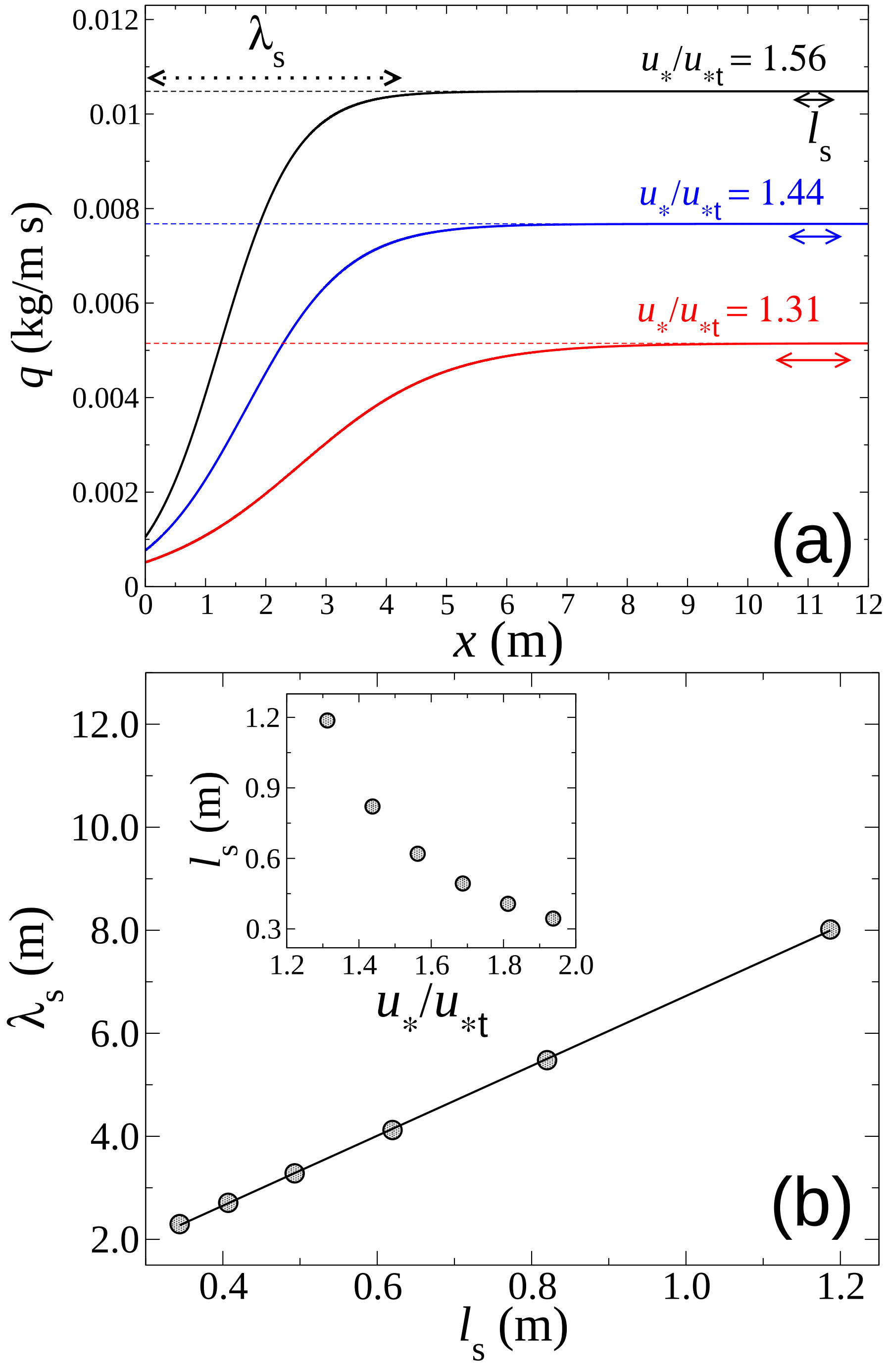

Figure 1.10: *Saturation length*: relevant length scale of dunes. In (a) we see the sand flux q, calculated over a flat sand bed, as function of downwind distance, x. An influx $q_{\mathrm{in}}/q_{\mathrm{s}} = 0.1$ has been used and parameters for Earth have been taken. λ_{s} is the distance after which q has increased from q_{in} to 99% of q_{s}. ℓ_{s}, which is calculated with eq. (1.33), is indicated in the figure for each value of wind strength $u_*/u_{*\mathrm{t}}$. We see in (b) that λ_{s} is of the order of 7 times ℓ_{s}. In the inset of (b) we see how ℓ_{s} depends on the wind strength.

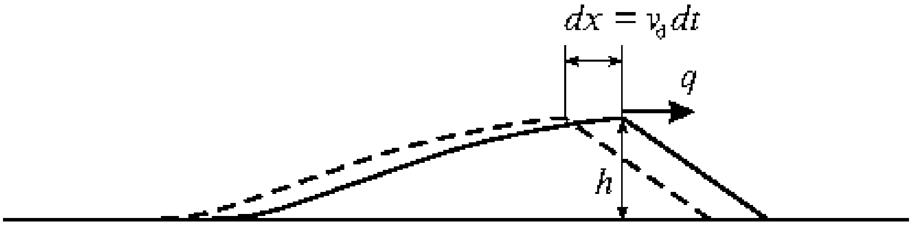

Figure 1.11: Migration velocity of barchans and transverse dunes (after Sauermann (2001)). The deposition of the volume of sand $h\,dx = q\,dt/\rho_{\mathrm{sand}}$ advances the dune by $dx = v_{\mathrm{d}}dt$.

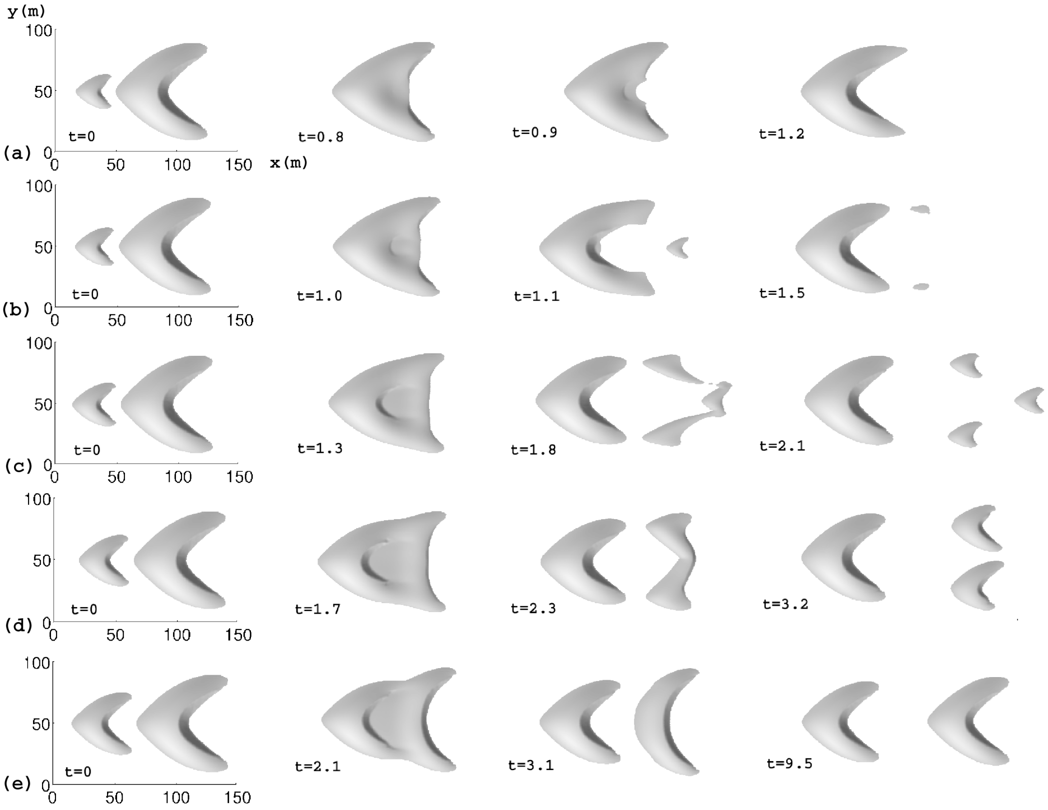

Figure 1.12: Four simulation snapshots of barchan dune interaction. Cases (a) — (e) correspond to different initial heights for the upwind, smaller barchan. After Durán et al. (2005).

1.4 Conclusion

In this chapter, we presented the equations of the dune model, which we will use in the following chapters to calculate saltation and dune formation on Earth and on Mars. The original model introduced in Sauermann et al. (2001) and Kroy et al. (2002) and later improved by Schwämmle and Herrmann (2005) has been described in details in section 1.3. Moreover, we presented the relations found by Durán and Herrmann (2006a) for some of the model parameters: the mean saltation height z_{m}, the effective height z_1 at which the wind velocity is computed within the saltation layer, and the effective restitution coefficient of the grain-bed interaction, α. The equations presented in section 1.3.4 allow determine z_{m}, z_1 and α for different physical conditions.

In the next chapter, we start calculating saltation transport on Mars, while the formation of dunes is discussed in chapter 3. With a mean pressure of 6.0 mb, and a temperature of 200 K, the atmosphere of Mars, which consists of 95% of CO_2, has an average density of 0.02 $\mathrm{kg/m^3}$. This is almost 100 times lower than the Earth's atmosphere. Because the particle size of Martian dunes is not significantly different than the grain diameter of terrestrial dunes (Edgett and Christensen 1991; Fenton et al. 2003), it follows from expression (1.43) that the minimal wind speed for sand transport on Mars is about 10 times higher than on Earth. In the following, we will see the striking consequences of the high-energy winds for saltation transport and dune formation on Mars.

Chapter 2

Sand transport on Mars

There are many evidences that the surface of Mars has been continuously modeled by aeolian processes. Investigation of the geologic and atmospheric data and high resolution images sent from Mars missions led to the conclusion: current wind regimes are able to transport dust and sand on Mars. In this chapter, data obtained from orbiters and landers are presented which provide information about the wind velocity profile on Martian soil and on the grain size of Martian dunes. The implications of such *in situ* measurements and General Circulation Model results for saltation transport on Mars are discussed. Next, we apply the dune model to study saltation on Mars. We calculate the sand flux as function of the wind velocity on Mars, and estimate the quantities of the model that control the average trajectories of Martian saltating particles.

2.1 Aeolian transport on Mars: evidences and measurements from orbiters and landers

According to Sheehan (1996), it was the italian astronomer Giovanni Virginio Schiaparelli, in the year of 1877, the first who observed that some regions of Mars appeared systematically covered with "clouds". Today we know that those clouds, which in fact were probably seen in earlier observations of Beer and Mädler as long ago as the 1830s (Sheehan 1996), were clouds of *dust* which may remain suspended in the atmosphere of Mars for several months. When orbiter Mariner 9 — the first successful Mars mission which brought a revolution in our understanding of the Martian geologic processes — reached Mars in 1971, the planet was completely obscured by a global dust storm: not even the polar caps were visible.

Mariner 9 had to wait a few weeks for the storm to cease, after which the mission operated for about 1 year and sent to Earth over $7,000$ television images of the surface of Mars with a resolution of 1.0 km. The images revealed a variety of surficial features that have left little doubt that wind transports Martian surface materials (Sagan et al. 1972; Cutts and Smith 1973; McCauley 1973). Among the windforms observed by Mariner 9 we may mention wind streaks associated with craters, modified crater rims, streamlined ridges, linear grooves and sand dunes, the existence of which indicated that saltation of sand grains could occur on Mars. Moreover, some streaks of kilometers to tens of kilometers in dimension changed on characteristic timescales of a few weeks suggesting that Martian fine particulates are currently movable (Sagan et al. 1972).

Nearly five years later, Viking landers 1 & 2 arrived on Mars, at $22.5°$N; $48.0°$W, and $47.5°$N; $225.9°$W, respectively, and provided the first opportunity for *in situ* study of the Martian surface. Several lines of evidence for aeolian transport of particles were uncovered by the cameras of the Viking landers, such as wind tails behind rocks, ventifacts (abraded or grooved rocks) and streaks of dimensions between a few centimeters to hundred meters (Mutch et al. 1976a; Mutch et al. 1976b; Mutch et al. 1976c; Sagan et al. 1977; Sharp and Malin 1984). The landers performed measurements of pressure, temperature, and wind speed at a height of 1.6 m (Chamberlain et al. 1976; Kieffer 1976), the results of which yielded important insights into the frequency of occurrence and intensity of Martian aeolian activity.

Figure 2.1: Aeolian features at the Viking 1 landing site. The large boulder in the left of the picture is about 10 m from the spacecraft and about 2 m across. It is possible to see wind tails at the lee of rocks, and also small dunes, which are indicated by the arrows. After Mutch et al. (1976c).

During almost the whole mission, at both landing sites winds were calm and very little changes on the surface were observed. Because the wind velocity at the Viking lander sites was measured at a single height, it was not possible to determine the friction speed u_* and the roughness z_0 which define the wind profile (chapter 1). Typical values of friction speed at the lander sites were estimated from assumed values of z_0 between 1.0 mm and 1.0 cm, and were between $u_* = 0.25$ and 0.6 m/s (Sutton et al. 1978), far below estimated values of saltation threshold, 2.0 m/s. While contact with Viking 2 was lost in 1980 and less data from this station is available, Viking 1 sent images, atmospheric and wind data from Mars until 1982, after 2245 Martian sols, i.e. over 3 Martian years.

It was surprising that no movement of surface material was witnessed from the Viking 1 images taken after and before extreme dust storms during the first 2 Martian years. In the first year, Viking 1 surface sampler constructed five small sand piles on the soil, and on sol 1601 the piles that were reimaged appeared practically unchanged. No change on the soil patterns could be detected as well.

It was not before the third winter, after 2.5 Martian years or five Earth years, that the Viking 1 cameras could register the first *in situ* evidence for aeolian transport on the surface of an extraterrestrial planet. Arvidson et al. (1983) reported enthusiastically this observation: "*(...) The movement of the rock, the alternations of the conical piles, clods, trenches, and other features, and the increase in scene contrast demonstrate that an erosion event or events of substantial magnitude occurred during the third winter season, probably between Sols 1720 and 1757*". In fact, on sol 1742, an image was acquired showing an enormous storm in progress, which has been named "The Martian Dust Storm of Sol 1742" (Moore 1985). The changes in the surface have been attributed to the strong winds associated with that storm, and included significant erosion of the sand piles and formation of ripple-like bed with wavelengths of several centimeters. Therefore, the bed modifications represented as well the first evidence that *saltation* can occur under present atmospheric condition of Mars.

Indeed, it was clear from Viking 1 data that only rarely, under current climate regimes, do winds exceed the threshold for entrainment of sand grains. Arvidson et al. (1983) proposed a rough estimate of the time the wind lasted above the threshold for saltation at the landing site. First, they noticed that u_* should not have been far above $u_{*\mathrm{t}}$ for saltating grains would be expected to enter suspension for u_* several times $u_{*\mathrm{t}}$. Then, they assumed that during the storm, u_* was only 10% above the threshold, and they calculated the time required for the piles to be completely eroded. Using a simple relation proposed by White (1979) in which the sand flux is proportional to $u_*^3(1 - u_{*\mathrm{t}}/u_*)(1 + u_{*\mathrm{t}}^2/u_*^2)$, Arvidson et al. (1983) found that the piles would have disappeared from the ground if such a wind would have lasted for more than a few tens of seconds. No more changes on the surface were detected during the mission: over a period of time of 3 Martian years (or 6 Earth years), the wind strength in the Viking 1 landing site was only a few seconds above the threshold for saltation.

Moore (1985) suggested that the wind velocities would have sporadically reached larger peaks over the period delimited by the images that revealed the changes. In the gusts of highest activity, u_* could have achieved values between 2.2 and 4.0 $\mathrm{m/s}$, and could have lasted even for a longer time than a few seconds as proposed above. Moore (1985) noticed, however, that the soil at the landing site was more akin to Earth's surfaces where progressive exposures of nonerodible elements reduce erosion rates in a significant way. In this manner, Moore (1985) proposed for the first time an upper bound value for wind friction speed on a Martian soil.

The discoveries by Mariner 9 and Viking landers nucleated an enormous amount of theoretical and experimental work on the aeolian regimes and transport of particles on Mars. Many authors speculated about the origin and age of dune deposits on Mars (Breed et al. 1979; Tsoar et al. 1979; Thomas 1982), and NASA developed MARSWIT, the first wind tunnel simulating Martian atmospheric conditions, which was used to study the conditions for saltation entrainment (Greeley et al. 1976; Iversen et al. 1976; Pollack et al. 1976; Greeley et al. 1980; Iversen and White 1982) and to investigate the trajectories of saltating grains and rates of soil abrasion on Mars (White et al. 1976; White 1979). Furthermore, the original numerical model of atmospheric circulation of Mars by Leovy and Mintz (1969) has been repeatedly refined with inclusion of topography (Mass and Sagan 1976), CO_2 condensation and diurnal variations in the convective boundary layer (Pollack et al. 1981), as well as radiative effects of atmospheric dust on solar and thermal radiation (Pollack et al. 1990). By combining predictions of seasonal wind strength and direction obtained from General Circulation Models (GCM) with surface features imaged by Mariner and Viking orbiters, Greeley et al. (1993) finally presented the first reliable evidence that the enigmatic Martian bright streaks could be formed by current winds on Mars. Moreover, GCM results have shown that the widely spread yardangs must have appeared under more ancient climate conditions, and no conclusion was reported about saltation and dune formation on the present Mars (Greeley et al. 1993).

Many authors have further used data from Mariner 9 and Viking spacecrafts, which included moderate resolution images and infrared thermal mapping, to study the geology of Mars. Many dune forms, mostly of dark sand, could be later identified mainly in the north pole of Mars and on the floor of craters (Lancaster and Greeley 1990; Edgett and Blumberg 1994; Edgett and Christensen 1994; Lee and Thomas 1995). From infrared data of the Viking spacecraft, Edgett and Christensen (1991) found, using thermal models (Kieffer et al. 1977; Haberle and Jakosky 1991), that the main diameter of the grains which compose Martian sand dunes is $d = 500 \pm 100$ μm. The dark dunes presented in general no superimposed craters (Tsoar et al. 1979; Marchenko and Pronin 1995), indicating that the dunes were not formed at the time of meteorite bombardment when climate conditions on Mars were probably different than that in the present (Melosh and Vickery 1989). Indeed, Edgett (1997) reported the discovery of an equatorial field of bright dunes which appeared stabilized and mantled by fine-grained material that probably originated from explosive volcanism.

Edgett's paper about bright dunes, published in November 1997, was probably the last paper about sand dunes on Mars before the new era of studies on the Martian geology. In July 1997, Pathfinder Soujorner was the first rover to land on Martian soils. And in September 1997, it was arriving on Mars the most successful Mars mission ever launched: the Mars Global Surveyor (MGS), which carried aboard, among others, the high resolution Mars Orbiter Camera (MOC). The MOC camera provided images of the surface of Mars with resolution up to 1.5 m, and already in the first four months of work, MOC sent to Earth an enormous amount of images which revealed details of aeolian features of Mars never captured by previous missions (Malin et al. 1998).

One of the first most intriguing discoveries of MGS MOC was that in many regions of Mars, large dark dunes appeared wandering over small, bright bedforms. It was clear from the images that the bright dunes were ancient bedforms and were not active today, while the dark dunes were formed by more recent wind regimes. This is illustrated in the MOC images in fig. 2.2, which shows two dune fields of coexisting dark and bright dunes. According to Thomas et al. (1999), the bright dunes are made of grains much lighter than the basaltic grains of the dark dunes. Martian bright bedforms are probably composed of gympsum, or some other sulphate that would have limited lifetimes travelling in saltation on Mars (Thomas et al. 1999). Once such soft material grains enter saltation, they are rapidly broken into smaller particles that are then carried into suspension. In fact, in the MOC images analysed by Thomas et al. (1999), the bright dunes appeared at small distances from outcroppings of bright source materials, probably associated with playa deposits, or derived from ground water, flood or hydrothermal activity (Thomas et al. 1999). On the other hand, it became evident from the MOC images that dark dune fields on Mars are able to exist far from obvious sources.

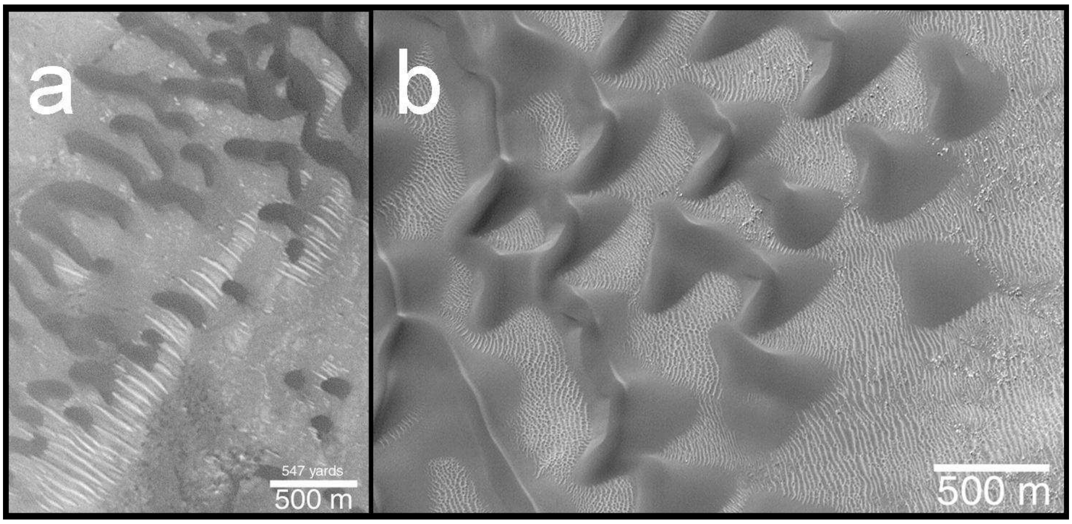

Figure 2.2: These Mars Global Surveyor (MGS) Mars Orbiter Camera (MOC) images show large, dark Martian dunes wandering on a soil covered with small, bright, inactive bedforms. In **a.**, we see a dune field on the floor of an impact crater in western Arabia Terra, at $10.7°$N, $351.0°$W. The dunes in **b.** are located in the Proctor Crater, near $47.9°$S, $330.4°$W.

The MGS MOC images constituted valuable material for planetary scientists and geophysicists interested in the evolution and aeolian processes of Mars. One example of the relevance of the MOC images was the PhD Thesis of Lori Fenton: "*Aeolian processes on Mars: atmospheric modeling and GIS analysis*" (Fenton 2003), in which the sedimentary history of Proctor Crater (Proctor dunes are shown in fig. 2.2b) could be determined on the basis of Mars Global Surveyor spacecraft images and thermal data. The Mars Orbiter Camera has been operating until 2th November 2006, and has provided a wealth of high resolution images of dune fields, making possible infer about the regional conditions of wind and flux that led to the formation of Martian dark dunes (Bourke et al. 2004; Bourke 2006).

On the other hand, Pathfinder rover operated only for 2 months. Nevertheless, this mission sent to Earth important data about Mars geology, atmosphere, and *in situ* images showing a variety of evidences for aeolian transport (Golombek et al. 1997; Schofield et al. 1997; Smith et al. 1997; Greeley et al. 1999; Golombek et al. 1999). Moreover, Pathfinder performed, for the first time, measurements of the wind velocity profile on a Martian soil, which allowed determine the shear velocity u_* and the aerodynamic roughness z_0 at the landing site.

The Mars Pathfinder (MPF) Lander Wind Sock Experiment (Sullivan et al. 2000) consisted of three wind socks mounted at heights of 33.1 cm, 62.4 cm, and 91.6 cm above

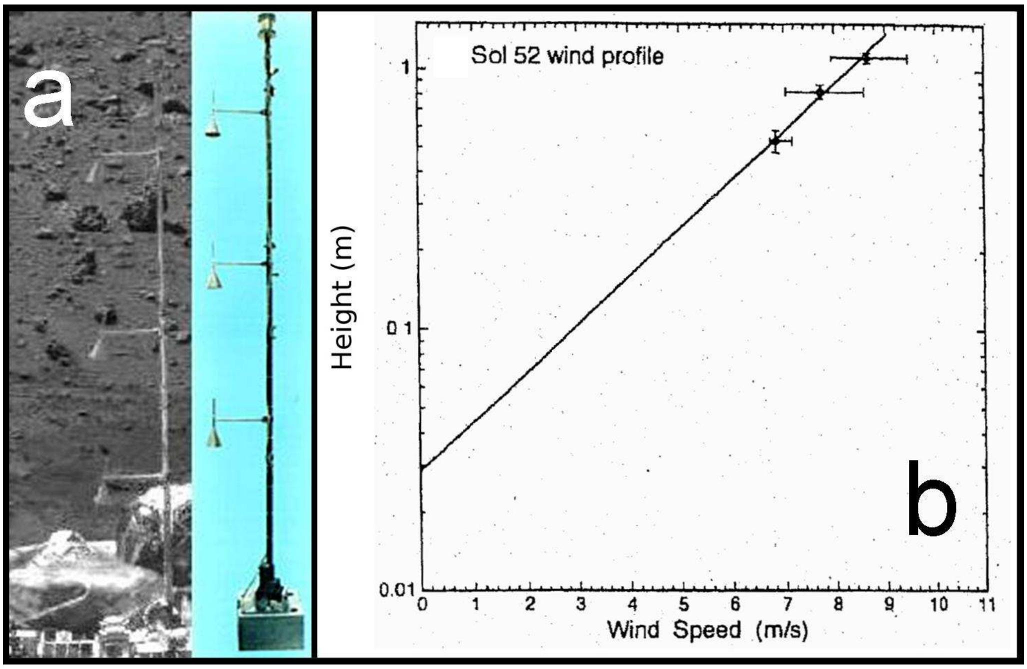

Figure 2.3: **a.** In the Mars Pathfinder Lander Wind Sock Experiment, three windsocks measured the wind velocity u at different heights z above the ground. The values of wind speed $u(z)$ measured on sol 52 are given by the data points in **b.** (after Sullivan et al. (2000)). The line gives the best fit using the logarithmic wind profile, from which values of $u_* = 0.95$ m/s (inclination of the line) and $z_0 = 0.029$ m (height at which $u = 0$) are obtained (Sullivan et al. 2000).

the base of the ASI/MET (Atmospheric Science/Meteorology) mast (fig. 2.3). The wind socks were aluminum cones of length 10 cm and width 3 cm. Their orientations and tilts provided information on the wind speed and direction at each of the three heights. In fig. 2.3, we show one typical wind profile at Martian sol 52 (after Sullivan et al. (2000)). Winds on the Pathfinder landing site were gentle, and values of u_* above 1.0 $\mathrm{m/s}$ seldom occurred during the experiments. This has been considered a consequence of the season during which MPF operated (Greeley et al. 2000), since general circulation model calculations applied for the landing site during the season of the experiments predicted in fact wind speeds below particle threshold (Haberle et al. 1999). Furthermore, values of z_0 obtained from the data were extremely large, and mostly above 3.0 cm (Sullivan et al. 2000). However, as noticed by Sullivan et al. (2000), global values of z_0 between 1.0 mm and 1.0 cm seem reasonably consistent for Mars since the Pathfinder site is probably rockier and rougher than most plains units on Mars (Golombek et al. 1997; Golombek et al. 1999).

Among observed wind-related processes at the Pathfinder site, dust devils were one of the most resounding *in situ* observations, since they could be related to the nucleation of global dust storms on Mars. Dust devils were first registered indirectly through observations of abrupt changes in wind direction and pressure (not seen in the coarse temporal sample from the Viking landers data), which were correlated with short-lived reduction in the power generated by the Pathfinder solar panels — an indicative that the apparent vortices entrained dust (Schofield et al. 1997). Later, Metzger et al. (1999) analysed images of the Pathfinder camera and concluded that the vortices in fact carried dust particles, travelling with a velocity of $0.5 - 4.6$ m/s.

Indeed, no changes were observed in the wind tails, streaks, small dunes or ventifacts encountered at the Pathfinder site. To verify whether those "inactive" aeolian features could have resulted from present wind regimes, Greeley et al. (1999) and Greeley et al. (2000) compared the orientations of several wind-related features with GCM wind direction predictions for the landing site. They found that the orientation of the wind tails at the lee of rocks, wind streaks downwind of craters, ripplelike patterns and small barchanoid duneforms correlated well with the direction of the strongest winds predicted from GCM calculations, which occur during the Martian northern winter under current conditions. Greeley et al. (2000) found moreover that the wind strength which formed the dunes was sufficient for saltation but *not* for rock abrasion and formation of the ventifacts, which in the landing site had a different orientation related to the dunes and were formed by ancient winds. In this manner, Greeley et al. (2000) concluded that the small dunes at the Pathfinder site have swept through the area repeatedly under current regimes, burying rocks and other surface features of more ancient origin.

Sand ripples or small dunes did not represent the characteristic features at the MPF site. In contrast, several fields of sand ripples appear at the landing sites of the lattest NASA Mars Exploration Rover missions "Spirit" and "Opportunity" (Greeley et al. 2004; Sullivan et al. 2005; Squyres et al. 2006), which landed, respectively on 4 and 25 January 2004. The bedforms occur mainly within "traps" in the interior of craters, as for example in Eagle crater (Sullivan et al. 2005), and in the "Victoria" and "Endurance" craters (fig. 2.4), which are located near Opportunity landing site (1.95°S, 354.47°E) at Meridiani Planum. Ripples are also common at Gusev Crater, near 14.57°S, 175.48°E, location at which Spirit rover landed (Greeley et al. 2004). Neither at Spirit nor at Opportunity landing sites could any movement of the ripples be detected. On the other hand, Spirit and Opportunity have been sending high resolution images which show evidences for current entrainment, transport and deposition of fine particles by the wind at both sites.

In addition to Spirit and Opportunity rovers, three further Mars missions, all orbiters, are currently in activity. These are the "2001 Mars Odissey" and "Mars Reconnaissance Orbiter", both NASA orbiters launched, respectively, on April 2001 and August 2005; and the "Mars Express", which is an orbiter sent by ESA on June 2003. Among diverse scientific goals, the orbiters aim to provide details of the Martian atmosphere, and to image a few selected areas of Mars with resolution up to a few centimeters. One example is the image of the ripples at Victoria crater seen in fig. 2.4, which has been taken by Mars Reconnaissance with a resolution of 29 cm. It is clear that the regional views provided by such images may be important for the interpretations of aeolian processes at the sites where the rovers landed.

For instance, images of Meridiani Planum taken by the MOC camera before and after the major 2001 global dust storm allowed develop a recent aeolian history of the Opportunity landing site on the basis of the data sent by the rover (Sullivan et al. 2005). The MOC camera revealed a bright streak at the lee of the Eagle crater, which changed orientation

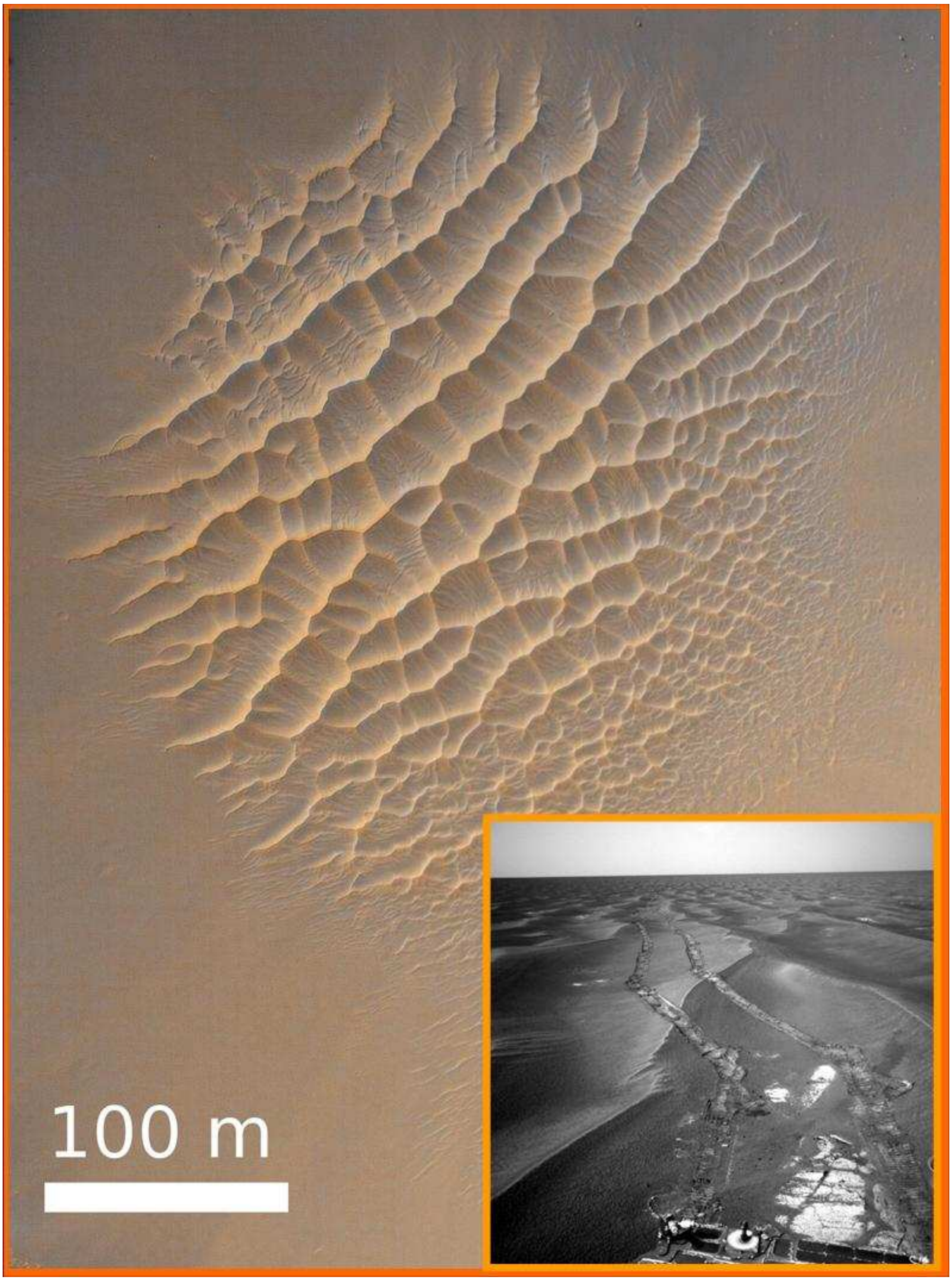

Figure 2.4: The larger image shows ripples on the floor of Victoria Crater on Mars, which is located near the Opportunity Rover landing site. The image has been taken by the Mars Reconnaissance Orbiter. The image in the detail shows ripples in the Endurance crater. The image has been taken by the camera of the Opportunity rover. It is possible to see the tracks on the soil, which have been left by the rover.

during the 2001 storm. Surprisingly, the orientation of the streak since that storm indicates nearly the same wind direction as inferred from the ripples on the floor of the crater. In this manner, Sullivan et al. (2005) concluded that the ripples may be "activated" under current atmospheric conditions of Mars. To move, the ripples must experience shear velocities associated with dust storms, around $u_{*\mathrm{t}} \approx 2.0$ m/s (Sullivan et al. 2005).

Moreover, Sullivan et al. (2005) observed that in the plains units outside of the Eagle crater, ripples also occurred, which, however, did not oriented in the same direction of the streak and of the intra-crater ripples. Images taken by the rover revealed that the outter ripples at Meridiani Planum are covered with $1-2$ mm fragments of haematite-enriched concretions, which are associated with a higher threshold wind speed for saltation, between 3.0 and 4.0 m/s (Sullivan et al. 2005). The major 2001 global storm was not strong enough to move the fragments. In this manner, the threshold velocity of the fragments represent an upper bound for the wind shear velocity at the landing site during the storm. We note that the range of maximum u_* at Meridiani Planum is similar to the one estimated for the Viking landing site during the "Martian Dust Storm of Sol 1742" (Moore 1985).

Summarizing, while very fine particles are currently being transported and deposited by the wind, Mars missions could find only very few evidences for grain saltation. The first observation was made by Viking 1 lander: one unique saltation event, with probable duration of a few seconds, occurred within 6 Earth years or 3 Martian years (Arvidson et al. 1983; Moore 1985). Later, evidence for saltation at Meridiani Planum has been reported by Sullivan et al. (2005), who observed that the orientation of the ripples in the Eagle crater correlated with the direction of bright streak at the lee of that crater. Since the streak has been created after the 2001 major dust storm, the correlation of the direction of the streak with the orientation of the ripples supported the hypothesis that saltation on Mars occurs as gusts of major aeolian activity associated with dust storms.

However, Mars missions could never detect a saltation event *in situ*. Moreover, sporadic coverage of orbiting spacecraft could never detect movement of sand dunes, which would imply saltation occurs in the dune fields of the north pole and in the interior of craters. Measurements of the average trajectories of saltating grains and of the intensity of grain-bed collisions could be performed only in wind tunnel laboratories simulating typical conditions of Mars (White et al. 1976; White 1979; Williams and Greeley 1980; Greeley and Iversen 1985; Marshall et al. 1998). Still none of such experiments could give at least some insight into the formation of dunes on the present Mars. It has been suggested that Martian dunes have been formed in the past, when atmospheric pressure of Mars was much higher than in the present (Breed et al. 1979).

Could Martian dunes have been formed by the thin atmosphere of the present Mars? It is this challenging question that motivates the present work. We want to find, from comparison of the different shapes of Martian dunes with the model results, the wind regimes that formed the dunes observed in the images of Mars. To solve the equations of sand transport, we need, first, to calculate the "microscopic" quantities of the model that control saltation on the present Mars. These quantities, which have been listed in chapter 1, are calculated in the next section, where we also estimate the rate of sand transported on Mars during saltation. The calculations of Martian dunes are, thereafter, presented in the following chapter.

2.2 Martian saltation

We expect saltation to be very different depending on the location on Mars. The reason is that the average atmospheric pressure and temperature may vary within an extremely wide range compared to the terrestrial case. Furthermore, higher rates of sand transport are expected on Mars due to the higher shear velocity. Besides u_*, the following are the quantities that govern saltation: the grain diameter d, and density, ρ_{grain}; the atmospheric density, ρ_{fluid}, and viscosity, η; and the gravity, g. These quantities are used to calculate the saltation model parameters according to the expressions given in chapter 1. In this section, we estimate the average trajectories of saltating grains and the sand flux under different atmospheric conditions on Mars. The results presented in this section are then used in the next chapters, to solve the equations of sand transport and the formation of dunes on Mars.

2.2.1 Atmosphere and sand

The Mars Global Surveyor Radio Science (MGSRS) Team has been providing valuable atmospheric data of Mars (MGSRS 2006). In particular, the temperature T and the pressure P near the surface have been systematically measured in many locations of Mars. Figure 2.5 shows one example of a typical "Martian Weather" map, in which the crosses indicate some of the locations of Mars at which values of T and P are available.

We use the ideal gas equation to calculate the local atmospheric density, ρ_{fluid}, from the MGSRS pressure and temperature data. An atmosphere of 100% CO_2 is considered. Furthermore, the dynamic viscosity η of the Martian air is a function of the temperature T, and is calculated using Sutherland's formula (Crane Company 1988):

$$\eta = \eta_0 \left[\frac{0.555T_0 + C}{0.555T + C}\right] (T/T_0)^{3/2}, \tag{2.1}$$

where for CO_2 we have $\eta_0 = 0.0148$ centipoise, $C = 240$, $T_0 = 527.67$°R (Crane Company 1988). We note that in eq. (2.1), the temperature is given in degrees Rankine (°R), where 1°K $=1.8$°R. The result obtained from eq. (2.1) is given in centipoise, and must be multiplied by 10^{-3} to convert to kg$/$m·s. Finally, the kinematic viscosity ν is calculated with the equation $\nu = \eta/\rho_{\mathrm{fluid}}$.

The particle size of Martian aeolian dunes

Data sent from orbiters have been also used to determine the size of the grains which compose Martian dark dunes. The size of the grains is related to the resistance of the surface or dune to a change in temperature. This resistance is measured by the *thermal inertia*, $I = k\rho_{\mathrm{sand}}c$, where ρ_{sand} is the bulk density of the surface, c is the specific heat and k is called thermal conductivity (Neugebauer et al. 1971).

Normally, the thermal inertia of a surface is calculated by establishing the diurnal thermal behaviour of the surface, which requires a minimum of two observations of the same

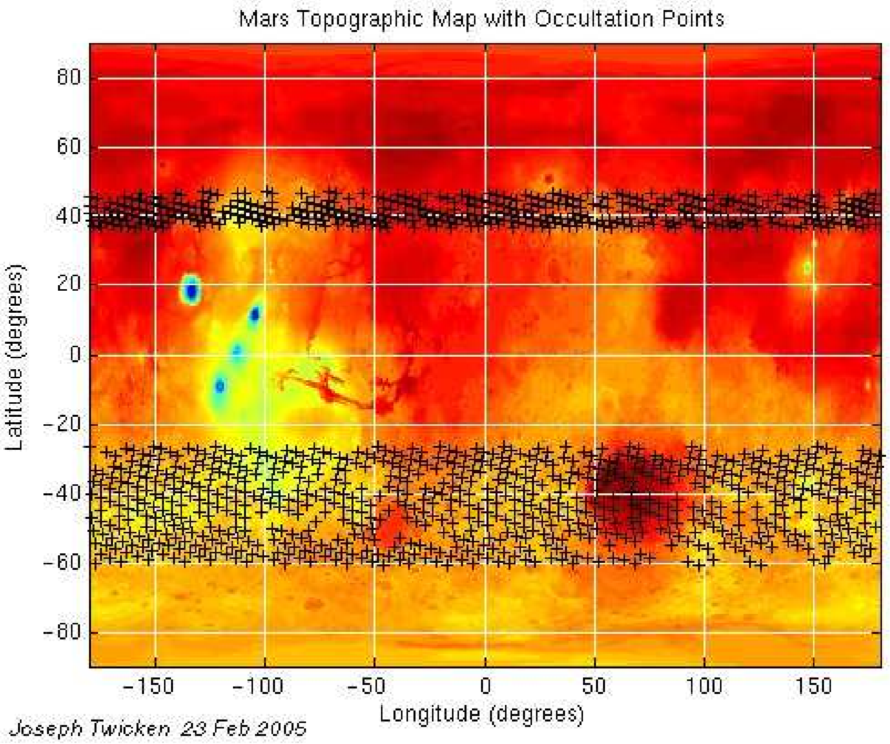

Figure 2.5: Typical “Martian Weather” map recorded by the Mars Global Surveyor Radio Science (MGSRS) Team. Highest points on Mars are indicated in dark blue and the lowest points are indicated in dark red. The crosses indicate some of the locations where annotated values of temperature and pressure are available. Data of this map have been acquired between March and May of 2004.

surface at different times of the day. Next, the measurements can be fit to a modeled diurnal temperature variation curve and thereby used to fix the value of I (Kieffer et al. 1977; Haberle and Jakosky 1991). On the other hand, while ρ_{sand} is around $2.0 \cdot 10^3$ kg/m^3 and $c = 0.16$ cal g^{-1}K^{-1} for most minerals on Mars (Edgett and Christensen 1991), the thermal conductivity depends on the grain size and on the atmospheric pressure (Wechsler and Glaser 1965). For the range of atmospheric pressures on Mars, k increases nearly monotonically with the grain diameter d (Kieffer et al. 1973). In this manner, the value of k obtained using calculated thermal inertia I from orbital data yields the diameter of the grains which compose the dune.

Edgett and Christensen (1991) have used thermal inertia data to obtain the grain diameter of dunes in intra-crater fields of dark dunes on Mars. They found that the grain diameter of Martian dune is $d = 500 \pm 100$ μm, which is coarser than the diameter of terrestrial dune grains, 250 μm. Why should the sand of Martian dunes be coarser than the sand of Earth’s dunes?

There is minimal size for a particle to saltate and form dunes: below this minimal value, the particle remains suspended in the atmosphere. The critical grain diameter depends on the vertical fluctuating component of the wind velocity u' (Tsoar and Pye 1987). If the standard deviation of u', which scales with the wind friction speed, is greater than the settling velocity of the grain, $v_{\rm f}$, then the particle will remain suspended. The transition suspension/saltation is given by the ratio $v_{\rm f}/u_{*{\rm ft}}$ (Bagnold 1941; Tsoar and Pye 1987). Particles for which this ratio lies below (above) the transition line $v_{\rm f}/u_{*{\rm ft}} = 1.0$ enter suspension (saltation).

We calculate the critical diameter for the transition suspension/saltation on Mars and on Earth. The threshold shear velocity for saltation, $u_{*{\rm ft}}$, is calculated using eq. (1.43), while the settling velocity $v_{\rm f}$ is calculated with eq. (1.42). The drag coefficient $C_{\rm d}$ is obtained with expression (1.47), and α is obtained with eq. (1.54). Furthermore, we use nominal pressure $P = 6$ mb and temperature $T = 200$ K for Mars. The ratio $v_{\rm f}/u_{*{\rm ft}}$ as function of the grain diameter d, on both planets, is shown in fig. 2.6. The dashed line indicates the transition value $v_{\rm f}/u_{*{\rm ft}} = 1.0$.

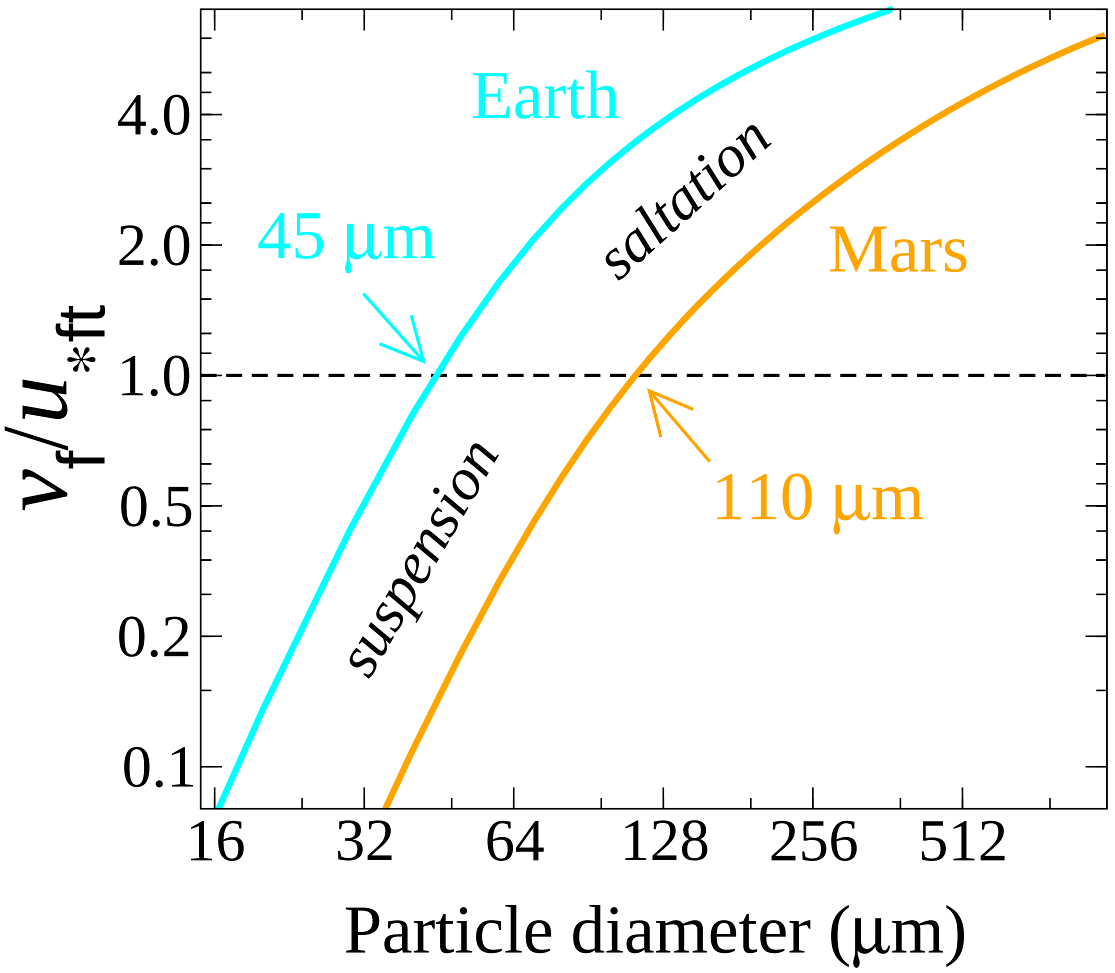

Figure 2.6: Ratio between the falling velocity $v_{\rm f}$ and the threshold friction speed for saltation, $u_{*{\rm ft}}$, calculated for Mars and for Earth as function of the grain diameter d. Dashed line indicates the saltation/suspension transition at $u_{\rm f}/u_{*{\rm ft}} = 1.0$, and intercepts the Martian (terrestrial) continuous line at $d = 110\mu$m ($d = 45\mu$m).

As we can see from fig. 2.6, particles with diameter smaller than $45\ \mu$m enter suspension on Earth, while the critical value of d on Mars is larger, around $110\ \mu$m. Furthermore, we see that the ratio between the average grain size of dunes and the critical diameter is around 5.0 on both planets. In fact, pure saltation is expected to occur only if $v_{\mathrm{f}}/u_{*\mathrm{t}} > 2.5$, which explains why the sand of dunes is effectively much larger than the critical diameter (Edgett and Christensen 1991). In this manner, we expect the grains of Martian sand dunes to be coarser than the grains of terrestrial dunes.

The result of fig. 2.6 is consistent with the observation that small ripples of grains with diameter around $100\ \mu$m occur at Meridiani Planum (Sullivan et al. 2005). The falling velocity used here accounts for the drag coefficient of the turbulent wind associated with the motion of saltating grains (eq. 1.47). In this case, the value of C_{d} for a grain falling vertically in the fluid under the action of gravity is corrected by a term of the order of 2α, which contains information about the shape of the grain trajectory. If we considered the falling velocity v_{f} without this correction, then the critical diameter would be $52\ \mu$m on Earth, and $210\ \mu$m on Mars, as obtained previously (Greeley and Iversen 1985; Edgett and Christensen 1991). The terrestrial value would be, then, not different than that in fig. 2.6, since, on Earth, $\alpha \approx 0.45$ and $2\alpha \approx 1.0$. However, the correction reduces the critical diameter on Mars because α on Mars is smaller than on Earth, as we will see below, typically between 0.2 and 0.3. This is associated with the shape of the grain trajectories of Mars, which are more “flat” than that of Earth’s grains.

2.2.2 Saltation trajectories and sand flux

Martian saltation has been simulated in wind tunnel experiments using a range of particle size and typical conditions of pressure and temperature of Mars (White et al. 1976; White 1979; Williams and Greeley 1980; Greeley and Iversen 1985; Marshall et al. 1998). It has been shown that (i) grains on Mars travel must faster and higher than Earth’s grains; (ii) the saltation trajectories are also typically longer and “flatter” on Mars (lower aspect ratio height/length); and (iii) the rate of sand transport is higher on Mars, i.e. more grains are mobilized into saltation than on Earth. Typical dimensions of such wind tunnel experiments (maximum length of MARSWIT is around 10 m) do not allow determine important quantities as for instance the transients of flux saturation and the equilibrium velocity of saltating grains, which are important to understand the formation of dunes.

Here we calculate the quantities controlling Martian saltation which we need to solve the sand transport equations and the evolution of dunes in the following chapters. The model parameters that govern the grain trajectories are the average saltation height, z_{m} (eq. (1.50)); the reference height z_1 (eq. (1.53)) at which the effective wind velocity u_{eff} is calculated; and the effective restitution coefficient, α (eq. (1.54)). The grain diameter used is $d = 500\mu$m, which gives $z_0^{\mathrm{sand}} = 25\ \mu$m (eq. (1.51)). Moreover, the saturated sand flux q_{s} (eq. (1.31)) depends on the saturation velocity of the saltating grains, v_{s} (eq. (1.41)). The quantities controlling saltation on Mars are calculated in table 2.1.

In table 2.1, the model parameters have been calculated using different values of pressure P and temperature T valid for Mars. We see that the minimal friction speed for saltation,

P (mbar)	T (K)	$u_{*\mathrm{t}}$ (m/s)	z_m (m)	z_1 (m)	α	v_s (m/s)	q_s (kg/m·s)
5.0	150	1.804	0.789	0.011	0.300	13.132	0.152
5.0	200	2.162	1.154	0.014	0.227	18.017	0.170
5.0	250	2.487	1.543	0.017	0.184	22.957	0.187
7.5	150	1.449	0.553	0.009	0.339	9.964	0.127
7.5	200	1.736	0.810	0.012	0.257	13.617	0.141
7.5	250	1.996	1.082	0.015	0.209	17.338	0.154
10.0	150	1.241	0.431	0.008	0.371	8.205	0.111
10.0	200	1.486	0.630	0.011	0.280	11.173	0.123
10.0	250	1.708	0.841	0.014	0.228	14.210	0.135
1000	300	0.218	0.016	0.004	0.431	1.419	0.009

Table 2.1: Main quantities controlling saltation on Mars under several values of pressure P and temperature T, and a *constant* $u_*/u_{*\mathrm{t}} = 1.5$. The threshold shear velocity $u_{*\mathrm{t}}$, the mean saltation height z_m, and the model variables z_1 and α depend on the atmospheric conditions, and have been calculated for a constant grain diameter $d = 500$ μm and density $\rho_\mathrm{grain} = 3200$ kg/m^3, and with a dynamic viscosity obtained from the temperature. The grain velocity v_s and the saturated flux q_s have been calculated with eqs.(1.41) and (1.31), respectively. The corresponding values for terrestrial saltation are shown for comparison. On Earth, the value $u_* = 1.5u_{*\mathrm{t}}$ means a shear velocity of 0.32 m/s.

$u_{*\mathrm{t}}$, on Mars may vary by a factor of 2. This is because $u_{*\mathrm{t}}$ depends on the atmospheric density (chapter 1). The condition of highest atmospheric density in table 2.1 corresponds to $P = 10.0$ mb and $T = 150$ K, for which $\rho_\mathrm{fluid} = 0.035$ kg/m^3, while $\rho_\mathrm{fluid} = 0.011$ kg/m^3 for $P = 5.0$ mb and $T = 250$ K. We note that ranges of P and T even wider than the ones studied here may occur on Mars (MGSRS 2006).

We calculate v_s and q_s in table 2.1 using a constant value of $u_*/u_{*\mathrm{t}} = 1.5$, since this is a representative value for saltation on Earth (Fryberger and Dean 1979). The corresponding values calculated for Earth are shown in the last row of table 2.1, where we used $d = 250$ μm, density $\rho_\mathrm{fluid} = 1.225$ kg/m^3 and viscosity $\eta = 1.8$ kg/m·s, while $g = 9.81$ m/s^2.

As we can see in table 2.1, the values of sand flux on Mars are typically 10 times larger than on Earth. This is in agreement with the findings of White (1979) using wind tunnel simulations of saltation on Mars. We also see that Martian particles travel with a higher velocity, while the mean saltation height z_m on Mars is larger than on Earth, and may be over 1.0 m depending on the atmospheric conditions.

While the ratio $u_*/u_{*\mathrm{t}}$ in table 2.1 is constant, in the upper inset of fig. 2.7 we calculate q_s for a *constant* wind velocity $u_* = 3.0$ m/s using values of P and T within the range studied in table 2.1. We see that the same wind friction speed transports more sand where P is higher and T is lower, which means lower ρ_fluid and $u_{*\mathrm{t}}$.

In the main plot of fig. 2.7 we show how the flux and the particle velocity at a given location on Mars depend on $u_*/u_{*\mathrm{t}}$. In the main plot we fix $T = 200$ K and calculate the saturated flux q_s for different values of atmospheric pressure P as function of $u_*/u_{*\mathrm{t}} - 1$.

In the lower inset, the same calculations are made for the grain velocity $v_{\rm s}$. We see that for a given value of $u_*/u_{*{\rm t}}$, both the flux and the grain velocity are larger for lower atmospheric pressure P. This is because the shear velocity $u_{*{\rm t}}$ required for sand transport is higher for lower P, while $v_{\rm s}$ scales with $u_{*{\rm t}}$ and $q_{\rm s}$ scales with $u_{*{\rm t}}^2$ (see chapter 1).

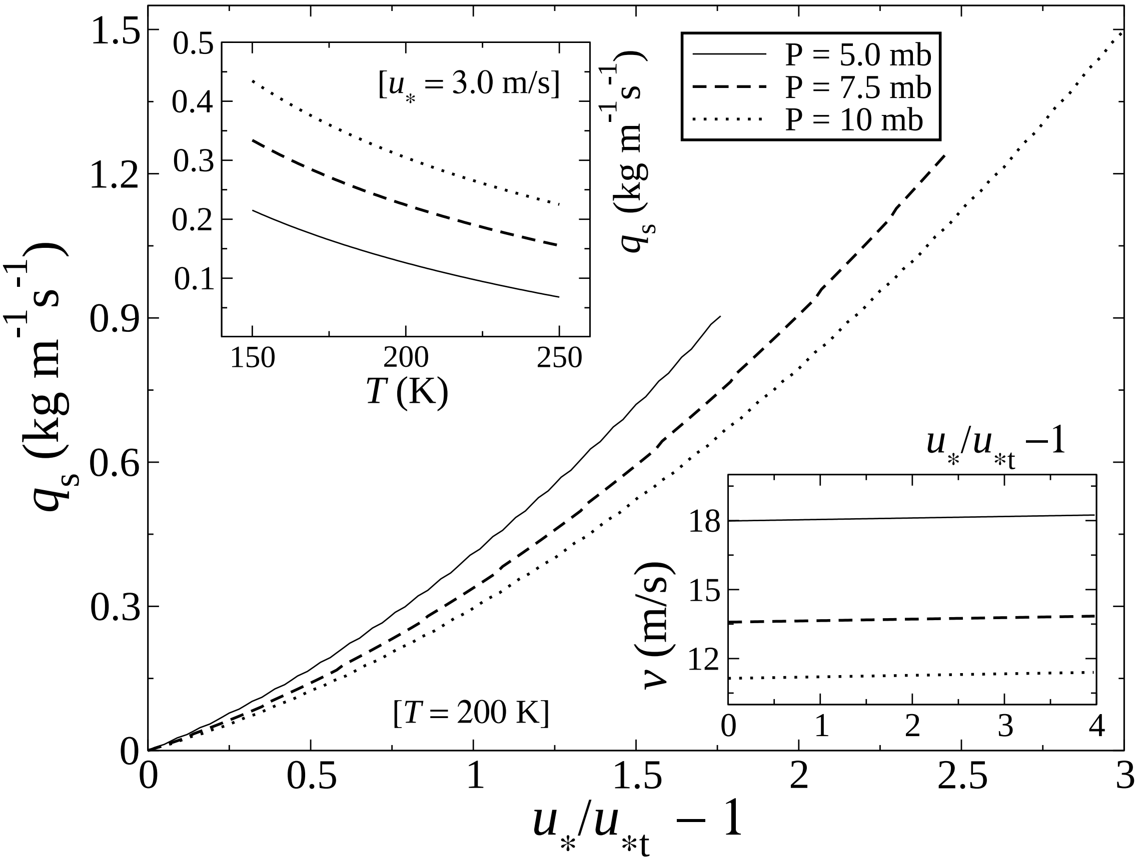

Figure 2.7: Main plot: Saturated sand flux $q_{\rm s}$ as a function of the relative shear velocity $u_*/u_{*{\rm t}} - 1$ for different values of atmospheric pressure — and therefore different values of $u_{*{\rm t}}$ — obtained with a temperature $T = 200$ K. The lower inset on the right shows the corresponding values of the average grain velocity $v_{\rm s}$. In the upper inset on the left, we show the saturated flux for $u_* = 3.0$ m/s calculated for different values of temperature valid on Mars.

The lower inset of fig. 2.7 shows that the grain velocity in the equilibrium is determined by the atmospheric conditions and has only a weak dependence on the friction speed u_*. This is seen in table 2.2, in which we show $v_{\rm s}$ and $q_{\rm s}$ calculated for different values of $u_*/u_{*{\rm t}}$ on Mars and on Earth. In this table, calculations for Mars are performed using $P = 6.0$ mb and $T = 200$ K. From the results of table 2.2, we see that the grain velocity $v_{\rm s}$ scales with the threshold friction speed $u_{*{\rm t}}$, and is essentially a constant independent of u_*. Because the threshold wind friction speed on Mars is 10 times higher than on Earth, the average velocity of saltating grains on Mars is one order of magnitude higher than the velocity of Earth's grains. Again, $v_{\rm s}$ may have different values depending on the location on Mars, while $q_{\rm s}$ depends further on u_*.

u_*/u_{*t}	v_s (m/s) [Earth]	v_s (m/s) [Mars]	q_s (m/s) [Earth]	q_s (m/s) [Mars]
1.05	1.367	15.854	0.0007	0.0128
1.10	1.373	15.857	0.0015	0.0262
1.25	1.390	15.867	0.0040	0.0703
1.50	1.419	15.883	0.0090	0.1563
1.70	1.442	15.896	0.0139	0.2366
2.00	1.447	15.916	0.2258	0.3760

Table 2.2: Average velocity v_s of saltating grains on Earth and on Mars as a function of the relative shear velocity u_*/u_{*t}. Temperature $T = 200$ K and Pressure $P = 6.0$ mb was used for Mars.

In summary, using the atmospheric data provided by MGSRS (2006), we can calculate the quantities controlling saltation at a given location on Mars, for example, at a given dune field. From the MGSRS "Weather" maps (e.g. fig. 2.5), we obtain the value of P and T characteristic of the area at which the dune field is located. Next, the density and viscosity are calculated from P and T, using the ideal gas law and eq. (2.1), while the model parameters are obtained using the grain diameter $d = 500\ \mu$m of Martian sand dunes. The wind velocity u_* in the dune fields on Mars is an unknown quantity. It must be determined from the calculations of dunes, as we will see in the next chapter.

Indeed, there is still one missing quantity for Mars which we need to solve the sand transport equations: γ, which appears in eq. (1.33). γ is given by the product $r\tilde{\gamma}$, where r is related to the saltation trajectories, and $\tilde{\gamma}$ gives the strength of the erosion rate. To obtain γ, measurements of the transient of flux saturation are needed in order to compare with model predictions. The terrestrial value $\gamma = 0.2$ has been obtained by Sauermann et al. (2001) from comparison with experimental and numerical data of saturation transient (Anderson and Haff 1991; McEwan and Willetts 1991; Butterfield 1993), which are not available for Mars. Moreover, r and $\tilde{\gamma}$ cannot be obtained separately.

Let's estimate the ratio between the values of r on Mars and on Earth. r is given by eq. (1.34), and depends, thus, on α, v_s, and on the vertical velocity at the instant of ejection, v_z^{eje}. Modelling v_z^{eje} implies considering microscopic interactions of the grains with the sand bed, which is out of the scope of the model (Sauermann et al. 2001). In fact, there is a distribution of angles and velocities of ejection (Anderson and Haff 1988; Anderson and Haff 1991; Rioual et al. 2000). The information about the average angle and velocity of ejection after splash is included in the effective restitution coefficient of the grain-bed collisions, α.

Moreover, we can model the splash using an effective particle which *rebounds* at the sand bed (Durán and Herrmann 2006a). The effective particle emerges from the bed with a velocity v_{eje} making an angle θ_{eje} with the horizontal. In this case, the restitution coefficient of the sand, $\zeta = |\vec{v}_{\text{eje}}|/|\vec{v}_{\text{imp}}|$, gives the ratio between the ejection velocity $|\vec{v}_{\text{eje}}|$ and the velocity at the moment of impact, $|\vec{v}_{\text{imp}}|$. For simplicity, we consider that the particle moves in the direction of the wind (x). Thus, we have:

$$\alpha = \frac{v_z^{\mathrm{eje}}}{v_x^{\mathrm{imp}} - v_x^{\mathrm{eje}}} = \frac{\zeta \sin\theta_{\mathrm{eje}}}{\cos\theta_{\mathrm{imp}} - \zeta \cos\theta_{\mathrm{eje}}}, \tag{2.2}$$

where θ_{imp} and θ_{eje} are the angles of impact and ejection (rebound), respectively, and are defined with respect to the horizontal.

The ratio between α values on Mars and on Earth is:

$$\frac{\alpha_{\mathrm{M}}}{\alpha_{\mathrm{E}}} = \frac{\zeta^{\mathrm{M}} \sin\theta_{\mathrm{eje}}^{\mathrm{M}}}{\zeta^{\mathrm{E}} \sin\theta_{\mathrm{eje}}^{\mathrm{E}}} \left[\frac{\cos\theta_{\mathrm{imp}}^{\mathrm{E}} - \zeta^{\mathrm{E}} \cos\theta_{\mathrm{eje}}^{\mathrm{E}}}{\cos\theta_{\mathrm{imp}}^{\mathrm{M}} - \zeta^{\mathrm{M}} \cos\theta_{\mathrm{eje}}^{\mathrm{M}}} \right], \tag{2.3}$$

where we use “E” for Earth and “M” for Mars. On Earth, the angles of impact and ejection are, respectively, $\theta_{\mathrm{imp}}^{\mathrm{E}} \approx 10^\circ$ and $\theta_{\mathrm{eje}}^{\mathrm{E}} \approx 36^\circ$ (Anderson and Haff 1988; Almeida et al. 2006). On the other hand, White (1979) has shown that impact angles $\theta_{\mathrm{imp}}^{\mathrm{M}}$ on Mars are close to the earth’s ($5^\circ - 15^\circ$) if the grain diameter there is above 400μm, but he did not report on the ejection angles $\theta_{\mathrm{eje}}^{\mathrm{M}}$. We may set $\theta_{\mathrm{imp}}^{\mathrm{M}} \approx 10^\circ$ and disregard the dependence of the impact angle on the shear velocity (White 1979), since we are interested in the trajectories at saturation, where v_{s} is almost independent of u_* (table 2.2).

From eq. (2.3), the Martian angle of ejection $\theta_{\mathrm{eje}}^{\mathrm{M}}$ is the one for which $\sin(\theta_{\mathrm{eje}}^{\mathrm{M}})$ equals the quantity

$$f(\theta_{\mathrm{eje}}^{\mathrm{M}}) = \sin\theta_{\mathrm{eje}}^{\mathrm{E}} \frac{\alpha_{\mathrm{M}}}{\alpha_{\mathrm{E}}} \frac{\zeta^{\mathrm{E}}}{\zeta^{\mathrm{M}}} \frac{\cos\theta_{\mathrm{imp}}^{\mathrm{M}} - \zeta^{\mathrm{M}} \cos\theta_{\mathrm{eje}}^{\mathrm{M}}}{\cos\theta_{\mathrm{imp}}^{\mathrm{E}} - \zeta^{\mathrm{E}} \cos\theta_{\mathrm{eje}}^{\mathrm{E}}}. \tag{2.4}$$

Since the density of the sand on Mars is not too different than on Earth, we may use the approximation $\zeta^{\mathrm{M}} \sim \zeta^{\mathrm{E}}$. We solve eq. (2.4) numerically for the angle of ejection $\theta_{\mathrm{eje}}^{\mathrm{M}}$ on Mars, under the assumptions above. In this manner, we find that $\theta_{\mathrm{eje}}^{\mathrm{M}}$ is around 17° (fig. 2.8, solid curves), which is nearly $1/2$ of the terrestrial ejection angle, 36°.

The quantity r may be written in terms of the ejection angle θ_{eje}:

$$r = \frac{v_{\mathrm{s}}}{\Delta v_{\mathrm{hor}}} = \alpha \frac{v_{\mathrm{s}}}{v_z^{\mathrm{eje}}} = \frac{v_{\mathrm{s}}}{v_{\mathrm{eje}}} \left[\frac{\alpha}{\sin\theta_{\mathrm{eje}}} \right]. \tag{2.5}$$

In the equation above, the quantity in the brackets can be calculated both for Mars and for Earth. On Mars, $\alpha \approx 0.24$ and $\sin\theta_{\mathrm{eje}}^{\mathrm{M}} = \sin 17^\circ \approx 0.29$; while on Earth, $\alpha \approx 0.45$ and $\sin\theta_{\mathrm{eje}}^{\mathrm{E}} = \sin 36^\circ \approx 0.60$. In this manner, the quantity in the brackets is around 0.8, both for Mars and for Earth. The ratio $r_{\mathrm{M}}/r_{\mathrm{E}}$ is:

$$\frac{r_{\mathrm{M}}}{r_{\mathrm{E}}} = \frac{\left(v_{\mathrm{s}}^{\mathrm{M}}/v_{\mathrm{eje}}^{\mathrm{M}}\right)}{\left(v_{\mathrm{s}}^{\mathrm{E}}/v_{\mathrm{eje}}^{\mathrm{E}}\right)} \approx 1.0, \tag{2.6}$$

since v_{eje} is proportional to the impact velocity v_{imp} (Anderson and Haff 1988), which in turn scales with v_{s} (Sauermann et al. 2001). Therefore, if we assume that the physics of saltation on Mars is the same as on Earth, then r (eq. 1.34) should be approximately the same on both planets.

Finally, $\tilde{\gamma} = \gamma/r$ remains, which has not yet been calculated for Mars. $\tilde{\gamma}$ determines the intensity of the splash events. How determine $\tilde{\gamma}$ on Mars? This is what we will see in the next chapter.

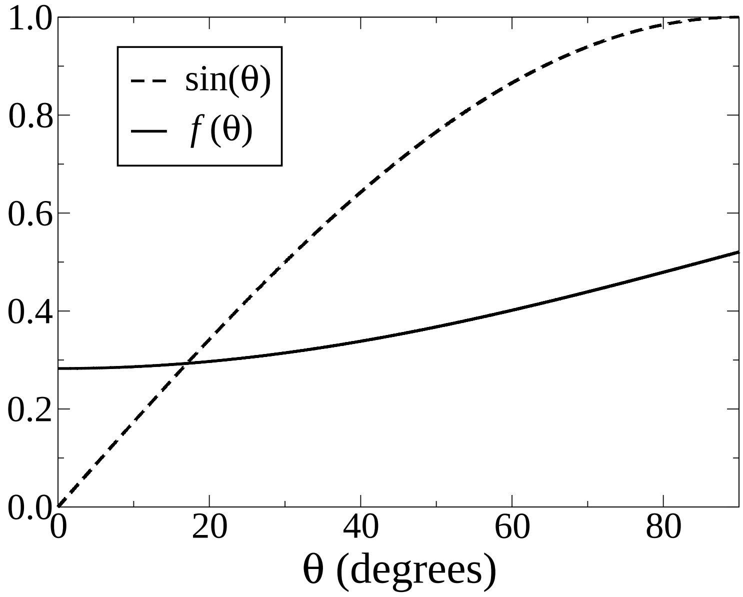

Figure 2.8: Calculation of the angle of ejection for Martian saltating (rebounding) particles. The solution is $\theta_{\mathrm{eje}}^{\mathrm{M}} = \theta$ for which $\sin(\theta)$ (dashed line) equals $f(\theta)$ (solid line) defined in eq. (2.4) and calculated restitution coefficient $\zeta^{\mathrm{M}} = 0.45$ as on Earth. The solution is $\theta_{\mathrm{eje}}^{\mathrm{M}} \approx 17°$.

2.3 Conclusion

We have seen that only rarely do winds on Mars transport sand grains through saltation. Orbiters and landers could detect evidences for saltation events by comparing images of Martian soils after and before major dust storms (Arvidson et al. 1983; Moore 1985; Greeley et al. 1999; Greeley et al. 2000; Sullivan et al. 2005). In this manner, it has been concluded that saltation on Mars occurs only within the gusts of extreme aeolian activity, which are associated with dust storms that may occur every 6 Earth's years (or 3 Martian years). Within such peaks of wind velocity, many authors estimated that u_* may reach maximum values between 2.2 and 4.0 $\mathrm{m/s}$, and may last above the threshold only for a few seconds (Arvidson et al. 1983; Moore 1985). Again, very unprobably must u_* achieve values of the order of 4.0 $\mathrm{m/s}$ on Mars (Sullivan et al. 2005).

Such values of u_* are effectively not far above the Martian threshold velocity for saltation, $u_{*\mathrm{t}} = 2.0$ $\mathrm{m/s}$ (Greeley et al. 1980). In fact, values of $u_*/u_{*\mathrm{t}}$ between 1.0 and 2.0 are typical in terrestrial dune fields (Fryberger and Dean 1979). However, once the wind succeeds entraining grains into flow, Martian particles travel much faster than their Earth's counterparts, and the sand flux on Mars is 10 times larger than on Earth (White 1979). Here we have calculated the quantities of the dune model governing saltation on Mars, and we have shown that the grain trajectories, the sand flux and the average saltation velocity may vary in an important way with the atmospheric conditions on Mars. Finally, to calculate saltation at a given location, we can take the local values of Martian pressure P and temperature T measured by the MGSRS Team (e.g. fig. 2.5).

In the following chapters, our aim is to find, from comparison with the model results, the different wind regimes and the sand flux associated with the diverse dune shapes observed on Mars and on Earth. We want to obtain the value of u_* which formed dunes on Mars. In the calculations of Mars dunes, the saltation model parameters are obtained following the procedure described here.

However, there is still one quantity which we need to solve the transport equations for Mars. This quantity is the entrainment rate of grains into saltation, $\tilde{\gamma}$. It is in the next chapter that we will obtain the Martian entrainment rate, from the size of barchan dunes on Mars.

Chapter 3

Barchan dunes on Mars and on Earth

Barchan dunes are the simplest and best understood type of dunes. Therefore, we start our exploration of Martian dunes with the investigation of a field of huge barchan dunes located in the Arkhangelsky Crater on Mars. We are interested in answering the following question: Could Martian dunes have been formed under the present atmospheric conditions of Mars?

We procedure in the following manner: (i) first, we show that the *shape* of barchan dunes is function of the wind velocity and of the sand flux between dunes; we find that barchan dunes on Mars have an elongated shape because the velocity of Martian winds is close to the minimal value for sand transport; (ii) next, we show that the wind velocity plays a major rule for the *scale* of dunes: the minimal size of a barchan dune decreases with the wind velocity. We find that the minimal size of Martian dunes can be reproduced with realistic winds only if the rate at which grains are entrained into saltation on Mars is one order of magnitude larger than on Earth; (iii) this led us to find one equation for the saltation entrainment which can be extended to diverse atmospheric conditions. Finally, we estimate the wind velocity on Mars from the shape of Martian barchans.

3.1 The shape of barchan dunes

Barchan dunes, also called “Wanderdünen” in german, are certainly the best known dunes (Bagnold 1941; Finkel 1959; Long and Sharp 1964; Hastenrath 1967; Lettau and Lettau 1969; Embabi and Ashour 1993; Besler 1997; Hesp and Hastings 1998; Jimenez et al. 1999; Sauermann et al. 2000; Hersen et al. 2002; Bourke et al. 2004; Elbelrhiti et al. 2005). They have a windward side, two horns, and a slip face at the lee side, where avalanches take place (fig. 3.1). Barchans appear under conditions of uni-directional wind, in places where there is not enough sand to cover the bedrock. Barchan dunes are subject of scientific and also environmental interest because of their high rate of motion. For instance, barchans $1-5$ m high may cover $30-100$ m in a year. Such dunes are found very often on coasts, where they emerge from the sea sand, the grains of which, after being deposited onto the beach, dry and are thereafter entrained into saltation.

In figs. 3.2 and 3.3 we see barchan dune fields on Earth and on Mars, respectively. It is remarkable that barchan dunes may have very different shapes. Field geomorphologists define as dune *shape* the proportions between dune height H, width W and length L of a dune. These quantities are defined in fig. 3.1.

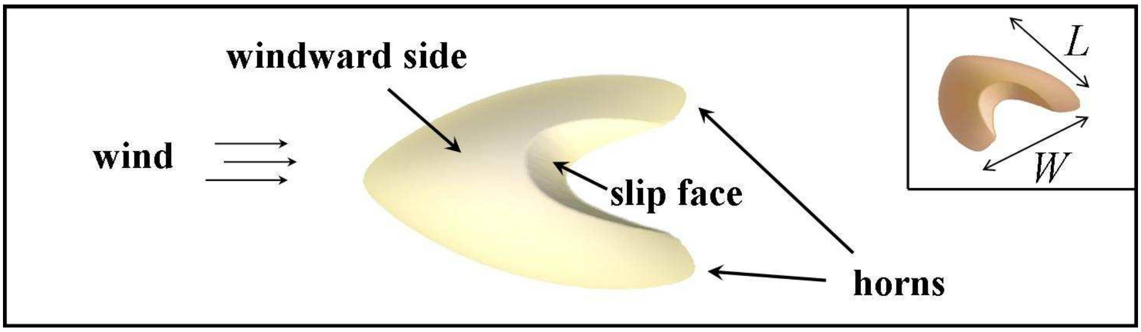

Figure 3.1: Sketch of a barchan dune showing the windward side, horns and slip face. In the inset we see the definitions of dune width W and length L.

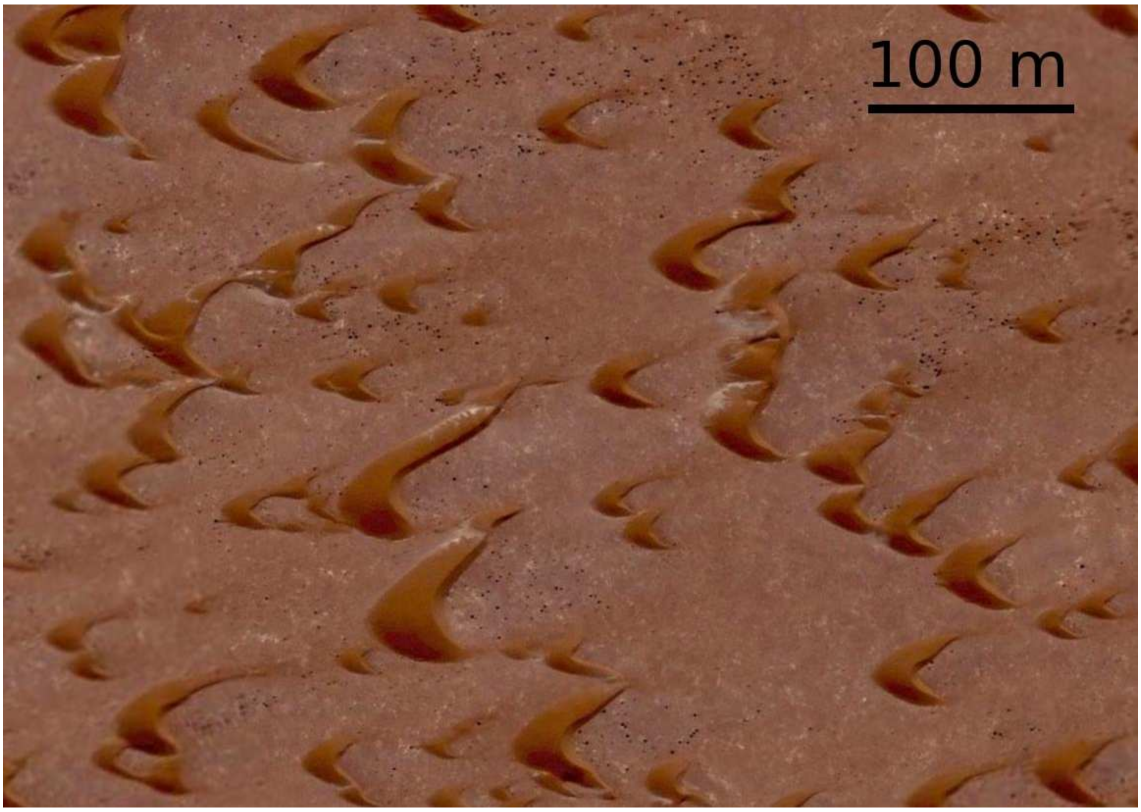

Figure 3.2: Barchan dunes in Morocco. We see that very small dunes do not display slip face or horns. Image from the World Wide Web.

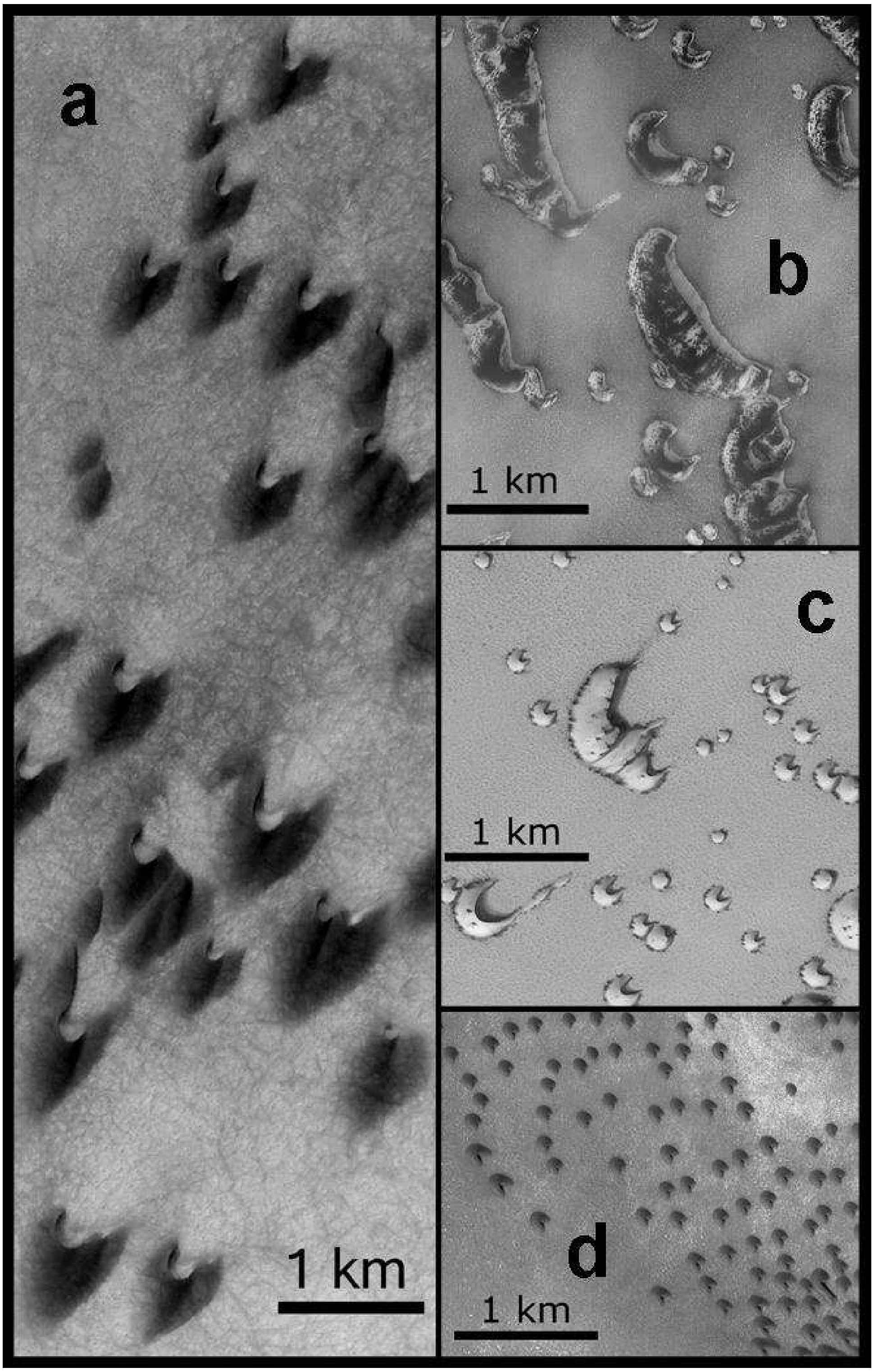

Figure 3.3: MOC images of martian dunes. **a.** Barchan dunes in the Arkhangelsky crater (42°S, 25°W). In **b.**, **c.** and **d.** we see north polar dunes in (76.3°N, 263.5°W), (76.6°N, 255.9°W) and (71.7°, 51.3°W), respectively.

What are the relevant variables that determine the barchan shape? On one hand, the grain diameter, gravity, and the atmospheric density are different on Mars, and therefore the size of dunes on Mars is different than on Earth, as we will discuss later in this Chapter. Further, the dune shape is a function of the *wind strength* and of the amount of mobile sand, or *inter-dune sand flux* (Bourke et al. 2004).

The wind shear velocity u_* may have very different values depending on the location of the field (Ash and Wasson 1983; Pye and Tsoar 1990). Illenberger and Rust (1988) found that rates of sand deposition can be ten times higher in coastal dune fields than those in mid-desert sand seas, due to the abundant sand supply on sandy beaches and the higher energy of coastal winds. Lancaster (1985), Tsoar (1986) and McKenna Neuman et al. (2000) suggested, based on field observations, that the frequency distribution of winds above the threshold may determine the overall morphology of dunes. As stressed by McKenna Neuman et al. (2000), "dunes in areas characterized by coarse sediment (higher effective threshold) and/or low wind speeds will tend to have lower, longer profiles (lower aspect ratio) compared with those in areas of fine sediments and/or strong winds" (McKenna Neuman et al. 2000). On the other hand, the inter-dune flux has been subject of field measurements (Lettau and Lettau 1969; Fryberger et al. 1984) and may vary significantly even in the same area (Fryberger et al. 1984). It depends on the amount of loose sand available between dunes, on the size and distribution of large immobile particles, humidity and the presence of sparse vegetation. The flux between barchans in a field is normally smaller than 50% of the maximum flux (Fryberger et al. 1984).

Let's investigate how the wind strength and the inter-dune flux influence the barchan *shape*. We perform different calculations of a barchan dune starting with the simplest initial surface, which is a Gaussian hill of height H and characteristic length σ as shown in fig. 3.4. In calculations we use open boundaries, an uni-directional wind of friction speed u_* and a constant sand influx $q_{\rm in}$ at the inlet. The influx is interpreted as the average inter-dune flux in a dune field. The Gaussian hill evolves in time until it achieves a final barchan shape. We then study how the dune shape depends on $u_*/u_{*{\rm t}}$ and $q_{\rm in}/q_{\rm s}$.

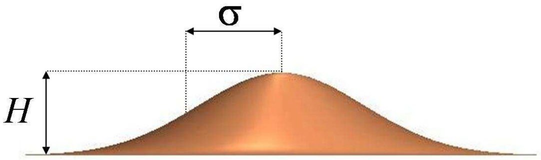

Figure 3.4: The initial surface is a Gaussian hill of height H and characteristic length σ.

In fig. 3.5, we see terrestrial barchan dunes calculated with different values of wind friction speed u_*, but with a constant value of $q_{\rm in}/q_{\rm s} = 0.20$. In the main plot of this figure, we see that the dune length L increases with the width W at different rates depending on the wind strength: the lowest wind speeds (circles) yield more *elongated* dunes independently of the dune size, while the ratio L/W for any value of W decreases with u_*. On the other hand, the lower inset of fig. 3.5 shows that the dune height increases linearly with the width W in a similar manner for all shear velocities.

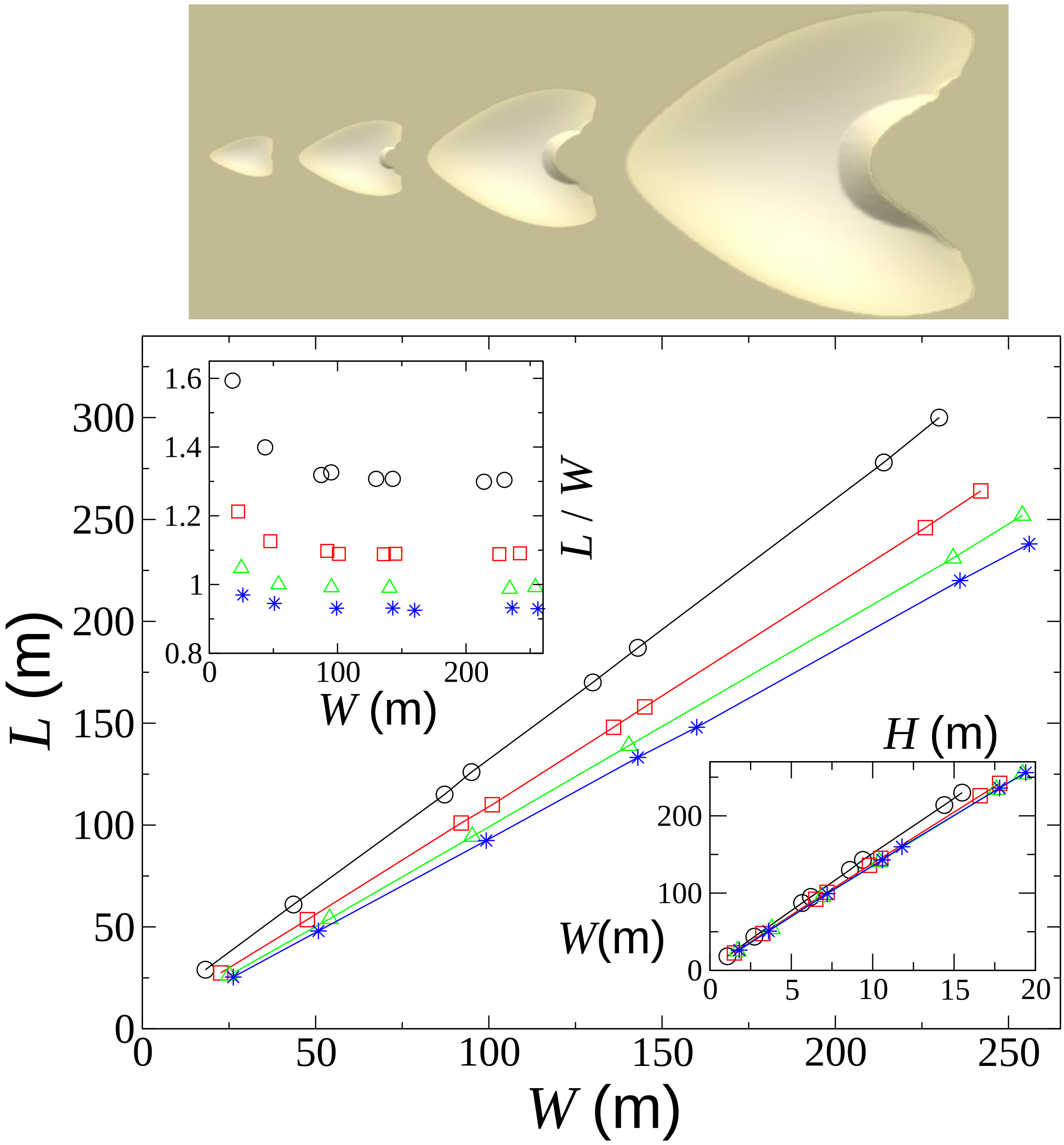

Figure 3.5: In the box on top, we show dunes of width 6.5, 12, 21 and 48 m, from the left to the right, calculated with $u_* = 0.36$ m/s and $q_{\rm in}/q_{\rm s} = 0.2$. Threshold shear velocity is $u_{*{\rm t}} = 0.22$ m/s. The main plot shows the linear relation between L and W for different values of shear velocity: $u_* = 0.3$ (circles), 0.36 (squares), 0.41 (triangles) and 0.46 m/s (stars). The upper-left-hand-corner inset shows the eccentricity L/W as a function of the dune width W for the corresponding values of u_*. In the bottom-right-hand-corner inset, we see that the width W of the dune increases with the height H in the same manner for all values of u_*.

The upper inset of fig. 3.5 shows that the *eccentricity* of the dune, L/W, depends on the dune size: it is larger the smaller the barchan dune, while the largest dunes have essentially a constant L/W. Dunes of different sizes, calculated with $u_*/u_{*{\rm t}} = 1.65$, are shown in the box on top of fig. 3.5. We see that the dune shape is in fact not scale invariant, as it has been recognized and explained previously (Sauermann et al. 2001; Kroy et al. 2002). On the basis of the results shown in fig. 3.5, we conclude that the shape of barchan dunes may be different depending on the field, since the wind strength may have distinct values depending on the geographical location (Pye and Tsoar 1990).

Here it must be emphasized that the wind strength we consider is a mean value of the wind velocities (above the threshold) associated with sand transport. In a given field, the wind is normally very fluctuating in time, a large fraction of which its velocity is even below the threshold for saltation (Pye and Tsoar 1990). Time series of wind speed measured in the field may be found for instance in McKenna Neuman et al. (2000) and Knight et al. (2004). The wind velocity u_* we use in our calculations is interpreted as a representative value of winds strong enough for saltation to occur — an average over the wind velocities above the threshold.

Indeed, even in the same field, dunes may display differences in their shapes. Dunes with asymmetries, for example, may be a result of small, local fluctuations in the wind direction and/or variations in the topography (Bourke et al. 2004). Further, the shape of the dune depends on the amount of sand *influx*, as we call the flux at the inter-dune area for the downwind barchan, which may vary significantly in a dune field (Fryberger et al. 1984).

One factor that determines the sand influx is the distribution of dunes upwind. While the net flux just after the slip face of a barchan dune is zero, the flux is nearly saturated at the tip of the dune horns. The sand which leaves the horns is transported through the inter-dune area and reaches the windward side of the downwind dune. The amount of sand transported depends on several variables. First, it depends on the shape of the dune horns; dunes with thicker horns lose more sand. We notice that this property can only be captured in a three-dimensional calculation of dunes, since the horns are not included in a two-dimensional model (Kroy et al. 2002; Kroy et al. 2005). On the other hand, the sand flux which arrives at the dune depends on the transport properties of the inter-dune area. While inter-dune areas with vegetation and humidity may trap the sand, on bedrock, the flux is essentially conserved, while the sand flux on areas with much sand is saturated.

We investigate how the dune shape depends on the influx at the inlet of the simulation grid, i.e. on the *inter-dune flux*. In fig. 3.6 we see how different a barchan dune of width $W = 180$ m appears with different values of $u_*/u_{*\mathrm{t}}$ and with $q_{\mathrm{in}}/q_{\mathrm{s}}$, which varies from 1 to 50%. Kroy et al. (2005) have shown that the aspect ratio H/L increases with u_*. Furthermore, there is an interesting feature which we can only see with three-dimensional calculations. The “slim” shape (small windward side compared to the dune width) of barchans is characteristic for areas of low $q_{\mathrm{in}}/q_{\mathrm{s}}$, and as the influx increases, the dunes become “fat” (large windward side).

The differences between “slim” and “fat” barchan shapes have been noticed by Long and Sharp (1964), who reported that these dunes also behave differently. Long and Sharp (1964) observed that the “fat” barchans at Imperial Valley, California, are the more “morphologically complex and areally larger dune masses”, and may be also a result of dune interaction, coalescence and dune fusion. Their interpretations are in accordance with our calculation results for a larger inter-dune flux and therefore a higher amount of sand

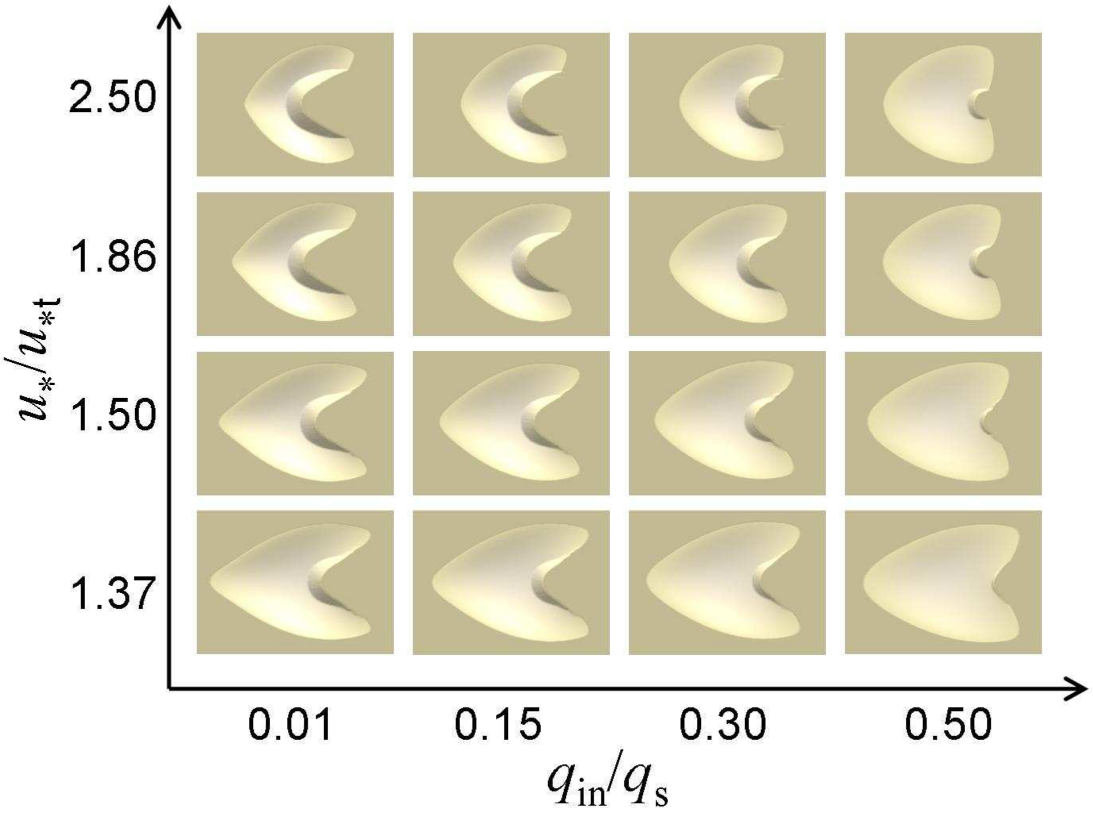

Figure 3.6: Barchan dunes of width $W = 180$ m calculated with different values of relative wind friction speed u_*/u_{*t} and influx q_{in}/q_s.

(influx) at the upwind of barchans.

One important issue which has been addressed by Long and Sharp (1964) is how the rate of movement of a barchan dune depends on the dune shape. Long and Sharp (1964) speculated that the fat dunes might move at different rates than slim dunes. First, if the outflux at the dune horns is smaller than the influx, the dune is unstable and is growing in time. In this case, a fat dune should move *slower* than its slim counterpart, because a greater volume of sand is needed to produce a corresponding increase in height of the fat dune. But if the influx more or less balances the loss of sand of the dune at the tip of its wings, then the opposite should occur: in the steady-state condition, “a fat barchan should move more rapidly since most of the sand causing advance is derived from the windward slope of the dune itself, and a fat barchan has a long windward slope as a source of supply” (Long and Sharp 1964).

From the field observations, Long and Sharp (1964) could not draw any conclusion about the influence of the dune shape on the dune velocity: these behave nearly independently of each other. This can be seen in fig. 3.7, where we plot the velocity in m/year of all dunes of width $W = 180$ m shown in fig. 3.6. We see that the velocity of dunes with the same width increases with u_*; however, u_* is nearly constant within a given barchan field. On the other hand, the dune velocity is nearly independent of the inter-dune flux

$q_{\text{in}}/q_{\text{s}}$, which may vary within a given dune field. Figure 3.7 illustrates the observation of Long and Sharp (1964) that in a given barchan field, the velocity of a dune is determined effectively by the dune size and is essentially independent of the dune shape.

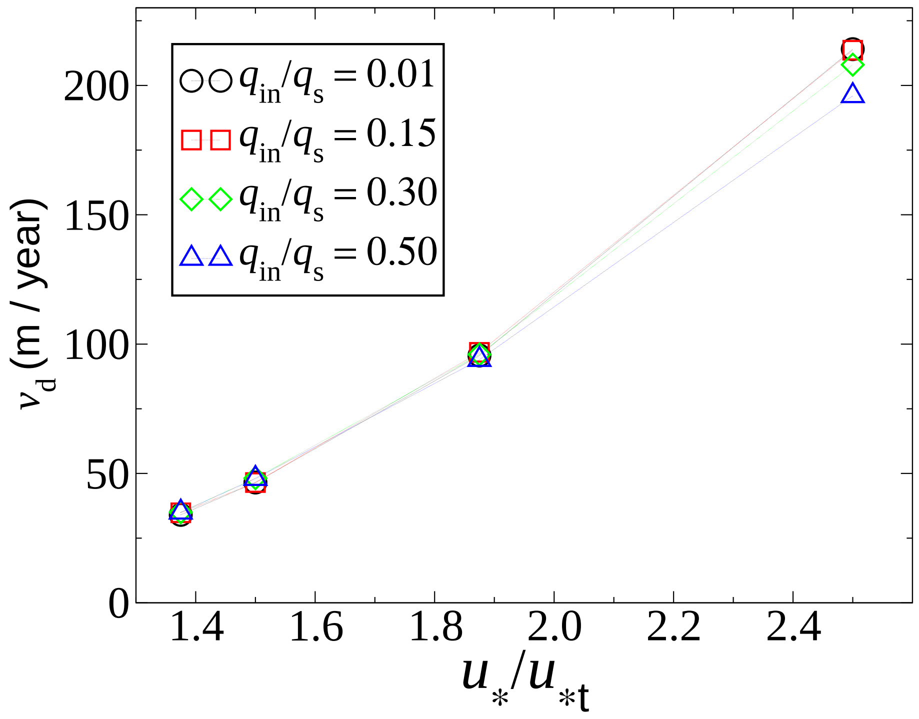

Figure 3.7: Migration velocity of a terrestrial barchan dune of width $W = 180$ m as function of the relative wind friction speed u_*/u_{*t}, calculated for different values of influx $q_{\text{in}}/q_{\text{s}}$.

3.2 Minimal size of a barchan dune

In fig. 3.5, we see that the dune shape depends on the dune size, and there is also one important feature, which can be also observed in the images (figs. 3.2 and 3.3) — The characteristic slip face and horns are absent from the smallest barchans. There is, thus, a critical size for a barchan dune to nucleate. Below this minimal size, sand dunes are called *domes*.

The minimal size of dunes is determined by the distance of flux saturation. This distance increases with the length of the saltating trajectories, ℓ, which in turn scales with the quantity

$$\ell_{\text{drag}} = d\rho_{\text{grain}}/\rho_{\text{fluid}}, \tag{3.1}$$

where d is the grain diameter, ρ_{grain} is their density, ρ_{fluid} is the density of the driving fluid, and ℓ_{drag} is the distance within which a sand grain lifted from the bed reaches the wind velocity (Andreotti et al. 2002a).

The proportionality between the minimal dune size and the saltation length and $\ell_{\rm drag}$ has been verified in the field and also in the laboratory. Hersen et al. (2002), supported by previously reported measurements on several terrestrial barchan dune fields, observed that the smallest dunes have heights of the order of $\ell_{\rm drag}$, and that the minimal width $W_{\rm min}$ of a barchan dune is approximately 20 times $\ell_{\rm drag}$. Since the sand of aeolian dunes is constituted by quartz grains of mean diameter $d = 250$ μm and density $\rho_{\rm grain} = 2650$ kg/m^3, we obtain, using the air density $\rho_{\rm fluid} = 1.225$ kg/m^3, $\ell_{\rm drag}$ (and therefore $H_{\rm min}$) $\approx$ 50 cm, and $W_{\rm min}$ around 10 m. It is somewhat intriguing that Hersen et al. (2002) could find a similar relation for the minimal size of aquatic dunes although saltation in water is much attenuated because of the high density of the driving fluid (Hersen et al. 2002). In their experiment, they found dunes 1000 times smaller than the aeolian dunes, since $\rho_{\rm fluid}$ of water is 10^3 kg/m^3.

As observed recently, there are other physical variables besides $\ell_{\rm drag}$ which appear relevant to explain the scale of dunes (Kroy et al. 2005). Barchans are also found on Mars, where the atmospheric density is 100 times smaller than on Earth. Because the mean grain diameter $d = 500$ μm and density $\rho_{\rm grain} \approx 3200$ kg/m^3 are not very different from the Earth's, we would expect dunes on Mars to be accordingly 200 times larger, and at least around 2 km in width, since $\ell_{\rm drag}$ on Mars is nearly 100 m. However, we find on Mars dunes of only a few hundred meters in width (fig. 3.3). On the basis of this surprising inconsistence, it has been suggested that still unknown microscopic properties of the Martian saltation must be understood and taken into account in order to correctly predict the size of dunes on Mars (Kroy et al. 2005).

In fig. 3.3, we see that the size and the shape of the domes and of the dunes are particular for each field. We have also seen that different dunes are obtained depending on $u_*/u_{*{\rm t}}$ and $q_{\rm in}/q_{\rm s}$. In fact, the properties of dunes are related to the specific conditions of wind and flux in the field (Bourke et al. 2004).

Here we investigate how the field variables, $u_*/u_{*{\rm t}}$ and $q_{\rm in}/q_{\rm s}$, influence the minimal dune size. We first study the minimal size of terrestrial dunes. In particular, we look for the smallest barchan dune for each set of $\{u_*/u_{*{\rm t}},\, q_{\rm in}/q_{\rm s}\}$. We also want to investigate how the shape of the minimal dune depends on the wind strength and the flux in the interdune area. To determine the minimal size, we perform simulations of dunes of different sizes, where we begin with sand hills of different heights H with a constant $H/\sigma \approx 0.2$. The dimensions of the largest dune below which slip face and horns are absent define the minimal dune size.

The shear velocity u_* is the only of the studied field variables which explicitly enters expression (1.33) for the saturation length of the flux, $\ell_{\rm s}$. We expect the dimensions of the smallest dune obtained in calculations to decrease with the shear velocity, since the saturation length also decreases with u_*. We calculate the minimal width $W_{\rm min}$ and length $L_{\rm min}$ of the barchans for different values of u_* between $u_{*{\rm t}}$ and $2.3u_{*{\rm t}}$. We notice that a value of $2.3\,u_{*{\rm t}} \approx 0.5$ m/s is associated with a wind velocity of 8.6 m/s or 31 km/h at a height of 1 m, using a roughness length $z_0 = 1$ mm. Wind velocities larger than 8.0 m/s are among the strongest measured on dune fields, and are found for instance in northeastern Brazil (Jimenez et al. 1999; Parteli et al. 2006c).

As we can see in the main plot of fig. 3.8, the minimal dune width decreases from 13.0 m to 3.0 m if u_* changes from $1.37u_{*\mathrm{t}}$ or 0.3 m/s to $2.3\,u_{*\mathrm{t}}$ or 0.5 m/s. On the basis of the result of fig. 3.8, it is interesting that the smallest barchans found in the Lençóis Maranhenses in northeastern Brazil (Parteli et al. 2006c) have widths between 5 and 10 m. Wind shear velocities reported for that region reach values between 0.35 and 0.45 m/s (1.6 and 1.9 times $u_{*\mathrm{t}}$) (Jimenez et al. 1999; Sauermann et al. 2003; Parteli et al. 2006c).

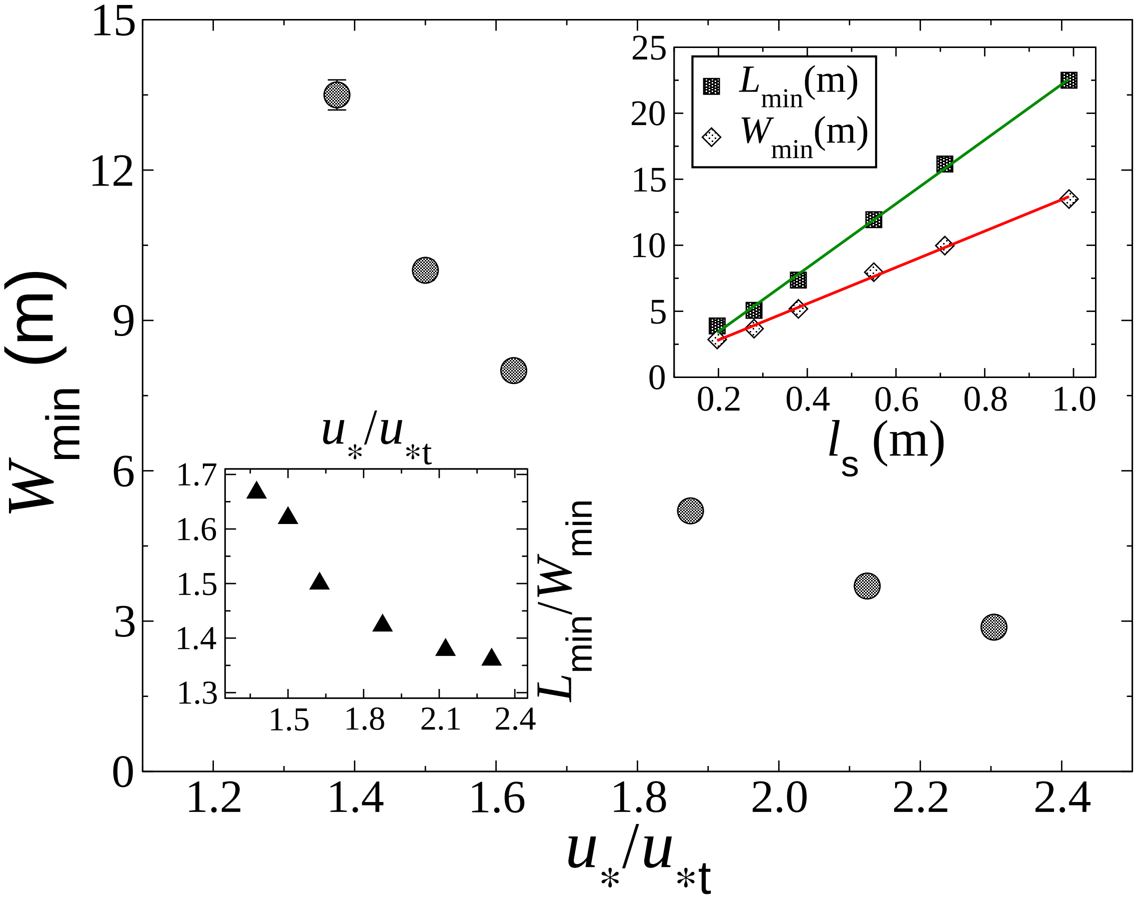

Figure 3.8: Main plot: Minimal dune width W_{min}, as a function of the relative shear velocity $u_*/u_{*\mathrm{t}}$, obtained with $q_{\mathrm{in}}/q_{\mathrm{s}} = 0.20$. The lower inset shows the "eccentricity" $L_{\mathrm{min}}/W_{\mathrm{min}}$. In the upper inset, we show L_{min} (squares) and W_{min} (diamonds) as functions of the characteristic length of flux saturation, ℓ_{s}, calculated with the corresponding values of $u_*/u_{*\mathrm{t}}$ in the main plot. The straight lines are displayed to show the linear increase of the dimensions of the minimal dune with the saturation length ℓ_{s}.

The result of the main plot of fig. 3.8 is a consequence of the expression obtained for the saturation length (eq. (1.33)), which is proportional to the mean saltation length ℓ but also decreases with the pre-factor $\gamma[(u_*/u_{*\mathrm{t}})^2 - 1]$ of the multiplication process of saltation. The denominator of eq. (1.33) gives the efficiency of the wind in carrying grains into saltation. This increases, in turn, with the relative wind strength $(\tau - \tau_{\mathrm{t}})/\tau_{\mathrm{t}}$ and with the amount of grains available from grain-bed collisions — the faster the population of saltating grains in the air increases, the faster the flux saturates. The linear increase of the minimal dune width W_{min} and length L_{min} with ℓ_{s} can be seen in the upper inset of fig.

3.8, where we see that the saturation length is the relevant length scale of barchan dunes. The width of the smallest barchan, $W_{\rm min}$, is around $12 - 14$ times $\ell_{\rm s}$, while the minimal dune length $L_{\rm min}$ is approximately $22 - 24\ \ell_{\rm s}$.

In the lower inset of fig. 3.8 we see that the "eccentricity" $L_{\rm min}/W_{\rm min}$ of the smallest dune also changes with the shear velocity. Since dunes of different sizes have different eccentricities L/W (see fig. 3.5) the quantity $L_{\rm min}/W_{\rm min}$ is particular to the minimal dune, and is useful for the characterization of a dune field.

In fig. 3.9, we show the shape of the smallest dunes obtained with different values of $u_*/u_{*{\rm t}}$ and $q_{\rm in}/q_{\rm s}$. Furthermore, fig. 3.10 shows the eccentricity $L_{\rm min}/W_{\rm min}$ of the smallest dune as a function of $q_{\rm in}/q_{\rm s}$ for different values of $u_*/u_{*{\rm t}}$. In the inset of this figure, we show the minimal dune width $W_{\rm min}$ as a function of $q_{\rm in}/q_{\rm s}$. We see that the minimal dune width increases with the sand influx, and that the eccentricity $L_{\rm min}/W_{\rm min}$ decreases almost linearly with $q_{\rm in}/q_{\rm s}$.

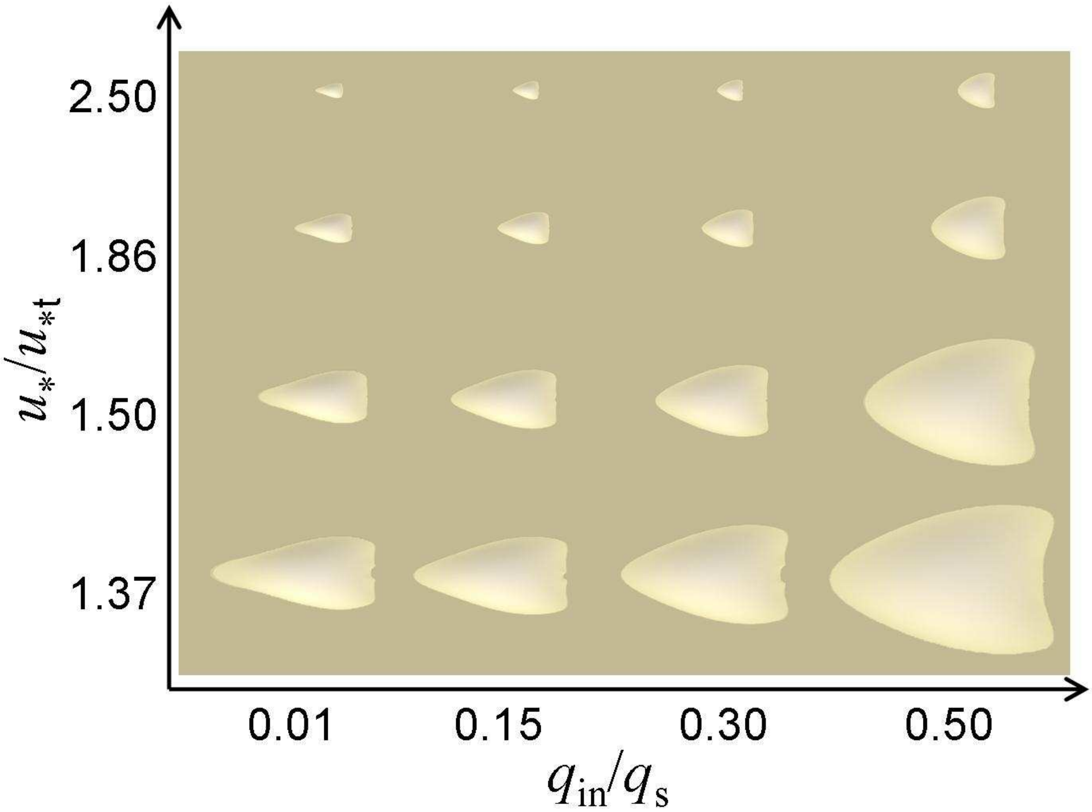

Figure 3.9: Minimal dunes calculated with different values of relative wind friction speed $u_*/u_{*{\rm t}}$ and influx $q_{\rm in}/q_{\rm s}$. The filled area has dimensions 73 × 104 m.

In summary, we conclude that the size and the shape of the smallest dune provide, respectively, a local indicative of the wind velocity and the amount of mobile inter-dune sand in a barchan field.

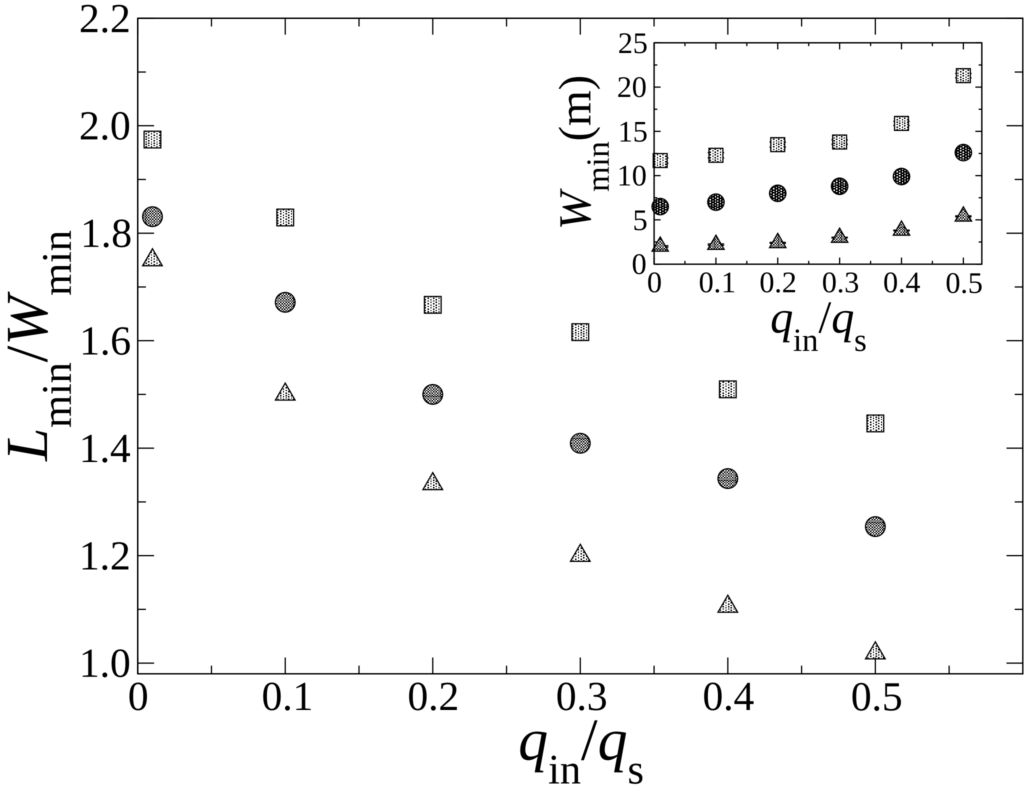

Figure 3.10: Main plot: Eccentricity $L_{\mathrm{min}}/W_{\mathrm{min}}$ of the smallest dune as a function of $q_{\mathrm{in}}/q_{\mathrm{s}}$ calculated for different values of shear velocity: $u_*/u_{*\mathrm{t}} = 1.37$ (squares), 1.64 (circles) and 2.50 (triangles). The corresponding values of minimal dune width W_{min} are shown in the inset.

3.3 Dune formation on Mars

Huge, dark barchan dunes have been observed on the floor of several craters on Mars. Similarly to Earth's barchans, they form corridors and large dune fields, as in the Arkhangelsky crater (fig. 3.3). It appears surprising that intra-crater dunes on Mars look in general similar: they have mostly an elongated shape (Bourke et al. 2004). It is also interesting to notice that Martian barchans do not have in general superimposed craters (Marchenko and Pronin 1995), which would imply they have been formed in the past where the density of the Martian atmosphere was probably larger than in the present (Melosh and Vickery 1989).

If Martian dunes have been formed by the present Martian atmosphere, winds one order of magnitude stronger than on Earth have been responsible for their appearance (Greeley et al. 1980). Such winds, in fact, occasionally occur on Mars (Moore 1985; Greeley et al. 1993; Sullivan et al. 2005). In the present work, we assume that Martian dunes have been formed by the present atmospheric conditions of Mars. On the basis of the results presented above, our aim is to find, from comparison with calculations, the conditions of wind and sand which have given the dunes the shape observed in the MOC images.

3.3.1 The shape of the barchan dunes in the Arkhangelsky Crater on Mars

The barchan dunes in the Arkhangelsky crater ($41.0°$S, $25.0°$W) are among the largest barchans on Mars, and have been imaged by the MOC camera with a resolution of 4.5 m. Furthermore, there are very good reasons to begin our study with the Arkhangelsky dunes: they have a wide spectrum of dune sizes, and they are the only field of large dunes imaged by the MOC camera in which barchans appear well separated from each other, have not been significantly altered by secondary winds, and do not appear joined at their horns forming chains of barchanoids. For example, such features are observed in the giant dunes at Kaiser crater and Proctor crater (Fenton et al. 2003).

From comparison with the shape of the Arkhangelsky dunes, in particular of the minimal dune as discussed in the last section, we can estimate the pair $\{u_*/u_{*\mathrm{t}}, q_{\mathrm{in}}/q_{\mathrm{s}}\}$ in the Arkhangelsky crater. Many of the model parameters we need to calculate dunes on Mars are known, as discussed in Chapter 2. The atmospheric pressure P and temperature T near the Arkhangelsky crater are, respectively, 5.5 mbar and 210 K (MGSRS 2006). These values yield a local Martian atmospheric density $\rho_{\mathrm{fluid}} = 0.014$ kg/m^3, and a fluid viscosity $\eta \approx 1.06$ kg/m·s. Using the mean grain diameter $d = 500$ μm, grain density $\rho_{\mathrm{grain}} = 3200$ kg/m^3, and gravity 3.71 m/s^2, it follows that the threshold wind friction speed for saltation in the Arkhangelsky crater is $u_{*\mathrm{t}} = 2.12$ m/s. Further, the values of most of the saltation model parameters are determined using the equations presented in section 1.3.

However, there is still one missing quantity for Mars: the model parameter γ, which we need to calculate the saturation length ℓ_{s} (eq. (1.33)). As we explained in chapter 2, γ must be obtained from comparison with measurements of saturation transients (Sauermann et al. 2001), which are not available for Mars. Moreover, γ is defined as $\gamma = r\tilde{\gamma}$, where r on Mars is nearly the same as on Earth (eq. (2.6)), but we do not know the entrainment rate of grains into saltation, $\tilde{\gamma}$, on Mars.

In this manner, we have in fact three unknown quantities: $u_*/u_{*\mathrm{t}}$, $q_{\mathrm{in}}/q_{\mathrm{s}}$ and γ. We thus proceed in the following manner: first, we fix one parameter: the average inter-dune flux in the Arkhangelsky crater, $q_{\mathrm{in}}/q_{\mathrm{s}} = 0.20$. This value is representative for fields of terrestrial barchan dunes propagating on bedrock (Fryberger et al. 1984), and on the basis of fig. 3.9, we expect that a significant error appears only if $q_{\mathrm{in}}/q_{\mathrm{s}}$ is much larger than 20%, which is a condition rarely met in fields of barchans (Fryberger et al. 1984). Next, we select one dune in the Arkhangelsky crater, which has width $W = 650$ m, and whose shape we try to reproduce first with the correct choice of γ and u_* (Parteli et al. 2005).

If we take the same $\gamma = 0.2$ as on Earth, we obtain a surprising result: the Gaussian hill does not evolve into a barchan dune, unless we take values of u_* far above the realistic values — these are between 2.0 and 4.0 m/s (Moore 1985; Sullivan et al. 2005). However, if we take values of γ approximately ten times larger, then barchans are obtained, as shown in fig. 3.11. We see that the elongated shape characteristic of the Arkhangelsky dunes is obtained with values of $u_*/u_{*\mathrm{t}}$ smaller than 1.5, which means u_* around 3.0 m/s. For a constant value of $\gamma = 2.0$, the dune shape deviates from the Arkhangelsky barchans for increasing values of u_*. Thus, the shear velocity in the Arkhangelsky Crater must be close to the threshold for saltation transport. This explains the elongated shape of intra-crater barchan dunes on Mars.

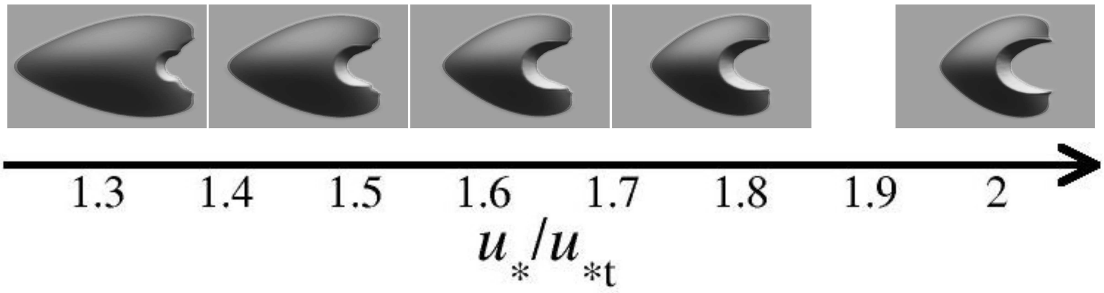

Figure 3.11: Barchan dunes of width $W = 650$ m calculated using parameters for Mars, with $\gamma = 10\,\gamma_{\mathrm{Earth}}$, and different values of wind shear velocity $u_*/u_{*\mathrm{t}}$.

3.3.2 Entrainment of saltating grains on Mars

The wind shear velocity $u_* \approx 3.0$ m/s estimated for the Arkhangelsky crater is well within predicted values of u_* on Mars. But why should the Martian γ be ten times larger than on Earth? Because $r = \gamma/\tilde{\gamma}$ on Mars is not different than the Earth's value, we must understand why the Martian entrainment rate, $\tilde{\gamma}$, differs from the one on Earth.

Once saltation initiates, the grains which enter into flow come mainly from the splash resulting from grain-bed collisions. This means that the amount of particles which are launched into the saltation sheet must be proportional to the average number of particles ejected from the splash. In this manner, the entrainment rate $\tilde{\gamma}$ is proportional to the total number of grains ejected after grain-bed collisions.

Anderson and Haff (1988) showed that the number of splashed grains is proportional to the velocity $|\vec{v}_{\mathrm{imp}}|$ of the impacting grains. Let us rescale $|\vec{v}_{\mathrm{imp}}|$ with $|\vec{v}_{\mathrm{esc}}| = \sqrt{gd}$, which is the velocity necessary to escape from the sand bed (Andreotti et al. 2002a). This velocity has value approximately 4.5 cm/s, both on Mars and on Earth. Further, $|\vec{v}_{\mathrm{imp}}|$ scales with the mean grain velocity, $|\vec{v}_{\mathrm{s}}|$. In this manner, we obtain

$$\tilde{\gamma} \propto |\vec{v}_{\mathrm{s}}|/\sqrt{gd}. \tag{3.2}$$

Typical values of the average velocity of saltating grains on Mars are shown in fig. 2.7 and in Table 2.2 as function of the relative wind friction speed $u_*/u_{*\mathrm{t}}$. We see that the grain velocity on Mars is one order of magnitude larger than on Earth: $|\vec{v}_{\mathrm{s}}|$ scales with $u_{*\mathrm{t}}$ and has only a very weak dependence on u_* which we neglect. In this manner, we can write $\tilde{\gamma} \propto u_{*\mathrm{t}}/\sqrt{gd}$. Since we know that $\gamma = 0.2$ on Earth, where $g = 9.81$ m/s^2, $d = 250\ \mu$m and $u_{*\mathrm{t}} = 0.218$ m/s, we obtain

$$\gamma = 0.045\frac{u_{*\mathrm{t}}}{\sqrt{gd}}. \tag{3.3}$$

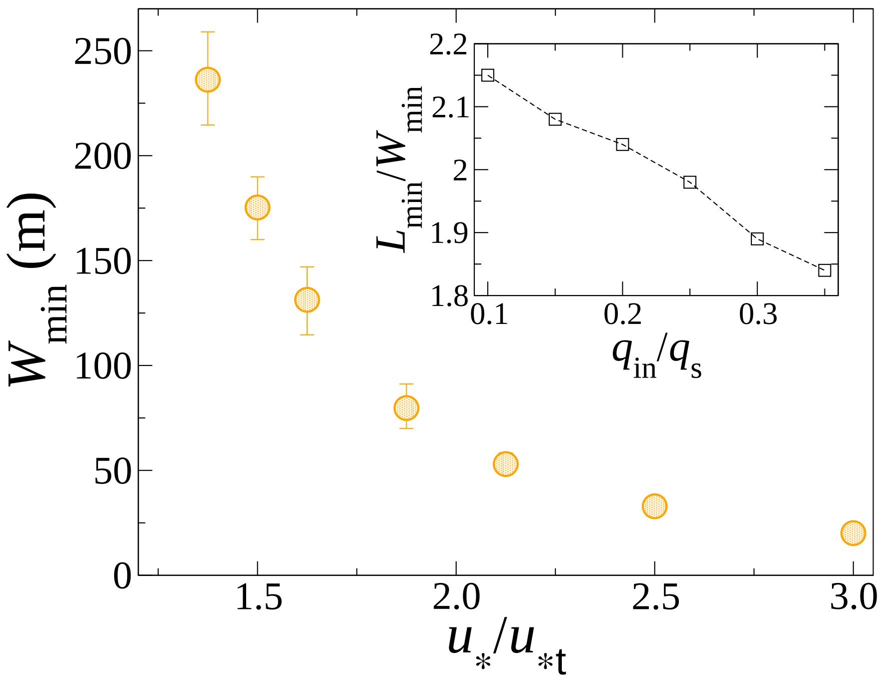

Figure 3.12: Main plot: Minimal width W_{min} of barchan dunes on Mars as a function of the relative shear velocity $u_*/u_{*\mathrm{t}}$. The value $W_{\mathrm{min}} \approx 200$ m is associated with a shear velocity around $1.45\,u_{*\mathrm{t}}$ or 3.07 m/s. In the inset, we show the eccentricity of the minimal dune as a function of $q_{\mathrm{in}}/q_{\mathrm{s}}$, calculated using $u_*/u_{*\mathrm{t}} \approx 1.45$. We see that the eccentricity $L_{\mathrm{min}}/W_{\mathrm{min}} \approx 2.0$ of the domes in the Arkhangelsky Crater is reproduced with an inter-dune flux of 25% of the saturated flux.

Equation (3.3) gives $\gamma \approx 2.24$ in the Arkhangelsky crater, which is in fact one order of magnitude higher than the Earth's value, as found in a different way in the last section.

Now that we have calculated γ on Mars we can use the results of Section 3.2 to obtain $u_*/u_{*\mathrm{t}}$ and $q_{\mathrm{in}}/q_{\mathrm{s}}$ in the Arkhangelsky dune field from the minimal dune size.

In fig. 3.3a we see that the smallest dune in the Arkhangelsky Crater has width $W_{\mathrm{min}} = 200$ m and length $L_{\mathrm{min}} = 400$ m. On the other hand, in the main plot of fig. 3.12 we show the minimal dune width W_{min} as function of the relative shear velocity $u_*/u_{*\mathrm{t}}$ obtained with parameters for the Arkhangelsky crater. In this figure, we show an astonishing finding: the minimal size of Mars dunes decreases from 250 m for u_* close to the threshold shear velocity to nearly 20 m for $u_* \approx 6.0$ m/s or three times the threshold. This is a variation of one decade in the minimal dune size. Furthermore, we conclude that the value of $W_{\mathrm{min}} = 200$ m is obtained with u_* around $1.45\,u_{*\mathrm{t}}$ or 3.07 m/s. This is the same result obtained previously in this section from comparison with the elongated shape (fig. 3.11).

Next, we show in the inset the eccentricity $L_{\mathrm{min}}/W_{\mathrm{min}}$ of the minimal "Arkhangelsky" dune as function of $q_{\mathrm{in}}/q_{\mathrm{s}}$. We see that the ratio $L_{\mathrm{min}}/W_{\mathrm{min}} \approx 2.0$ is obtained if the average inter-dune flux q_{in} is approximately 25% of the saturated flux q_{s}.

Figure 3.13 shows the results obtained using $u_* = 1.45\,u_{*\mathrm{t}}$ and $q_{\mathrm{in}}/q_{\mathrm{s}} = 0.25$. In this figure, we show four Arkhangelsky dunes of different sizes next to dunes calculated with the model. Further, the plot in fig. 3.13 shows the length L as function of width W of the Arkhangelsky dunes (circles) and of the dunes obtained in calculations (full line). We see that the values of $u_*/u_{*\mathrm{t}}$ and $q_{\mathrm{in}}/q_{\mathrm{s}}$ obtained for the Arkhangelsky crater on Mars not only reproduce the minimal dune but also describe well the dependence of the shape on the dune size.

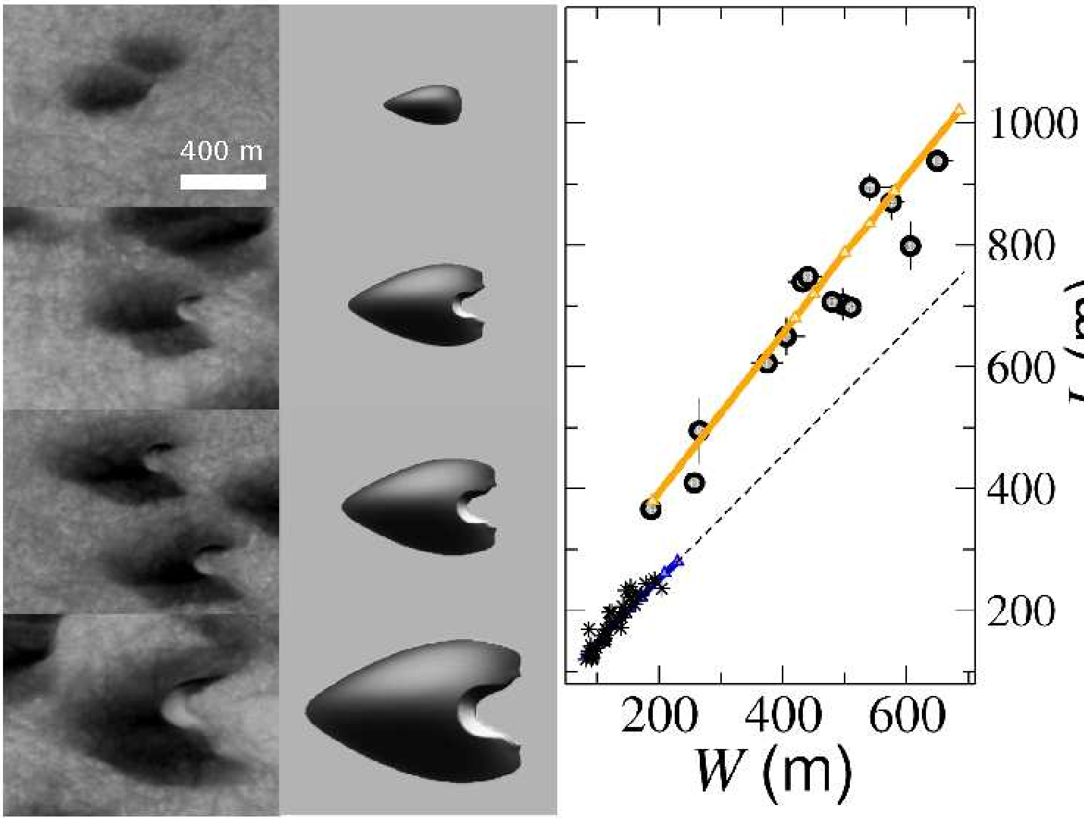

Figure 3.13: Barchan dunes in the Arkhangelsky Crater on Mars (fig. 3.3a). We see MOC images on the left and calculated dunes on the right. The plot shows L vs W of the Arkhangelsky barchans (circles) and north polar barchans (fig. 3.16) at $77.6°$N, $103.6°$W (stars). The continuous (dashed) line corresponds to dunes calculated with $P = 5.5$ mbar, $T = 210$ K, $q_{\mathrm{in}}/q_{\mathrm{s}} = 0.25$ and $u_* = 3.07$ m/s ($P = 8.0$ mbar, $T = 190$ K, $q_{\mathrm{in}}/q_{\mathrm{s}} = 0.29$ and $u_* = 2.92$ m/s).

What is the consequence of a ten times larger entrainment rate on Mars? The higher rate at which grains enter saltation on Mars amplifies the "feedback effect" and reduces the distance of flux saturation. As the quantity $\gamma = \tilde{\gamma} r$ enters the definition of the saturation length ℓ_{s} (eq. (1.33)), it plays an essential role for the scale of dunes, in addition to the mean saltation length ℓ or the quantity ℓ_{drag}.

The distance of flux saturation, λ_{s}, scales with the saturation length ℓ_{s}, and also depends on the sand influx q_{in} (fig. 3.14). For the value of $q_{\mathrm{in}}/q_{\mathrm{s}} = 0.25$ found for the Arkhangelsky crater, λ_{s} is around six times the characteristic length ℓ_{s} (fig. 3.15), which, on one hand, effectively increases with ℓ. However, here we found that $\lambda_{\mathrm{s}} \propto \ell_{\mathrm{s}} \propto \ell/\gamma$ on Mars is, on the other hand, reduced by the larger Martian splash.

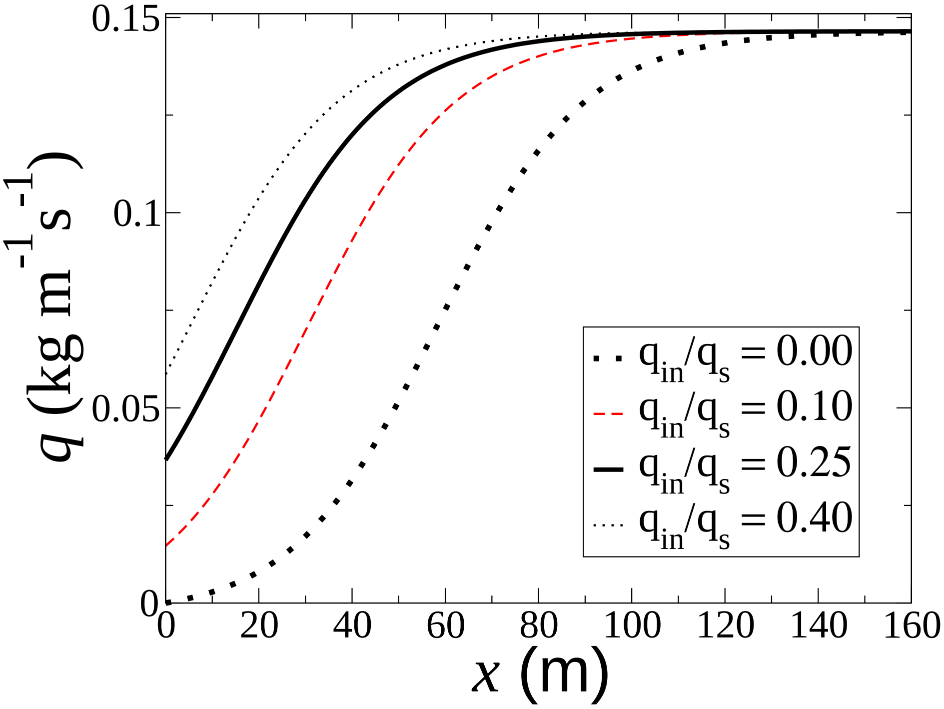

Figure 3.14: Flux q as function of downwind distance x calculated over an "Arkhangelsky" flat sand bed using different values of $q_{\rm in}/q_{\rm s}$.

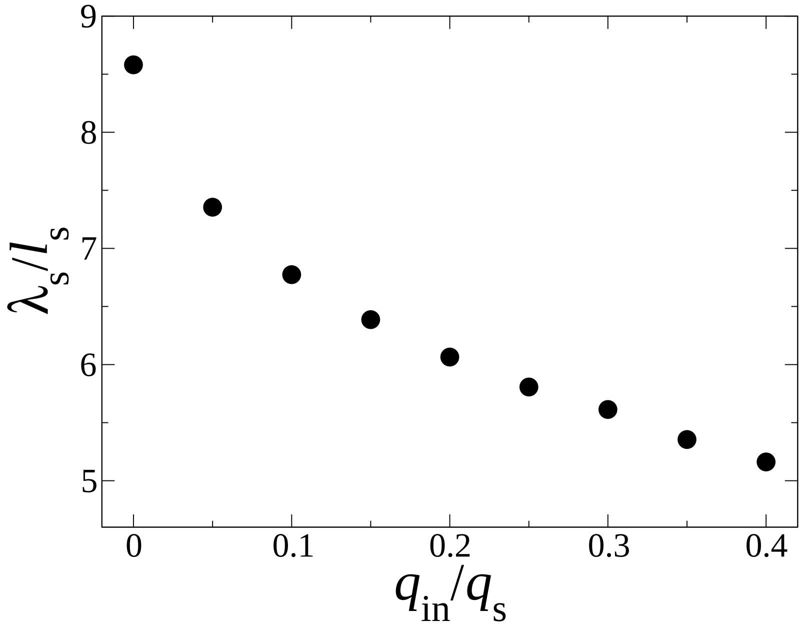

Figure 3.15: Distance of flux saturation $\lambda_{\rm s}$ normalized by $\ell_{\rm s}$, as function of the influx $q_{\rm in}/q_{\rm s}$. Here $\lambda_{\rm s}$ is the distance after which the flux has 99% of its maximum value $q_{\rm s} = 0.1465$ kg m^{-1} s^{-1}, and $\ell_{\rm s} = 15.5$ m as in the Arkhangelsky Crater.

The results presented in this Section explain why the Arkhangelsky dune simulated with the terrestrial γ did not evolve into a barchan dune (Section 3.3.1). If we take the same $\gamma = 0.2$ as on Earth, the saturation length obtained for the Arkhangelsky crater, using $u_* = 3.0$ m/s, is around 170 m, which gives λ_{s} around 1.0 km, and $W_{\mathrm{min}} \approx 13\ell_{\mathrm{s}} \approx 2.2$ km. The Arkhangelsky dune we wanted to simulate had width 650 m, which is smaller than the minimal width. However, with the value of $\gamma = 2.24$ obtained with eq. (3.3), the saturation length in the Arkhangelsky crater is 15.5 m, which gives $\lambda_{\mathrm{s}} \approx 90$ m and yields the correct value of $W_{\mathrm{min}} \approx 200$ m.

In this manner, substituting eq. (3.3) into eq. (1.33), we have obtained a closed set of sand transport equations from which the value of wind friction speed $u_*/u_{*\mathrm{t}}$ and interdune flux $q_{\mathrm{in}}/q_{\mathrm{s}}$ in a given dune field on Mars can be determined from comparison with the shape and the size of the minimal dune, on the basis of the results presented in section 3.2.

We tested the scaling relation (3.3) with a second Martian barchan field which is near the north pole (fig. 3*a*), and where $W_{\mathrm{min}} \approx 80$ m and $L_{\mathrm{min}} \approx 130$ m. At the location of the field, $P = 8.0$ mbar and $T = 190$ K (MGSRS 2006), and thus $u_{*\mathrm{t}} \approx 1.62$ m/s. From W_{min} and L_{min}, we obtain $u_*/u_{*\mathrm{t}} \approx 1.8$ or $u_* = 2.92$ m/s and $q_{\mathrm{in}}/q_{\mathrm{s}} \approx 0.30$. In fig. 3.16, we see that the behaviour L against W of the barchans in this field (stars) is well captured by the model (full line).

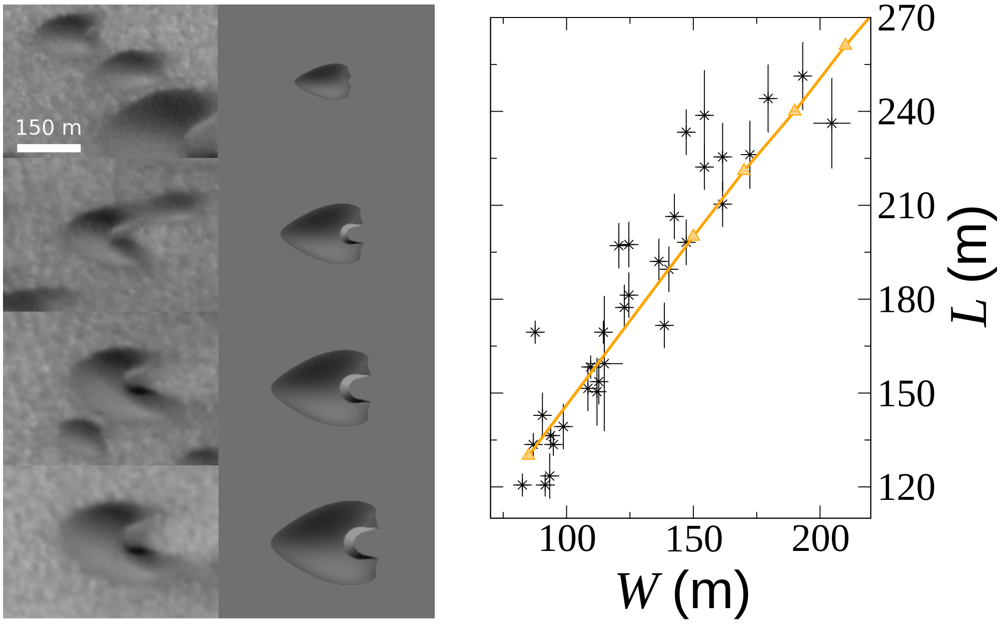

Figure 3.16: Calculations of martian north polar barchans, near $77.6°$N, $103.6°$W (fig. 3*a*). We see MOC images of dunes of different sizes on the left, and on the right we see dunes calculated using $P = 8.0$ mbar, $T = 190$ K, $u_* = 2.92$ m/s and $q_{\mathrm{in}}/q_{\mathrm{s}} = 0.29$. The plot shows L vs W for the real dunes (stars) and for the calculated ones (full line).

It is interesting that the u_* obtained for the north polar field is very similar to that in the Arkhangelsky Crater, although $u_{*\mathrm{t}}$ is lower in the north polar field due to the higher

$\rho_{\rm fluid}$. Moreover, the values of $u_*/u_{*\rm t}$ obtained for Mars are within the range of the ones measured in terrestrial barchan fields (Fryberger and Dean 1979; Embabi and Ashour 1993; Sauermann et al. 2003). Indeed, we see in fig. 3.17 that, if such winds do exist on Mars today with the same frequency as they do on Earth, Mars barchans would move ten times faster than those on Earth.

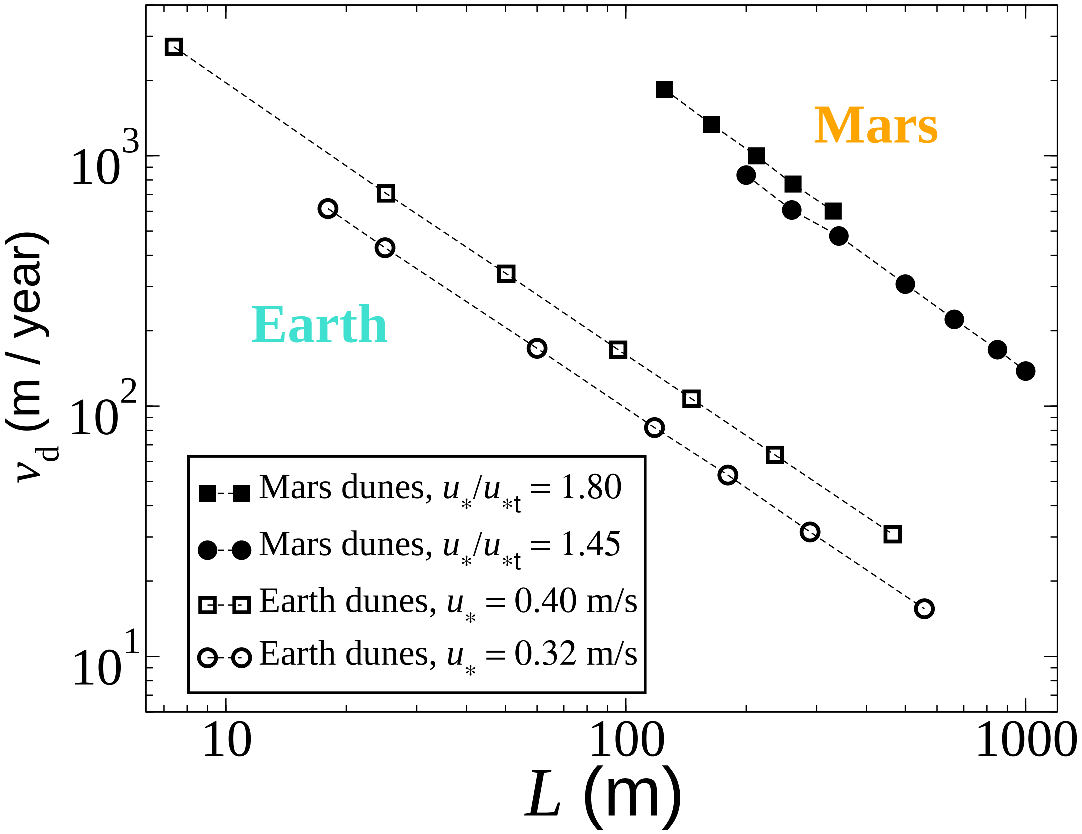

Figure 3.17: Dune velocity, $v_{\rm d}$, as function of the dune length L. We see that Mars dunes (filled symbols) move typically ten times faster than Earth dunes (empty symbols) of same L, obtained with similar values of $u_*/u_{*\rm t}$ as on Mars — $u_{*\rm t} = 1.45$ (circles) and 1.8 (squares).

Rounded barchans

In the north polar region of Mars, there occur particular dune shapes that deviate from the elongated intra-crater barchans. One example of a field with rounded north polar barchans is shown in fig. 3.3d. The dunes of this field have a mysterious shape that remembers the "*fortune cookies*". We have applied the minimal dune size method to obtain the wind shear velocity in this field. From the data of MGSRS (2006) we have $P = 8.5$ mbar and $T = 170$ K at the field, which is near 71.7°N, 51.3°W. From $W_{\rm min} \approx 75$ m and $L_{\rm min} \approx 100$ m, we find $u_*/u_{*\rm t} \approx 2.09$ or $u_* = 3.06$ m/s, while $q_{\rm in}/q_{\rm s} \approx 0.49$. In fig. 3.18, we show the results of the calculations using these values of $u_*/u_{*\rm t}$ and $q_{\rm in}/q_{\rm s}$.

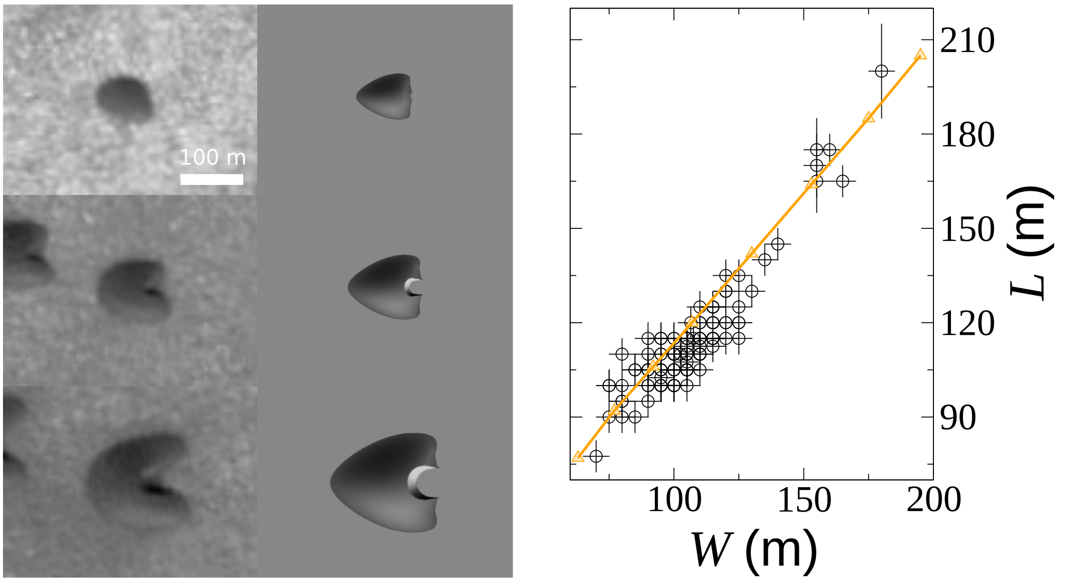

Figure 3.18: Martian north polar "*fortune cookies*" barchans near 71.7°N, 51.3°W (fig. 3.3d). MOC images of the dunes are shown on the left, while dunes on the right have been calculated using $P = 8.5$ mbar, $T = 170$ K, $u_* = 3.06$ m/s, and $q_{\mathrm{in}}/q_{\mathrm{s}} = 0.49$.

Again, the value of u_* obtained is essentially the same we found for the dunes in figs. 3.13 and 3.16, although values of u_{*t} vary significantly over the different fields (Table 3.1). In the plot of fig. 3.18, we see that the value $u_* = 3.06$ m/s reproduces the relation L vs W of the "fortune cookies" dunes. However, we see that the calculated barchans do not present the rounded windward foot of the dunes in the images. Moreover, the horns of the calculated dunes are different. The dunes obtained in calculations do not remember "fortune cookies".

The rounded shape of the "*fortune cookies*" barchans is consequence of a complex wind regime. Dunes as those in figs. 3.3b−d cannot be obtained from calculations with unidirectional wind. This is intriguing, because even though calculated dunes with similar relations L vs W can be obtained, the dunes look different from the rounded barchans observed in the images. The shape of rounded barchan dunes will be explained in Chapter 6.

Barchan field	ρ_{fluid} (kg/m^3)	u_{*t} (m/s)	v_{g} (m/s)	γ
Arkhangelsky	0.014	2.12	17.8	2.24
77.6°N, 103.6°W	0.022	1.62	12.3	1.71
71.7°N, 51.3°W	0.026	1.47	10.5	1.55
Earth	1.225	0.22	1.5	0.20

Table 3.1: Main quantities controlling saltation on Mars and on Earth.

3.4 Conclusion

Summarizing, we found from calculations of Martian barchans, using the present atmospheric conditions of Mars, that the rate at which grains enter saltation on Mars is one order of magnitude higher than on Earth. The higher entrainment rate is consequence of the larger splash on Mars: Martian saltating grains travel with a velocity 10 times higher than Earth's grains (chapter 2) and produce much larger splash events (Marshall et al. 1998) leading to higher γ values (Table 3.1).

We also found that winds on Mars do not exceed 3.0 ± 0.1 m/s, which is well within the range of estimated wind speeds that must occur during major dust storms on Mars (Moore 1985; Sullivan et al. 2005). Our results explain the elongated shape of intra-crater barchan dunes, predict the correct value of minimal dune size, and reproduce the dependence of the barchan shape with the size.

In this manner, our results show that the larger splash events have a crucial implication for the formation of dunes on Mars. While on one hand the lower Martian g and ρ_{fluid} result in longer grain trajectories (White 1979), the higher rate at which grains enter saltation on Mars shortens the saturation transient of the flux, which determines the minimal dune size. This explains the previously reported (Kroy et al. 2005) failure of the scaling $W_{\mathrm{min}} \propto \ell$ for Mars.

Finally, fig. 3.17 shows that barchan dunes on Mars move ten times faster than on Earth, which is not observed in reality. This is because winds on Mars are only seldom above the threshold for saltation, as explained in chapter 2. In that chapter, we have seen that saltation transport on Mars occurs probably during a few seconds in time intervals of several years. If, for example, winds on Mars achieve $u_* \approx 3.0$ m/s during 40 s every 5 years (Arvidson et al. 1983), then, from fig. 3.17, we see that a Martian barchan of length 200 m would need 5 years $\times 10^{-3} \cdot (3600 \cdot 24 \cdot 365)/40 \approx 4,000$ years to move 1.0 m. It is therefore probable that spacecrafts orbiting Mars will never reveal any movement of Martian barchan dunes.

Chapter 4

Transverse dunes and transverse dune fields

The type of dune studied in the present Chapter appears under the same wind regime of barchan dunes, i.e. under unidirectional wind. The difference is the amount of sand on the ground.

In fact, we can classify dunes appearing from unimodal wind regimes in the following manner. *Barchan dunes* appear for lowest sand amount. As the amount of barchans on the bedrock increases, these may join at their horns forming chains of *barchanoids*, which present a characteristic sinuosity (fig. 4.1). As the sand availability increases, barchanoids may give rise to *transverse dunes*, which align perpendicularly to the wind direction. Therefore, barchanoids have been also called “sinuous transverse dunes” (Hesp et al. 1989a).

Figure 4.1: Barchans join at their horns to form barchanoids in the Lençóis Maranhenses, northeastern Brazil. If there were sand covering the ground, closely spaced transverse dunes would appear as the ones we will study in this Chapter. Image credit: Morais Brito.

However, there can also occur another scenario, in which transverse dunes develop on a *dense sand sheet* (figs. 1a, 1.3b and 1.6b). In this case, the space between dunes is filled with sand. Such dunes are found very often on coastal areas of our planet because of the high littoral drift (Hesp et al. 1989a).

In this Chapter, we present field measurements of a transverse dune field which develops on a dense sand sheet in northeastern Brazil. We show that such *transgressive* (Hesp et al. 1989a) dunes behave differently than barchans: their shape does not depend on the dune size. Moreover, when we try to calculate transverse dunes using the dune model as recently done by Schwämmle and Herrmann (2004), we find that values of inter-dune spacing obtained in the simulations are far above the measured ones. This led us to the conclusion that the *separation bubble* at the lee of transverse dunes must be defined in a different way. In fact, the separation bubble, which has been modeled in an heuristic manner to account for the flow separation at the dune lee (Sauermann 2001; Kroy et al. 2002), is still far from being understood (Wiggs 2001; Walker and Nickling 2002; Parsons et al. 2004; Herrmann et al. 2005). We show that a simple modification of the separation bubble — by just shortening the separation streamlines defined by eq. (1.37) — yields results comparable to the measurements.

4.1 Profile measurement and simulation of a transverse dune field in the Lençóis Maranhenses

Lençóis Maranhenses is the name given to the coastal sand desert in the Maranhão State, northeastern Brazil. The area of 155 thousand hectares and a coast of a length of 50 km is delimited by the coordinates $02°19'$S, $02°45'$S; and $42°44'$W; $43°29'$W (fig. 4.2), and has become National Park in 1981. However, this desert, which has huge sand dunes moving from the beach onto the continent under action of strong winds reaching 70 km$/$h, presents some particular features. While aridness is the key word to characterize a desert, the Lençóis Maranhenses have rivers, lakes and lagoons, and annual rain between 1500 mm and 2000 mm (fig. 4.3), which is an amount quite different from the mean rainfall in desert areas (in general less than 250 mm). The high humidity level yields appropriate conditions for a high diversity of vegetation forms, flora and fauna (Magalhães 2000). In spite of the Management Plan recently approved (IBAMA 2003), which aims to support scientific research in the area, very few projects have been carried out so far in the Lençóis Maranhenses (Floriani et al. 2003).

The word "Lençóis" means "sheets" in portuguese. It refers to the typical landscape of the area, namely, the barchanoidal and transverse dune forms that propagate downwind and change continuously the complex landscape of the area. It has been speculated that the process of dune formation in the Lençóis Maranhanses initiated approximately $10,000$ years ago (Floriani et al. 2003). The grains that form the dunes in the Lençóis come from the sea and are deposited on the beach in intervals of approximately 12 hours (IBAMA 2003). A recent sedimentologic study revealed that the sand of the dunes in the Lençóis is composed by quartz grains of mean diameter varying between $d = 0.12$ and 0.35 mm (IBAMA 2003), which are values around the average diameter $d = 250\mu$m previously

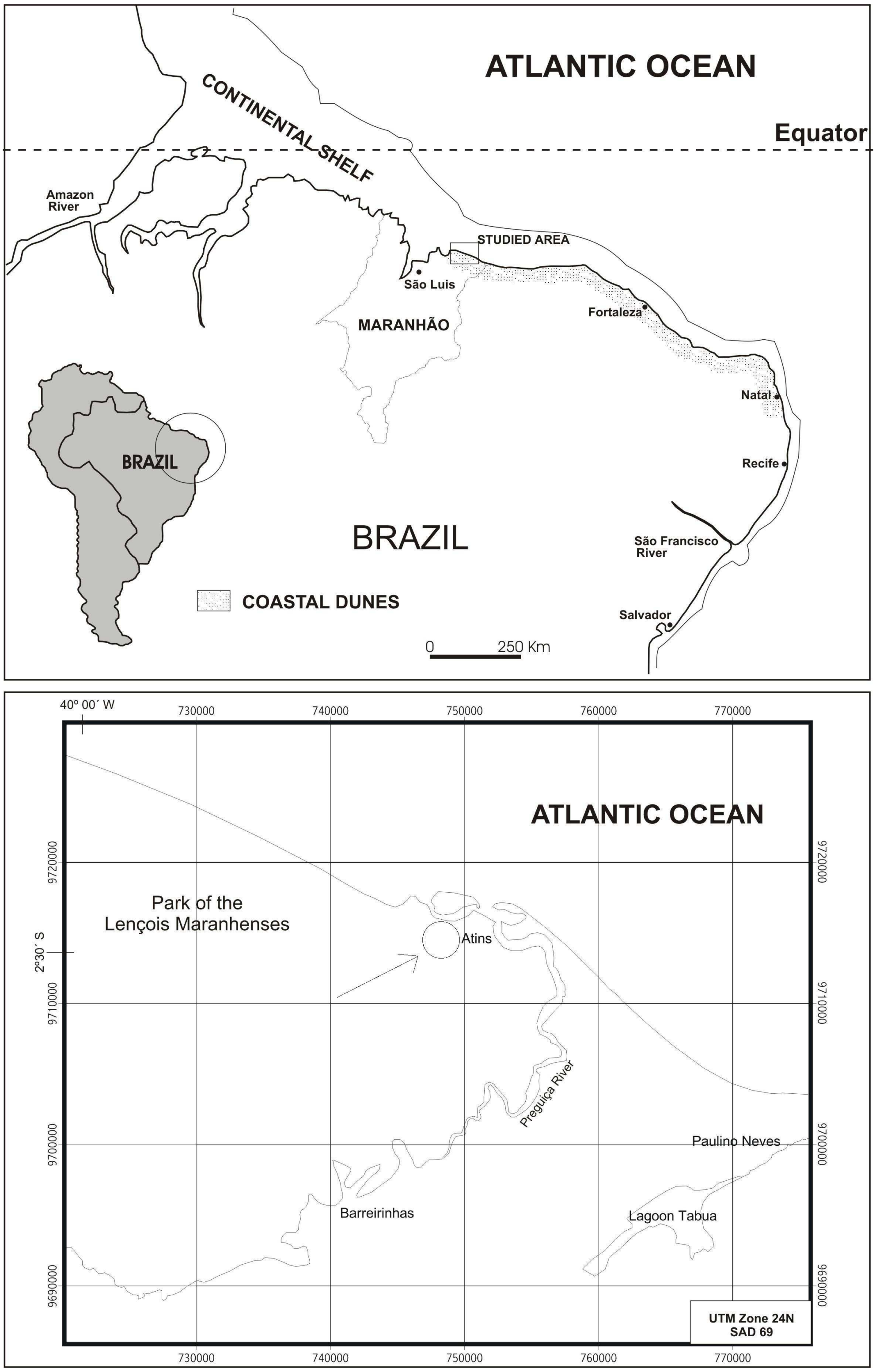

Figure 4.2: Map of the Lençóis Maranhenses region. The studied transverse dune field is located near the village of Atins, MA.

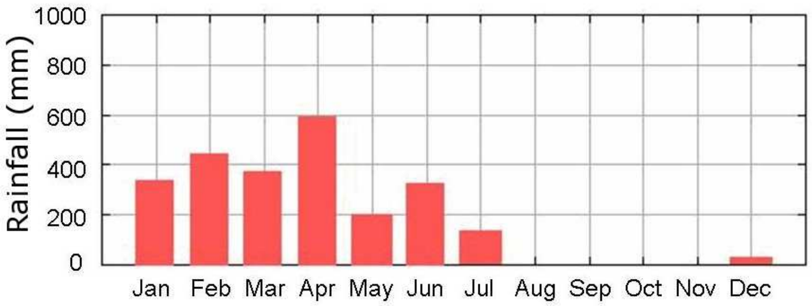

Figure 4.3: Rainfall throughout the year. Vertical axis is in mm month^{-1}.

reported for grains of sand dunes in other fields (Bagnold 1941; Lancaster 1981; Livingstone 1989; Pye and Tsoar 1990).

The wind velocity in the region of the Lençóis Maranhenses reaches an average value of 8.3 m$/$s in the dry season, and 6.1 m$/$s in the wet season. The wind rose in fig. 4.4 shows that the wind blows mainly from the East. The average temperature over the year is 28.5° and reaches a mean value of 31° during the dry season (IBAMA 2003). The region experiences a relative air humidity of 68%, which is due to the numerous lakes and lagoons present in the area (IBAMA 2003). The rainfall distribution is very concentrated, as we can see in fig. 4.3. In the first months of the year, high rainfall makes sand transport difficult, thus implying low dune mobility. A large fraction of the interdune lakes formed in this period disappear in the dry season. The landscape of the dune field appears to change continuously, indeed dune mobility implies that the lakes often reappear in different places with different contours. The lowest rainfall indices in the studied area refer to the period between August and November. The field work has been carried out from 23 to 29 of September of 2003, in the middle of the dry season.

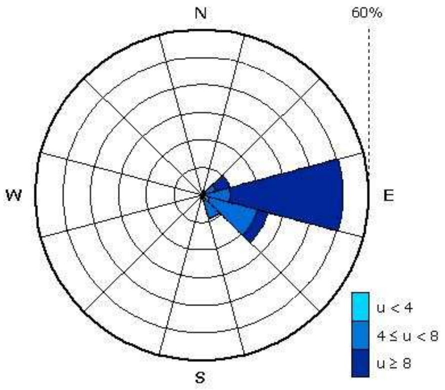

Figure 4.4: Wind rose for the region of the Lençóis Maranhenses corresponding to the period from January to December of 2003. We see that the wind blows mainly from the East. The velocity of the wind (“u”) is shown in units of m$/$s.

4.1.1 The coastal dunes of the Lençóis Maranhenses

The first systematic analysis of the geomorphology and classification of dunes of the Lençóis Maranhenses has been published in portuguese by Gonçalves et al. (2003). From interpretation of field dates analysis, aerophotograph and landsat images, these authors defined five groups of aeolian forms: free dunes; vegetated dunes; fixed dunes; dunes "esteiras" and blow out forms. In particular, Gonçalves et al. (2003) classified barchanoids and transverse dunes according to their sinuosity, inter-dune spacing and rate of movement. According to Gonçalves et al. (2003), barchanoids are "3D dunes", which are formed by barchans which join at their horns, and have large inter-dune spacing (fig. 4.1). The distance between such dunes is proportional to their sinuosity, i.e. dunes with many oscillations perpendicularly to the wind direction are well separated from each other. On the other hand, "2D dunes" are transverse dunes which have low sinuosity and short inter-dune spacing. Gonçalves et al. (2003) proposed two mechanisms to explain the origin of these dunes. First, "2D dunes" might be a result of the interaction of "3D dunes" with vegetation at their extremities, which retards dune motion. Alternatively, "2D dunes" are observed in areas of larger amount of sand.

4.1.2 Area of investigation

The dune field we measured in the Lençóis Maranhenses is located in the vicinity of Atins, a small village in the Maranhão State (MA), just 1 km from the sea (figs. 4.2 and 4.5). We measured the height profile of seven transverse dunes of the field in fig. 4.5(b). These dunes develop on a dense sand sheet and are, therefore, "2D dunes", according to the definition of Gonçalves et al. (2003).

The transverse dune field investigated is typical on high energy beaches experiencing high littoral drift, and is also called a "transgressive dune field", which develops on a dense sand sheet (Hesp et al. 1989a). The most remarkable difference between the studied dunes and the typical barchanoidal forms in the Lençóis is in fact the distance between the dunes: the transgressive dunes of fig. 4.5(b) have negligible inter-dune spacing compared to their width. These observations suggest that the higher sand availability — as mentioned by Gonçalves et al. (2003) — must be decisive for the differentiation between the two kinds of transverse dune fields. The shape of transverse dunes is strongly influenced by effects of lateral sand transport and recirculating flow at the dune lee (Frank and Kocurek 1996; Wiggs 2001; Walker and Nickling 2002).

As described below, we discovered that the small and variable inter-dune spacing characterizing such a transgressive or "2D" dune field is associated with a fluctuating value of the distances between the brink and the crest of transverse dunes.

4.1.3 Measurements

A tachymeter was used to measure the height variations at 77 different points along the surface of the dunes, which define a profile with a length of almost 720 m, as shown in

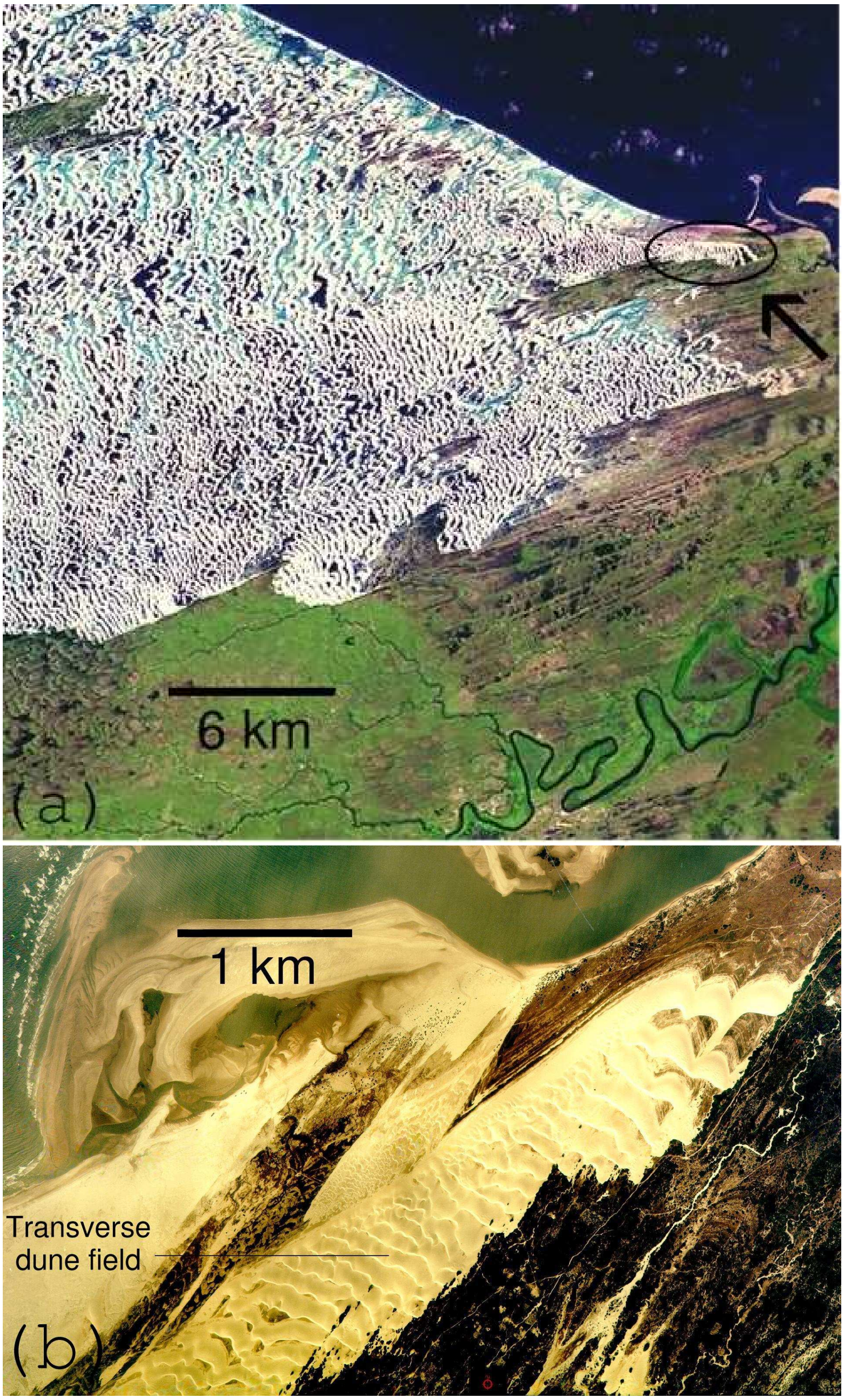

Figure 4.5: In (a) we show a Landsat image (1984) of the Lençóis Maranhenses, where the studied transverse dune field is indicated by the arrow. In (b) we show an image of the studied field, from Embrapa Monitoramento por Satélite, 1999.

fig. 4.6. To interpolate the entire profile of the transverse dune field, we used the relative distances and height differences between the measured points and a fixed angle $\theta_c = 34°$ for the slip face for each dune. The reference height $h = 0$ is set at the foot of the slip face of dune 3, whereas $x = 0$ corresponds to the brink of dune 1, for which we did not measure the whole profile. Our measurements have error estimates of 0.1 m for the height coordinate and 1 m for the horizontal axis.

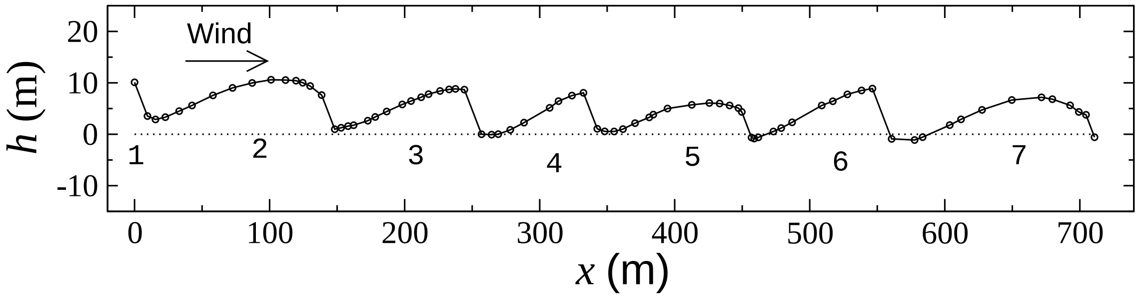

Figure 4.6: Height profile of the transverse dune field studied.

The measured transverse dunes have heights of typically $7 - 10$ m and a crest-to-crest distance, D_{cc}, of $90 - 130$ m, as shown in Table 4.1. The sixth column of this Table shows the aspect ratio r_{ws} of these dunes, which is obtained by dividing their heights at the crest, H_{crest}, by the corresponding values of the length of the windward side, L_0, and we find that $r_{ws} = 0.08 \pm 0.02$ is consistent for all dunes. The quantities listed in Table 4.1 are defined in fig. 4.7.

Dune	H_{crest}(m)	H_{brink}(m)	d_c(m)	L_0(m)	$r_{ws} = H_{crest}/L_0$	$D_{cc}(i, i+1)$(m)
1	–	6.6 ± 0.1	–	–	–	–
2	9.6 ± 0.1	6.6 ± 0.1	32 ± 1	123 ± 1	0.078 ± 0.005	132 ± 1
3	8.8 ± 0.1	8.6 ± 0.1	7 ± 1	96 ± 1	0.092 ± 0.005	94 ± 1
4	7.0 ± 0.1	7.0 ± 0.1	0 ± 1	65 ± 1	0.108 ± 0.005	95 ± 1
5	6.9 ± 0.1	4.9 ± 0.1	24 ± 1	95 ± 1	0.073 ± 0.005	119 ± 1
6	9.7 ± 0.1	9.7 ± 0.1	0 ± 1	88 ± 1	0.110 ± 0.005	124 ± 1
7	7.9 ± 0.1	4.3 ± 0.1	35 ± 1	127 ± 1	0.062 ± 0.005	–

Table 4.1: For each dune in the profile of fig. 4.6 we identify in columns 2, 3, 4, 5 and 6, respectively: The dune height at the crest, H_{crest}, the height at the brink, H_{brink}, the crest-brink distance d_c, the windward side length L_0 and the aspect ratio r_{ws}. The seventh column shows the crest-to-crest distance $D_{cc}(i, i+1)$ between the $i-$th and $(i+1)-$th dunes. H_{crest}, H_{brink}, d_c and L_0 are shown in fig. 4.7 for dune 5.

It is surprising that although the dunes have more or less the same height, the position of the brink with respect to the crest, d_c, varies strongly. This is in strong contrast with the situation of single barchans, for which it has been observed from field measurements in southern Morocco that the brink gets closer to the crest for higher barchan dunes (Sauermann et al. 2000). In addition, differences between small and large barchans have been

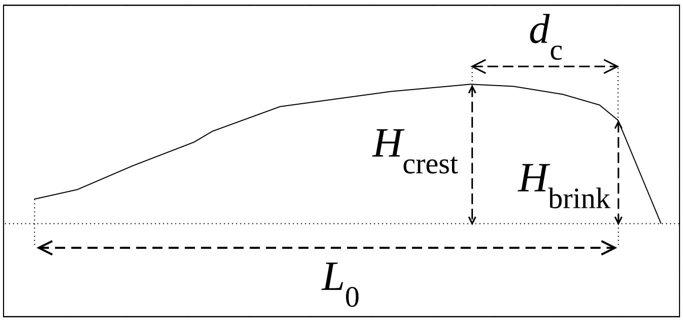

Figure 4.7: Profile of dune 5 in fig. 4.6 with definition of variables $H_{\rm crest}$, $H_{\rm brink}$, $d_{\rm c}$ and L_0 in Table 4.1. Heights (H) are measured relative to the foot of the slip face.

recently reported by Hesp and Hastings (1998). On the other hand, Long and Sharp (1964) have more generally identified two kinds of barchan dunes: the “slim” and “fat” barchans, which behave differently (Chapter 3). Bagnold (1941) regarded this phenomenon as the product of the lag in-between changes of wind conditions and the resulting changes in sand movement.

The upper inset of fig. 4.8 shows the inclination $\theta_{\rm ws}$ of the windward side (circles) together with the aspect ratio $r_{\rm ws}$ (triangles) of the measured transverse dunes. Here $\theta_{\rm ws}$ is defined through the relation $\tan\theta_{\rm ws} = H_{\rm crest}/(L_0 - d_{\rm c})$, where $d_{\rm c}$ is the horizontal distance measured from the crest to the brink of the dune. From the value $\tan\theta_{\rm ws} = 0.10 \pm 0.02$, we get $\theta_{\rm ws} \approx 6^\circ$. The main plot of fig. 4.8 shows that the difference between the heights at the crest and at the brink is essentially quadratic in $d_{\rm c}$. Moreover, fig. 4.9 shows that the transverse dunes present a nearly parabolic shape at their crest. In this figure, we lump the profiles of dunes $2-6$ together, and we can see that the windward sides of all dunes at their crests superimpose in a single parabolic curve with maximum at point “C”. The vertical (horizontal) axis of the main plot gives the profile $\tilde{H}$ (horizontal distance $\tilde{x}$) measured relative to point “C” for all dunes. The empty circles in the inset of fig. 4.9 represent the sampled profiles for all dunes close to point “C”, as indicated by the dotted lines, while the continuous line corresponds to the curve $y = -k_1 x^2$, with $k_1 = 0.0025$.

For dune 3, we performed correlated measurements of the wind velocity u and the sand flux q on two different points along its windward side. This dune has a height $H_{\rm crest} = 8.8$ m measured from the foot of its slip face up to the crest, and the length of its windward side is approximately 100 m. We placed an anemometer at a height of 1 m over the ground, and the registered wind velocity was averaged over time intervals of 10 min. An average wind velocity of $\langle u_{\rm A}\rangle = 7.5 \pm 1.2$ m/s was registered at the brink of the dune (point “A”). Then, we moved the anemometer to a point at about the middle of the windward side (point “B”), and the average wind velocity registered there was $\langle u_{\rm B}\rangle = 5.4 \pm 0.5$ m/s. A second anemometer, placed at one point outside of the dune field, at about 10 m from the transverse dunes on a sand sheet where a field of small barchans developed close to the ocean, registered an average wind velocity of $\langle u_{\rm r}\rangle = 5.3 \pm 0.7$ m/s, also at a height of 1 m. We did not measure the wind velocity at different heights over the ground, and thus we could not estimate the shear velocity u_{*0} and the aerodynamic roughness z_0 of the surface. If we take, for example, a roughness length $z_0 = 2.5\times10^{-3}$ m, we then obtain the

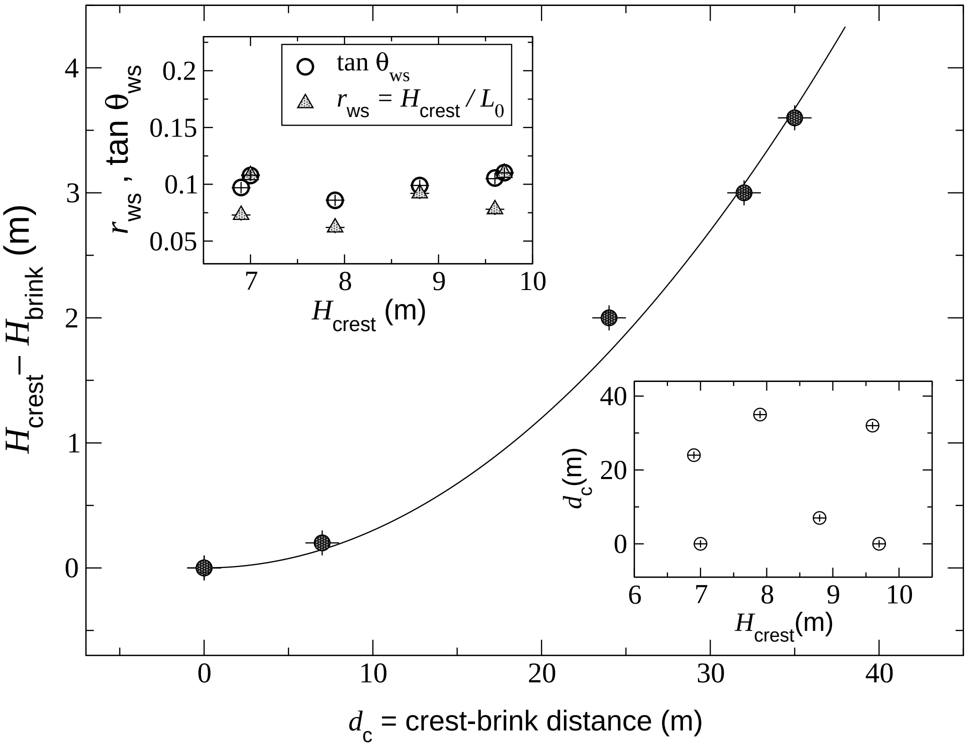

Figure 4.8: Difference between dune heights at the crest and at the brink, as a function of the distance d_c between the referred two points for the measured dunes. For dunes 4 and 6 the crest coincides with the brink, while the corresponding data for dune 1 were not recorded. The observed quadratic relation is a consequence of the parabolic shape of the dune at the crest. The upper inset shows the aspect ratio $r_\mathrm{ws} = H_\mathrm{crest}/L_0 = 0.08 \pm 0.02$ (triangles) and the average windward side inclination $\tan\theta_\mathrm{ws} = H_\mathrm{crest}/(L_0 - d_\mathrm{c}) = 0.10 \pm 0.02$ (circles), $\theta_\mathrm{ws} \approx 6°$. The lower inset shows the crest-brink distance versus the height of the crest.

undisturbed shear velocity over the plane $u_{*0} \approx 0.36$ m/s, using $u(z = 1\mathrm{m}) = 5.35$ m/s. It is interesting to note that these were essentially the same values of u_{*0} and z_0 found on the dune field of Jericoacoara, also in northeastern Brazil (Sauermann et al. 2003). Since we could not measure accurately the values of these quantities, we use in our simulations (see Section 5) estimated values of u_{*0} close to 0.4 m/s and z_0 between $0.8 - 3$ mm.

At the same positions of the dune where the anemometer was placed, as shown in fig. 4.10, we fixed 3 cylindrical traps to measure the corresponding sand flux. Each trap consists of a cylinder of 1 m height and 4.8 cm diameter, and has an open vertical slot of 1 cm width. The traps were turned with their slit facing the wind and their bottom buried in the sand (see fig. 4.10). The back of the traps has an opening of 2 cm width covered by a permeable fabric with pores smaller than the grain diameter. Initially, the traps were placed with their back showing in the wind direction. Then, they were simultaneously turned to align their openings with the wind direction and sand was collected, in a similar way as in Sauermann et al. (2003). From the mass m of the collected sand, the width w of the opening and the time T necessary to fill the traps, we calculated the sand flux $q = m/(Tw)$, for which

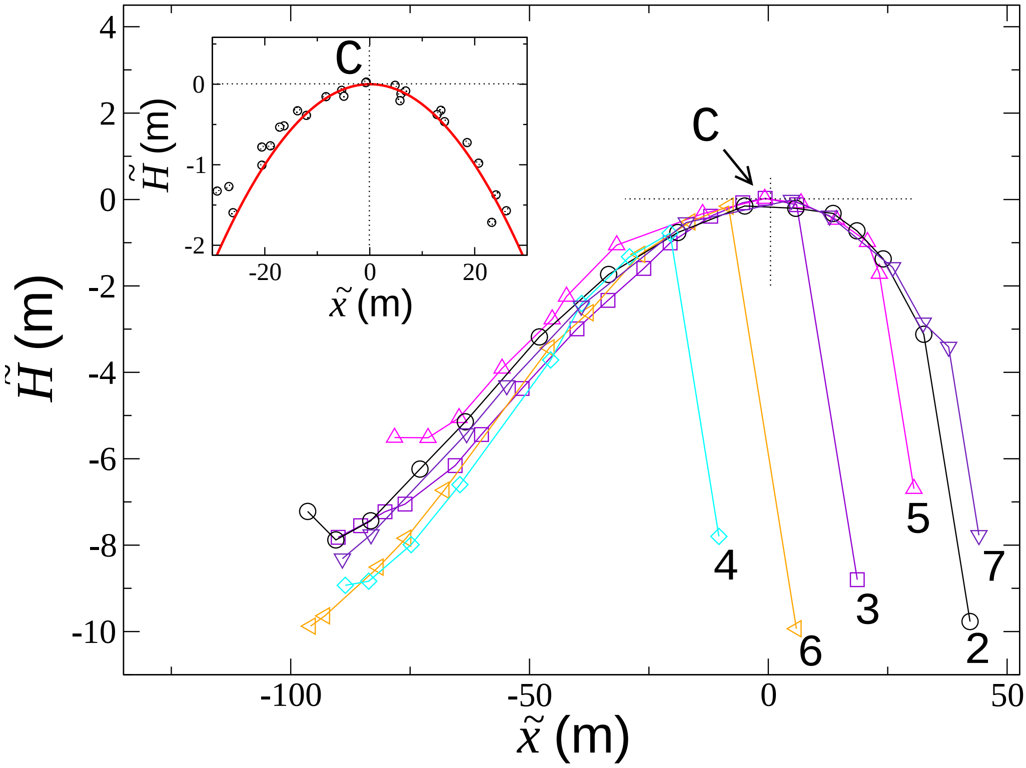

Figure 4.9: The main plot shows the height profile of dunes $2-6$, where the dunes are identified by numbers at their slip faces, and are represented by different symbols. The windward sides of these dunes are shown superposed to each other in such a way to form a parabola with maximum at "C"$(0,0)$. This behaviour is more clearly shown in the inset, where the circles represent the height profile of all dunes of the main plot, and are fitted by a parabola (continuous line). The symbol "$\sim$" over H and x indicates that these variables are measured, both in the inset and main plot, relative to point "C" for each dune. The dotted lines in the inset and main plot are guides to the eye meant to localize the maximum "C" of the parabola.

we use $m = \pi r_{\mathrm{t}}^2 h_c \times \rho_{\mathrm{grain}}$, with $r_{\mathrm{t}} = 2.4$ cm and $\rho_{\mathrm{grain}} = 2650$ kg/m^3. For each point, two traps were used which captured grains travelling up to a height $h_c \approx 17$ cm and another one at a height of 1.5 cm above the ground. The mean values $\langle q \rangle$ obtained from two runs using these traps are, for points "A" (brink) and "B" (middle of windward side) respectively, $\langle q_{\mathrm{A}} \rangle = 0.023 \pm 0.005$ kg/m·s and $\langle q_{\mathrm{B}} \rangle = 0.009 \pm 0.001$ kg/m·s, where the error estimates are defined by the maximum and minimum values registered for q at each point, as in the case of the measurements of the wind velocity. A rigorous treatment of our measurements of sand flux would require reference to a recent work on sampling efficiency of a vertical array of aeolian sand traps (Li and Ni 2003). Since we have only two measurement points for wind and flux, we report here the measured values but in this work we do not show comparison with model predictions for these data. We present typical simulations of the transverse profile and compare our results with the observed dune shape.

Figure 4.10: Measuring wind velocity and sand flux using an anemometer and the three traps at the different points of dune 3 in fig. 4.6.

4.1.4 Separation bubble for closely spaced transverse dunes

Schwämmle and Herrmann (2004) have shown that the shape of transverse dunes calculated with the dune model is nearly invariant in the y direction (perpendicular to the wind flow). Thus, we can perform simulations of transverse dunes calculating the wind and the flux in the x direction only.

In this case, we neglect the y component of the shear stress (eq. (1.6)), and eq. (1.32) for the sand flux becomes

$$\frac{\partial q}{\partial x} = \frac{1}{\ell_{\mathrm{s}}} q \left(1 - \frac{q}{q_{\mathrm{s}}}\right). \tag{4.1}$$

Furthermore, the grain velocity is given by eq. (1.41), and the time evolution of the surface is computed with the equation

$$\frac{\partial h}{\partial t} = -\frac{1}{\rho_{\mathrm{sand}}} \frac{\partial q}{\partial x}, \tag{4.2}$$

where $\rho_{\mathrm{sand}} = 0.62\,\rho_{\mathrm{grain}}$. When the slope of the dune at the lee exceeds 34°, the surface relaxes to avalanches and one separation streamline is defined for each dune.

We apply the continuum dune model to calculate transgressive dune fields in two dimensions. Since we are interested in reproducing the profile of a sequence of transverse dunes that develop within a longer field (fig. 4.5b), we use periodic boundary conditions for the x direction as in Schwämmle and Herrmann (2004). However, we observe that calculation of transverse dunes as originally carried out by Schwämmle and Herrmann (2004) yields fields with too large inter-dune spacing compared to the field in fig. 4.6. Here we propose a modification of the separation bubble model which allows for closely spaced dunes. The model of the separation streamlines is phenomenological, and is based on our observations of inter-dune distances in the measured field.

Flow separation and dune spacing

We observed in the field that the net inter-dune sand flux in the wind direction was zero from the foot of the upwind slip face up to the beginning of the windward side of the downwind dune. We found that the horizontal distance between the brink of dune i and the point at which the windward side of dune $i+1$ begins, i.e. $x_{i+1} - x_{\mathrm{brink},i}$ for the dunes in the measured field, is between 1.5 and 4 times the height of dune i at its brink, $H_{\mathrm{brink},i}$ (see inset of fig. 4.11).

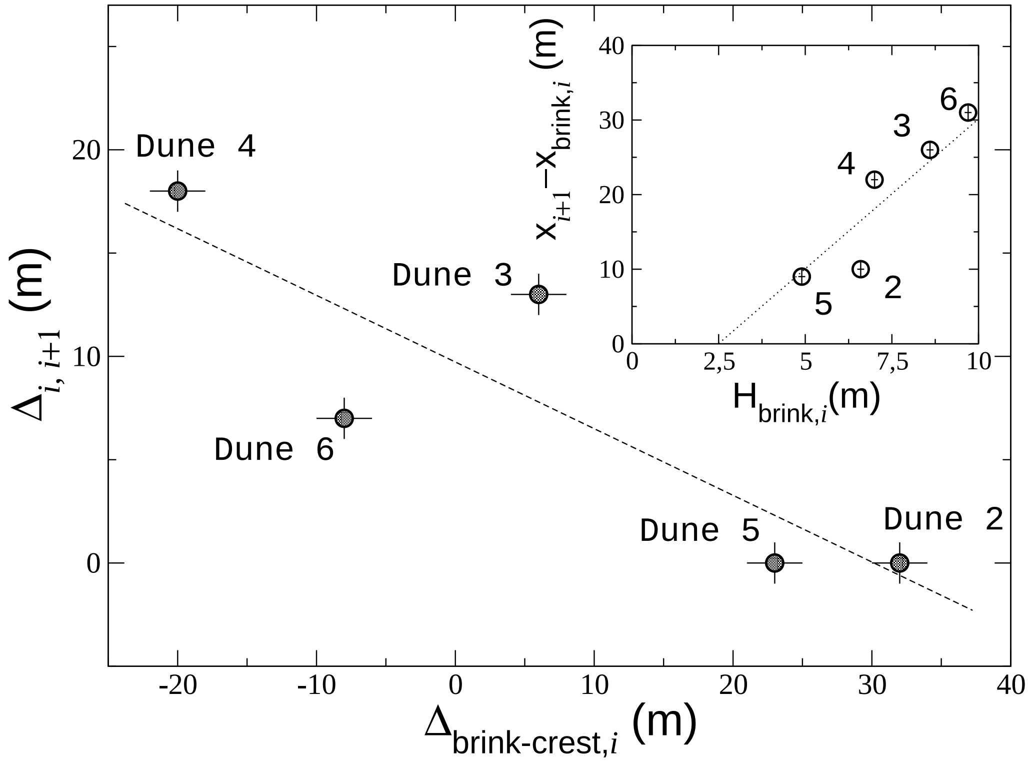

Figure 4.11: Main plot: Distance between the slip face foot of dune i and the windward side foot of dune $i + 1$ as a function of the distance measured between the brink and the maximum of the parabola according to fig. 4.9. As we can see, the length of the separation bubble appears to decrease linearly with $\Delta_{\mathrm{brink-crest},i}$. The inset shows the distance $x_{i+1} - x_{\mathrm{brink},i}$ between the foot of the windward side of dune $i + 1$ and the brink position of dune i as a function of the height of dune i at the brink, $H_{\mathrm{brink},i}$. The dotted line in the inset represents the curve $y = 4 \times (H_{\mathrm{brink},i} - 2.5)$, which is a guide to the eye meant to show that inter-dune distances are below four times the dune height at the brink.

These inter-dune distances are not achievable with the original model separation bubble. In Schwämmle and Herrmann (2004), the streamlines of the separation bubble were fitted by the third order polynomial $s(x)$ (eq. (1.37)), whose parameters were calculated from the continuity conditions of the profile $h(x)$ at the brink of the dune and at the reattachment point, as well as of dh/dx at the brink. Moreover, the third order polynomial was calculated in such a manner that the separation bubble didn't descend steeper than $14°$ (Kroy et al. 2002; Schwämmle and Herrmann 2004). This leads to large values of the horizontal distance from the brink up to the reattachment point, $x_{\mathrm{reat}} - x_{\mathrm{brink}}$ being typically between 6 and 10 times the dune height. Our aim is to modify the original separation bubble in order to capture the values of inter-dune distance in the measured transverse dune field.

As we can see in fig. 4.11, inter-dune spacing depends strongly on the position of the brink relative to the crest. Here, we plot the horizontal distances between the dunes, $\Delta_{i,i+1}$, measured from the foot of the slip face of dune i to the beginning of the windward side of dune $i+1$, as a function of the distance between the brink of dune i and the maximum of the parabola in fig. 4.9. In other words, dunes that have the position of the brink at the left (right) of the maximum of the parabola (point "C") in fig. 4.9 are associated with a proportionally larger (shorter) inter-dune spacing relative to the corresponding downwind dune.

Parsons et al. (2004) have found lengths of 3 to $15h$ for the separation zone using CFD simulations, where h is the height of the transverse dune. However, they only studied sharp crested transverse dunes, where the crest coincided with the brink. Simulations and measurements of surface shear stress over transverse dunes in a wind tunnel (Walker and Nickling 2003) have reported similar reattachment lengths for such sharp crested dunes. Moreover, McKenna Neuman et al. (2000) have noticed differences in the behaviour of the streamlines, flow expansion and deposition for sharp crested dunes in relation to the rounded ones.

In a recent work, the profile of the wind over the transverse dunes studied here has been calculated using FLUENT (Herrmann et al. 2005). It was shown in this work that there is in fact a strong dependence of the length of the separation bubble with the shape of the dune at its crest, where dunes with a large crest-brink distance, i.e. very round dunes, almost do not show recirculating flow at their lee side (fig. 4.12).

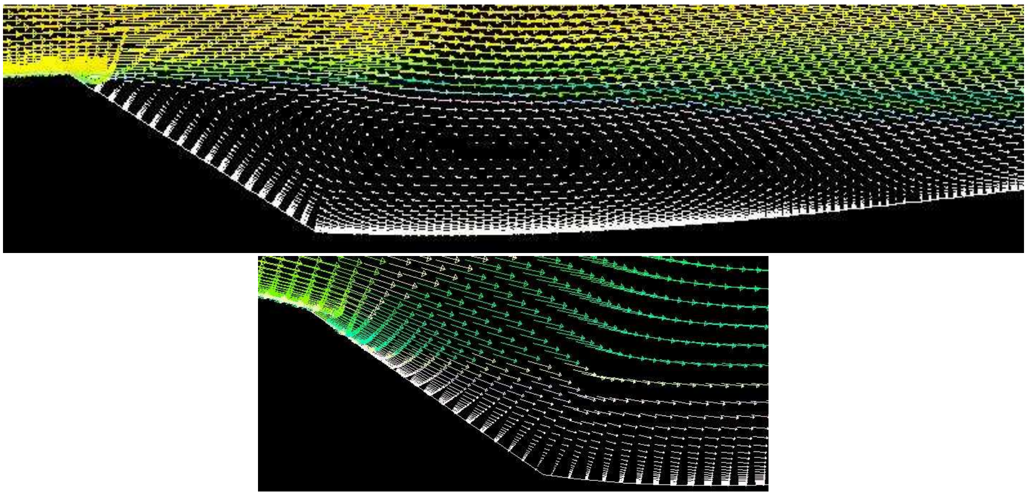

Figure 4.12: Velocity vectors at the lee side of dunes number 5 (bottom) and 6 (top), calculated by V. Schatz (Herrmann et al. 2005) with FLUENT (Fluent 1999). The recirculating flow on the foot of the slip face denotes the separation bubble. It is large for dune number 6, but nearly non-existent for dune number 5.

Phenomenological model for the separation streamlines at the dune lee

From the observations above, we conclude that the length of the separation streamlines should depend not only on the dune height at the brink, but also on the crest-brink distance.

We have observed in the field that the inter-dune spacing decreases approximately linearly with the distance $\Delta_{\text{brink}-\text{crest}}$ between the crest and the brink (fig. 4.11). If the horizontal distance between brink and crest is described by a parabola of the form $H_{\text{crest}} - H_{\text{brink}} = k_1 \Delta^2_{\text{brink}-\text{crest}}$, then in a first approximation we could define the distance from the *crest* to the reattachment point to follow also a quadratic relation $H_{\text{crest}} = k_2 (x_{\text{reat}} - x_{\text{crest}})^2$. We will use this relation to determine the point of reattachment x_{reat} of the separation bubble, $x_{\text{reat}} = \sqrt{H_{\text{crest}}/k_2} + x_{\text{crest}}$. In order to give an insight into the meaning of the parameter k_2, we notice that for a dune with height 7 m at its crest, a value of $k_2 = 0.02$ gives $x_{\text{reat}} - x_{\text{crest}} = 18$ m, while $k_2 = 0.01$ leads to $x_{\text{reat}} - x_{\text{crest}} = 26$ m.

Therefore we define a modified separation bubble as $f(x) = s(x)$ for $x_{\text{brink}} < x < x_{\text{cut}}$ and

$$f(x) = [s(x) - h(x_{\text{reat}})] \cdot \{1 - \tanh[(x - R)/\lambda_{\text{c}}]\}/2 + h(x_{\text{reat}}), \tag{4.3}$$

for $x_{\text{cut}} \leq x < x_{\text{reat}}$, where $s(x)$ is the original separation bubble, $x_{\text{cut}} = x_{\text{brink}} + \xi(x_{\text{reat}} - x_{\text{brink}})$, $R = (x_{\text{cut}} + x_{\text{reat}})/2$, λ_{c} determines the slope of the streamlines at point R, and ξ is a parameter between 0 and 1, which determines the point at which the original polynomial is multiplied by the function $\tanh$. The lengths involved in the modified separation bubble are schematically shown in fig. 4.13.

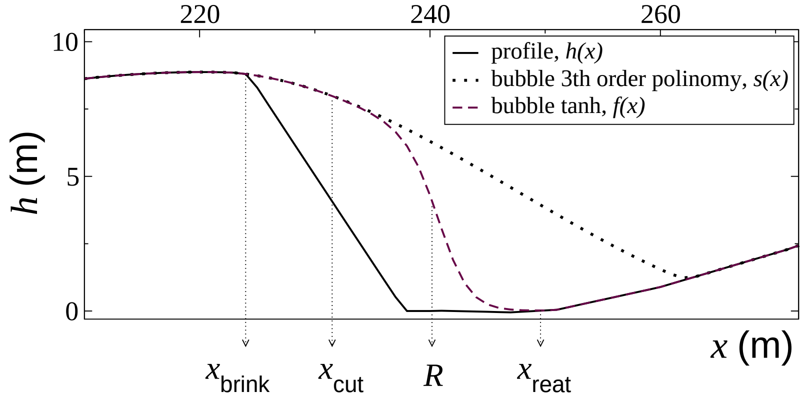

Figure 4.13: Profile $h(x)$ of measured dune 3 with the modified separation bubble $f(x)$. The 3rd order polynomial separation bubble $s(x)$ is shown for comparison.

Equation (4.3) gives a shorter separation bubble than the *original* function $s(x)$. It keeps the slope of the original separation bubble close to the brink, and presents a steeper descent to the reattachment point. We set $k_2 = 0.014$, which gives a distance of 25 m from the crest of dune 3 up to the reattachment point at its lee side, and λ_{c} and ξ are typically 0.1 and 0.9, respectively.

Calculation of closely spaced transverse dunes

Figures 4.14(a) to (f) show simulation snapshots of a typical transverse dune field of 2 km length obtained with our model. The values of the model parameters are in accordance with Sauermann et al. (2001). The wind shear velocity and its threshold value for sustained saltation are respectively 0.44 $\mathrm{m/s}$ and 0.32 $\mathrm{m/s}$, and we use a roughness length z_0 between 0.8 and 3.0 mm (Parteli et al. 2006c). For comparison, we show in fig. 4.14(g) the measured profile. The mean slope of the windward side in fig. 4.14(f) is between 0.065 and 0.09, which are values close to the windward side inclination found in the measured field ($0.08 - 0.12$). We see in fig. 4.15 that the calculated dunes have a shape essentially parabolic at their crest, as found for the measured dunes (fig. 4.9).

Furthermore, we see in fig. 4.14 that the distance between crest and brink for the simulated transverse dunes of similar heights varies strongly as in the case of the measured dunes. This striking observation appears to be a consequence of the interaction between transverse dunes in a field. Barchans behave more like isolated dunes and exchange less sand than a field of closely spaced transverse dunes. Schwämmle and Herrmann (2004) have shown that the brink position of transverse dunes is in general closer to the crest if the dune is downwind of another one. Such sharp crested dunes with “triangular” cross section are found in our simulations during the evolution of the field, as shown in fig. 4.14(c). However, they appear only when interacting with another dune like solitary waves, a feature that can be illustrated comparing figs. 4.14(c) and (d). In order to investigate dune interaction in more detail, transverse dunes have to be studied more as done recently for barchan dunes (Schwämmle and Herrmann 2003).

The typical dune shape found in our simulations is the “rounded” one, i.e. where the brink is clearly distinguishable from the crest. Tsoar (1985) has shown that the ‘rounded’ dunes are ‘*more stable*’ than the ‘triangular’ ones, since the sharp-crested shape experiences strong flux at the brink. We have found such peaks of sand flux when trying to simulate the evolution of ‘triangular’ transverse dunes with our model, and we have seen that they lose this shape after some iterations, becoming ‘round’. On the other hand, we could not find dunes with the ‘triangular’ shape in our simulations of dune fields, but those interacting like solitary waves, as mentioned above. However, we do not conclude from this that the measured sharp crested dunes found in fig. 4.6 should be interacting like solitary waves with their neighbours. We remark that our model assumes lateral invariance, from which the profile variations found for these dunes in the $y-$direction, as we see in fig. 4.5(b), are not included. Consequently, variations in the lateral shear stress are not considered, which could influence the dune shape at the brink. In spite of this limitation, the variable crest-brink distances found in the field have been captured by the model.

The separation bubble in our model is the region of zero flux downwind, which implies that the observed inter-dune distances provide an upper bound for the separation length. To use a longer bubble, our model could be improved in order to capture the complexity of the wind and flow in the bubble (Walker and Nickling 2002; Wiggs 2001; Frank and Kocurek 1996). Possibly, in this case, sharp crested dunes could be found in simulations of closely spaced transverse dunes.

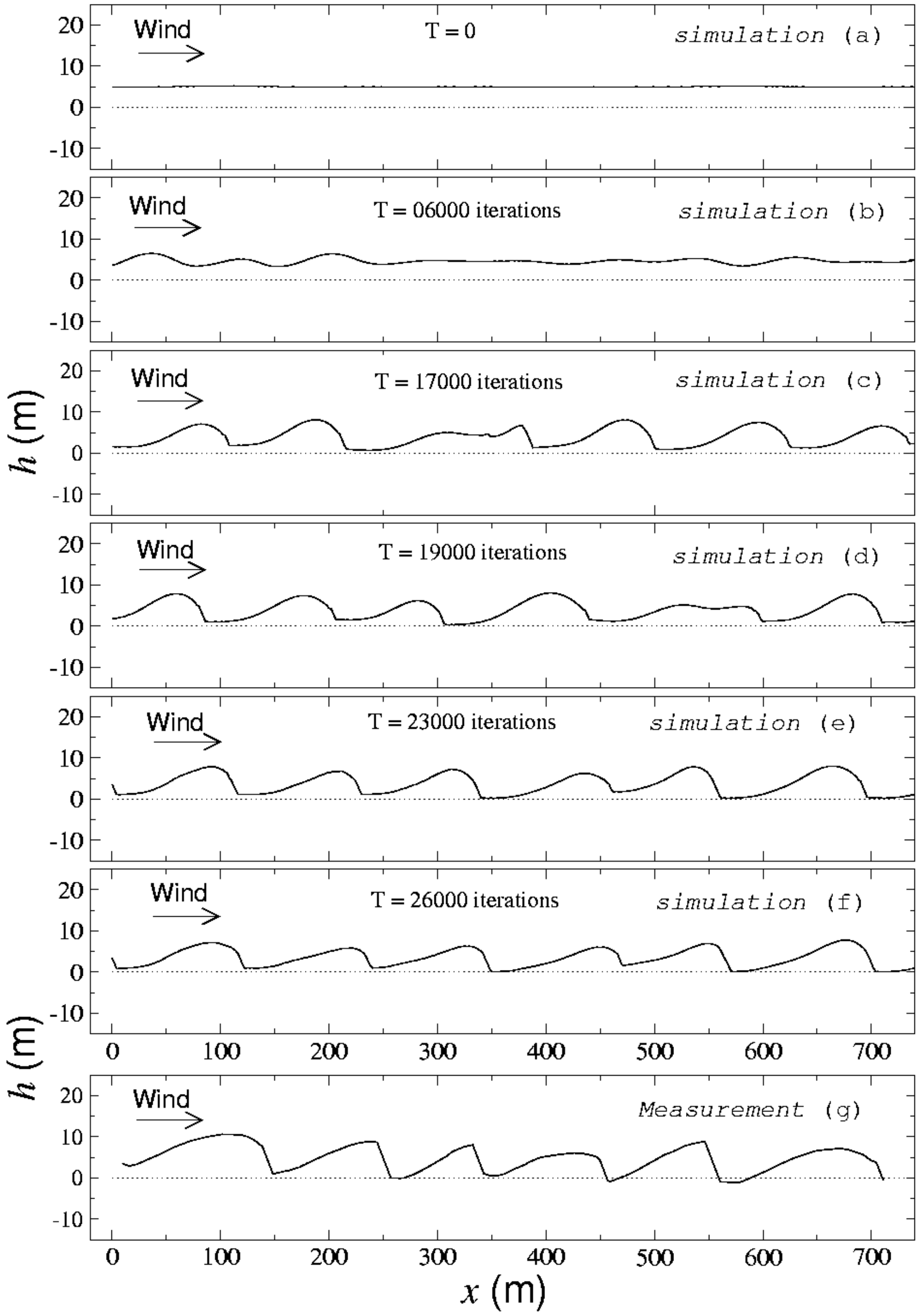

Figure 4.14: From (a) to (f) we show snapshots of the simulation of a transverse dune field obtained from our two-dimensional model. Model parameters are mentioned in the text. The shear velocity u_{*0} and its threshold u_{*t} are respectively 0.44 m/s and 0.32 m/s. For comparison, the measured profile is shown in (g).

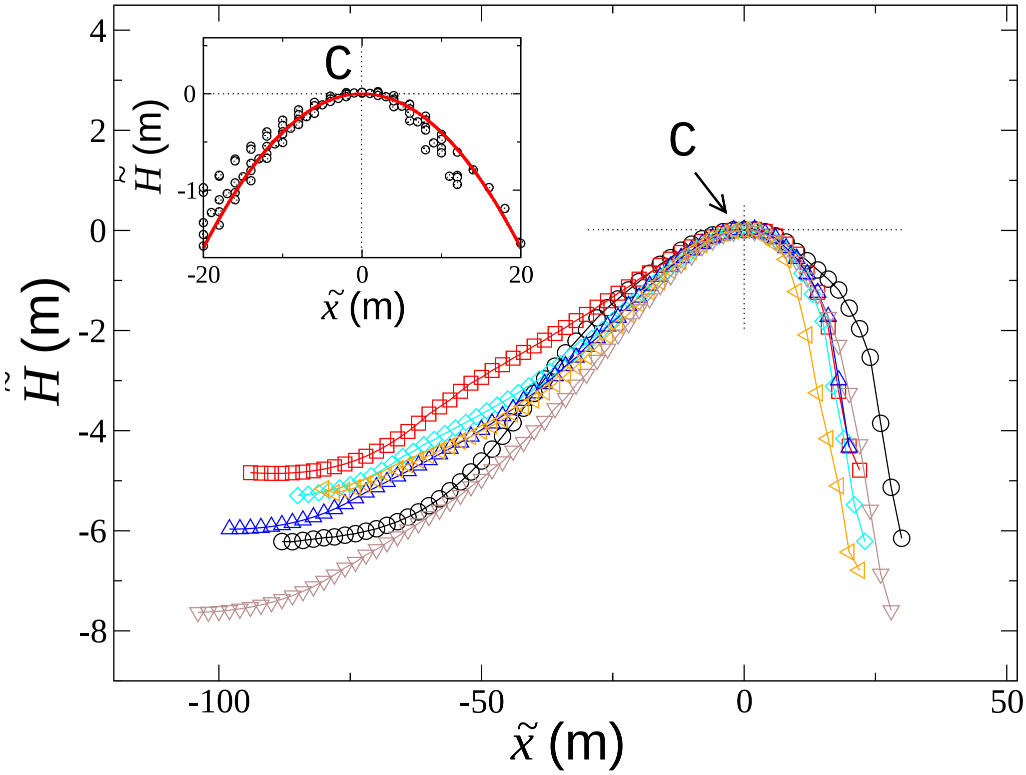

Figure 4.15: The crest of the calculated dunes may be also described by a parabola as in the case of the measured dunes (fig. 4.9). The main plot shows the profiles of all calculated dunes in fig. 4.14(g). The continuous line in the inset corresponds to the equation $y = -k_1x^2$, with $k_1 = 0.004$.

4.2 Conclusion

We presented an extensive study of the formation of transverse dune fields developing on a sand sheet (“transgressive” dune fields). We studied the shape and the inter-dune spacing of real transverse dunes, and we applied the dune model to reproduce the measured field (Parteli et al. 2006c).

In conclusion, we found that the the shape of transverse dunes is nearly independent of the dune height. Dunes with the same height have a variable position of the brink relative to the crest (figs. 4.6, 4.8 and Table 4.1), which is in contrast with the situation of barchans, the crest-brink distance of which decreases with the dune size (Sauermann et al. 2000).

Moreover, we found that real transverse dunes developing on sand sheets are closely spaced. The separation bubble $s(x)$ (eq. (1.37)) yields calculated fields with much larger inter-dune spacing than observed in real fields. Thus, we modified the separation bubble, by shortening the length of the separation streamline of each dune. The modified bubble (eq. (4.3)) is consistent with the phenomenological relation between the length of the bubble and the crest-brink distance of the dune, which we observed in the field (fig. 4.11). We then calculated transgressive dune fields using the modified bubble and obtained transverse dunes with similar values of aspect ratio and inter-dune spacing as in the real field. We also found that the position of the brink relative to the crest of the calculated dunes is independent of the dune height (fig. 4.14(f)).

However, our calculations yielded only the “rounded” shape of transverse dunes (fig. 4.14). Sharp-crested (“triangular”) dunes could not be obtained in two-dimensional calculations of closely spaced dunes. We conclude that other factors are important for the dynamics of transgressive dune fields, which have been neglected in the calculations. For example, the lateral flux may contribute to the increase of the amount of sand within the bubble and for the inter-dune sand transport. In the model, the flux in the bubble is considered as zero, which introduces too large inter-dune flats that are not observed in reality. Possibly, the modification of the two-dimensional separation bubble would not be necessary if lateral flux were considered. It would be therefore interesting to perform simulations of three-dimensional transverse dune fields in the future, in order to verify the role of the lateral flux for the inter-dune spacing. Then, the model can be also extended to calculate transgressive dunes on Mars.

The outlook of this work is to calculate the formation of coastal transverse dunes using the three-dimensional dune model (Chapter 1). It would be interesting to check whether barchans emerging from the coast may appear in the calculations and join at their horns to form barchanoids and transgressive dune fields as found in the Lençóis Maranhenses. Calculations of coastal dune fields will be presented in the next Chapter.

Chapter 5

Modelling formation of dune fields

In this Chapter, our aim is to investigate the formation and evolution of dune fields. What are the processes that nucleate the appearance of dunes? How do these evolve in time? What does determine the pattern of a coastal dune field? We introduce a simple model for transverse dune fields, to study the evolution and propagation of transverse dunes on bedrock and on a dense sand sheet. We adapt this model to study the formation of coastal dune fields, in which dunes appear from the beach. The equations of the simple model account for the phenomenological observations from our field measurements in the Lençóis Maranhanses, i.e. inter-dune spacing, the length of the separation bubble, and the aspect ratio of the dunes. Next, we investigate the formation of dunes from a coastal beach, performing calculations in three dimensions with the complex dune model.

5.1 A simple model for a transverse dune field

Summarizing the results of the last Chapter: transverse dunes that evolve on sand sheets behave differently: they do not only have a shape that is independent of their height; they also have shorter inter-dune spacing than dunes appearing on bedrock (Gonçalves et al. 2003).

In this Section, we want to investigate the behaviour of transverse dunes with a simple model, in which the dynamics of the field is controlled by the dune heights and by the influx of sand at the origin of the field. First, we consider dunes developing on bedrock. We study the dynamics of the field starting with different initial configurations of the field, and model the formation of a coastal dune field where small dunes propagate from the beach onto a bedrock. In the next Section, we will adapt this model to investigate what happens when dunes evolve on a sand sheet. In this case, we add two new ingredients to the model: the separation bubble, such as measured in the field of the Lençóis Maranhenses, and the saturation length of the flux, which determines the position of the downwind dune after reattachment of the flow at the lee of the dune upwind.

Model equations

We consider a set of N dunes distributed along the x axis, each one with a variable height h_i, but zero width. The dunes are allowed to move in the x direction with a velocity $v_i \equiv \mathrm{d}x_i/\mathrm{d}t$ given by:

$$v_i = \frac{a}{h_i}, \tag{5.1}$$

where x_i is the position of the $i-$th dune, $i = 1, 2, \ldots, N$, and a is a constant phenomenological parameter that contains information about the wind speed, the grain size, etc.

For a dune that migrates shape invariantly through sand avalanches on its slip face, the sand flux ϕ over the dune behaves as $\mathrm{d}\phi/\mathrm{d}h =$ constant, where $h(x)$ is the height profile of the dune. For the model studied in this Section, we consider the height h_i of the dune at the position of the crest, and set for the $i-$th dune:

$$\phi_i = b\, h_i, \tag{5.2}$$

where b is our second phenomenological parameter, again depending on wind speed, grain size, etc. Note that eq. (5.2) means that the rate of sand transport over the crest is larger for the bigger dunes than for the smaller ones. As a consequence, exchange of sand is expected between neighbouring dunes with different heights, as a bigger dune tends to lose sand more rapidly than a smaller one.

To model the inter-dune interaction, we first observe that for a two-dimensional slice of a dune, the mass of sand in the dune, or equivalently, its area A, increases with the height of the dune as $A \sim h^2$. On the other hand, the amount of sand transported depends on the difference between the sand fluxes on the crests of the neighbouring dunes, i.e. if $\mathrm{d}A_i$ is the volume change for the $i-$th dune during a time interval $\mathrm{d}t$, then $\mathrm{d}A_i \sim (\mathrm{d}h_i)^2 \sim (\phi_i - \phi_{i-1})$. Thus, we write:

$$\frac{\mathrm{d}h_i}{\mathrm{d}t} = -c \times \sqrt{|\phi_i - \phi_{i-1}|} \times \mathrm{sign}(\phi_i - \phi_{i-1}), \tag{5.3}$$

where c is the third parameter of our model that depends on the shape of the dune, and the last factor on the right side ensures that more sand is transported from the larger dune to the smaller one. We set the sand influx to point in the positive wind (x) direction and assume it to be constant. We call the sand influx ϕ_0, which can be seen as an effective dune fixed at the position $x_0 = 0$, with a constant height $h_0 = \phi_0/b$. Equations (5.1), (5.2) and (5.3) are repeatedly iterated, which gives the time evolution of the dune field.

Dynamics of a transverse dune field

First, we study the evolution of a set of N dunes with initial positions $x_i(0)$ and heights $h_i(0)$, for different configurations with $N = 10$, as shown in fig. 5.1.

In the first group of simulations (I), the dunes are equally spaced along the x axis at $t = 0$, and have the same heights $h_i(0) = H, i = 1, 2, \ldots, N$ (fig. 5.1(a)). In the second group (II), we take random values for the heights $h_i(0)$ chosen from an homogeneous distribution between 0 and 1, but still the dune spacing is regular (fig. 5.1(b)). And in the third group (III), both the values for the heights and the positions of the dunes along the x axis are chosen randomly (fig. 5.1(c)).

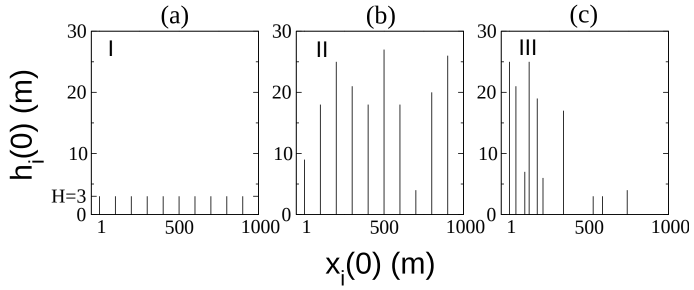

Figure 5.1: Different realizations of a set of N dunes with positions $x_i(0)$ and heights $h_i(0)$ at $t = 0$. In (a) dunes are equally spaced, and have the same height H (group I). Dunes in group II have regular spacing and random heights (b), while in group III, both the positions and heights are random (c).

The trajectory of the dunes along the x axis and the changes in their heights are shown as a function of the time in figs. 5.2(a) and (b) respectively, for particular realizations corresponding to each one of the initial states I, II and III. The values of the phenomenological parameters are $a = 300$ m^2/year, $b = 1500\,\mathrm{year}^{-1}$ and $c = 0.05$, and the sand influx is chosen to be $\phi_0 = 2.25 \times 10^4\,\mathrm{m/year} \approx 4.3\,\mathrm{cm/min}$. In the simulations, each iteration corresponds to 0.01 year. As can be seen from these figures, after a certain number of iterations $t \sim T_\infty$, all dunes reach the same height $h_i(T_\infty) = \phi_0/b = 15$ m, and consequently the same velocity $v_i(T_\infty) = a/h(T_\infty) = (a \times b)/\phi_0 = 20$ m/year, independently on the initial configuration.

In the discussion above, the distances between the dunes were large enough that their relative order was the same during the whole evolution of the field. However, if a smaller, faster migrating dune is very closely behind a larger, slower one, they can reach the same position after some finite time. Dune coalescence has been studied for instance in Lima et al. (2002), in which a critical distance $D_{\min}$ between two neighbouring dunes was considered, below which they collide and become one single dune. In our model, we set $D_{\min} = 0$. For simplicity, dune coalescence is implemented here through the emergence of a single dune, with height $h_{\mathrm{c}} = \sqrt{h_i^2 + h_{i+1}^2}$. Consequently, the number of dunes N in the field decreases by unity, whenever two dunes coalesce.

The main plot of fig. 5.3 shows the variable $x_i(t)$ for a set of $N(0) = 20$ dunes with random values of $x_i(0)$ and $h_i(0)$ for $t = 0$. The values of ϕ_0 and of the parameters a, b and c are the same as in figs. 5.2(a) and (b), but now their distances in the initial state are much smaller. The number of dunes as a function of time for the realization in this figure is shown in the upper-left-hand-corner inset. Note that this number decreases monotonically until the last coalescence between dunes has occurred, and the final number of dunes, $N(\infty) = 3$, has been reached. As we can see from the bottom-right-hand-corner inset, coalescence of dunes doesn't modify the result that the dunes in the field do all have the same height in the final state.

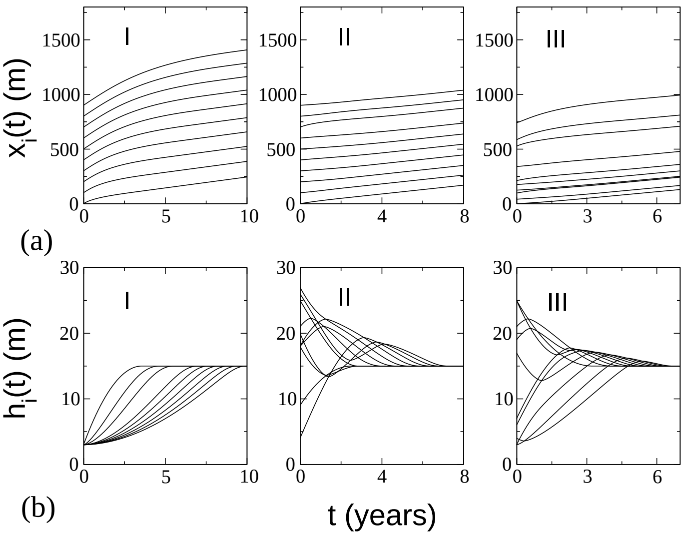

Figure 5.2: (a) Trajectory of the $N = 10$ dunes along the $x-$axis as function of time, for each of the realizations shown in fig. 5.1. Evolution of the heights of the dunes for each case is shown in (b). Values of the parameters used are $a = 300$ m^2 /year, $b = 1500$ year^{-1}, $c = 0.05$, and $\phi_0 = 2.25 \times 10^4$ m/year.

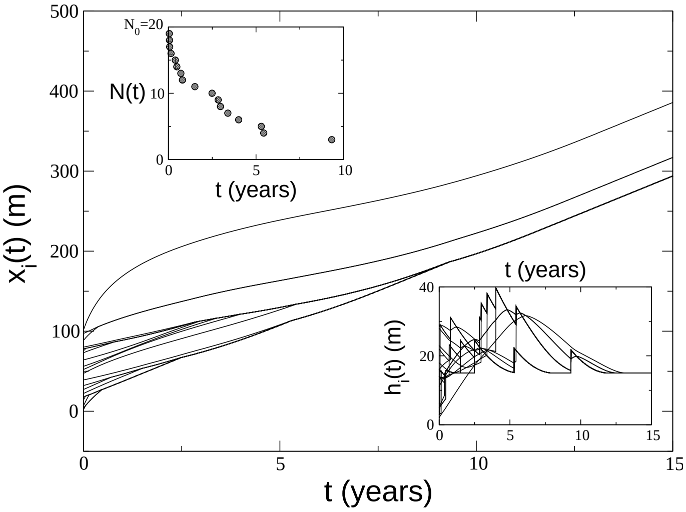

Figure 5.3: The main plot shows the time evolution of the position $x_i(t)$ for a set of $N(0) = 20$ dunes with coalescence for values of parameters used in fig. 5.2. The number of dunes as function of the time, $N(t)$, is shown in the upper-left-hand-corner inset of this figure. From the bottom-right-hand-corner inset, we can see that dune coalescence does not change the fact that all dunes have the same height for $t \to T_\infty$.

For a given distribution of dunes in the field at $t = 0$, the number $N(\infty)$ of dunes in the final state tends to be larger for smaller values of the parameter a, the other parameters b, c and ϕ_0 being fixed. This is because a controls the velocity of the dunes, and coalescence is more frequent in a field with faster dunes. In the same way, the closer the dunes are in the initial state, the more they are going to coalesce in average. As an example, we show in fig. 5.4 the behaviour of $N(\infty)$ as a function of the length L of the system, i.e. the initial distance between the first dune and the last one in the field, for a set having a fixed number of $N(0) = 50$ dunes, using the same values of the phenomenological parameters as in fig. 5.1. As we can see in this figure, the smaller (larger) the value of L, the more (less) the dunes tend to coalesce. The statistical error bars are obtained from different realizations of dunes with random heights and positions at time $t = 0$. The full line shown in fig. 5.4 corresponds to the fit:

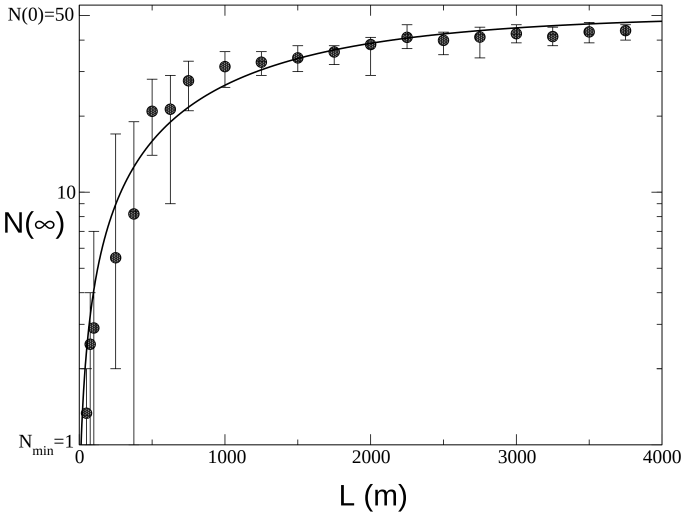

Figure 5.4: Average number of dunes $N(\infty)$ for $t = T_\infty$, as function of the size L of the system, i.e. the distance between the first dune and the last one in the initial state. The statistical error bars are obtained from an average over different realizations $(x_i(0), h_i(0))$ of $N(0) = 50$ dunes at $t = 0$. The full line corresponds to the fit using the equation $N(\infty) = N(0)\,[1 - q * \exp(-L/L^*)]$, with $q \simeq 1$ and $L^* \simeq 1.34 \times 10^3$ m.

$$N(\infty) = N(0)\,[1 - q * \exp(-L/L^*)], \tag{5.4}$$

where $N(0) = 50$, $q \simeq 1$, and $L^* \simeq 1.34 \times 10^3$ m.

In fig. 5.5, we show for three different values of L the corresponding curves $N_L(t)$, averaged over five realizations of $(x_i(0), h_i(0))$, as a function of time t. The values of L shown are $L = 100$ m (circles), $L = 500$ m (triangles) and $L = 1000$ m (squares). The dashed line corresponds to a straight line in a linear-log fit to the curve corresponding to $L = 100$ m. We can observe that $N_L(t)$ decays approximately logarithmically with time, independently of L. After a variable time interval $T_c \leq T_\infty$, coalescence stops and an asymptotic value $N(\infty)$ is reached.

As all dunes attain the same height $h_0 \propto \phi_0$ for $t = T_\infty$, the time to reach the final state depends on the strength of the sand influx in the field, ϕ_0. A plot of T_∞ as a function of ϕ_0 for the initial configuration I of fig. 5.1a is presented in fig. 5.6. As we can see from this figure, T_∞ scales after a transient interval of variation in $\phi_0 - bh_i(0)$:

$$T_\infty \sim \sqrt{|\phi_0 - \phi|}, \tag{5.5}$$

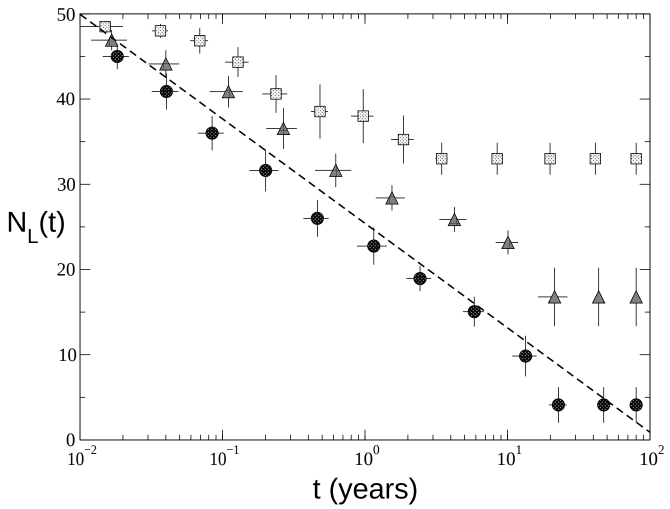

Figure 5.5: Three $N_L(t) \times t$ curves corresponding to averages over different initial realizations of the type III $(x_i(0), h_i(0))$ of a set of $N(0) = 50$ dunes, which are let to evolve with coalescence. The curves correspond to $L = 100$ m (circles) $L = 500$ m (triangles) and $L = 1000$ m (squares), where L is the distance between the first dune and the last one in the initial state of the field. Time is plotted on a logarithmic scale. The dashed straight line is a guide to the eye meant to fit to the curve for $L = 100$ m (circles).

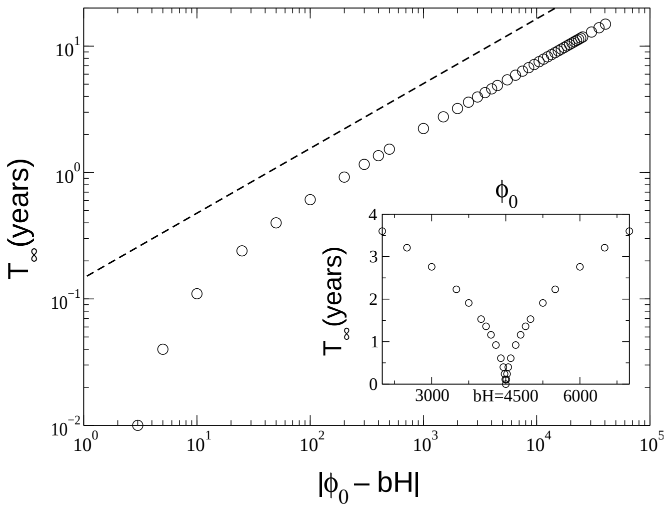

Figure 5.6: Dependence of the time T_∞ to reach the final state, on the relative sand flux $|\phi_0 - bH|$ for the initial configuration I shown in fig. 5.1a. The circles shown in the main plot correspond to the case $\phi_0 > bH$, and line represents eq. (5.5). The inset shows T_∞ as a function of ϕ_0 for the same set of dunes.

i.e. the closer the value of ϕ_0 to $\phi = bh_i(0) = bH$, the more rapidly the system will reach the final state. From eq. (5.3), we see that the phenomenological parameter c controls the rate of sand transport between neighbouring dunes. We have found that the number of iterations to reach the final state decreases as $1/c$, which in fact is independent of the initial height H of the dunes.

Summarizing, the simple model presented in this Section yields transverse dunes that have all the same height. This is independent of the initial heights and spatial distribution of dunes in the field. In the next Section, we apply this simple model to study the realistic case of dunes emerging from the beach, in order to reproduce the formation of a coastal transverse dune field.

5.2 Modelling formation of a coastal transverse dune field

Transverse dunes are very common on coasts because of the large influx of sand coming from the beach and the strong unidirectional character of the wind (Illenberger and Rust 1988). Figure 5.7 shows very small barchans in the beginning of the Lençóis Maranhenses. These barchans are situated close to the field of the measured transgressive dunes (fig. 4.5b). Coastal "baby" barchans join to form small barchanoids and transverse dunes of heights of a few meters in the beginning of the field, as we can also see in fig. 1a. Let's apply the simple model introduced in the previous Section to reproduce the appearance of a coastal transverse dune field.

Figure 5.7: The genesis of the Lençóis Maranhenses coastal dune field. "Baby" barchans of heights smaller than 1 m emerge from the beach. They increase in size forming small transverse dunes that will later reach several tens of meters in height.

We also want to include some additional ingredients, which are described below, in order to make the model more realistic (Lee et al. 2005).

A geometrical description of the main elements of the model is shown in fig. 5.8, where two dunes of heights h and H, $H > h$, have their profiles represented by triangles. The dune width L is related to its height h as $L = (r_1 + r_2)h$, where $r_1 = 10$ and $r_2 = 1.5$ are constants determined from the shape of the dunes in the Lencçóis Maranhenses (Parteli et al. 2006c) and from the fact that the slip face defines an angle of approximately 34°

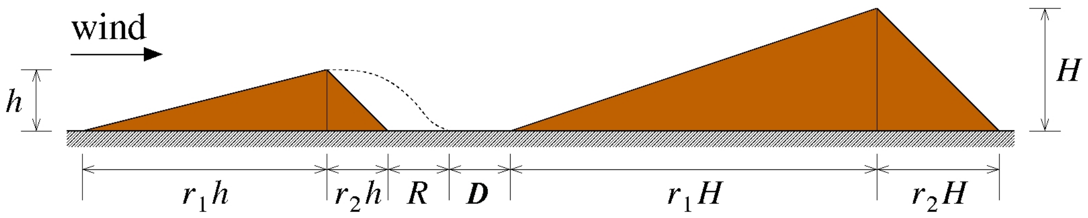

Figure 5.8: Schematic representations of the situation of two transverse dunes.

with the horizontal (Bagnold 1941). Furthermore, we include the “separation bubble” at the lee of the dunes. We use a separation bubble of length $4h$ in accordance with our field observations in the Lençóis Maranhenses. Thus, the quantity R in fig. 5.8 has length $4h - r_2 h = 2.5h$ for all dunes.

The separation bubble of the dunes has an important implication in interactions of closely spaced dunes, since the net sand flux inside the bubble is zero (Kroy et al. 2002). The distance measured from the reattachment point of the separation bubble of dune i to the foot of the windward side of the next dune downwind, $i + 1$, is called here D.

Since we are now considering the dune width in the computation of the field dynamics, we must define how two dunes interact when they get close to each other. Dune interaction is assumed to occur whenever the separation bubble of dune i “touches” the windward side of the downwind dune $i + 1$, or in other words, when $D < 0$ in fig. 5.8. Further, the way two dunes interact depends on their relative sizes (Schwämmle and Herrmann 2003; Durán et al. 2005). If the sizes of the dunes are not too different, the dune downwind decreases in size giving sand to the smaller dune upwind, and they essentially interchange their roles, like if the smaller dune would cross the larger one. This “solitary wave” behaviour of dunes have been shown to occur both for barchans (Schwämmle and Herrmann 2005) and for transverse dunes (Schwämmle and Herrmann 2004; Parteli et al. 2006c). On the other hand, if the faster dune is significantly smaller than the higher dune downwind, coalescence occurs: The small dune bumps into the larger one and gets “swallowed up” (Schwämmle and Herrmann 2003; Durán et al. 2005).

In this simple model, dune interaction is defined according to the parameter ζ: if the ratio of the dune volumes $(V_h/V_H)_{\text{initial}} = (h/H)^2_{\text{initial}}$ is smaller than ζ, then the dunes coalesce, and the final dune has height $h_c = \sqrt{h^2 + H^2}$ (Parteli and Herrmann 2003), as considered previously in this Section; the number of dunes in the field decreases by unity whenever two dunes coalesce. However, if $(h/H)^2_{\text{initial}} > \zeta$, then solitary wave behaviour occurs: dunes interchange their roles and the relation between their initial and final heights is as follows (Durán et al. 2005):

$$\left(\frac{h^2}{H^2}\right)_{\text{final}} = C\sqrt{\left(\frac{h^2}{H^2}\right)_{\text{initial}} - \zeta}, \tag{5.6}$$

obeying the following mass conservation equation:

$$(h^2 + H^2)_{\text{initial}} = (h^2 + H^2)_{\text{final}}. \tag{5.7}$$

Equation (5.6) is a simplified approximation of the phenomenological observation reported by Durán et al. (2005) for interactions between barchans, where it is shown that $(V_h/V_H)_{\mathrm{final}} \propto \exp\{-0.22/[(V_h/V_H)_{\mathrm{initial}} - \mathrm{const.}]\}$. Although this has been obtained for barchans, we apply eq. (5.6) to transverse dunes since careful analysis of 3d simulation results for the shear stress on barchan dunes have shown that the central cut of these dunes may be a good description for the height profile of transverse dunes (Sauermann 2001). While in Durán et al. (2005) the value of ζ that fits the observations for barchans is around 0.15, in the present work we consider ζ as a model parameter to study interaction of transverse dunes in the field. The value of the constant C in eq. (5.6) is determined from a fit to the data by Durán et al. (2005) using the value $\zeta = 0.15$, and is found to be $C \approx 1.3$. We thus identify two limit cases of the parameter ζ: When $\zeta \rightarrow 0$, no coalescence occurs, and the number of dunes in the field remains constant, while for $\zeta \rightarrow 1$ every collision of two dunes results in coalescence and the consequent decrease in the number of dunes in the field. The relations (5.6) and (5.7) are two *independent* equations that are used to determine the final dune heights after each iteration in which dunes interact like solitary waves.

Dynamics

Transverse dunes with random heights of values uniformly distributed between h_a and h_b are injected into the field at a constant rate $1/\Delta t$ from the origin $x = 0$ downwind, moving with velocity $v_{\mathrm{d}}(h)$ given by eq. (5.1). The time interval Δt may vary between 1 and 100 time steps. Typical values of dune heights in the beginning of a dune field are observed to be around 1 m. Thus, to study formation of transverse dune fields, h_b will be set close to $h_a = 1$ m. However, in cases (i) and (ii) we will use larger values for h_b, thus providing a wider spectrum of dune heights in order to study the effect of coalescence and solitary wave behaviour in the evolution of a dune field. In our simulations, each time step is defined as 0.01 year. Thus, after each iteration dunes move a distance downwind given by $(0.01 \times a)/h$ m, and may interact with each other according to the rules mentioned before. The typical simulation time for 10000 iterations is a few tens of seconds running on a Pentium IV.

We study three cases: (i) Dunes are injected into a field with no sand on the ground; (ii) Dune fields are studied when the ground is covered with a sand bed, where a phenomenological parameter, the saturation length of flux, is introduced. (iii) Finally, we add to case (ii) a differential equation to simulate a sand influx, which changes the heights of the dunes over the field evolution.

Dunes on bedrock

In cases (i) and (ii) we investigate the evolution of the field due only to interactions of dunes through coalescence and solitary wave behaviour, according to relations (5.6) and (5.7), which are the mechanisms leading to changes in the heights of the dunes. In this case, the mean dune height in the field doesn't go beyond the maximum height h_b of the injected dunes.

Figure 5.9 shows the snapshot of a transverse dune field at $t = 10^4$ time steps (100 years) for case (i) when 100 dunes are injected into the field at regular time intervals $\Delta t = 0.01$ year, using $a = 100$ $\mathrm{m}^2/\mathrm{year}$, $h_b = 10$ m, and $\zeta = 0.234$. Each vertical line segment in this plot corresponds to the height at the crest of a single dune.

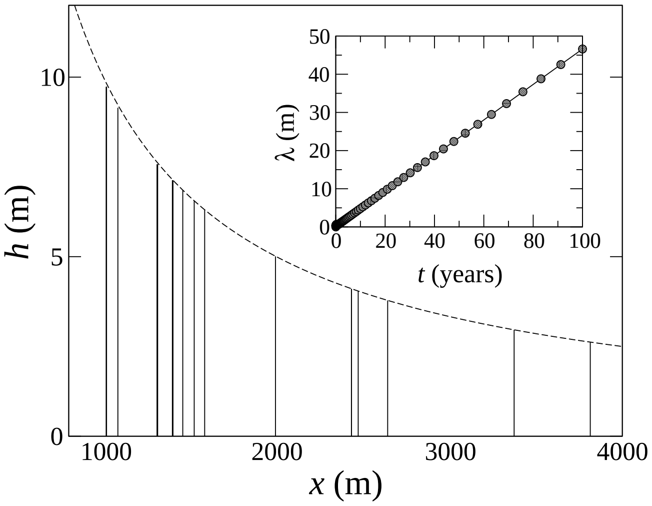

Figure 5.9: The main plot shows the profile of a simulated dune field after $t = 100$ years, obtained after input of 100 dunes from wind direction. Dune crests are represented by the vertical line segments. The dashed line represents the curve $h = 10^4/x$. Model parameters are $a = 100$ $\mathrm{m}^2/\mathrm{year}$, $\Delta t = 0.01$ year and $\zeta = 0.234$. The inset shows the average dune spacing, representing $\lambda \simeq 0.46\,t$.

In fact, $h_b = 10$ m is a value quite unrealistic to study the origin of a dune field where dunes are injected from the beach. However, as mentioned above, we are in this first part of our work only interested in studying the effect of interactions between dunes during the field evolution. Figure 5.9 shows that the initial number of dunes has been reduced by coalescence. Furthermore, we can see that the height of the dunes in the field decreases as the inverse of the dune position downwind: The smaller dunes are found at the end of the field. The dashed line in the main plot represents the curve $h = 10^4/x$. The prefactor A of the curve $h(x) = A/x$ is time dependent, and may be determined from eq. (5.1), which leads to $h(x) = at/x$. The reason for this behaviour is that small dunes bump into larger ones giving rise to the large height profile at the beginning of the field, while dunes interacting like solitary waves contribute to the emergence of the small dune heights observed at larger values of x, and the consequent temporal increase of the field length, i.e. the distance between the dunes at both extremities of the field. We have also observed that the curve $h(x) = A/x$ is independent of the value of ζ. The inset of fig. 5.9 shows that the mean spacing λ between the dunes increases indefinitely with time, since the small dunes at the end of the field, due to their higher velocities, get more and more apart from the larger ones. The average dune spacing λ for one particular realization of transverse dune field may be written as a linear function of the time t with coefficient in terms of the heights of the first and last dunes, h_1 and h_N, respectively, as well as of the total number of dunes in the field, N:

$$\lambda = \frac{a}{N-1}\left(\frac{1}{h_N} - \frac{1}{h_1}\right)t. \tag{5.8}$$

For the dune field shown in fig. 5.9, we have $N = 61$, $h_1 = 2.6$ m and $h_2 = 9.7$ m, then we find that the coefficient of eq. (5.8) is approximately 0.46, which agrees with the slope of the curve shown in the inset of this figure.

In summary, our findings for case (i) show transverse dune fields with decreasing dune heights with distance and an increasing dune spacing with time, since the smaller faster dunes wander at the end of the field. However, field measurements (Lancaster 1983) have shown that dune spacing *increases* with the dune height, as opposed to the situation found in fig. 5.9, where spacing between smaller dunes is mostly larger than for higher dunes. Furthermore, one relevant aspect to be noticed in the dune field of fig. 5.9 is the quite irregular dune spacing, where “clusters” of dunes are even observed, which are not found in real transverse dune fields.

The effect of inter-dune sand

An important difference between transverse dune fields and the dune fields simulated so far using our model lies in the availability of sand on the ground. In dune fields where transverse dunes appear on a sand sheet, regular spacing and similar dune heights are observed (Parteli et al. 2006c). This is because if there is sand on the ground, the distance between the dunes must be of the order of the saturation length of the flux, $\lambda_{\rm s}$. In a transverse dune field developed on a sand bed, $\lambda_{\rm s}$ may be measured from the reattachment point of the separation bubble of the upwind dune (see fig. 5.8), where the wind strength increases from zero (value of the wind strength in the separation bubble) and sand transport initiates (Sauermann et al. 2001). When the flux becomes saturated, i.e. after a distance $D = \lambda_{\rm s}$ from the reattachment point, sand is deposited at the foot of the windward side where the wind strength decreases, and the surface at the beginning of the downwind dune is not eroded. It follows that no dune can move faster than its upwind neighbor.

To simulate such dune fields, we introduce in our model the phenomenological constant $\lambda_{\rm s}$ by fixing for the quantity D in fig. 5.8 a maximum value $D_{\max} = \lambda_{\rm s}$. We set $\lambda_{\rm s} = 2$ m. As a consequence, the *maximum* crest-to-crest distance in the field, $D_{\rm cc}$, is calculated as:

$$D_{\rm cc} = r_2 h + R + \lambda_{\rm s} + r_1 H, \tag{5.9}$$

according to the definitions in fig. 5.8. It is important to notice that the maximum spacing $D_{\rm cc}$ in the field, as predicted by eq. (5.9), is not a constant, but does depend on the dune size, and is larger in dune fields of higher dunes.

Figure 5.10 shows two simulated dune fields when the saturation length $\lambda_{\rm s}$ is taken into account (case (ii)). The profile shown in fig. 5.10(a) corresponds to $t = 90$ years, where dunes of initial heights between $h_a = 1$ m and $h_b = 2$ m have been injected into the field (now a ground covered with sand) using $\Delta t = 0.1$ year, $a = 150$ m^2/year and $\zeta = 0.3$.

As we can see in this figure, all transverse dunes reach approximately the same height, around 1.6 m, and present a quite regular spacing. Figure 5.10(b) shows another dune field obtained at $t = 500$ years with $h_a = 1$ m and $h_b = 10$ m, $\Delta t = 0.1$ year, $a = 150$ m^2/year and $\zeta = 0.3$, where we find dunes regularly spaced and of heights around 8 m. As we can see, the value of the final dune height depends on the initial values of h_a and h_b. Moreover, comparison of fig. 5.10 with fig. 5.9 shows that the introduction of the saturation length leads to much more stable transverse dune fields, since the smaller dunes wandering fast at the end of the field are now not found anymore.

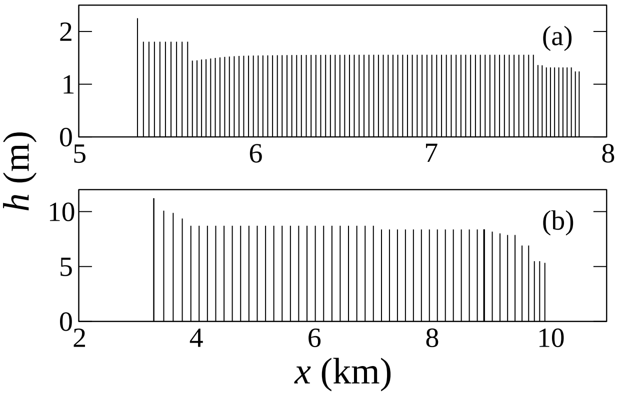

Figure 5.10: Transverse dune field obtained when the saturation length of the flux, λ_{s}, is considered. Model parameters are $\Delta t = 0.1$ year, $a = 150$ m^2/year, $\zeta = 0.30$, and (a) $t = 90$ years (b) $t = 500$ years. The heights of the 100 injected dunes at $t = 0$ are random numbers between 1 and (a) 2 m, (b) 10 m. We see that the two fields present a quite regular dune spacing.

The time evolution of the number of dunes in the field is shown in fig. 5.11 for three different values of the parameter ζ, using again $\Delta t = 0.1$ year and $a = 300$ m^2/year. As we can see in this figure, after injection of the 100 dunes into the field (at $t = 10$ years as indicated by the dashed line), the number of dunes decreases quite regularly in time, as also found by Schwämmle and Herrmann (2004) from a two-dimensional model of transverse dune fields. Furthermore, after a certain time, when dunes reach the same height, the number of dunes gets constant, N_f. In fig. 5.11, we present the final number of dunes N_f as a function of ζ, averaged over 1000 realizations, when $h_b = 2$ m (circles) and $h_b = 10$ m (squares), using $h_a = 1$ m, $\Delta t = 0.1$ year and $a = 300$ m^2/year. As we can see in this figure, for small values of ζ ($\zeta \rightarrow 0$), the number of dunes remains at the initial value $N = 100$, since coalescence occurs less frequently. In particular, this effect is more visible when $h_b = 2$ m (circles), because in this case dunes have more similar initial heights (between 1 and 2 m), and coalescence between dunes occurs even more rarely. As the value of ζ increases, N_f decreases because dunes coalesce more often in the field; for large values of ζ, as discussed before, N_f is equal to 1. One aspect of particular interest in fig. 5.11 is that N_f decreases quite suddenly with ζ if the initial heights of the dunes are very similar (curve represented by circles). In particular, we have found that as $h_b \rightarrow h_a = 1$ m, N_f decreases rapidly to unity at $\zeta \approx 0.30$. On the other hand, for a wider range of heights of the injected dunes ($h_b \gg h_a$), N_f decreases more smoothly with ζ, since in this case even small values of ζ are large enough for coalescence to occur.

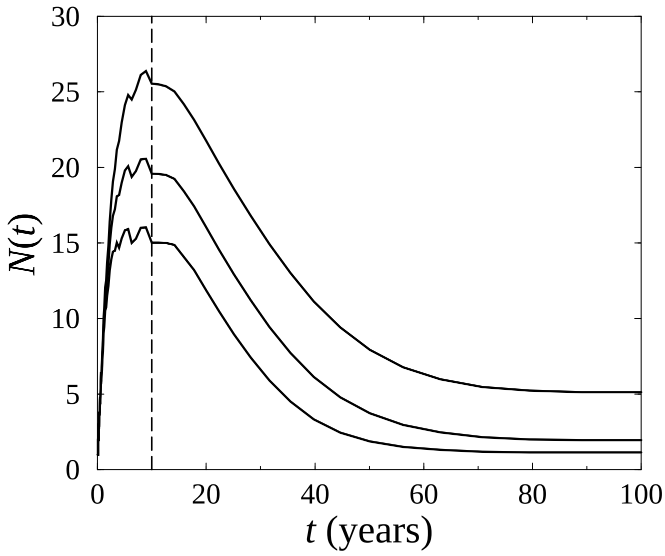

Figure 5.11: Number of dunes in the field, $N(t)$, as a function of time t for $\zeta = 0.34$, 0.35 and 0.36 (from top to bottom) averaged over 1000 realizations. The dashed line indicates the time when input of the 100 injected dunes with random heights between 1 and 2 meters finishes. $\Delta t = 0.1$ year and $a = 300$ m^2/year.

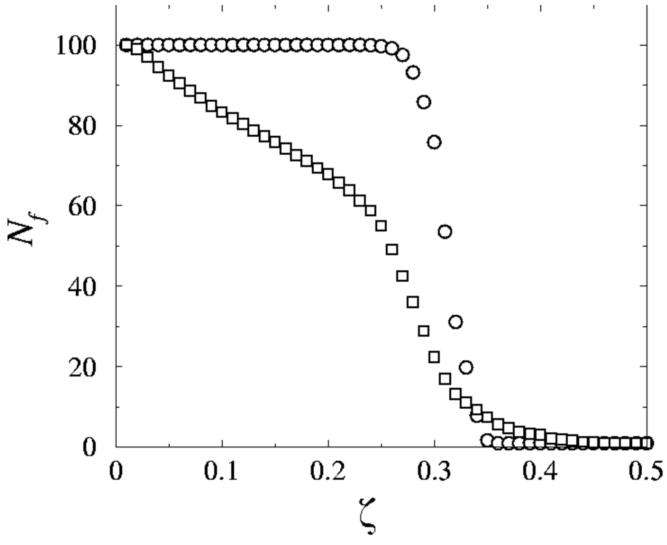

Figure 5.12: Final number of dunes N_f as a function of ζ, averaged over 1000 realizations. The heights of the 100 injected dunes are random numbers between 1 m and h_b, where $h_b = 2$ m (circles) and 10 m (squares). The number of dunes decreases in time due to coalescence between dunes. $\Delta t = 0.1$ year and $a = 300$ m^2/year.

Figure 5.13 shows the average dune spacing λ as a function of time using $\Delta t = 0.1$ year, $a = 100$ m^2/year, $\zeta = 0.3$, and considering the saturation length $\lambda_{\rm s} = 2$ m. As we can see from comparison of this figure with the inset of fig. 5.9, the inter-dune distances evolve in time in a very different way as compared to the case where the saturation length λ_{s} was not taken into account. Figure 5.13 shows that the dune spacing now increases until it reaches a *saturation value*, which corresponds to the equilibrium state of the field, where dunes have similar heights as shown in fig. 5.10.

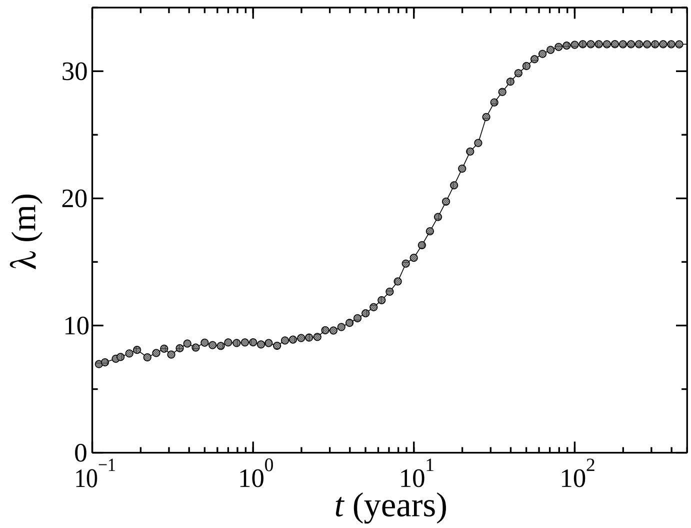

Figure 5.13: Mean dune spacing λ as a function of time, averaged over 1000 realizations of dune fields using $\zeta = 0.3$, $a = 100$ m^2/year and $\Delta t = 0.1$ year, after injection of the 300 dunes, which have initial random heights between 1 m and $h_b = 2$ m. Computational time is 300 minutes on a Pentium IV computer to obtain this figure.

A very similar result was found recently by Werner and Kocurek (1999) using a transverse dune model in two dimensions based on defect dynamics. They found that λ increases logarithmically in an intermediate time interval until getting constant, as observed in fig. 5.13. The model of Werner and Kocurek (1999) consists of a set of differential equations to describe the dynamics of the endlines of two-dimensional transverse dunes (length and width). In their model, which was used to predict ages of real dune fields (Werner and Kocurek 1999), interaction between dunes led to a decrease in the number of defects in the field. We would like to remark that, although fig. 5.13 suggests that $\lambda(t)$ increases approximately with $\log(t)$ for $8 \leq t \leq 40$, we could not find more than one decade of this possible logarithmic behaviour of dune spacing in time.

Thus, the model defined in case (ii) in the absence of any sand influx reproduced formation of dune fields of regular spacing, just by injection of dunes downwind onto an empty ground, which interact by coalescence or solitary wave behaviour according to relations (5.6) and (5.7). This situation is different from the case studied in Parteli and Herrmann (2003), where a constant sand influx is considered, and a field of transverse dunes of random initial heights evolves in time until a constant final height is reached, which is proportional to the sand influx. There, a regular spacing was only found in the case where the initial dune spacing and heights were considered to be also regular.

Indeed, a serious limitation of the model so far is that the final height of the dunes is limited according to their initial values. There is in fact an important ingredient that is still lacking in the model. Coastal dunes are subjected to a strong *sand influx* from the beach. We now define the following equation for the dune height:

$$\frac{dh_i}{dt} = c \times \sqrt{|\phi_0 - \phi_i|}, \tag{5.10}$$

where ϕ_0 is the constant influx, $\phi_i = bh_i$ is the sand flux at the position of dune i (Parteli and Herrmann 2003), and b and c are phenomenological constants which depend on the conditions of the field as wind velocity, and sand supply. It is important to notice that eq. (5.10) does not include sand transport between dunes, as opposed to the case studied in Parteli and Herrmann (2003). The important contribution is the strong influx originating at the beach.

We follow the same rules for dune interaction as mentioned before and consider transverse dunes evolving on a sand sheet, where the saturation length λ_s is taken into account as in the previous case. In the inset of fig. 5.14, we show a typical transverse dune field obtained after $t = 100$ years using eq. (5.10) and injecting dunes with heights $h_a = h_b = 1$ m at rate $1/\Delta t$, where $\Delta t = 1.0$ year. The parameters used are $a = 1000$ m^2/year, $b = 10^3$ year^{-1}, $c = 0.01$, $\phi_0 = 1.0 \times 10^4$ m/year, and $\zeta = 0.3$. As we can see, in the beginning of the field, dune heights *increase* with the position downwind. Furthermore, some kilometers later, dunes reach regular spacing and similar heights $h_0 = \phi_0/b$ (Parteli and Herrmann 2003). The scenario presented in fig. 5.14 corresponds to an *evolving* field where dunes are continuously injected; it is no equilibrium state. Such a picture can be found for instance in many parts of the coastal dune field of the Lençóis Maranhenses. Therefore, our model can reproduce dune fields observed on the coast, where new dunes are continuously appearing in the beginning of the field, at the beach.

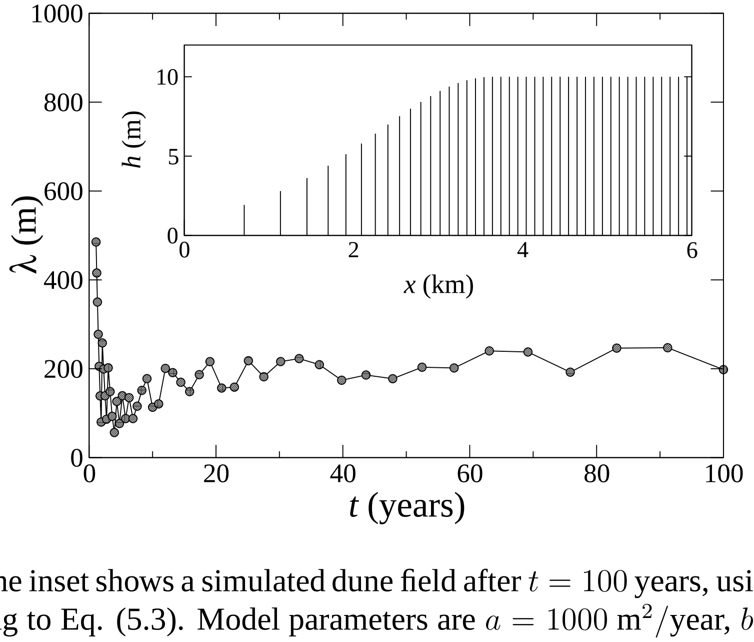

Figure 5.14: The inset shows a simulated dune field after $t = 100$ years, using the constant influx according to Eq. (5.3). Model parameters are $a = 1000$ m^2/year, $b = 10^3$ year^{-1}, $c = 0.01$, $\phi_0 = 1.0 \times 10^4$ m/year, $\zeta = 0.3$ and $\Delta t = 1.0$ year. The main plot shows the dune spacing λ as a function of time averaged over 1000 realizations.

The main plot of fig. 5.14 shows the dune spacing as function of time averaged over 1000 realizations. It can be seen that, after a certain number of time steps, the dune spacing

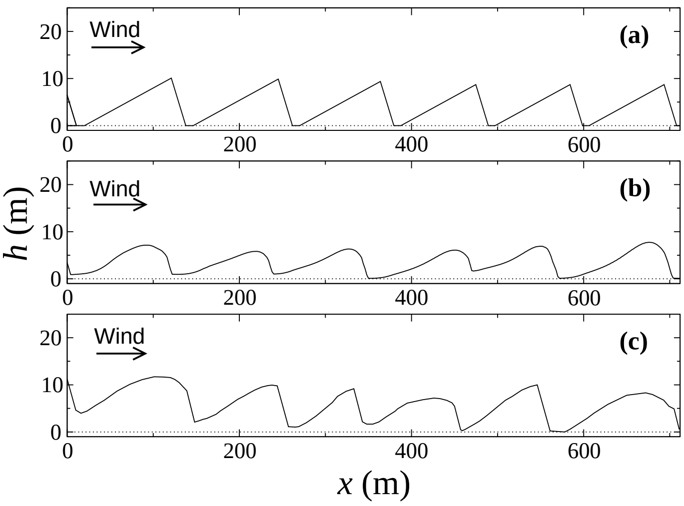

Figure 5.15: In (a) we show a typical dune field obtained with our model where the saturation length λ_s is considered, with $a = 300$ m^2/year, $\Delta t = 0.1$ year and $\zeta = 0.3$, $N = 100$ injected dunes and $t = 1000$ years. (b) and (c) are respectively the simulation of transverse dunes and the measured profile studied in 4.1.

reaches a constant value corresponding to the inter-dune distances for which dunes present the equilibrium height of 10 m. In fig. 5.15, we compare the dune field obtained from our simulations (fig. 5.15(a)) with the profile of the measured dunes in the Lençóis Maranhenses (fig. 5.15(c)) and simulation results from the two-dimensional model of closely spaced transverse dunes (fig. 5.15(b)) (Parteli et al. 2006c). The height profile of the dunes shown in (a) follows the relations defined in fig. 5.8.

In summary, we found that the sand influx from the beach is of fundamental importance to reproduce realistic values of dune heights observed in real coastal transverse dune fields from realistic values of initial dune heights. Without inclusion of eq. (5.10) into the simple model studied in this Section, dunes with small initial heights in the beginning of the field cannot grow to the heights observed in real dune fields, as can be seen in figs. 5.10(a) and 5.10(b), where the final dune height is always around h_b.

One aspect to be mentioned is the calculation of the parameter ζ for transverse dunes. Due to the great simplicity of our model, no conclusion could be made about a single threshold value $\zeta = \zeta_{\rm transverse}$ which would describe interactions of transverse dunes, as done recently for barchans in 3 dimensions, where $\zeta_{\rm barchan} \approx 0.15$ (Durán et al. 2005). To this point, simulations of transverse dunes in two dimensions would be required. It would be also interesting to check whether the results found in figs. 5.11, 5.13 and 5.14 may be found from other numerical models of transverse dune fields in two and/or three dimensions.

5.3 When a dune field is born

The simple model studied in the previous Section reproduced the fact that small dunes emerging from the beach converge to form extensive fields in which dunes have approximately the same height and where inter-dune spacing is quite regular. Now we want to use the complex dune model presented in Chapter 1 to calculate the formation and the early stages of the evolution of terrestrial coastal dune fields, as those in Baja California, Mexico (fig. 1a), and in the Lençóis Maranhenses in Brazil (fig. 4.5).

In the calculations, the most important ingredient is the input of sand at the inlet of the simulation. The flux is *saturated*, i.e. $q_{\rm in} = q_{\rm s}$, at the sandy beach. The beach is simulated using a linear ridge (fig. 6.6b) of height 1.0 m and width 40 m, oriented transversely to the wind direction and with center of mass only 20 m apart from the inlet. Thereafter, the sand ridge increases in volume and extends in width, becoming unstable and giving rise to small transverse dunes, which detach from the beach and wander away (fig. 5.16). These unstabilities are of the same type as the ones found from two-dimensional calculations of transverse dunes performed by Andreotti et al. (2002b) and Schwämmle and Herrmann (2004). Furthermore, there is one aspect that can be only seen in the three-dimensional calculations presented in this Chapter. When the transverse dunes reach the bedrock, they become unstable and give rise to barchan dunes. First, at least one of the transverse dunes in the field decays into barchans. Then, the shear stress is not anymore invariant

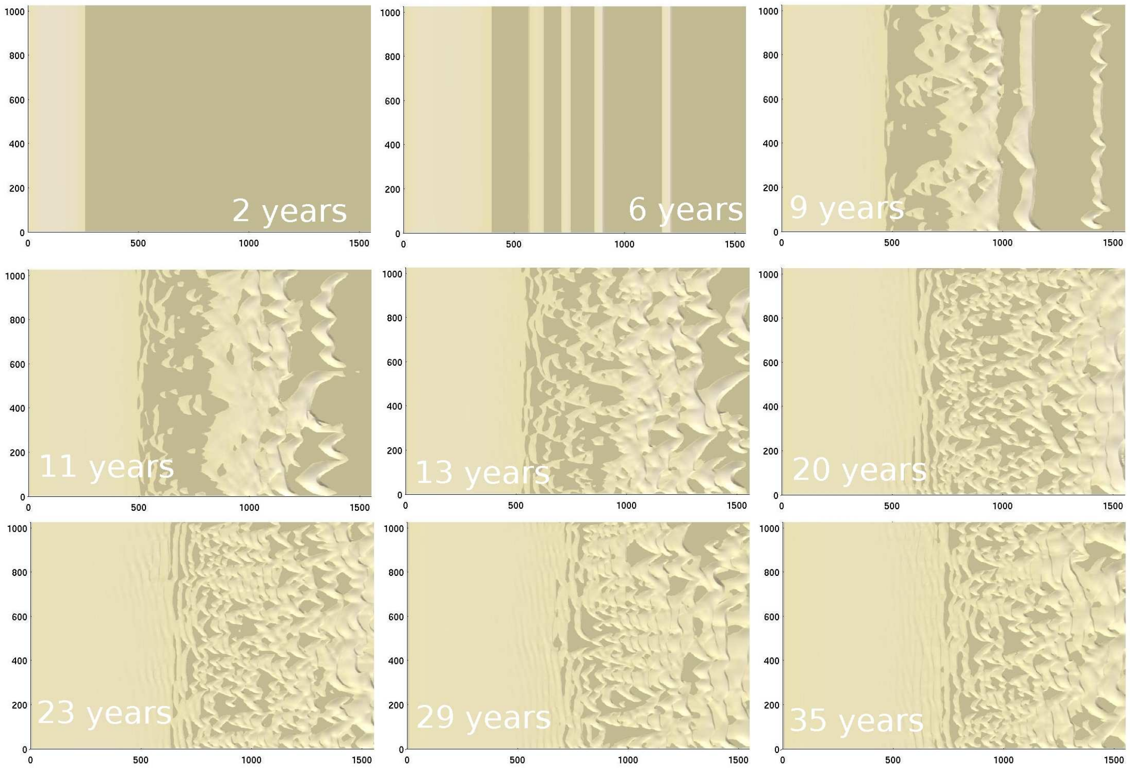

Figure 5.16: Snapshots of the evolution of a coastal dune field, calculated with $u_*/u_{*{\rm t}} = 1.75$ (i.e. with $u_* \approx 0.38\,{\rm m/s}$). Wind blows from the left to the right.

in the y direction, and all laterally invariant transverse dunes at the beginning of the field disappear. Thereafter, barchans develop in their place.

It is interesting that, since the flux is saturated, dunes will steadily appear. Moreover, we can see in fig. 5.16 that the small barchans tend to join at later stages, forming transverse dunes. The main plot of fig. 5.17 shows the evolution of the maximum height H of the dune field as function of time t for the particular case of $u_*/u_{*\mathrm{t}} = 1.75$. The total length of the studied field is 2.4 km, and its width is ≈ 1.0 km. We see that, if such a wind blows steadily in the same direction, the height of the field increases at a rate of approximately 70 cm a year.

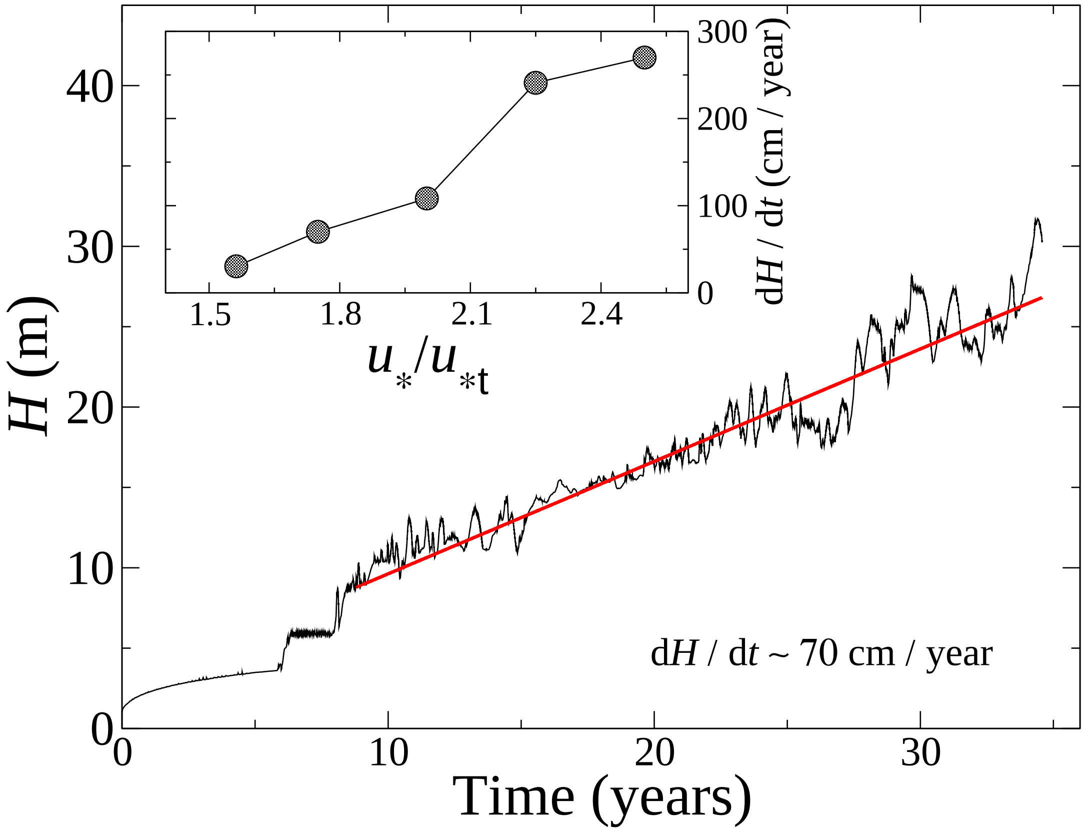

Figure 5.17: The fluctuating curve in the main plot shows the time evolution of the maximum height of a 2.4 km long coastal dune field calculated with $u_*/u_{*\mathrm{t}} = 1.75$. The straight line shows the linear fit to the data: the maximum height of the field increases at a rate of 70 cm per year. The inset shows the rate at which the height of the field increases with time as function of $u_*/u_{*\mathrm{t}}$.

In the calculations, the only parameter is the wind strength, u_*, which determines the dune size (Chapter 3). Moreover, the field evolves differently depending on u_*. The inset of fig. 5.17 shows that the rate $\mathrm{d}H/\mathrm{d}t$ increases with $u_*/u_{*\mathrm{t}}$. In fig. 5.18 we see the appearance of the field after 25 years, obtained with $u_*/u_{*\mathrm{t}} = 1.57$ (a), 1.75 (b) and 2.00 (c). As we can see from this figure, there appears to be a tendency of transverse dunes to form faster the higher the wind speed. In fact, we found that the field calculated in (a), with $u_*/u_{*\mathrm{t}} = 1.57$, evolves in time in such a way that transverse dunes appear at later stages.

Furthermore, it can be recognized comparing fig. 5.18 with fig. 5.16 that a decrease in wind strength implies to “slow down” the evolution of the field.

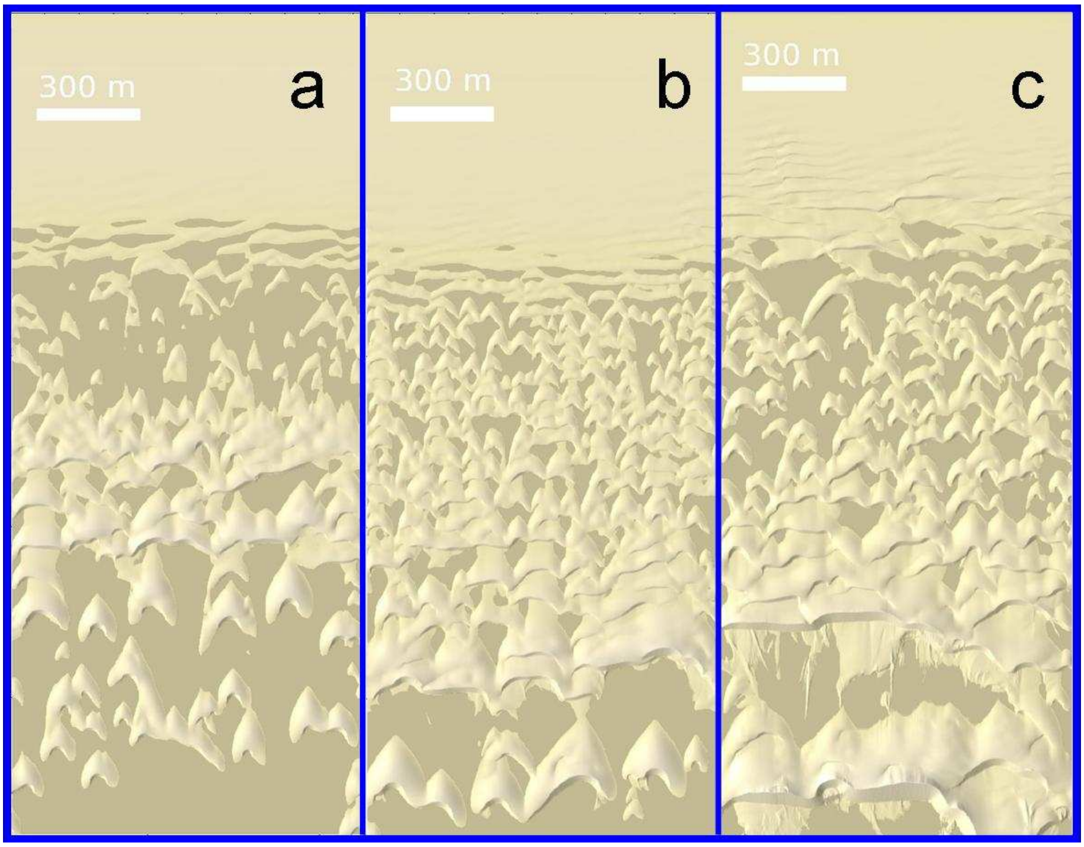

Figure 5.18: Coastal dune fields calculated with $u_*/u_{*t} =$ **a)** 1.57, **b)** 1.75 and **c)** 2.0. Each image corresponds to the snapshot at $t \approx 25$ years. Wind is blowing from top to bottom.

5.4 Conclusion

We proposed a simple model for a transverse dune field which reproduced the observation that the dunes in a given field have approximately all the same height (Parteli and Herrmann 2003). We found that this result is independent of the initial configuration of the field, as well as on coalescence effects between migrating dunes (figs. 5.2 and 5.3).

Next, we applied the model to calculate the formation of a coastal dune field (Lee et al. 2005), including the phenomenological parameters to account for our field observations in the Lençóis Maranhenses: a separation bubble of length 4 times the dune height; a dune aspect ratio (height over width) of 0.1; and initial dune heights of 1.0 m. For dunes evolving on a sand sheet, the model reproduces the observation (Werner and Kocurek 1999) that the dune spacing reaches a saturation value (fig. 5.13). Moreover, we found that the strong influx from the beach is responsible for the appearance of coastal dune fields with increasing dune height with distance downwind. The simple model also reproduces the observation that both the dune height and the inter-dune spacing in coastal transverse dunes reach an equilibrium value after a few kilometers onto the continent (figs. 5.14 and 5.15).

Finally, we used the complex dune model to calculate the formation of a coastal dune field. We found that small barchans emerge from the beach, wander downwind and join at their horns to form barchanoids and transverse dunes. We also found that the appearance of the field depends on the wind shear velocity u_*. As $u_*/u_{*\mathrm{t}}$ increases, the characteristic size of the barchans at the beginning of the field decreases, as consequence of the decrease of the saturation length ℓ_s (Chapter 3). Moreover, we found that the appearance of the field changes as $u_*/u_{*\mathrm{t}}$ decreases: the small dunes appear larger and form barchanoids at short distances after the beach.

Thus, the formation of a costal dune field can be calculated on the basis of a sand source (the beach), submitted to an undirectional wind, and the appearance of the field is determined by the wind strength, $u_*/u_{*\mathrm{t}}$. Such calculations can help significantly understand coastal processes, with inclusion of oscillating wind strength, variable wind direction, vegetation, topography, and inter-dune water ponds.

Chapter 6

Seif dunes: forms and formation

The dune morphologies we investigated so far appear under conditions of uni-directional wind. Whilst barchans and transverse dunes are the best understood dunes, nearly two thirds of the terrestrial deserts are covered with a different dune type, which appears under more complex wind regime. *Linear dunes*, also called *longitudinal* or *seif* dunes, are sand dunes that elongate parallel to the prevailing wind direction (Warren 1972; Fryberger and Dean 1979; Tsoar 1983; Rubin and Hunter 1985; Rubin and Hunter 1987; Hesp et al. 1989b; Tsoar 1989; Rubin and Ikeda 1990; Chakraborty 1993; Wang et al. 1993; Bullard et al. 1995; Bristow et al. 2000; Kocurek and Ewing 2005; Zhang et al. 2005).

In fig. 6.1, we see a field of linear dunes in Mauritania. Further, on top of fig. 6.1 we show the annual and seasonal sand roses associated with the linear dune field. The sand roses of areas with linear dunes reveal that these dunes are formed under the influence of a *bidirectional* wind regime, i.e. two strong sand-moving winds originating in adjacent quarters (Fryberger and Dean 1979).

Seif dunes may reach several kilometers in length, and have been also found on Mars (Edgett and Blumberg 1994; Lee and Thomas 1995). In general, they present a characteristic sinuosity, which is still poorly understood. Furthermore, linear dunes appear in areas of relatively high availability of sand, and they occur as discrete ridges separated by inter-dune flats, the inter-dune spacing generally increasing with increasing dune size (Hesp et al. 1989b). Indeed, linear dunes can have very different forms, as we see in figs. 6.2 and 6.3. Where the amount of sand on the ground is low, however, diverse dune shapes can be observed, which are up to now unexplained (Section 6.2.2).

In this Chapter, we investigate the significance of bimodal wind regimes for the formation of different dune morphologies. First we investigate one field of Martian dunes where *both* linear and rounded barchan dunes occur. In particular, there is one intriguing feature in this field: the linear dunes do not display the sinuosity of typical seif dunes, and are rather very straight. The fact that this special longitudinal dunes appear together with barchans raised the question: might seif dunes in fact form in areas of unidirectional winds? The calculations show that a linear dune submitted to an unidirectional wind is unstable and disappears, giving place to a row of barchans propagating downwind (Schatz et al. 2006). Next, we show that linear dunes can only appear under certain conditions of bimodal

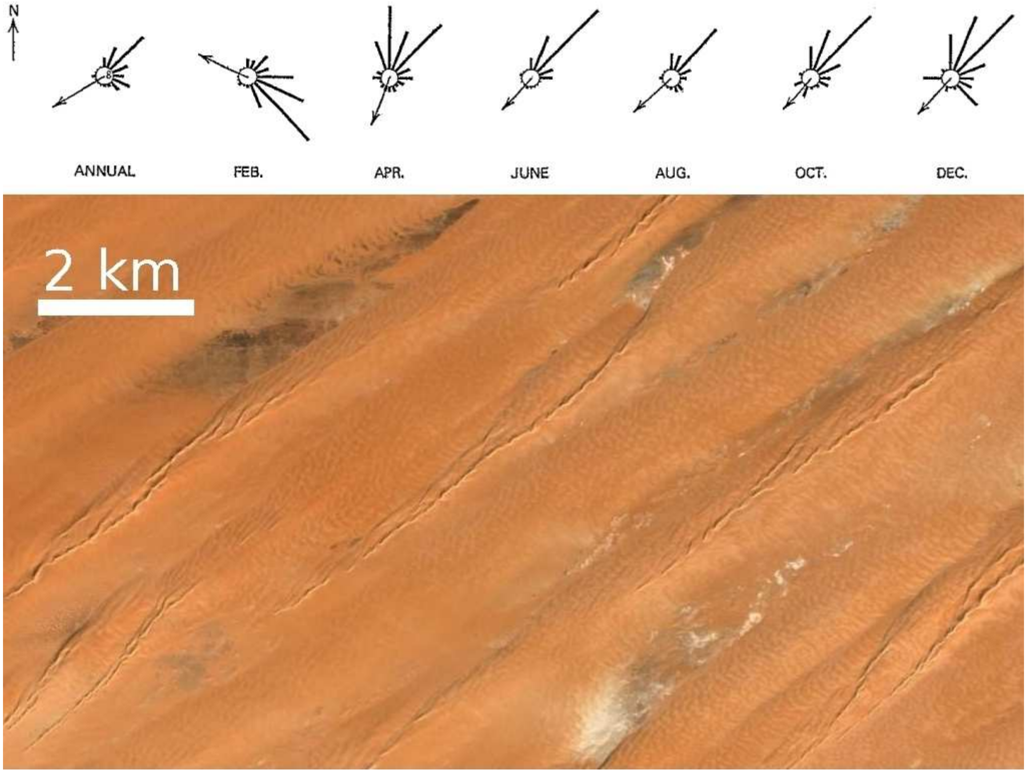

Figure 6.1: Linear dunes near Fort-Gourard, Mauritania, at 22.2°N, 10.37°W. North is from bottom to top. On top of the image, we see the annual and seasonal sand roses associated with the field, after Fryberger and Dean (1979).

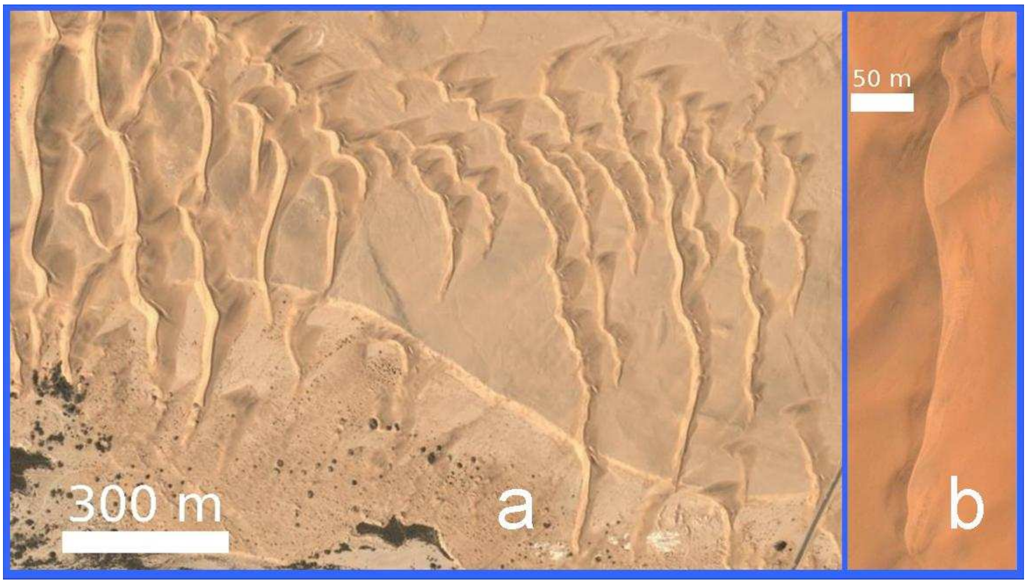

Figure 6.2: Seif dunes on Earth, at **a.** 22.41°S, 14.32°E near Swakopmund, Namibia; **b.** 15.44°N, 47.14°E, Yemen.

wind regimes: changes in the angle between the wind directions and the frequency of the oscillation of the wind have been the origin of complex dune shapes, from rounded barchans to longitudinal dunes.

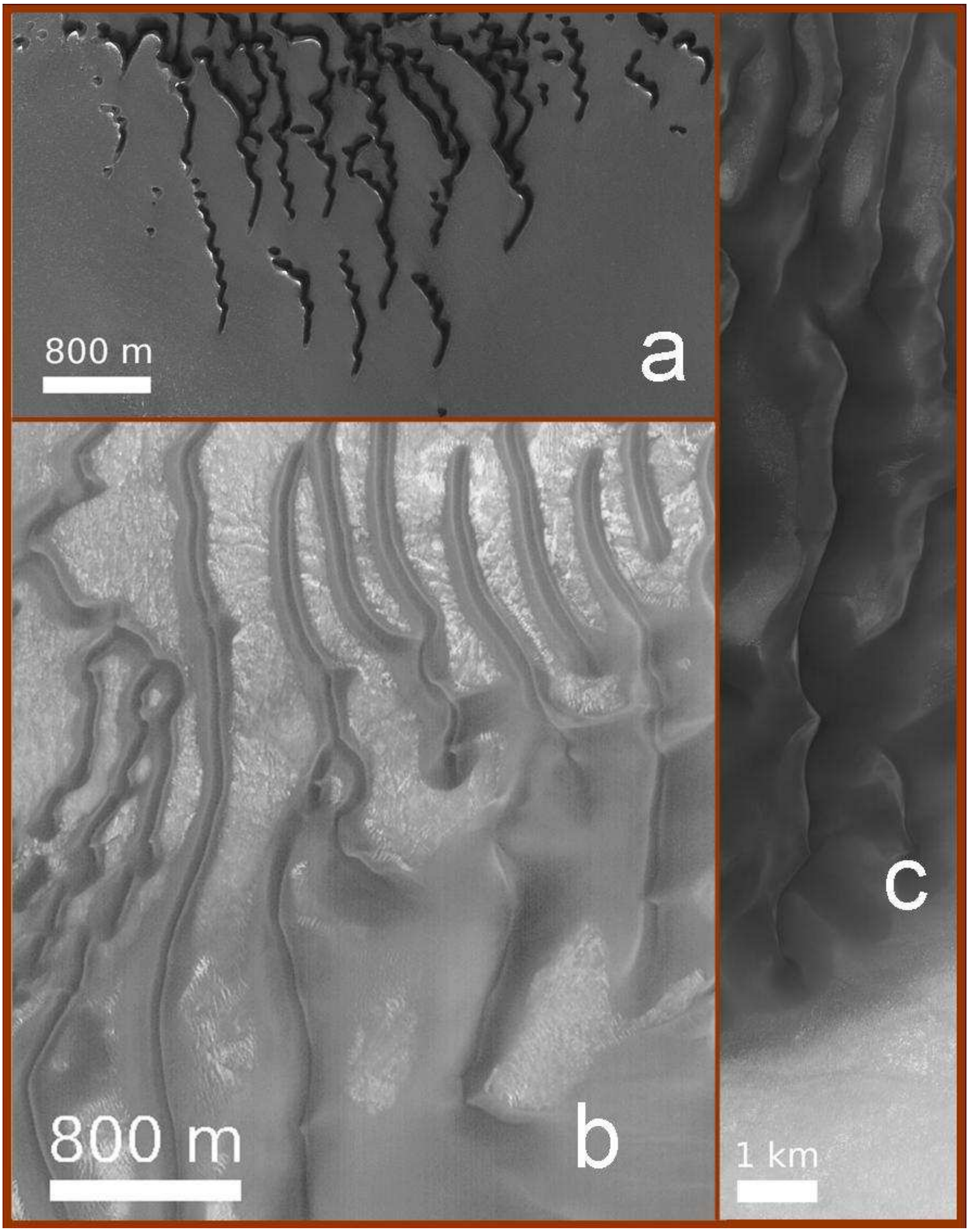

Figure 6.3: MGS MOC images of linear dunes on Mars, at **a.** 79.8°N, 127.1°W; **b.** 45.4°S, 331.1°W; **c.** 49.0°S, 326.3°W.

6.1 Evidence for indurated dunes in the Martian north polar region?

In Chasma Boreale, a region in the north pole of Mars, there appear unusual dune morphologies which are shown in fig. 6.4. What is surprising in Chasma Boreale is the coexistence of rounded barchans and linear dunes in the same field. The linear dunes in fig. 6.4a simply should not occur with the barchans, unless they are unlike terrestrial linear dunes, and formed, somehow, in an unidirectional wind regime.

Elongated, elliptical or dome-shaped dunes, such as those in fig. 6.4b might be the product of successive induration as the slip face advances forward and becomes smaller and smaller, until it disappears, as was observed by Kerr and Nigra (1952) for oil-soaked barchans on Earth (fig. 6.4c). In the Saudi Arabia case, the dunes were sprayed with oil, then additional sand arrived at the fixed dune, blew over its top, and became deposited on the lee side, whereupon the dune was again sprayed with oil. This process continued and, over time, the slip face of each dune became successively smaller, and the dune more rounded and elliptical. This is not typical behaviour for lee-side deposition of sand in a dune field, but is a product of the process of successively inhibiting sand movement, in this case, using oil, on the main body of each dune.

The similarity of the oil-soaked dunes to the rounded Chasma Boreale dunes suggests that the Martian examples could have been formed in a similar way, with ice, frozen carbon dioxide, or mineral salts taking the place of oil as the cause for induration. In fact, crusting or induration of regolith fines and aeolian bed forms has been observed at all five successful Martian landing sites, Viking 1, Viking 2, Mars Pathfinder, Spirit, and Opportunity (Arvidson et al. 1989; Arvidson et al. 2004; Moore et al. 1999; Thomas et al. 2005). Indeed, the landers and rovers did not visit any of the classic, dark Martian dunes. Although some of the Chasma Boreale rounded barchans have been repeatedly imaged by the MOC camera during the past four Martian years and show no evidence for movement (fig. 6.4a), they do not exhibit grooves or steep-walled avalanche chutes which would provide evidence for induration.

The hypothesis that the rounded barchans and straight linear dunes in Chasma Boreale are indurated has been tested with the dune model (Schatz et al. 2006).

Rounded barchans

In fig. 6.4c we see, on top, two MOC images which show a rounded barchan and a dome dune in Chasma Boreale. The sketch of the deposition in the lee of an oil-soaked barchan is shown next to these images, at right. In this sketch, the initial barchan and the final shape are drawn, while the dashed lines show the positions of the slip face in intermediate stages, until an elliptical, dome-like shape is produced.

Schatz et al. (2006) calculated the process of forming a successively indurated barchan using parameters for Mars. In these calculations, each successive stage of the dune development is set indurated (non-mobile), while at the same time new sand is added from the

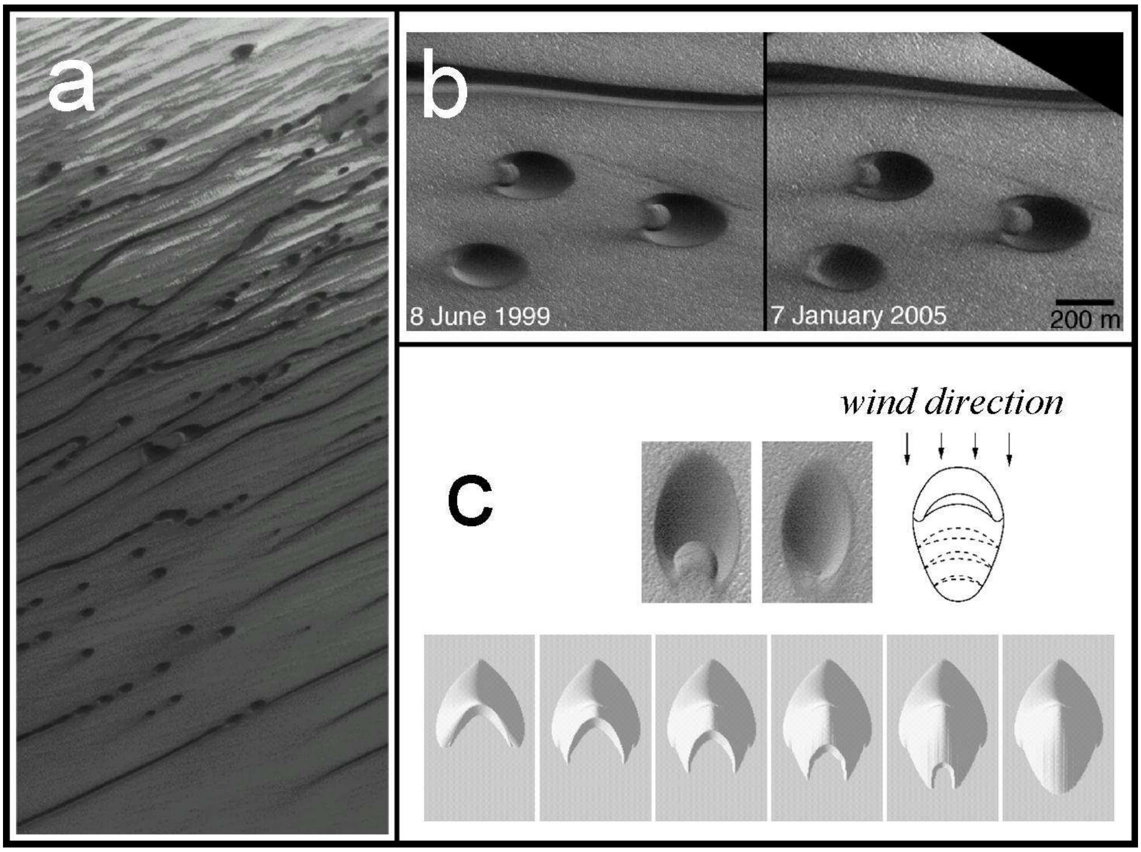

Figure 6.4: **a.** In this MOC image (S02-00901), which covers an area about 3 km wide, we see rounded barchans and linear dunes in Chasma Boreale, near $84.2°$N, $37.9°$W. The rounded barchans in **b.**, which are located near $84.9°$N, $26.6°$W, have been imaged repeatedly by the MOC camera. Relative to the features on the substrate across which they are moving, the dunes do not appear to have moved during the mission. **c.** Are Chasma Boreale dunes *indurated*? On top: two MOC imaged Chasma Boreale rounded dunes of width $\approx$ 240 m (left) and sketch of the deposition in the lee of an oil-soaked barchan, after Kerr and Nigra (1952) (right). On bottom, we see the calculation of indurated dunes performed by V. Schatz (Schatz et al. 2006). From the left to the right, an indurated barchan undergoing the transition to the elliptical dune.

upwind direction. Snapshots of a typical calculation are shown in fig. 6.4c. The initial barchan has width similar to the Chasma Boreale barchans, and as we see in fig. 6.4c, the barchan evolves into an elliptical, dome shape (right). Some small differences between simulation and the satellite image: (i) in simulations, the brink of the initial barchan is still visible at later stages. In reality, this visible ridge would be slowly eroded even if the dune was indurated; (ii) the slip face in the image appears to be very long, but the foot of the slip face is hard to discern; a slip face extending nearly to the end of the horns would imply a very high slip face brink, which would be in contrast with the flat rounded shape suggested by the shadows and with the height of other Martian dunes described by Bourke et al. (2004).

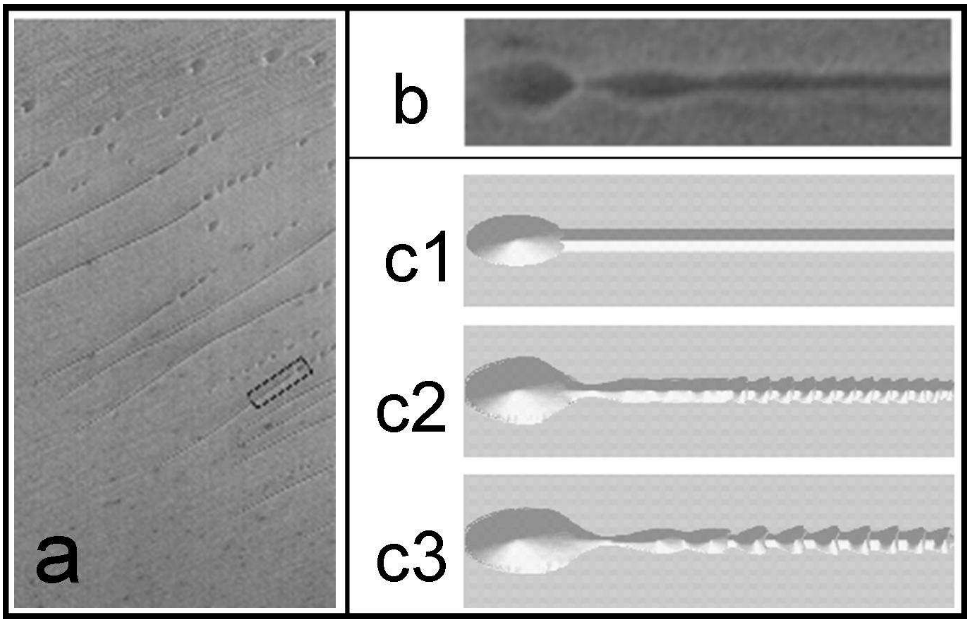

Figure 6.5: (a) MOC image E15-00784 of Chasma Boreale dunes. (b) Detail (box) of image E15-00784. (c) Simulation of the evolution of a straight linear dune downwind of a dome. Besides small variations in thickness, small barchans can be seen to develop, which are not observed on Mars.

Chasma Boreale Linear Dunes

The domes and rounded barchans occur together with straight linear dunes (figs. 6.4a and 6.5a), with which they appear merged, in some cases, to create a single bed form. The upwind end of the linear dunes, immediately downwind of the domes, shows a knotted structure (fig. 6.5b). Schatz et al. (2006) performed a simulation of such dunes, starting from a straight ridge in wind direction located just downwind of an unerodable dome. As can be seen in fig. 6.5c, the knots at the upwind end are reproduced in early steps of the simulation. Their formation is analogous to the instability of a sand bed under unidirectional winds (Andreotti et al. 2002b; Schwämmle and Herrmann 2004). Later on, however, the simulated linear dune decays into a string of barchans. That this has not happened in Chasma Boreale can be explained if the linear dunes are indurated or were formed by erosion in the first place. Although simulations do not show how the linear forms were initiated, they do suggest (as in the case of the elongated, dome-shaped barchans) that the sands are presently or very recently indurated.

Summary

The simulation results presented in fig. 6.5 lead to the following conclusion: if the wind direction in Chasma Boreale dune field is unimodal — which is suggested by the appearance of barchans — the sand of the Chasma Boreale dunes must be *indurated*, for the straight longitudinal dunes would otherwise not occur.

On Earth, increased moisture, decreased wind power and the growth of vegetation are contributors to immobilization. On the other hand, the rounded shape of Chasma Boreale dunes and domes resembles that of the oil-soaked Arabian dunes of Kerr and Nigra (1952), and suggests that sand induration by ice, frozen CO_2 or mineral salts could have led to the unusual dune forms in Chasma Boreale. This hypothesis is supported by calculations using the dune model.

6.2 Sand dunes formed by a wind of oscillating direction

From the results of the last Section, it becomes clear that seif dunes cannot develop under unimodal wind regimes. From comparison of the shape of linear dunes with the behaviour of the wind, many authors concluded that these dunes must be a result of a *bimodal* wind regime. Although many wind directions are seen in sand roses of linear dune fields, there are two wind directions which are associated with the strongest winds, and which effectively yield the longitudinal shape (Fryberger and Dean 1979). Normally one of the wind directions prevails for a period of several months, after which the wind changes to the other direction. Thus, we can model a bimodal wind regime using a wind of *oscillating* direction.

The bimodal wind is implemented in the following manner: a wind of constant strength u_* and constant direction, as in the case of barchans and transverse dunes, and a constant influx between 20% and 40% of the saturated flux are set at the inlet of the simulation; with these conditions, the field is periodically rotated between two positions defining an angle $\theta_{\rm w}$. The field remains at one of the positions for a time $T_{\rm w}$, after which its orientation is suddenly changed to the other direction, which lasts for the same time $T_{\rm w}$. The oscillation of the wind in the field is therefore simulated by the oscillation of the direction of the field itself. In fig. 6.6, we show a schematic diagram with the wind directions defining the angle $\theta_{\rm w}$, where we also show two initial surfaces used in the calculations: (a) a Gaussian hill and (b) a linear ridge of Gaussian cross section.

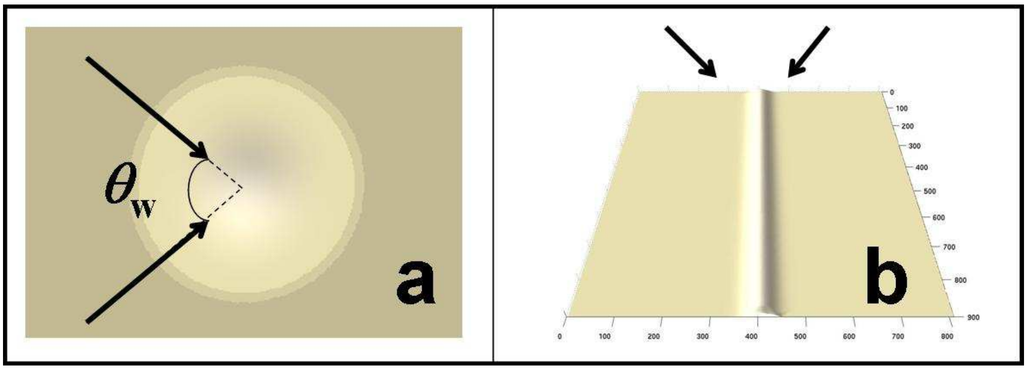

Figure 6.6: Modelling bimodal wind regimes. The wind directions (arrows) define an angle $\theta_{\rm w}$. One of the initial surfaces used in calculations is a Gaussian hill (**a.**). In **b.** we see another initial surface: a linear sand ridge, which has a Gaussian cross section.

There are, in this manner, two parameters of the bimodal wind: the angle $\theta_{\rm w}$ between the wind directions, and the characteristic time $T_{\rm w}$ of each direction. However, we remark that the value of $T_{\rm w}$ used in our calculations is interpreted as an *effective* time, during which the wind blows steadily, and with a constant strength u_*. As discussed in Chapter 3, real winds have strength of a very oscillating nature, and the wind strength is only a fraction of the year above the threshold for saltation. The effective time $T_{\rm w}$, therefore, is a fraction of the time $T_{\rm real}$ during which the wind lasts at one direction:

$$T_{\rm w} = f_{\rm w} T_{\rm real}, \qquad 0 < f_{\rm w} < 1. \tag{6.1}$$

Winds that are strong enough to transport sand may be classified into categories according to their intensity and direction (Fryberger and Dean 1979). These are quantified by means of the sand rose (Chapter 1), where winds blowing from different directions are represented by vectors of different lengths. The length of the vector of the direction i is given by:

$$d_{\rm w}^i = \frac{U_i^2(U_i - U_{\rm ft})}{100} f_{\rm w} \approx \frac{8u_i^2(u_i - u_{\rm ft})}{100} f_{\rm w}^i, \tag{6.2}$$

where U_i and $U_{\rm ft}$ (u_i and $u_{\rm ft}$) are, respectively, the wind velocity in the direction i and the threshold for entrainment in knots (in m/s), measured at a height of 10 m. $f_{\rm w}^i$ gives the fraction of the year (in percent) during which winds of this category occur, while the factor 100 is added to reduce the length of the vectors in the plot (Fryberger and Dean 1979; Tsoar 2005). The quantity $d_{\rm w}^i$ is called the annual rate of sand drift relative to the direction i, and is written in vector units.

The sum over all sand drift values in the sand rose gives the *drift potential*, DP, which is a measure of the potential wind power in a sandy area: it represents the potential maximum amount of sand that could be eroded by the wind during a year for all wind directions. If we define a representative value of wind velocity U (or u) in a given field, DP may be written as function of the total annual fraction $f_{\rm w}$ in which the wind velocity has been larger than the threshold:

$$DP = \sum_i d_{\rm w}^i = \frac{U^2(U - U_{\rm ft})}{100} f_{\rm w} \approx \frac{8u^2(u - u_{\rm ft})}{100} f_{\rm w}, \tag{6.3}$$

Using the logarithmic profile (eq. (1.1)) with $z = 10$ m and a typical roughness of $z_0 = 1.0$ mm we obtain $u \approx 23\, u_*$. Thus, we can write eq. (6.3) in terms of the shear velocity u_*:

$$DP \approx 9.7 \times 10^4\, u_*^2(u_* - u_{*{\rm ft}}) f_{\rm w}. \tag{6.4}$$

The fraction of time $f_{\rm w}$ the representative wind velocity u_* occurs during a year can be, thus, expressed in terms of DP and u_* using eq. (6.4). Values of DP in real dune fields are often below 300, while the shear velocity u_* is typically less than $1.7\, u_{*{\rm ft}}$ (Fryberger and Dean 1979). Since $u_{*{\rm ft}} = 1.25 u_{*{\rm t}} \approx 0.27$ m/s, we use u_* between 0.3 and 0.4 m/s in calculations of terrestrial seif dunes. The value of $f_{\rm w}$, in this manner, decreases with the value of u_* we take, for a constant DP.

For instance, in the Zallaf field of seif dunes, in Lybia, the dominant wind oscillates between two directions, with $T_{\rm real}$ being of the order of several hours (McKee and Tibbitts 1964), while the longitudinal dunes of Sinai experience a bimodal wind regime with

$T_{\mathrm{real}} = 6$ months (Tsoar, private communication). If $T_{\mathrm{real}} = 0.5$ year, then the value of $T_{\mathrm{w}} = f_{\mathrm{w}} T_{\mathrm{real}}$ associated with a dune field in which $DP = 200$ is, using an effective shear velocity of 0.35 m/s, $T_{\mathrm{w}} \approx 3.0 \times 10^6$ s or ≈ 1.0 month. If we choose a shear velocity $u_* = 0.4$ m/s, then $T_{\mathrm{w}} \approx 2$ weeks gives the same DP.

6.2.1 The shape of linear dunes

We investigate the behaviour of a straight linear ridge submitted to a wind of oscillating direction. We begin calculations with a linear ridge of height 15 m that has a Gaussian cross section. In fig. 6.7, we show the time evolution of the linear ridge under different values of θ_{w} and with $T_{\mathrm{w}} = 10^6$ seconds or ≈ 12 days. The shear velocity used in calculations has been $u_* = 0.4$ m/s and an influx of 20% of q_{s} has been set at the inlet of the simulation.

Figure 6.7 suggests that there is a minimal value of θ_{w} for longitudinal dunes to be formed: for all values of $\theta_{\mathrm{w}} \leq 80°$ studied in fig. 6.7, the ridge decays into a string of barchans, in a similar manner as found in Schatz et al. (2006). This case, in which $\theta_{\mathrm{w}} = 0$, has been reported in Section 6.1. On the other hand, the longitudinal shape calculated with $\theta_{\mathrm{w}} = 120°$ persists during the time evolution of the dune. The fact that only the case $\theta_{\mathrm{w}} = 120°$ studied in fig. 6.7 yields linear dunes does not change for the range of values of T_{w} studied, between $5.0 \cdot 10^4$ s, or 14 hours, and $5.0 \cdot 10^6$ s or 2 months.

Summarizing, the results of fig. 6.7 suggest that there is a minimal angle θ_{c}, which is between $80°$ and $120°$, that bimodal wind regimes must define between the directions of sand transport for longitudinal dunes to appear. It was not possible to obtain θ_{c} from calculations with linear ridges such as those in fig. 6.7. We will estimate θ_{c} later in this Chapter.

It is interesting that the results of calculations match very well the observations of Rubin and Hunter (1987), who investigated experimentally the formation of longitudinal *ripples*. In the experiments, Rubin and Hunter (1987) created bidirectional wind regimes by rotating a sand-covered plywood board in relatively steady sea breezes of the California coast. The board remained in each of its two positions for a given time, after which it was rotated to the other position. The two positions defined the angle between the two effective wind directions, in a similar manner as in our calculations.

Rubin and Hunter (1987) found that ripples oriented transverse to the resultant wind direction appear if the angle between the two directions is smaller than $90°$, and that longitudinal ripples are formed only for angles larger than this critical value. Experiments with aquateous dunes performed by Rubin and Ikeda (1990) led to a similar conclusion: $\theta_{\mathrm{c}} = 90°$ is the *critical* angle above which longitudinal bedforms appear. If on one hand the experiments of Rubin and Hunter (1987) and Rubin and Ikeda (1990) did not prove that other controls, such as wind strength and sand amount, have no effect on the bedform trend, their results demonstrated that the appearance of linear ripples and aquateous dunes can be explained independently of such controls.

The above calculations for the straight linear ridge have been also carried out using a

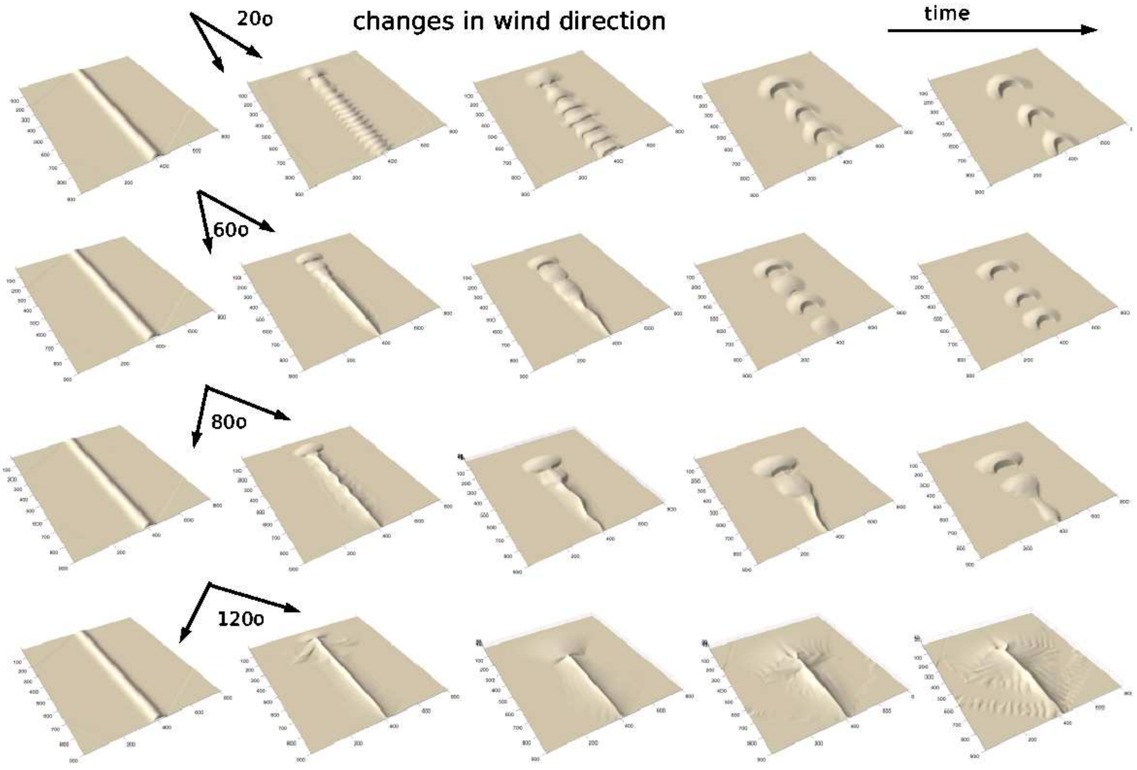

Figure 6.7: Evolution of a linear ridge under bimodal wind. The angle θ_{w} between the vectors indicates the angle between the wind directions, each one of which lasts for a time period $T_{\mathrm{w}} \approx 12$ days. We see that the ridge decays into barchans for all studied values of $\theta_{\mathrm{w}} \leq 80°$.

dense sand bed of thickness 100 m as initial condition. This means perform experiments similar to the ones of Rubin and Hunter (1987) and Rubin and Ikeda (1990), but for aeolian sand dunes. The results are summarized in fig. 6.8. This figure shows, for three different values of T_{w}, one single snapshot of the calculation using (a) $\theta_{\mathrm{w}} = 60°$ and (b) $\theta_{\mathrm{w}} = 120°$. As we see in fig. 6.8, the fact that linear dunes appear above $\theta_{\mathrm{c}} = 90°$ as predicted previously (Rubin and Hunter 1987) did not change with the initial condition used in calculations. The fields shown in 6.8a are of barchanoidal dunes, which develop transverse to the resultant wind direction, while for $\theta_{\mathrm{w}} = 120°$ longitudinal bedforms appear.

Indeed, each dune field shown in fig. 6.8 has a particular form. The longitudinal dunes in the fields of fig. 6.8b have approximately all the same height, and their shape is particular to each field. We see that the sinuosity of seif dunes increase with T_{w}. Moreover, in fig. 6.8a, we see that for large values of T_{w} the barchanoidal dunes tend to develop in the direction of the dominant wind rather than in the resultant wind direction. Thus, we see that the shape of the bedform depends further on the characteristic time of the wind, T_{w}.

The dependence of the longitudinal dune shape on the characteristic time T_{w} of the wind can be understood if we note that the effective time a given change in the shape is achieved

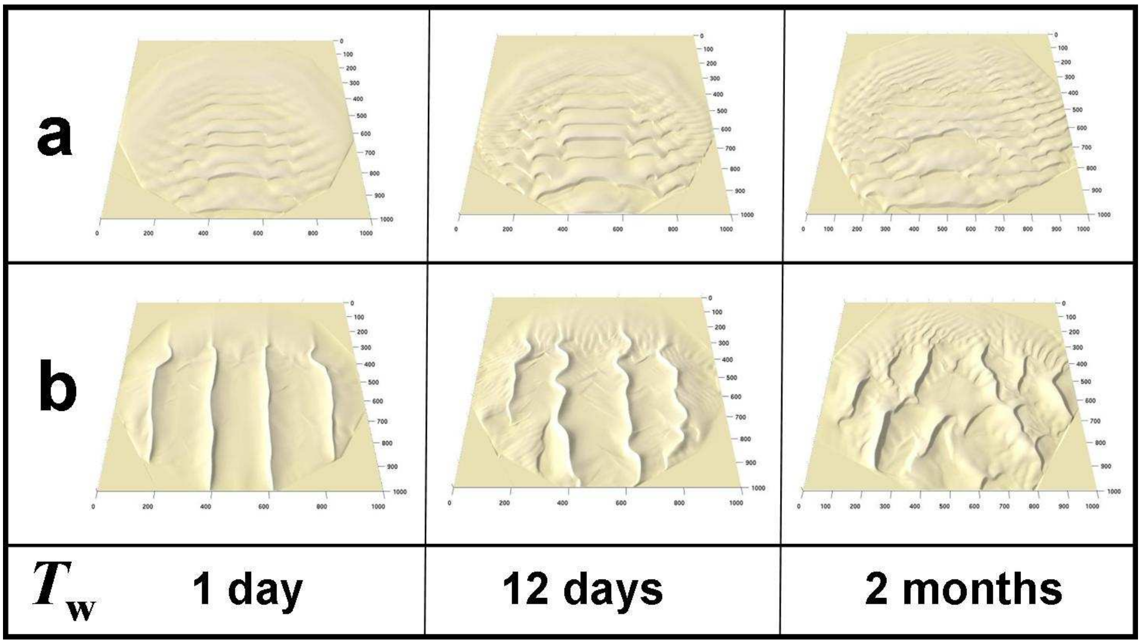

Figure 6.8: Dune fields formed on a sand bed under bimodal wind regime. Initial condition is a flat sand bed of thickness 100 m. In **a.**, we see three different calculations for $\theta_{\mathrm{w}} = 60°$: from the left to the right, one simulation snapshot of a dune field with $T_{\mathrm{w}} = 10^5$, 10^6 and 5.0×10^6 s. In **b.**, the same is shown for an angle $\theta_{\mathrm{w}} = 120°$.

should depend on the volume of the bedform. We have seen in Chapter 1 that smaller barchan dunes move faster because a smaller amount of sand must be transported: the turnover time of the dune increases with its volume. In this manner, for a constant value of T_{w}, the smallest dunes will experience the most changes. We can say that a bedform with given volume appears systematically “smaller” as the time T_{w} of the wind increases. The role of the dune volume for the shape of dunes subjected to a bimodal wind will be illustrated in the next section for the case of dunes developing in areas with low sand amount.

6.2.2 From barchans to seif dunes

Many exotic dune forms, as those in fig. 6.9, often occur on bedrock. Such dunes cannot appear in areas of one-directional winds, for in this case barchans should be formed as seen in Chapter 1. We conclude that dunes shown in fig. 6.9 were formed by complex wind regimes, and in many images, it is possible to recognize that the dominant winds define a resultant direction.

Here we show that a high diversity of dune shapes effectively appear in areas of low sand availability under a bimodal wind regime, depending on the angle θ_{w} and on the characteristic time of the wind directions, T_{w}. In our calculations, we take as initial surface a Gaussian hill as in the calculation of barchan dunes. Figure 6.10 shows the time evolution of a Gaussian hill of initial height 10 m under a bimodal wind regime of

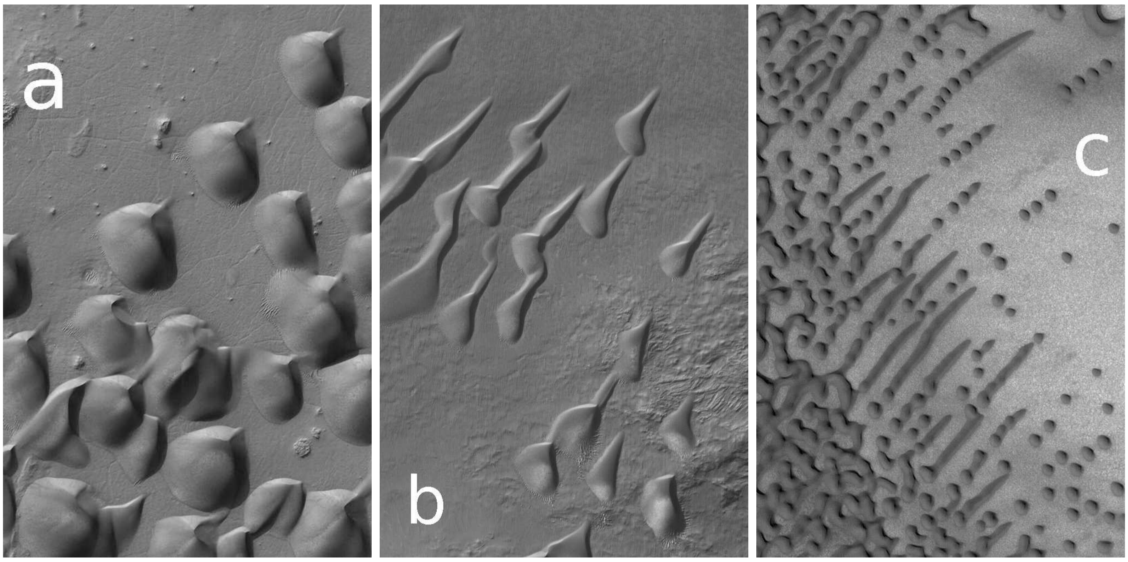

Figure 6.9: Mars Global Surveyor (MGS), Mars Orbiter Camera (MOC) images of sand dunes on Mars. From the left to right: Dunes near **a.** $48.6°$S, $25.5°$ W; **b.** $49.6°$S, $352.9°$ W, and **c.** $76.4°$N, $272.9°$W. Each image has ~ 3 km cross section.

constant characteristic time $T_{\mathrm{w}} = 10^5$ s for different values of θ_{w}. As we see from this figure, the hill evolves in agreement with the predictions of Rubin and Hunter (1987) and Rubin and Ikeda (1990), in the same manner as obtained with a linear ridge and a sand bed: below the critical angle $\theta_{\mathrm{c}} = 90°$ (Rubin and Hunter 1987; Rubin and Ikeda 1990), barchans are obtained, which display however, a rounded shape. Moreover, we see that for $\theta_{\mathrm{w}} = 100°$, complex bedforms are obtained, which consist of rounded domes appearing upwind of a linear ridge. The coexistence of transverse and longitudinal bedforms has been observed in fact by Rubin and Ikeda (1990) using two-directional winds with angles between $90°$ and $120°$.

In fact, we have found that the critical angle θ_{c} is around $95°$. This is shown in fig. 6.11 where we present the calculations using θ_{w} between $80°$ and $100°$. We see that only for $\theta_{\mathrm{w}} = 96°$ does the dune evolve into a longitudinal dune. This value is essentially the same found by (Rubin and Hunter 1987). Indeed, we notice that θ_{c} could slightly depend on the influx, or on the shear velocity, the influence of which is not studied in the present work.

The evolution of the linear dune depends further on the size of the initial Gaussian taken in calculations. If the dune is too small, then a barchan dune is obtained which alternates its orientation according to the dominant wind. On the other hand, the evolution of the dune also changes if we take a Gaussian of much larger size. If the sand volume is too large, we find that the hill develops a small “cusp” downwind, which, however, does not increase in length. In fact, for a given wind regime, we expect dunes of different sizes to behave differently, since decreasing the dune size is equivalent to increase the value of T_{w}, as discussed previously in this Chapter.

For each value of θ_{w}, we perform calculations taking initial Gaussian hills of different heights H_0 and using different values of T_{w}. We find that, independently of the dune

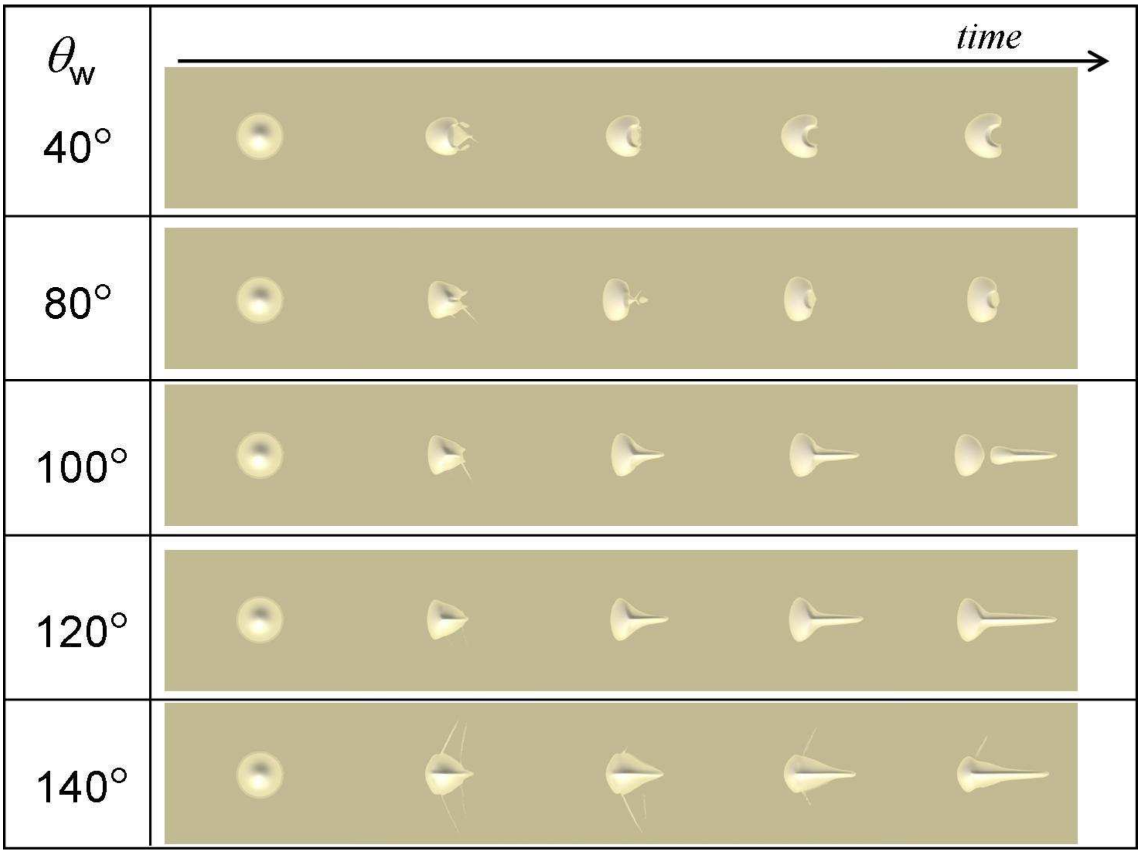

Figure 6.10: Time evolution of a Gaussian hill ($H = 10$ m and $\sigma = 10$ m) under bimodal wind for different values of the angle θ_w between the wind directions. We see that the Gaussian hill evolves into an elongated dune for $\theta_\mathrm{w} \geq 100°$. Moreover, *only* if $\theta_\mathrm{w} \geq 120°$ does the elongated dune evolve into a seif dune. Value of T_w is 10^5 s.

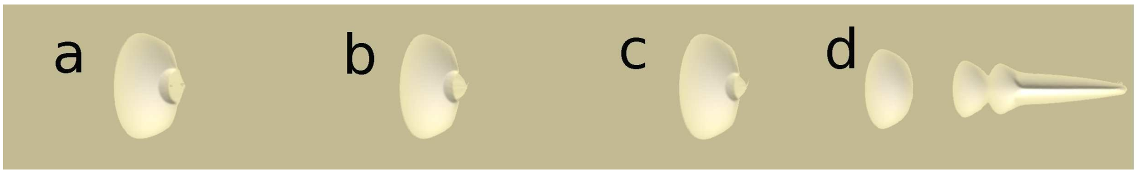

Figure 6.11: Dunes calculated using bimodal winds of θ_w around the critical value $90°$ predicted from experiments with ripples and aquateous dunes (Rubin and Hunter 1987; Rubin and Ikeda 1990). Values of θ_w are **a.** $84°$; **b.** $90°$; **c.** $92°$; **d.** $96°$.

volume and of θ_w, the hill evolves into a barchan dune for large enough values of T_w. Moreover, as T_w is systematically reduced, different dune shapes appear depending on the angle θ_w, in the same order for all dune sizes.

Therefore, we present our results in terms of a normalized characteristic time, which we call t_w, in such a manner to include the information of the dune volume. We define the normalized time t_w using the turnover or migration time T_m of the barchan dune that appears for large values of T_w. T_m is defined as the time which the barchan needs to cover a distance equal to its width, and is written as

$$T_{\mathrm{m}} = \frac{W^2}{aQ}, \tag{6.5}$$

where $Q = q_{\mathrm{s}}/\rho_{\mathrm{sand}}$, and $a \approx 50$ gives the proportionality between the velocity v_{d} of the dune and the ratio Q/W: $v_{\mathrm{d}} = aQ/W$, which is obtained from the model results. We note that Q is the saturated flux normalized by the density of the sand $\rho_{\mathrm{sand}} = 0.62\rho_{\mathrm{grains}}$, and has units of length^2/time. We then define the reduced time t_{w} as

$$t_{\mathrm{w}} = \frac{T_{\mathrm{w}}}{T_{\mathrm{m}}}. \tag{6.6}$$

The different dune shapes obtained in calculations are shown in fig. 6.12 as function of θ_{w} and $\ln t_{\mathrm{w}}$. We see that when T_{w} is similar to T_{m}, i.e. $\ln t_{\mathrm{w}} \approx 0$, then a barchan dune is obtained. Furthermore, we see that a variety of dune shapes appear from a bimodal wind regime in which $T_{\mathrm{w}} < T_{\mathrm{m}}$, which leads to negative values of $\ln t_{\mathrm{w}}$. In a general fashion, the dunes obtained are oriented transverse to the resultant wind direction if θ_{w} is smaller than 90° (Rubin and Hunter 1987), while longitudinal bedforms appear for higher angles. For increasing values of $\theta_{\mathrm{w}} \longrightarrow 180^\circ$, "reversing" dune shapes appear, which are not studied in the present work.

Bimodal sand dunes on Mars

Because linear dunes like the ones found on Earth were almost not observed in the first images of Mars taken by Mariner 9 and Viking orbiters, it has been suggested that non-unimodal wind regimes should be very rare on Mars (Lee and Thomas 1995). However, on bedrock and in areas of low sand availability, there appear Martian dunes of a high diversity of shapes, where barchans and domes oriented transversely to the prevailing wind should occur in an uni-directional wind regime. Some of such dune types, which are up to now unexplained, are shown in fig. 6.9.

Here we calculate the dune shapes which appear in fig. 6.9 using a bimodal wind regime. In both directions the wind strength is the same, namely $u_* = 3.0$ m/s as found from calculations of Martian barchans in Chapter 3. In this manner, the value of $u_*/u_{*\mathrm{t}}$ is particular to each field, since $u_{*\mathrm{t}}$ depends on the field location (Table 6.1). The initial condition is a Gaussian hill as before, whose volume is taken according to the volume of the dune.

The calculations of the Martian dune shapes in the images of fig. 6.9 are shown in fig. 6.13. We find that the different forms are determined by the angle θ_{w} between the wind directions. All dune shapes have been achieved with a time T_{w} in the range of 1 to 5 days. The dune shape in fig. 6.13a′ has been obtained with $\theta_{\mathrm{w}} = 100^\circ$ and with $T_{\mathrm{w}} = 250000$ s ≈ 2.9 days, while $\theta_{\mathrm{w}} = 140^\circ$ and $T_{\mathrm{w}} = 500000$ s ≈ 5.8 days has been used to calculate the dune in b′.

Moreover, we found that the structure observed in the dune field of fig. 6.9c can be obtained by a change in the local wind regime. The dune shape in fig. 6.13c′ has been

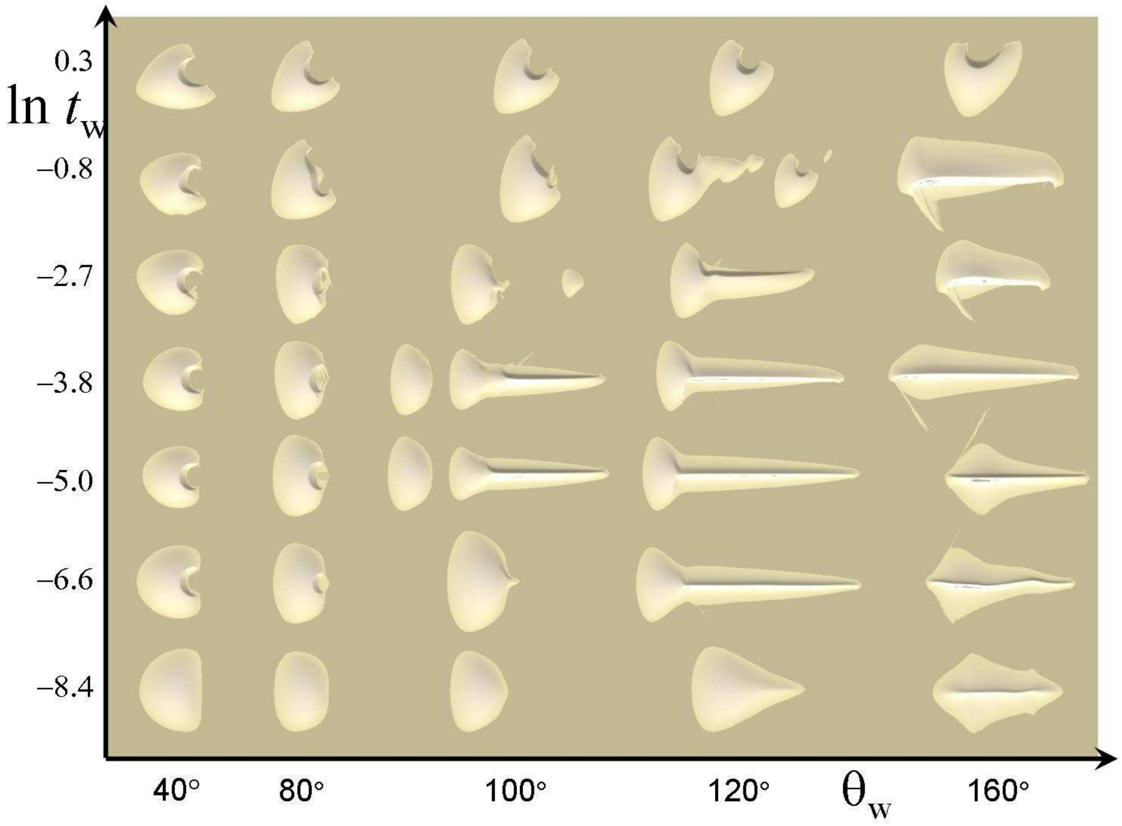

Figure 6.12: Sand dunes formed by a wind of oscillating direction. In the diagram we see different calculations of dunes obtained with different values of θ_w and $t_\mathrm{w} \equiv T_\mathrm{w}/T_\mathrm{m}$, where T_m is the characteristic time of the dune. Each shape shown in the diagram corresponds to one single snapshot of calculation with one particular pair of $\{\theta_\mathrm{w}, t_\mathrm{w}\}$.

obtained in the following manner: (i) first, an elongated dune form as the one in fig. 6.13b′ is formed with an angle $\theta_\mathrm{w} = 120°$ and with $T_\mathrm{w} = 60000$ s ≈ 0.7 day; (ii) next, the angle θ_w has been suddenly reduced to $80°$, which is below the critical angle for the appearance of longitudinal bedforms (Rubin and Hunter 1987). Thereafter, the linear dune becomes unstable and decays into a string of rounded barchans as seen in fig. 6.13c.

It is interesting to notice that our calculations provide a different explanation for the formation of the Martian dune field in fig. 6.9c than that proposed by Bourke (2006). We found that the field in fig. 6.9c consists of linear dunes which are decaying into barchans, while Bourke (2006) suggested an alternative view: the small barchans would merge to form the linear dunes.

The results of fig. 6.13 provide evidence for bimodal wind regimes on Mars. We find that a variety of Martian dune forms which appear in craters and which develop on bedrock have been formed by a wind whose direction alternates between two main orientations. We conclude that if more sand were available in those places, longitudinal dunes would in fact appear as observed in terrestrial sand seas. However, we remark that the wind strength $u_* = 3.0$ m/s used in our calculations must be interpreted as a representative

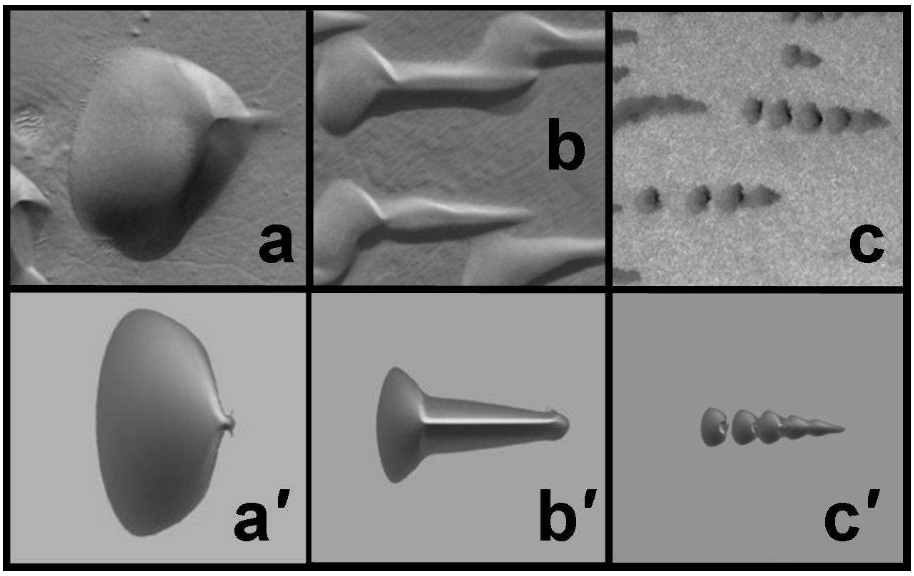

Figure 6.13: **a.**, **b.** and **c.** show dunes from fields in figs. 6.9a, 6.9b and 6.9c, respectively. Cross section of each image is 1090 m. **a′.**, **b′.** and **c′.** show dunes calculated with bimodal winds. In **a**′ we see one dune obtained with $\theta_{\rm w} = 100°$ and $T_{\rm w} = 2.5 \times 10^5$ s; pressure is $P = 5.5$ mb and temperature $T = 175$ K as near to the Wirtz Crater on Mars. Dune in **b′.** has been obtained with $\theta_{\rm w} = 140°$ and $T_{\rm w} = 5.0 \times 10^5$ s and using $P = 5.0$ mb and $T = 185$ K. And dune in **c′.** has been obtained using $P = 8.5$ mb and $T = 150$ K, and with a complex wind regime: First, elongated dunes as in **b**′, with $\theta_{\rm w} = 120°$ and $T = 6.0 \times 10^4$ s are obtained. Next, an angle $\theta_{\rm w} = 80°$ is set and the pattern in fig. **c**′ is obtained.

Field	location	$\rho_{\rm fluid}$ (kg/m^3)	$u_{*{\rm t}}$ (m/s)	$q_{\rm s}$ (kg/m·s)
fig. 6.13a	48.6°S, 25.5°W	0.017	1.89	0.19
fig. 6.13b	49.6°S, 352.9°W	0.014	2.06	0.15
fig. 6.13c	76.4°N, 272.9°W	0.03	1.35	0.24

Table 6.1: For each dune field in fig. 6.13, the fluid density $\rho_{\rm fluid}$ and the threshold $u_{*{\rm t}}$ is calculated from the local pressure and temperature which are taken from the MGS Radio Science data (MGSRS 2006). In spite of the broad range of $u_{*{\rm t}}$, all dune forms in fig. 6.13 have been obtained with one single value of $u_* = 3.0$ m/s.

wind strength which is above the threshold for saltation and is responsible for the average behaviour of the bedform. As commented before, such values of wind shear velocity represent the highest peaks of aeolian activity on Mars, and have been observed only during gusts of dust storms (Moore 1985). In fact, as observed by the landers, average winds on Mars are normally very modest, with u_* between 0.4 and 0.6 m/s (Sutton et al. 1978). In this manner, we expect the Martian fraction $f_{\rm w} = T_{\rm w}/T_{\rm real}$ to be indeed much lower than the Earth's, and $T_{\rm real}$ as large as for Martian wind regimes to be classified as unimodal (Lee and Thomas 1995).

On the other hand, the largest peak of wind activity on the Viking 1 landing site, which was capable to mobilize particles and form ripples on the ground, lasted only a few seconds. The gust of wind activity occurred just after nearly 2000 days since the arrival of the lander (Chapter 2). Let's assume that winds above the threshold on Mars occur generally during $\Delta t_{\mathrm{saltation}} = 40$ s at intervals of 5 years (2000 days or $1.728 \cdot 10^8$ s). A characteristic time $T_{\mathrm{w}} \approx 1 - 5$ days means $T_{\mathrm{w}} = 86,400 - 432,000$ seconds. Further, dividing T_{w} by $\Delta t_{\mathrm{saltation}} = 40$s, the characteristic time corresponds to $2,160 - 10,800$ gusts of saltation transport. In other words, the Martian real time T_{real} is

$$T_{\mathrm{real}} = \frac{T_{\mathrm{w}}}{\Delta t_{\mathrm{saltation}}} \times 5.0 \;\text{ years} \approx 10,800 - 54,000 \;\text{ years}. \tag{6.7}$$

Therefore, the real time of oscillation of the wind direction on Mars found from our calculations is of the order of 10^4 years.

Linear dune from a barchan horn

One classical picture of the formation of seif dunes is that of a *barchan* dune which gets one of its wings extended further and further due to changes in wind direction (Lancaster 1980; Tsoar 1984), as shown in fig. 6.14. In this case, one of the directions of the bimodal wind is the *primary* direction, i.e. the one which formed the barchan. The wind lasts at this direction for a time T_{w1}. The *secondary* wind direction makes an angle θ_{w} with the primary wind, and its characteristic time is T_{w2}.

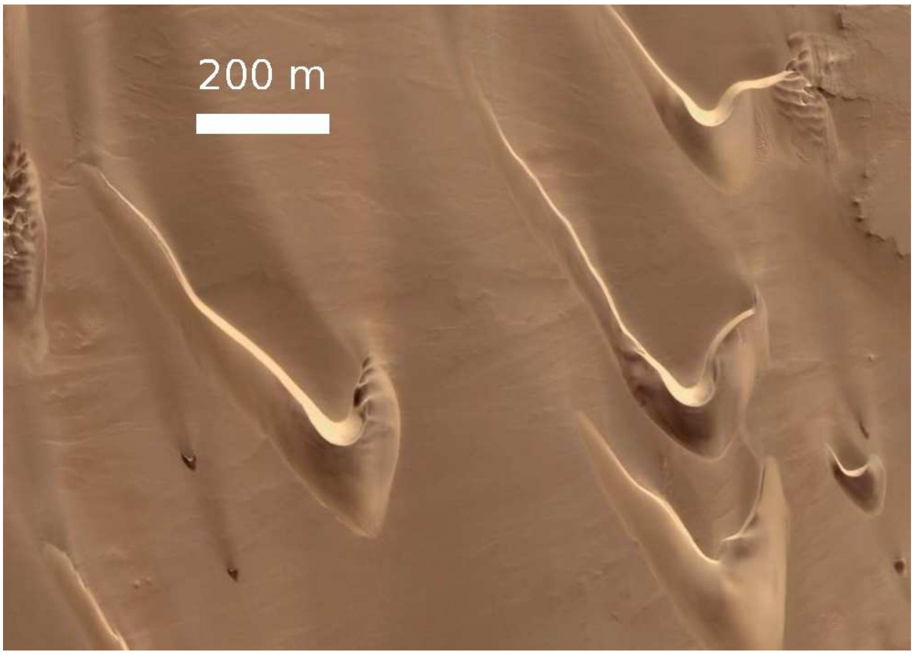

Figure 6.14: Linear dunes appearing from one of the horns of barchans in Namibia, near $18.46°$S, $12.25°$E.

The evolution of a barchan dune under a bimodal wind regime as described above has been calculated using the dune model (Parteli et al. 2006d). The white arrows in fig.

6.15 just above the dunes indicate the primary and secondary wind components, and the resultant wind direction is represented by the blue arrow in each case. In the calculations, the bimodal wind defines an angle $\theta_{\mathrm{w}} = 120^{\circ}$. Each dune shape displayed in fig. 6.15 corresponds to one snapshot of the calculation using a particular value of the ratio $r = T_{\mathrm{w2}}/T_{\mathrm{w1}}$.

We find that the evolution of the dune depends on the ratio between the transport rates of the wind directions. The barchan horn elongates into the resultant direction only if the wind lasts at the secondary direction for more than 25% of the primary direction, i.e. if $T_{\mathrm{w2}}/T_{\mathrm{w1}} \geq 0.25$. Further, if this ratio increases, the velocity of the elongation also increases (Parteli et al. 2006d). Moreover, we find that for $r = 1.0$ or $T_{\mathrm{w2}} = T_{\mathrm{w1}}$, dune shapes as those in fig. 6.12 are obtained, depending on T_{w} and θ_{w}.

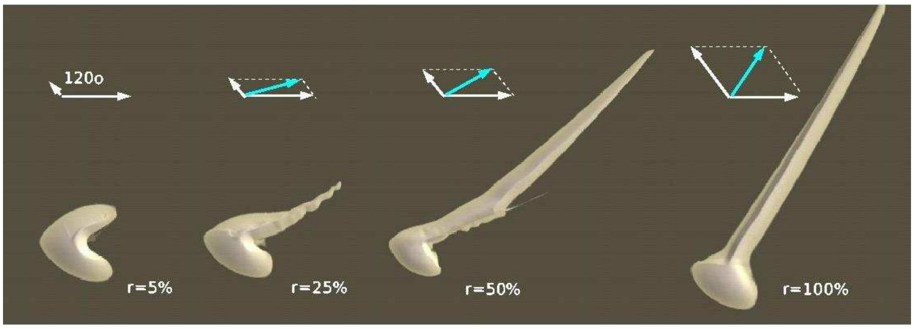

Figure 6.15: Dune shape as function of $r = T_{\mathrm{w2}}/T_{\mathrm{w1}}$, the ratio between the times of the wind directions. The shapes shown for $r \leq 25\%$ are *stationary* shapes, whereas for $r \geq 25\%$, the elongated dune horn increases further and further. The case $r = 100\%$ corresponds to $t_{\mathrm{w}} = 0.078$ ($\ln t_{\mathrm{w}} = -2.5$ in diagram of fig. 6.12). Calculations by O. Durán (Parteli et al. 2006d).

It is interesting that barchans with an elongated horn appear only in very few Martian fields, which is in contrast to the abundance of such dune forms on Earth. Bimodal sand dunes appear often on Mars, but their shapes are rather similar to the ones in fig. 6.12. The typical ratio of the transport rates, $T_{\mathrm{w2}}/T_{\mathrm{w1}}$, of bimodal winds on Mars must be, therefore, close to unity. In other words, secondary wind directions must be rare on Mars.

6.3 Conclusion

In conclusion, we found that bimodal winds form longitudinal dunes *if* the angle between the wind directions is above a critical value θ_{c}, which is around 90°. This value is essentially the same as found from experiments with linear ripples (Rubin and Hunter 1987) and subaqueous dunes (Rubin and Ikeda 1990). Furthermore, this finding is independent of the initial conditions used in calculations: a Gaussian hill; a linear sand ridge; and a flat, dense sand bed.

Moreover, we found that the shape of the linear dune depends on the characteristic time $T_{\rm w}$ of the wind directions. Linear dunes display enhanced “sinuosity” the larger the value of $T_{\rm w}$. This explains the appearance of bedforms such as those in figs. 6.2a and 6.3a, where we see that each linear dune has slip face at only one of its sides.

We have calculated the shape of sand dunes appearing on bedrock under the influence of bimodal wind regimes. In this case, barchan dunes would appear under unidirectional wind. Our calculations revealed that a diversity of dune shapes develop depending on the angle between the wind directions, $\theta_{\rm w}$, and on the characteristic time of the wind, $T_{\rm w}$. We then introduced the normalized time $t_{\rm w} = T_{\rm w}/T_{\rm m}$, where $T_{\rm m}$ is the migration time of the barchan dune that appears for $\theta_{\rm w} = 0$, and presented our results in fig. 6.12.

We have also studied a different kind of bimodal wind regime: a secondary wind, with lower transport rate, i.e. lower characteristic time, elongates the horn of a barchan dune formed by the primary wind direction (Parteli et al. 2006d). However, the seif dune forms only if the secondary wind lasts for a time of the order of 25% of the primary wind (fig. 6.15).

Finally, we calculated the shape of bimodal dunes on Mars, and found that winds on Mars have characteristic time $T_{\rm w}$ of the order of $1-5$ days. This means, however, $T_{\rm real}$ of the order of 10^4 years, if we consider that saltation transport occurs during some tens of seconds every 5 years (Arvidson et al. 1983).

It is indeed remarkable that the most important result of our study, the minimal angle $\theta_{\rm c} \approx 90^{\circ}$, is essentially the same obtained from experiments with ripples and subaqueous dunes. Moreover, it is surprising that this estimate did not change in spite of the important difference in the procedure to generate the bimodal wind: in both Rubin and Hunter (1987) and Rubin and Ikeda (1990), the rotation of the field was performed in a gradual manner, where the time necessary to change from one direction to the other took up to $1/5$ of $T_{\rm w}$. This means that the modellization using instantaneous changes in wind directions as performed here can be effectively applied to simulate wind regimes of real dune fields on Earth and on Mars. Indeed, we could not find a significant dependence of our results on the wind strength u_* and on the influx $q_{\rm in}/q_{\rm s}$. Future work is required to see whether the critical angle $\theta_{\rm c}$ could vary in an important way depending on these variables.

Chapter 7

Conclusions

In this Thesis, we have used the dune model introduced by Sauermann et al. (2001) and Kroy et al. (2002), and later improved by Schwämmle and Herrmann (2004), to calculate sand transport and formation of dunes on Mars, and to study the shape of dunes as function of wind regimes on Mars and on Earth. We can summarize our results in the following manner.

(I) First, we began studying the simplest dune shape: the *barchan dune*, which appears under unidirectional wind and when there is not enough sand to cover the ground (Bagnold 1941). Barchan dunes are the best known dunes, and the shape of terrestrial barchans has been successfully reproduced with the model (Sauermann et al. 2003). Indeed, the shape of barchan dunes (its length to width to height relations) is determined by two quantities of the field: the wind velocity and the flux between dunes (Bourke et al. 2004). In the present work, we studied, for the first time, how the wind speed and the inter-dune sand flux influence the shape of a barchan dune (Parteli et al. 2006b). We have found that the elongated barchan shape (which is typical of intra-crater barchans on Mars) appears for low values of relative wind velocity $u_{*}/u_{*{\mathrm{t}}}$, and that the dune becomes "fat" with increasing inter-dune flux $q_{\mathrm{in}}/q_{\mathrm{s}}$ (fig. 3.6). Moreover, we found that we can determine both quantities by just studying the smallest dune, or the *minimal dune size* in a given field: the width W_{min} decreases with $u_{*}/u_{*{\mathrm{t}}}$, and the length-to-width ratio $L_{\mathrm{min}}/W_{\mathrm{min}}$ decreases with $q_{\mathrm{in}}/q_{\mathrm{s}}$ (figs. 3.8 and 3.10). This led us to the conclusion that we can discover what is the wind strength and inter-dune flux in an extra-terrestrial dune field by studying the minimal dune.

We then applied the minimal dune method to investigate the conditions of wind and flux in the dune field of the Arkhangelsky crater on Mars (Parteli et al. 2006a; Parteli et al. 2006b). Quantities controlling saltation on Mars were calculated in chapter 2. The only unknown quantity we needed to solve the sand transport equations was γ (eq. (1.35)), since the Martian entrainment rate of grains into saltation, $\tilde{\gamma}$ (eq. (1.11)), could not be estimated. We then set first $\gamma = 0.2$ as found for saltation on Earth (Sauermann et al. 2001).

However, when calculating dunes in the Arkhangelsky crater on Mars with $\gamma = 0.2$, we obtained a surprising result: no Martian dune was obtained in calculations for any value of wind velocity u_* between $u_{*\mathrm{t}} \approx 2.0$ m/s and the maximum value 4.0 m/s (Moore 1985; Sullivan et al. 2005). Only with $\gamma \approx 2.0$, i.e. nearly ten times higher than on Earth, and with low values of u_*, could dunes similar to the Arkhangelsky barchans be obtained (fig. 3.11). Therefore, we proposed one equation for γ (eq. (3.3)) which can be adapted to Mars and used this equation in our calculations. Finally, from the minimal dune size in the Arkhangelsky crater on Mars we found that the wind friction speed that formed dunes on Mars was 3.0 ± 0.1 m/s (figs. 3.12 and 3.13). Using this shear velocity, we found that barchans with different shapes in other regions on Mars can be reproduced as well. We also obtained the migration velocity of barchan dunes on Mars moving under a wind of constant strength $u_* = 3.0$ m/s (fig. 3.17).

(II) We proceeded in chapter 4 studying dunes that appear under unidirectional winds, but when the sand availability increases. Under such conditions, *transverse dunes* are formed, whose shape is nearly invariant in the direction perpendicular to the wind flow (figs. 1.3b and 1.6b). We presented field measurements of the shape of transverse dunes in the Lençóis Maranhenses, northeastern Brazil (fig. 4.5), and of the inter-dune spacing of transverse dunes (Parteli et al. 2006c). Then, we calculated transverse dunes using the dune model in two dimensions, and compared the results with the measured dunes.

We found two important results from our field measurements: the first result is that the shape of transverse dunes in a field is nearly independent of its height. This is in contrast with the case of barchan dunes. The crest of barchan dunes becomes closer to the brink the higher the dune (Sauermann et al. 2000), while the measured transverse dunes present a variable brink position though they have nearly all the same height (figs. 4.6 and 4.8). The second result of our field observations is that the sharp crested dunes have the largest values of inter-dune spacing, while “rounded” dunes are more closely spaced (figs. 4.6 and 4.11). This is because at the lee of the dune, there is an area of zero net flow downwind, which we call separation bubble (fig. 1.8). The separation bubble is longer for sharp crested or “triangular” dunes, and is nearly non-existent for the roundest dunes (fig. 4.12). This is in fact accounted for by the separation streamline formula of the model (eq. 1.37) (Kroy et al. 2002). However, the separation bubble $s(x)$ yields values of inter-dune spacing around $6-8$ times the dune height h (Schwämmle and Herrmann 2004), which are larger than the typical values $1.5-4h$ found in the transverse dune field (fig. 4.8). In this manner, we proposed a modified expression for the separation bubble (eq. (4.3)), which simple reduces the length of the separation bubble still maintaining its curvature at the brink. With the modified separation bubble, we calculated transverse dune fields obtaining values of inter-dune spacing similar to the ones measured in the field (fig. 4.14).

We note that the separation bubble proposed is phenomenological, and is based on our field measurements. The important feature of expression (4.3) is the shorter length of the separation streamline at the lee of the two-dimensional dunes. In fact, the complex recirculating nature of the flow at the lee of real dunes is the main factor determining the inter-dune distance, but we may also mention lateral transport (which has been neglected in the two dimensional calculations), vegetation growth and the influence of inter-dune lagoons. The separation bubble is modeled in an heuristic manner, both in its original (eq. (1.37)) and modified (eq. (4.3)) forms. In this thesis, we have seen that the accurate modelling of the separation bubble may be extremely important to calculate the evolution of dune fields, and to extend the model to study transverse dunes on Mars.

(III) In chapter 5 we have studied the formation of dune fields. We introduced a simple model for a transverse dune field (Parteli and Herrmann 2003), which is characterized by the distances between the dunes and their heights, and which is governed by three phenomenological equations (eqs. (5.1), (5.2) and (5.3)). First, we investigated the evolution of the dune field starting with different initial conditions (fig. 5.1) and a constant influx at the inlet. We found that, after a transient time, all dunes reach the same height, independently of the initial configuration (fig. 5.2) and of the fact that dunes may coalesce during their propagation in the field (fig. 5.3). We also found that, due to coalescence between dunes, the number of dunes in the field decays logarithmically with time (fig. 5.5), as found by Schwämmle and Herrmann (2004) from calculations of transverse dune fields with the complex dune model.

Although the simple model of Section 5.1 reproduced the observation that transverse dunes in a field have all approximately the same height, the calculations led to values of inter-dune spacing that are not observed in reality. We then adapted the model (Section 5.2) to account for the dune width, and to include new ingredients into the calculations (Lee et al. 2005), which are schematically shown in fig. 5.8 : (i) we considered the aspect ratio (length H over width L) of the dunes to be around $1/10$ as found from measurements in the Lençóis Maranhenses (fig. 4.8); (ii) we introduced the separation bubble at the dune lee having length $2.5\,H$ measured from the foot of the dune at the lee, as observed in the Lençóis Maranhenses (fig. 4.11); and (iii) we defined coalescence between dunes using eqs. (5.6) and (5.7) found from simulations of three-dimensional dunes interacting in a field (Durán et al. 2005). With these new phenomenological ingredients, and introducing small dunes at the beginning of the field, a surprising and unrealistic result was obtained when the dunes evolved on bedrock: the smallest, fastest dunes wandered to the end of the field, at the beginning of which very large dunes were observed (fig. 5.9). However, if dunes evolve on a sand sheet — as the ones measured in the Lençóis Maranhenses — then there appears sand between dunes, and the saturation length must be included in the calculations. Erosion of the sand bed begins just after the separation bubble, and after typically 2 m, the flux reaches saturation. Then, the foot of the downwind dune cannot be eroded anymore: this dune gets “trapped”. Taking the saturation length into account, dunes were obtained with regular spacing and height (fig. 5.10), and the inter-dune spacing was found to evolve nearly logarithmically in time (fig. 5.13) as also found by Werner and Kocurek (1999) using a more complex bidimensional model. Finally, we observed that the usual pattern of small dunes at the origin of the field increasing in height and reaching saturation values of height and interdune spacing can be reproduced by the simple model if we consider a strong influx of sand at the inlet of the field (figs. 5.14 and 5.15).

In Section 5.3, we calculated the formation of coastal dune fields using the complex model. Starting three-dimensional calculations with a sandy beach and an unidirectional wind of constant strength, we could observe the formation of patterns found in coastal landscapes: small barchans appear from the beach, wander onto the continent and merge to form barchanoids and huge transverse dunes a few kilometers downwind. The most important ingredient is the sand influx $q_{\rm in}$, which must be set equal to the saturated flux $q_{\rm s}$ at the inlet. In this manner, dunes steadily appear. We found that the maximum height of a coastal dune field increases linearly with time (fig. 5.17), whereas the height of the field increases faster the higher the value of $u_*/u_{*\mathrm{t}}$.

(IV) In chapter 6, we have studied the formation of dunes under bimodal winds. The dunes that emerge when there are two prevailing wind directions are called *longitudinal, linear* or *seif dunes*, which elongate in the direction of the resultant flow. From our calculations, we found that if the angle is below $\theta_{\mathrm{w}} \approx 90^{\circ}$, then linear dunes do not appear. For values of θ_{w} between 90° and 120°, linear dunes can be formed, which indeed appear unstable and may occur together with barchanoidal forms. For θ_{w} around 120° or larger, linear dunes appear, which become "reversal" dunes for $\theta_{\mathrm{w}} \rightarrow 180^{\circ}$. It is interesting that similar results had been found previously in experiments with ripples (Rubin and Hunter 1987) and subaqueous dunes (Rubin and Ikeda 1990), while in the present work we studied, for the first time, the case of aeolian dunes, using the dune model (Parteli et al. 2006d).

We found that the shape of linear dunes depends on the *characteristic time* T_{w} of the bimodal wind regime. This is the time the wind lasts at each of its directions. If this time is too large, then the dunes transform into a transverse (if they are formed from a dense sand bed) or barchan dune (if they develop on bedrock) whose orientation oscillates between the two directions. For example, a barchan of oscillating direction is obtained if T_{w} is equal to its *turnover time* (eq. (6.5)): the time the barchan needs to cover a distance equal to its length or width. For smaller values of T_{w}, several dune shapes, from rounded barchans and domes to elongated and reversal dunes appear, depending on θ_{w} (fig. 6.12). We also found that the "sinuous" shape of linear dunes that develop on a sand bed is function of T_{w}, the sinuosity decreasing with T_{w} (fig. 6.8).

It is important to notice that T_{w} means the characteristic time of a wind of constant strength $u_* > u_{*\mathrm{t}}$. Since the wind strength is, however, a large fraction of time below the threshold for saltation, the *real* time T_{real} of the oscillation is equal to several times T_{w}. Equivalently, $T_{\mathrm{w}} = f_{\mathrm{w}} T_{\mathrm{real}}$, with $0 < f_{\mathrm{w}} < 1$. Therefore, the dune model can be used to infer about the time sand-moving winds occur in a given linear dune field. In this way, we have obtained that bimodal winds of strength 3.0 m/s have formed different dune shapes on Mars with T_{w} of the order of 1 to 5 days (figs. 6.9 and 6.13).

Dune formation on Mars

In conclusion, we have calculated, using the dune model, the quantities governing saltation on Mars, and the formation and propagation of sand dunes under the present Martian atmospheric conditions.

Many authors have doubt that the coarse grains of diameter $d = 500\ \mu$m that form Martian sand dunes could be transported by winds of the present Mars. First, the wind friction speed u_* is most of the time around 0.5 m/s (Sutton et al. 1978), while the threshold for saltation is 2.0 m/s (Pollack et al. 1976; Greeley et al. 1980; Iversen and White 1982). This threshold is exceeded only seldom, during extreme dust storms that occur in intervals of several years, and even though saltation lasts a few seconds (Arvidson et al. 1983). Moreover, under the present atmospheric conditions of Mars, only barchans of width larger than 2 km were expected to appear, as mentioned in the first pages of this Thesis. The reason is that the minimal dune width is proportional to the length of flux saturation, which itself scales with the quantity $\ell_{\rm drag} = d\rho_{\rm grain}/\rho_{\rm fluid}$. In this manner, for Martian dunes to have the observed size, they must have been formed by an ancient, denser atmosphere (Breed et al. 1979), on the basis of the scaling with $\ell_{\rm drag}$.

In the present work, we have found the missing link to understand the formation of dunes by the present atmosphere of Mars: the larger splash of the Martian saltation. On one hand, saltating grains on Mars travel much longer than on Earth (White et al. 1976; White 1979), which increases the distance of flux saturation (fig. 1.2). In fact, the mean saltation length ℓ (eq. (1.17)) increases with $\ell_{\rm drag}$, since v^2/g scales with $u_{*{\rm t}}^2/g \sim d\rho_{\rm grain}/\rho_{\rm fluid}$. Indeed, saltating grains on Mars also travel with a velocity 10 times higher than on Earth (White 1979). As a consequence, they impact onto the sand bed with 10 times higher momentum than do their Earth's counterparts, and eject thus a much larger amount of grains. As Marshall and Stratton (1999) wrote: "*On Earth, only a few grains are splashed by impact. On Mars, it may be hundreds*". But as we can conclude from fig. 1.2, the more grains enter saltation after splash, the *faster* the flux saturates, i.e. the shorter will be the saturation length. In the model, the entrainment rate of grains into saltation is given by the quantity $\tilde{\gamma}$ (eq. (1.11)), which enters the expression of the saturation length, $\ell_{\rm s}$ (eq. (1.33)). The equation found for the entrainment rate (eq. (3.3)) predicts that the entrainment rate on Mars is 10 times higher than on Earth. Summarizing, Martian saltating particles travel ten times faster than Earth grains; this results in a much more intense splash and a ten times higher entrainment rate. Thus, the saturation length, as well as the minimal dune size, is reduced by a factor of 10, which resolves the previously reported (Kroy et al. 2005) failure of the scaling $W_{\rm min} \propto \ell$.

In this manner, we found that Martian dunes could have been formed by the present atmospheric conditions of Mars. Our calculations provide the first evidence that winds reaching a velocity $u_* = 3.0 \pm 0.1$ m/s, which are typical during the largest dust storms on Mars, may have formed the observed Martian dunes. Indeed, while this means that Martian dunes must not be "inactive", the timescales of the formation and evolution of dunes on Mars are immeasurable larger than that on Earth. On one hand, barchan dunes on Mars would move 10 times faster than on Earth if sand-moving winds would occur with the same frequency on both planets (chapter 3). But since $u_* \approx 3.0$ m/s is only achieved probably during 40 seconds each 5 years (Arvidson et al. 1983), a barchan of length 200 m is expected to move at a negligible rate of 1 m in $4,000$ years. This explains why orbiters never detect movement of barchans on Mars.

The calculations of exotic dune forms occurring on bedrock (figs. 6.9 and 6.13) provided evidence for bimodal wind regimes on Mars. We found that the characteristic time of the change in wind direction, $T_{\rm w}$, is of the order of $1 - 5$ days (Parteli and Herrmann 2006). This appears surprising since wind regimes on Mars were in fact expected to be narrow unimodal (Edgett and Blumberg 1994; Lee and Thomas 1995). Again, our results must be interpreted on the basis of the *real* time $T_{\rm real}$, which is several times larger since u_* is mostly below $u_{*{\rm t}}$. In fact, we obtained that $T_{\rm real}$ must have the timescale of 10^4 years if saltation occurs during some seconds each 5 years (eq. (6.7)).

It is interesting to notice that a significant change in wind direction (by 90° or more) is expected to occur after each extreme of the Martian *orbital* cycle, which is determined by the combined effect of the precession of its axis and the arrival at *perihelion* (the point of closest distance to the sun) (Arvidson et al. 1979; Thomas 1982; Lee and Thomas 1995; Fernández 1998; Malin et al. 1998; Thomas et al. 1999). Because of precession of its axis, each pole of Mars appears tilted to the sun in a cycle of $51,000$ years. Now the latitude which "looks" toward the sun at perihelion is $15°$S, but this "subsolar latitude at perihelion" (SLP) migrates $\pm 25°$ about the Equator over a 51kYr time span (Arvidson et al. 1979). This orbital cycle is the most important one for the climate of Mars, the hemisphere of the SLP having short, hot summers, and being the one of the major dust storms activity. In $25,500$ years, it is the northern hemisphere that will be tilted to the sun. "*The large amounts of fine dust currently deposited in the northern hemisphere in regions such as Tharsis, Arabia, and Elysium will be redistributed to the southern hemisphere*" (Sheehan 1996). This half cycle of $25,500$ years is in fact well within the range of characteristic time $10,800 < T_{\rm real} < 54,000$ years of bimodal winds found from our calculations of sand dunes on Mars.

Outlook

The discovery that the entrainment rate of saltating grains on Mars is 10 times higher than on Earth has been crucial for the calculations of Martian dunes. We saw in Chapter 3 that no dune would appear on Mars if it wasn't the pronounced erosion rate due to the large Martian splash events. It would be interesting to make a full microscopic simulation for the saltation mechanism of Mars similar to the one that was recently performed by Almeida et al. (2006) to confirm our findings microscopically.

We can now apply the dune model to address several questions that are of interest for geomorphologists and planetary scientists investigating the geology of Mars. For example, what is the origin of Martian dunes? Where does their sand come from? It is very plausible that the basaltic grains of Martian dunes have a volcanic origin (Edgett 1997). On the other hand, Martian dunes never appear associated with an obvious source (Thomas et al. 1999). This is in contrast, for instance, with the case of terrestrial coastal dunes, which appear from the sand deposited on the beach (e.g. fig. 1a).

On Mars, dune fields constitute mainly sand deposits trapped in the interior of craters. However, MOC images show that the dunes do not migrate into the largest craters, which are normally "protected" by raised rims. On the other hand, it is possible to see dunes wandering to *leave* the crater, as it is the case of the Arkhangelsky dunes. How did the sand, then, accumulated in the crater?

The MOC image in fig. 7.1a was one of the first images of dunes acquired by the Mars Global Surveyor, and shows an intriguing scene: a "pond-like" structure in the interior of a crater near $65°$S, $15°$W. The "pond" consists of a field of dark dunes next to a smooth surface with "islands" within it. The question is: how did this pond form? One explanation is that the impact of the meteorite created cracks on the ground; thereafter, lava came up through these cracks thus ponding on the interior of the crater. Another possible explanation (see http://www.msss.com for more details): *water* ran downslope the crater walls and ponded on the floor; the water dried up, leaving a dark surface of sand. Could water have played a decisive role for the formation of dune fields on Mars? If water has been in fact relevant for the appearance of dunes on Mars, the calculations of intra-crater dunes might be useful to estimate when the latest Martian water ponds dried up. Moreover, there is another possibility for source of dune sand on the north pole of Mars, which could be investigated with simulations. Figure 7.1b shows that the lower units of the north polar cap may be eroded by the wind, and provide the sand (the "Martian beaches"?) for the formation of dune fields.

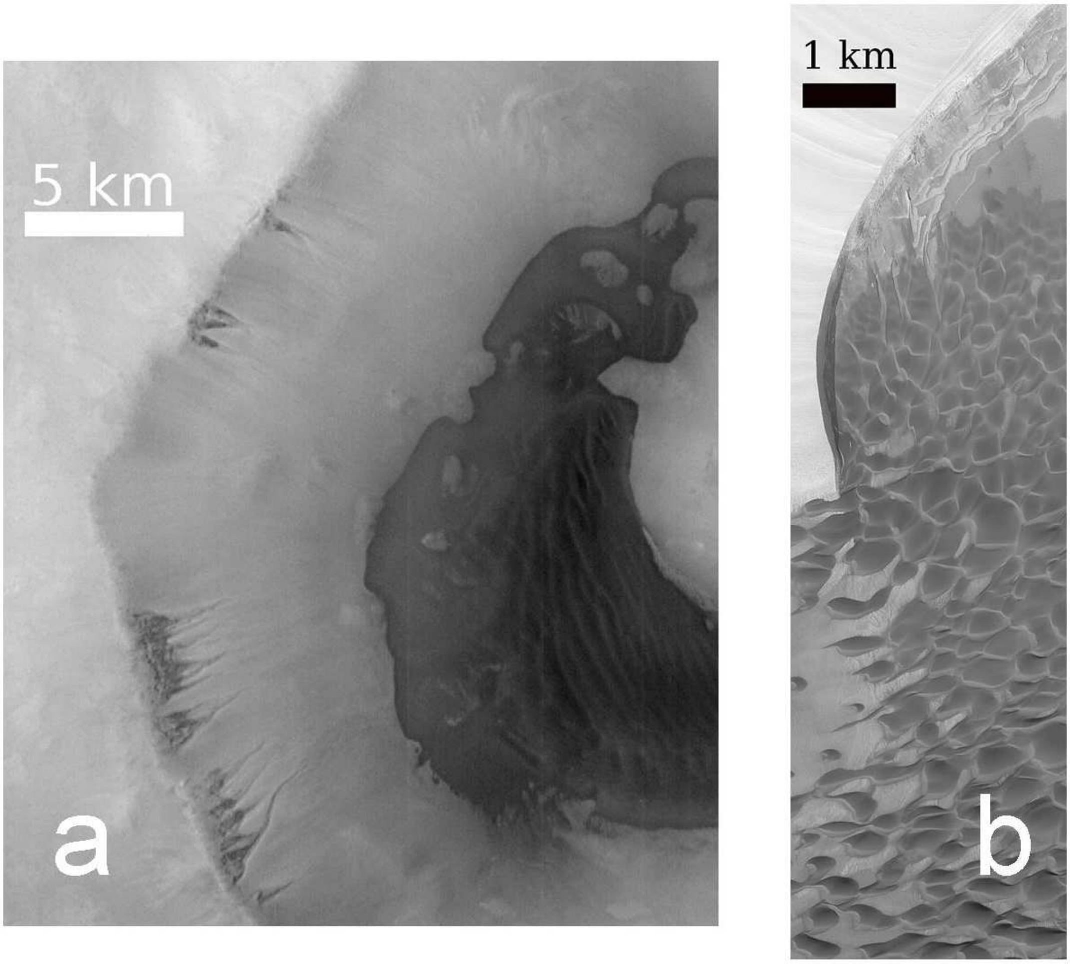

Figure 7.1: **a.** Martian dune fields as remains of intra-crater water ponds? The crater we see in this MOC image has 50 km of diameter, and is located near $65°$S, $15°$W. **b.** The Martian north polar cap is divided into an upper, bright layer, and a lower, dark one. While the upper units contain almost no sand, it is plausible that the lower units serve as sand source for dune fields. In this MOC image, we see the early stages of the formation of a north polar dune field.

In the calculations of dune fields, where dunes appear closely spaced, one important issue that must be addressed in the future is the separation bubble. This part of the modellization of dunes is still unresolved (Chapter 4). We have seen that closely spaced transverse dunes are obtained by reducing the length of the separation bubble. However, CFD calculations (Herrmann et al. 2005) show that the separation streamlines of the dunes may in fact extend up to almost the half length of the dune downwind. It is clear that simply setting the wind and flux as zero at the dune lee must hide important mechanisms of inter-dune sand transport. Therefore, one of the most important upcoming challenges in the calculations of transverse dunes will be the modellization of flow separation at the dune lee. Furthermore, the outlook of the calculations of dune fields is to include realistic ingredients, such as winds of oscillating strength and varying direction, vegetation, topography and inter-dune water pounds to investigate the evolution of coastal landscapes of our planet.

Another aspect that remains to be investigated in the future is the role of electrostatic interactions between grains in the dry Martian atmosphere. Merrison et al. (2004) found from wind tunnel experiments simulating Martian conditions that approximately 90% of dust particles of a few microns of diameter have a net electric charge, and that equal quantities of dust grains are charged positive as are negative. Furthermore, charged dust grains may easily adhere to form larger particles, which have been effectively suggested as a possible origin for saltating grains on Mars (Edgett 1997). As the grain size increases, however, we expect such electrostatic effects to be less noticeable, though we expect some increase in the threshold for saltation. Also the nature of the splash could be affected, and the model parameters α (effective restitution coefficient) and z_{m} (mean saltation height) should be obtained from comparison with wind tunnel saturated flux data that reproduce the dry environment of Mars.

Sand dunes on Earth, Mars, Venus and Titan

Sand dunes have been also found on Venus and on Saturn's moon Titan. Both on Venus (Arvidson et al. 1991; Weitz et al. 1994) and on Titan (Lorenz et al. 2006), only transverse and linear dunes have been detected from radar data, which reveal extraterrestrial dunes of sizes comparable to those on Earth. The transverse dunes at the Venusian *Fortuna-Meshkenet* dune field, centered at $67.^{\circ}$N, 91°E, have width ranging from 200 to 500 m and lengths ranging from 500 m to 10 km (Weitz et al. 1994). On the other hand, the Titanic *Belet* sand sea at 12°S, 100°W is a field of linear dunes that have slopes between 6° and 10° and heights comparable to the dune heights at Namibia sand sea. There have been no detection of barchans or other dune forms, which can be attributed to insufficient resolution of the radar images. Alternatively, it is plausible that granular materials that could be mobilized though saltation would be scarce on Venus (Weitz et al. 1994).

In this Thesis, we have proposed a general equation (eq. (3.3)) to calculate the entrainment rate of grains into saltation under different atmospheric conditions. This equation can be used, together with expressions presented in chapter 1, to calculate other dune forms on Mars, Venus or Titan. Therefore, it would be interesting to test the model equations with the calculation of saltation transport on Venus and Titan.

While granular materials on Venus are apparently of basaltic origin (Garvin et al. 1984), on Titan, the grains of dunes are made probably of hydrocarbons (Lorenz et al. 2006). In both cases, we can estimate the grain diameter d of the dunes assuming that d is about 5 times the critical grain diameter for the transition suspension/saltation (chapter 2). This critical diameter is around $25\ \mu$m on Venus and $60\ \mu$m on Titan, and thus we obtain $d = 125$ and $300\ \mu$m on Venus and on Titan, respectively. Next, the minimal friction speed $u_{*\mathrm{t}}$ can be calculated with eq. (1.46). In fact, wind shear velocities comparable to the threshold have been measured by the Soviet *Venera* landers on Venus (Garvin et al. 1984). The European *Huygens* probe, which landed on Titan, also measured surface wind speeds of the order of the saltation threshold (Tomasko et al. 2005). Therefore, it is effectively possible that saltation and dune formation occurs on the present Venus and Titan.

In Table 7.1, we see the quantities governing saltation on Earth, Mars, Venus and Titan. The mean grain velocity v_{s}, the saturated flux q_{s}, and the saturation length ℓ_{s}, have been calculated assuming a constant $u_*/u_{*\mathrm{t}} = 1.45$, as we found for the Arkhangelsky Crater on Mars (chapter 3). We see that the values of γ on Venus and on Titan are smaller than the Earth's value. This is because of the lower Venusian and Titanic $u_{*\mathrm{t}}$ and v_{s}. Moreover, the sand flux calculated for Venus is 10 times smaller than on Earth. This has been in fact prophesied by White (1981), who performed wind tunnel experiments using atmospheric conditions of Venus: *"(...) Hence, for wind speeds the same percentage above threshold on each planet, (...) approximately 10 times more material would be moved on Earth than on Venus."*. We also see that the lowest values of mean saltation heights are those of Venusian grains, which is a consequence of the extremely larger atmospheric pressure of Venus (93 bar).

Furthermore, in the last row of table 7.1, we give a quick estimation of the minimal size of a barchan dune on Venus and on Titan, assuming $W_{\mathrm{min}} \approx 13\ell_{\mathrm{s}}$ as on Earth and on Mars. Using the equation for the entrainment rate to calculate ℓ_{s}, we see that barchan dunes on Venus (if they existed) could be one order of magnitude smaller, while Titanic barchans should have similar minimal sizes as the Earth's. Again, the minimal size of a barchan dune depends on $u_*/u_{*\mathrm{t}}$ (chapter 3), while the barchan shape depends on the interdune flux, and also on the aerodynamic roughness. The last quantity could not be measured by Venus or Titan missions.

However, in the extension of the calculations to environments of atmospheric density much higher than the Earth's, the caveat must be added that the *aerodynamic entrainment* must play a more important role than the entrainment by grain-bed collisions, the larger the value of ρ_{fluid}. The larger ρ_{fluid}, the lower is the grain velocity, and therefore less momentum is transfered to the bed by impact. We expect in fact splash impacts to be much less effective in ejecting grains on Venus than on Earth or Mars. On the other hand, in the last cases, the aerodynamic entrainment has been essentially neglected, since it is only important to *initiate* saltation (Anderson and Haff 1988; Sauermann 2001). In the dune model, the contribution of the aerodynamic entrainment to the erosion rate Γ is written as (Sauermann 2001)

$$\Gamma_{\mathrm{a}} = \Phi_{\mathrm{a}} \left(\frac{\tau - \tau_{\mathrm{g}}}{\tau_{\mathrm{ft}}} - 1 \right). \tag{7.1}$$

The parameter Φ_{a} substitutes, therefore, the factor $\gamma\tau_{\mathrm{g}}/v_{\mathrm{s}}$ which appears in the case of the entrainment by impact, while for the aerodynamic entrainment rate, the fluid threshold $\tau_{\mathrm{ft}} > \tau_{\mathrm{t}}$ must be considered. If the splash becomes negligible compared to the aerodynamic entrainment, then this must be taken into account in the calculation of the saturation length. In fact, for saltation in water, where $\rho_{\mathrm{fluid}} = 1000$ kg/m^3, fluid entrainment is the mechanism that sustains the saltation transport (Kroy and Guo 2004).

	Earth	Mars	Venus	Titan
Gravity g (m/s^2)	9.81	3.71	8.87	1.35
Atmospheric density ρ_{fluid} (kg/m^3)	1.225	0.014	66.5	5.44
Particle density ρ_{grain} (kg/m^3)	2650	3200	3200	1000
Particle diameter d (mm)	0.25	0.50	0.125	0.30
Threshold friction speed $u_{*\mathrm{t}}$ (m/s)	0.22	2.12	0.022	0.028
Mean saltation height z_{m} (mm)	16.3	1132	0.56	3.7
ℓ_{drag} (m)	0.54	115.4	0.006	0.055
Entrainment rate γ	0.2	2.24	0.03	0.06
v_{s} (m/s)	1.41	17.8	0.17	0.21
q_{s} (kg m^{-1}s^{-1})	0.008	0.146	0.0008	0.0008
ℓ_{s} (m)	0.80	15.43	0.11	0.53
W_{min} (m)	10.4	200.4	1.5	7.0

Table 7.1: Quantities governing saltation on Earth, Mars, Venus and Titan. Quantities for Mars correspond to those at Arkhangelsky crater (chapter 3). Values of particle diameter on Venus and Titan are equal to 5 times the critical diameter for transition suspension/saltation, calculated with the condition $v_{\mathrm{f}}/u_{*\mathrm{ft}} = 1.0$ (Chapter 2). A viscosity of $\eta = 8.5 \times 10^{-6}$ kg/m·s is used for Titan (Lorenz et al. 1995). v_{s}, q_{s} and ℓ_{s} are obtained with $u_*/u_{*\mathrm{t}} = 1.45$, and $W_{\mathrm{min}} = 13\ell_{\mathrm{s}}$.

In summary, the dune model can be now extended to calculate the formation and propagation of sand dunes on other planets. Therefore, the dune model might be in the future a powerful tool in the investigation of the geological history, and of the present climate and wind regimes of any planet or celestial body that has sand on the surface and winds to form dunes.

References

Almeida, M . P., J. S. Andrade Jr., and H. J. Herrmann (2006). Aeolian transport layer. *Physical Review Letters 96*, 018001.

Anderson, R. S. (1987). Eolian sediment transport as a stochastic process: The effects of a fluctuating wind on particle trajectories. *J. Geol. 95*, 497–512.

Anderson, R. S. and P. K. Haff (1988). Simulation of eolian saltation. *Science 241*, 820.

Anderson, R. S. and P. K. Haff (1991). Wind modification and bed response during saltation of sand in air. *Acta Mechanica (Suppl.) 1*, 21–51.

Andreotti, B. (2004). A two-species model of aeolian sand transport. *Journal of Fluid Mechanics 510*, 47–70.

Andreotti, B., P. Claudin, and S. Douady (2002a). Selection of dune shapes and velocities. Part 1: Dynamics of sand, wind and barchans. *The European Physical Journal B 28*, 321–339.

Andreotti, B., P. Claudin, and S. Douady (2002b). Selection of dune shapes and velocities. Part 2: A two-dimensional modelling. *The European Physical Journal B 28*, 341–352.

Arvidson, R. E., E. A. Guinness, and S. Lee (1979). Differential aeolian redistribution rates on Mars. *Nature 278*, 533–535.

Arvidson, R. E., E. A. Guinness, H. J. Moore, J. Tillman, and S. D. Wall (1983). Three Mars Years: Viking Lander 1 Imaging Observations. *Science 222*, 463–468.

Arvidson, R. E., J. L. Gooding, and H. J. Moore (1989). The Martian surface as imaged, sampled, and analyzed by the Viking landers. *Rev. Geophys. 27*, 39–60.

Arvidson, R. E., V. R. Baker, C. Elachi, R. S. Saunders, and J. A. Wood (1991). Magellan: Initial Analysis of Venus Surface Modification. *Science 252*, 270–275.

Arvidson, R. E., et al. (2004). Localization and physical properties experiments conducted by Spirit at Gusev crater. *Science 305*, 821–824.

Ash, J. E. and R. E. Wasson (1983). Vegetation and sand mobility in the Australian desert dunefield. *Z. Geomorph. Suppl. Bd. 45*, 7–25.

Bagnold, R. A. (1941). *The physics of blown sand and desert dunes*. London: Methuen.

Barbosa, L. M. and J. M. L. Dominguez (2004). Coastal dune fields at the São Francisco River strandplain, northeastern Brazil: Morphology and environmental controls. *Earth Surface Processes and Landforms 29*, 443–456.

Besler, H. (1975). Messungen zur Mobilität Dünensanden am Nordrand der Dünen-Namib (Südwestafrika). *Würzburger Geographische Arbeiten 43*, 135–147.

Besler, H. (1997). Eine Wanderdüne als Soliton? *Physikalische Blätter 53*, 983–985.

Bouchaud, J. P., M. E. Cates, J. Ravi Prakash, and S. F. Edwards (1994). Hysteresis and metastability in a continuum sandpile model. *J. Phys. France I 4*, 1383.

Bourke, M. C., M. Balme, and J. Zimbelman (2004). A Comparative Analysis of Barchan Dunes in the Intra-Crater Dune Fields and The North Polar Sand Sea. *Proc. Lunar and Planetary Science Conf. 35*, 1453.

Bourke, M. C. (2006). A New Model for Linear Dune Formation: Merged Barchan Convoys on Mars. *Proc. Lunar and Planetary Science Conf. 37*, 2432.

Breed, C. S., M. J. Grolier, and J. F. McCauley (1979). Morphology and Distribution of Common 'Sand' Dunes on Mars: Comparison With the Earth. *Journal of Geophysical Research 84*, 8183–8204.

Bristow, C. S., S. D. Bailey, and N. Lancaster (2000). The sedimentary structure of linear sand dunes. *Nature 406*, 56–59.

Bullard, J. E., D. S. G. Thomas, I. Livingstone, and G. F. S. Wiggs (1995). Analysis of linear sand dune morphological variability, southwestern Kalahari Desert. *Geomorphology 11*, 189–203.

Butterfield, G. R. (1993). Sand transport response to fluctuating wind velocity. In N. J. Clifford, J. R. French, and J. Hardisty (Eds.), *Turbulence: Perspectives on Flow and Sediment Transport*, Chapter 13, pp. 305–335. John Wiley & Sons Ltd.

Chakraborty, C. (1993). Morphology, internal structure and mechanics of small longitudinal (seif) dunes in an aeolian horizon of the Proterozoic Dhandraul Quartzite, India. *Sedimentology 40*, 79–85.

Chamberlain, T. E., H. L. Cole, R. G. Dutton, G. C. Greene, and J. E. Tillman (1976). Atmospheric measurements on Mars: The Viking meteorology experiment. *Bull. Amer. Meteor. Soc. 57*, 1094–1104.

Chepil, W. S. (1958). The use of evenly spaced hemispheres to evaluate aerodynamic forces on a soil surface. *Trans. Am. Geophys. Union 39*, 397–403.

Claudin, P., and B. Andreotti (2006). A scaling law for aeolian dunes on Mars, Venus, Earth, and for subaqueous ripples. *Earth and Planetary Science Letters 252*, 30–44 (2006).

Counselman III, C. C., S. A. Gourevitch, R. W. King, G. B. Loriot, and R. G. Prinn (1979). Venus Winds Are Zonal and Retrograde Below the Clouds. *Science 205*, 85–87.

Crane Company (1988). Flow of fluids through valves, fittings, and pipe. Technical Paper No. 410 (TP 410). Also http://www.lmnoeng.com/Flow/GasViscosity.htm.

Cutts, J. A., and R. S. U. Smith (1973). Eolian Deposits and Dunes on Mars. *Journal of Geophysical Research 78*, 4139–4154.

Durán, O., V. Schwämmle and H. J. Herrmann (2005). Breeding and solitary wave behaviour of dunes. *Physical Review E 72*, 021308.

Durán, O. and H. J. Herrmann (2006a). Modellization of saturated sand flux. *J. Stat. Mech.*, P07011. doi:$10.1088/1742\text{-}5468/2006/07/P07011$.

Durán, O. and H. J. Herrmann (2006b). Vegetation against dune mobility. *Phys. Rev. Lett. 97*, 188001.

Edgett, K. S. and P. R. Christensen (1991). The Particle Size of Martian Aeolian Dunes. *Journal of Geophysical Research 96*, 22765–22776.

Edgett, K. S. and Dan G. Blumberg (1994). Star and Linear Dunes on Mars. *Icarus 112*, 448–464.

Edgett, K. S., and P. R. Christensen (1994). Mars aeolian sand: Regional variations among dark-hued crater floor features. *Journal of Geophysical Research 99*, 1997–2018.

Edgett, K. S. (1997). Aeolian Dunes as Evidence for Explosive Volcanism in the Tharsis Region of Mars. *Icarus 130*, 96–114.

Elbelrhiti, H., P. Claudin, and B. Andreotti (2005). Field evidence for surface-wave-induced instability of sand dunes. *Nature 437*, 720–723.

Embabi, N. S. and M. M. Ashour (1993). Barchan dunes in Qatar. *Journal of Arid Environments 25*, 49–69.

Fenton, L. K. (2003). Aeolian processes on Mars: atmospheric modeling and GIS analysis. PhD Thesis, California Institute of Technology, Pasadena, California.

Fenton, L. K., J. L. Bandfield, and A. W. Ward (2003). Aeolian processes in Proctor Crater on Mars: Sedimentary history as analysed from multiple data sets. *Journal of Geophysical Research 108*(E12), 5129, doi:10.1029/2002JE002015.

Fernández, W. (1998). Martian Dust Stroms: A Review. *Earth, Moon and Planets 77*, 19–46.

Finkel, H. J. (1959). The barchans of southern Peru. *Journal of Geology 67*, 614–647.

Floriani, D. C., J. C. Fukuda, and E. F. Pinto (2003). Lençóis Maranhenses National Park: The Largest Coastal Dunes Area in South America. In *Gerenciamento Costeiro, Unidades de Conservação*, IBAMA, Barreirinhas/MA, Brazil.

Fluent Inc. (1999). Fluent 5. Finite Volume Solver.

Frank, A. and G. Kocurek. (1996). Toward a model for airflow on the lee side of aeolian dunes. *Sedimentology 43*, 451–458.

Fryberger, S. G. and G. Dean (1979). Dune forms and wind regimes. In E. D. McKee (Ed.), *A Study of Global Sand Seas*, 137–140. United States Geological Survey, Professional Paper 1052.

Fryberger, S. G., A. M. Al-Sari, T. J. Clisham, S. A. R. Rizvi, and K. G. Al-Hinai (1984). Wind sedimentation in the Jafurah sand sea, Saudi Arabia. *Sedimentology 31*, 413–431.

Garvin, J. B., J. W. Head, M. T. Zuber, and P. Helfenstein. Venus: The Nature of the Surface from Venera Panoramas. *Journal of Geophysical Research 89*, 3381–3399.

Golombek, M. P., R. A. Cook, T. Economou, W. M. Folkner, A. F. C. Haldemann, P. H. Kallemeyn, J. M. Knudsen, R. M. Manning, H. J. Moore, T. J. Parker, R. Rieder, J. T. Schofield, P. H. Smith, and R. M. Vaughan (1997). Overview of the Mars Pathfinder Mission and Assessment of Landing Site Predictions. *Science 278,* 1743–1748.

Golombek, M. P., H. J. Moore, A. F. C. Haldemann, T. J. Parker, and J. T. Schofield (1999). Assessment of Mars Pathfinder landing site predictions. *Journal of Geophysical Research 104,* 8585–8594.

Gonçalves, R. A., L. G. O. Lehugeur, J. W. A. Castro, and A. E. S. Pedroto (2003). Classificação das Feições Eólicas dos Lençóis Maranhenses - Maranhão - Brasil (in Portuguese). *Mercator - Revista de Geografia da UFC 03,* 99–112.

Greeley, R., B. White, R. Leach, J. Iversen, and J. Pollack (1976). Mars: Wind Friction Speeds for Particle Movement. *Geophysical Research Letters 3,* 417–420.

Greeley, R., R. Leach, B. R. White, J. D. Iversen, and J. B. Pollack (1980). Threshold windspeeds for sand on Mars: Wind Tunnel Simulations. *Geophysical Research Letters 7,* 121–124.

Greeley, R. and J. D. Iversen (1985). *Wind as a Geological Process: On Earth, Mars, Venus and Titan.* Cambridge: Cambridge Univ. Press.

Greeley, R., R. E. Arvidson, C. Elachi, M. A. Geringer, J. J. Plaut, R. Stephen Saunders, G. Schubert, E. R. Stofan, E. J. P. Thouvenot, S. D. Wall, and C. M. Weitz (1992). Aeolian features on Venus: Preliminary Magellan results. *Journal of Geophysical Research 97*(E8), 13319–13345.

Greeley, R., A. Spypeck, and J. B. Pollack (1993). Martian Aeolian Features and Deposits: Comparisons With General Circulation Model Results. *Journal of Geophysical Research 98,* 3183–3196.

Greeley, R., M. Kraft, R. Sullivan, G. Wilson, N. Bridges, K. Herkenhoff, R. O. Kuzmin, M. Malin, and W. Ward (1999). Aeolian features and processes at the Mars Pathfinder landing site. *Journal of Geophysical Research 104,* 8573–8584.

Greeley, R., M. D. Kraft, R. O. Kuzmin, and N. T. Bridges (2000). Mars Pathfinder landing site: Evidence for a change in wind regime from lander and orbiter data. *Journal of Geophysical Research 105*(E1), 1829–1840.

Greeley, R. *et al.* (2004). Wind-Related Processes Detected by the Spirit Rover at Gusev Crater, Mars. *Science 305,* 810–813.

Haberle, R. M. and B. M. Jakosky (1991). Atmospheric Effects on the Remote Determination of Thermal Inertia on Mars. *Icarus 90,* 187–204.

Haberle, R. M., M. M. Joshi, J. R. Murphy, J. R. Barnes, J. T. Schofield, G. Wilson, M. Lopez-Valverde, J. L. Hollingsworth, A. F. C. Bridger, and J. Schäffer (1999). General circulation model simulations of the Mars Pathfinder atmospheric structure investigation/meteorology data. *Journal of Geophysical Research 104,* 8957-8974.

Hastenrath, S. (1967). The barchans of the Arequipa region, southern Peru. *Zeitschrift für Geomorphologie 11,* 300–331.

Herrmann, H. J., J. S. Andrade Jr., V. Schatz, G. Sauermann, and E. J. R. Parteli (2005). Calculation of the separation streamlines of barchans and transverse dunes. *Physica A 357*, 44–49.

Hersen, P., S. Douady, and B. Andreotti (2002). Relevant Length Scale of Barchan Dunes. *Physical Review Letters 89*, 264301.

Hesp, P., W. Illenberger, I. Rust, A. Mc Lachlan, and R. Hyde (1989a). Some aspects of transgressive dunefield and transverse dune geomorphology and dynamics, south coast, South Africa. *Zeitschrift für Geomorphologie N. F. 73*, 111–123.

Hesp, P., R. Hyde, V. Hesp and Q. Zhengyu (1989b). Longitudinal dunes can move sideways. *Earth Surface Processes and Landforms 14*, 447–451.

Hesp, P. A. and K. Hastings (1998). Width, height and slope relationships and aerodynamic maintenance of barchans. *Geomorphology 22*, 193–204.

Hunt, J. C. R., S. Leibovich, and K. J. Richards (1988). Turbulent wind flow over smooth hills. *Q. J. R. Meteorol. Soc. 114*, 1435–1470.

IBAMA, Instituto Brasileiro do Meio Ambiente e dos Recursos Naturais Renováveis,(2003). Plano de Manejo do Parque Nacional dos Lençóis Maranhenses (in Portuguese).

Illenberger, W. K. and I. C. Rust (1988). A sand budget in the Alexandria coastal dunefield, South Africa. *Sedimentology 35*, 513–521.

Iversen, J. D., J. B. Pollack, R. Greeley, and B. R. White (1976). Saltation Threshold on Mars: The Effect of Interparticle Force, Surface Roughness, and Low Atmospheric Density. *Icarus 29*, 381-393.

Iversen, J. D. and B. R. White (1982). Saltation threshold on Earth, Mars and Venus. *Sedimentology 29*, 111-119.

Iversen, J. D. and K. R. Rasmussen (1999). The effect of wind speed and bed slope on sand transport. *Sedimentology 46*, 723–731.

Jimenez, J. A., L. P. Maia, J. Serra, and J. Morais (1999). Aeolian dune migration along the Ceará coast, north-eastern Brazil. *Sedimentology 46*, 689–701.

Jiménez, J. A. and O. A. Madsen (2003). A Simple Formula to Estimate Settling Velocity of Natural Sediments. *Journal of Waterway, Port, Coastal and Ocean Engineering March/April*, 70–78.

Kerr, R. C., and J. O. Nigra (1952). Eolian sand control *Am. Assoc. Pet. Geol. Bull. 36*, 1541–1573.

Kieffer, H. H., S. C. Chase Jr., E. Miner, G. Münch, and G. Neugebauer (1973). Preliminary report on infrared radiometric measurements from the Mariner 9 spacecraft. *Journal of Geophysical Research 78*, 4291–4312.

Kieffer, H. H. (1976). Soil and Surface Temperatures at the Viking Landing Sites. *Science 194*, 1344–1346.

Kieffer, H. H., T. Z. Martin, A. R. Peterfreund, B. M. Jakosky, E. D. Miner, and F. D. Palluconi (1977). Thermal and albedo mapping of Mars during the Viking Primary Mission. *Journal of Geophysical Research 82*, 4249–4291.

Kleinhans, M. G., A. W. E. Wilberts, A. De Shaaf, and J. H. Van den Berg (2002). Sediment Supply-Limited Bedforms in Sand-Gravel Bed Rivers. *Journal of Sedimentary Research 72(5)*, 629–640.

Knight, M., D. S. G. Thomas and G. F. S. Wiggs (2004). Challenges of calculating dunefield mobility over the 21st century. *Geomorphology 59*, 197–213.

Kocurek, G., and R. C. Ewing (2005). Aeolian dune field self-organization – implications for the formation of simple versus complex dune-field patterns. *Geomorphology 72*, 94–105.

Kroy, K., G. Sauermann, and H. J. Herrmann (2002). Minimal model for aeolian sand dunes. *Physical Review E 66*, 031302.

Kroy, K. and X. Guo (2004). Comment on “Relevant Length Scale of Barchan Dunes”. *Physical Review Letters 93*, 039401.

Kroy, K., S. Fischer, and B. Obermayer (2005). The shape of barchan dunes. *Journal of Physics: Condensed Matter 17,* S1299–S1235.

Lancaster, N. (1980). The formation of seif dunes from barchans - supporting evidence for Bagnold’s model from the Namib Desert. *Z. Geomorph. N. F. 24*, 160–170.

Lancaster, N. (1981). Grain size characteristics of Namib Desert linear dunes. *Sedimentology 28*, 115–122.

Lancaster, N. (1983). Controls of dune morphology in the Namib sand sea. In M. E. Brookfield and E. S. Ahlbrant (Eds.), *Eolian Sediments and Processes. Developments in Sedimentology*, vol. 38, pp. 261–289.

Lancaster, N. (1985). Variations in wind velocity and sand transport rates on the windward flanks of desert sand dunes. *Sedimentology 32*, 581–593.

Lancaster, N., and R. Greeley (1990). Sediment Volume in the North Polar Sand Seas of Mars. *Journal of Geophysical Research 95*, 10921–10927.

Lee, P. and P. C. Thomas (1995). Longitudinal dunes on Mars: Relation to current wind regimes. *Journal of Geophysical Research 100,* 5381–5395.

Lee, J. H., A. O. Sousa, E. J. R. Parteli, and H. J. Herrmann (2005). Modelling formation and evolution of transverse dune fields. *International Journal of Modern Physics C 12*, No. 16, 1879–1892.

Leovy, C., and Y. Mintz (1969). Numerical Simulation of the Atmospheric Circulation and Climate of Mars. *Journal of the Atmospheric Sciences 26*, 1167–1190.

Lettau, K. and H. Lettau (1969). Bulk transport of sand by the barchans of the Pampa de La Joya in southern Peru. *Zeitschrift für Geomorphologie N.F. 13-2,* 182–195.

Li, Z. S. and J. R. Ni (2003). Sampling efficiency of vertical array aeolian sand traps. *Geomorphology 52*, 243–252.

Lima, A. R., G. Sauermann, H. J. Herrmann and K. Kroy (2002). Modelling a dune field. *Physica A 310,* 487–500.

Livingstone, I. (1989). Temporal trends in grain-size measures on a linear sand dune. *Sedimentology 36,* 1017–1022.

Long, J. T. and R. P. Sharp (1964). Barchan-dune movement in Imperial Valley, California. *Geological Society of America Bulletin 75*, 149–156.

Lorenz, R. D., J. I. Lunine, J. A. Grier, and M. A. Fisher (1995). Prediction of aeolian features on planets: Application to Titan paleoclimatology. *Journal of Geophysical Research 100*, 26377–26386.

Lorenz et al. (2006). The Sand Seas of Titan: Cassini RADAR Observations of Longitudinal Dunes. *Science 312*, 724–727.

Magalhães, B. (2000). Um mergulho nos Lençóis Maranhenses (In Portuguese). *Ciência Hoje 27*, 52–53.

Malin, M. C., M. H. Carr, G. E. Danielson, M. E. Davies, W. K. Hartmann, A. P. Ingersoll, P. B. James, H. Masursky, A. S. McEwen, L. A. Soderblom, P. Thomas, J. Veverka, M. A. Caplinger, M. A. Ravine, T. A. Soulanille, and J. L. Warren (1998). Early Views of the Martian Surface from the Mars Orbiter Camera of Mars Global Surveyor. *Science 279*, 1681–1685.

Marchenko, A. G., and A. Pronin (1995). Study of relations between small impact craters and dunes on Mars, abstracts of the 22nd russian-american microsymposium on planetology, *Tech. Rep. 63-64*, Vernadsky Institute, Moscow.

Marshall, J. R., J. Borucki, and C. Bratton (1998). Aeolian Sand Transport in the Planetary Context: Respective Roles of Aerodynamic and Bed-Dilatancy Thresholds. *Proc. Lunar and Planetary Science Conf. 29*, 1131.

Marshall, J. R. and D. Sratton (1999). Computer Modeling of Sand Transport on Mars Using a Compartmentalized Fluids Algorithm (CFA). *Proc. Lunar and Planetary Science Conf. 30*, 1229.

Mass, C., and C. Sagan (1976). A Numerical Circulation Model with Topography for the Martian Southern Hemisphere. *Journal of the Atmospheric Sciences 33*, 1418–1430.

McCauley, J. F., M. H. Carr, J. A. Cutts, W. K. Hartmann, H. Masursky, D. J. Milton, R. P. Sharp, and D. E. Wilhelms (1972). Preliminary Mariner 9 report on the geology of Mars. *Icarus 17*, 289–327.

McCauley, J. F. (1973). Mariner 9 Evidence for Wind Erosion in the Equatorial and Mid-Latitude Regions of Mars. *Journal of Geophysical Research 78*, 4123–4137.

McEwan, I. K. and B. B. Willetts (1991). Numerical model of the saltation cloud. *Acta Mechanica (Suppl.) 1*, 53–66.

McKee, E. D., and G. C. Tibbitts, Jr. (1964). Primary Structures of a Seif Dune and Associated Deposits in Libya. *Journal of Sedimentary Petrology 34*, 5–17.

McKenna Neuman, C., N. Lancaster, and W. G. Nickling (2000). The effect of unsteady winds on sediment transport on the stoss slope of a transverse dune, Silver Peak, NV, USA. *Sedimentology 47*, 211–226.

Melosh, H. J. and A. M. Vickery (2003). Impact erosion of the primordial atmosphere of Mars. *Nature 338*, 487–489.

Merrison, J., J. Jensen, K. Kinch, R. Mugford, and P. Nørnberg (2004). The electrical properties of Mars analogue dust. *Planetary and Space Science 52*, 279–290.

Metzger, S. M., J. R. Carr, J. R. Johnson, T. J. Parker, and M. T. Lemmon (1999). Dust devil vortices seen by the Mars Pathfinder cmera. *Geophysical Research Letters 26*, 2781–2784.

MGSRS, “Late Martian Weather”. Mars Global Surveyor Radio Science Team, http://nova.stanford.edu/projects/mgs/.

Moore, H. J. (1985). The Martian dust storm of Sol 1742. *Journal of Geophysical Research 90*, 163–174.

Moore, H. J., D. B. Bickler, J. A. Crisp, H. J. Eisen, J. A. Gensler, A. F. C. Haldemann, J. R. Matijevic, L. K. Reid, and F. Pavlics (1999). Soil-like deposits observed by Sojourner, the Pathfinder rover. *Journal of Geophysical Research 104*, 8729–8746.

Mutch, T. A., A. B. Binder, F. O. Huck, E. C. Levinthal, S. Liebes, Jr., E. C. Morris, W. R. Patterson, J. B. Pollack, C. Sagan and G. R. Taylor (1976a). The Surface of Mars: The View from the Viking 1 Lander. *Science 193*, 791–801.

Mutch, T. A., R. E. Arvidson, A. B. Binder, F. O. Huck, E. C. Levinthal, S. Liebes, Jr., E. C. Morris, D. Nummedal, J. B. Pollack, and C. Sagan (1976b). Fine Particles on Mars: Observations with the Viking 1 Lander Cameras. *Science 194*, 87–91.

Mutch, T. A., S. U. Grenander, K. L. Jones, W. Patterson, R. E. Arvidson, E. A. Gunness, P. Avrin, C. E. Carlston, A. B. Binder, C. Sagan, E. W. Dunham, P. L. Fox, D. C. Pieri, F. O. Huck, C. W. Rowland, G. R. Taylor, S. D. Wall, R. Kahn, E. C. Levinthal, S. Liebes, Jr., R. B. Tucker, E. C. Morris, J. B. Pollack, R. S. Saunders and M. R. Wolf (1976c). The Surface of Mars: The View from the Viking 2 Lander. *Science 194*, 1277–1283.

Nalpanis, P., J. C. R. Hunt, and C. F. Barrett (1993). Saltating particles over flat beds. *J. Fluid Mech. 251*, 661–685.

Neugebauer, G., G. Münch, H. Kieffer, and E. Miner (1971). Mariner 1969 Infrared Radiometer Results: Temperatures and Thermal Properties of the Martian Surface. *The Astronomical Journal 76*, 719–749.

Owen, P. R. (1964). Saltation of uniformed sand grains in air. *J. Fluid. Mech. 20*, 225–242.

Parsons, D. R., I. J. Walker, and G. F. S. Wiggs (2004). Numerical modelling of flow structures over idealized transverse aeolian dunes of varying geometry. *Geomorphology 59*, 149–164.

Parteli, E. J. R. and H. J. Herrmann (2003). A simple model for a transverse dune field. *Physica A 327*, 554–562. Also in F. Mallamace, and H. E. Stanley (Eds.), *The Physics of Complex Systems (New Advances and Perspectives)*, Proc. International School of Physics, “Enrico Fermi” 2003, pp. 153–171, IOS Press, 2004.

Parteli, E. J. R., V. Schatz, and H. J. Herrmann (2005). Barchan dunes on Mars and on Earth. In R. Garcia-Rojo, H. J. Herrmann and S. McNamara (Eds.), *Powders and Grains 2005*, Vol. 2, pp. 959–962. Balkema, Leiden.

Parteli, E. J. R. and H. J. Herrmann (2006). Saltation transport on Mars. Submitted to *Physical Review Letters*.

Parteli, E. J. R., O. Durán, and H. J. Herrmann (2006a). The Shape of the Barchan Dunes in the Arkhangelsky Crater on Mars. *Proc. Lunar and Planetary Science Conf. 37*, 1827.

Parteli, E. J. R., O. Durán, and H. J. Herrmann (2006b). Minimal size of a barchan dune. Submitted to *Physical Review E* (in press).

Parteli, E. J. R., V. Schwämmle, H. J. Herrmann, L. H. U. Monteiro, and L. P. Maia (2006c). Profile measurement and simulation of a transverse dune field in the Lençóis Maranhenses. *Geomorphology 81*, 29–42.

Parteli, E. J. R., O. Durán, V. Schwämmle, H. J. Herrmann, and H. Tsoar (2006d). Modelling seif dunes. preprint.

Pollack, J. B., R. Haberle, R. Greeley, and J. Iversen (1976). Estimates of the Wind Speeds Required for Particle Motion on Mars. *Icarus 29*, 395–417.

Pollack, J. B., C. B. Leovy, P. W. Greiman, and Y. Mintz (1981). A Martian General Circulation Experiment with Large Topography. *Journal of the Atmospheric Sciences 38*, 3–29.

Pollack, J. B., R. M. Haberle, J. Schäffer, and H. Lee (1990). Simulations of the General Circulation of the Martian Atmosphere 1. Polar Processes. *Journal of Geophysical Research 95*, 1447–1473.

Pye, K. and H. Tsoar (1990). *Aeolian sand and sand dunes*. London: Unwin Hyman.

Rasmussen, K. R., J. D. Iversen, and P. Rautahemio (1996). Saltation and wind-flow interaction in a variable slope wind tunnel. *Geomorphology 17*, 19–28.

Rioual, F., A. Valance, and D. Bideau (2000). Experimental study of the collision process of a grain on a two-dimensional granular bed. *Phys. Rev. E 62*, 2450–2459.

Rubin, D. M. and R. E. Hunter (1985). Why deposits of longitudinal dunes are rarely recognized in the geologic record. *Sedimentology 32*, 147–157.

Rubin, D. M. and R. E. Hunter (1987). Bedform alignment in directionally varying flows. *Science 237*, 276–278.

Rubin, D. M. and H. Ikeda (1990). Flume experiments on the alingment of transverse, oblique, and longitudinal dunes in directionally varying flows. *Sedimentology 37*, 673–683.

Sagan, C., J. Veverka, P. Fox, R. Dubisch, J. Lederberg, E. Levinthal, L. Quam, R. Tucker, J. B. Pollack, and B. A. Smith (1972). Variable Features on Mars: Preliminary Mariner 9 Television Results. *Icarus 17*, 346–372.

Sagan, C., D. Pieri, P. Fox, R. E. Arvidson, and E. A. Guinness (1977). Particle Motion on Mars Inferred From the Viking Lander Cameras. *Journal of Geophysical Research 82*, 4430–4438.

dos Santos, J. H. Souza, J. W. A. Castro, R. A. Gonçalves and N. F. B. dos Santos (preprint in Portuguese). Modelo Evolutivo do Campo de Dunas do Parque Nacional dos Lençóis Maranhenses – MA/Brasil.

Sauermann, G., P. Rognon, A. Poliakov, and H. J. Herrmann (2000). The shape of the barchan dunes of southern Morocco. *Geomorphology 36*, 47–62.

Sauermann, G. (2001). Modeling of Wind Blown Sand and Desert Dunes. PhD Thesis, Universität Stuttgart. Logos Verlag Berlin.

Sauermann, G., K. Kroy, and H. J. Herrmann (2001). A continuum saltation model for sand dunes. *Phys. Rev. E 64*, 31305.

Sauermann, G., J. S. Andrade Jr., L. P. Maia, U. M. S. Costa, A. D. Araújo, and H. J. Herrmann (2003). Wind velocity and sand transport on a barchan dune. *Geomorphology 54*, 245–255.

Schatz, V., H. Tsoar, K. S. Edgett, E. J. R. Parteli, and H. J. Herrmann (2006). Evidence for indurated sand dunes in the Martian north polar region. *Journal of Geophysical Research 111*, E04006, doi:10.129/2005JE002514.

Schatz, V. and H. J. Herrmann (2006). Numerical investigation of flow separation in the lee side of transverse dunes. *Geomorphology VV*, PPa–PPb. cond-mat/0510212.

Schofield, J. T., J. R. Barnes, D. Crisp, R. M. Haberle, S. Larsen, J. A. Magalhães, J. R. Murphy, A. Seiff, and G. Wilson (1997). The Mars Pathfinder Atmospheric Structure Investigation/Metorology (ASI/MET) Experiment. *Science 278*, 1752–1757.

Schwämmle, V. and H. J. Herrmann (2003). Solitary wave behaviour of sand dunes. *Nature 426*, 619–620.

Schwämmle, V. and H. J. Herrmann (2004). Modelling transverse dunes. *Earth Surface Processes and Landforms 29*, 769–784.

Schwämmle, V. and H. J. Herrmann (2005). A model of barchan dunes including lateral shear stress. *The European Physical Journal E 16*, 57–65.

Sharp, R. P., and M. C. Malin (1984). Surface geology from Viking landers on Mars: A second look. *Geological Society of America Bulletin 95*, 1398–1412.

Sheehan, W. (1996). *The Planet Mars: A History of Observation and Discovery.* The University of Arizona Press, Tucson.

Shields, A. (1936). Applications of similarity principles and turbulence research to bed–load movement. Technical Report Publ. No. 167, California Inst. Technol. Hydrodynamics Lab. Translation of: Mitteilungen der preussischen Versuchsanstalt für Wasserbau und Schiffsbau. W. P. Ott and J. C. van Wehelen (translators).

Smith, P. H., J. F. Bell III, N. T. Bridges, D. T. Britt, L. Gaddis, R. Greeley, H. U. Keller, K. E. Herkenhoff, R. Jaumann, J. R. Johnson, R. L. Kirk, M. Lemmon, J. N. Maki, M. C. Malin, S. L. Murchie, J. Oberst, T. J. Parker, R. J. Reid, R. Sablotny, L. A. Soderblom, C. Stoker, R. Sullivan, N. Thomas, M. G. Tomasko, W. Ward, and E. Wegryn (1997). Results from the Mars Pathfinder Camera. *Science 278*, 1758–1765.

Squyres, S. W., A. H. Knoll, R. E. Arvidson, B. C. Clark, J. P. Grotzinger, B. L. Jolliff, S. M. McLennan, N. Tosca, J. F. Bell III, W. M. Calvin, W. H. Farrand, T. D. Glotch, M. P. Golombek, K. E. Herkenhoff, J. R. Johnson, G. Klingelhöfer, H. Y. McSween, and A. S. Yen (2006). Two Years at Meridiani Planum: Results from the Opportunity Rover. *Science 313*, 1403–1407.

Sullivan, R., R. Greeley, M. Kraft, G. Wilson, M. Golombek, K. Herkenhoff, J. Murphy, and P. Smith (2000). Results of the Imager for Mars Pathfinder windsock experiment. *Journal of Geophysical Research 105*, 24547–24562.

Sullivan *et al.* (2005). Aeolian processes at the Mars Exploration Rover Meridiani Planum landing site. *Nature 436*, 58–61.

Sutton, J. L., C. B. Leovy and J. E. Tillman (1978). Diurnal Variations of the Martian Surface Layer Meteorological Parameters During the First 45 Sols at Two Viking Lander Sites. *J. Atmos. Sci. 35*, 2346–2355.

Thomas, P. (1982). Present Wind Activity on Mars: Relation to Large Latitudinally Zoned Sediment Deposits. *Journal of Geophysical Research 87*, 9999–10008.

Thomas, P. C., M. C. Malin, M. H. Carr, G. E. Danielson, M. E. Davies, W. K. Hartmann, A. P. Ingersoll, P. B. James, A. S. Mcewen, L. A. Soderblom, and J. Veverka (1999). Bright dunes on mars. *Nature 397*, 592–594.

Thomas, M., J. D. A. Clarke, and C. F. Pain (2005). Weathering, erosion and landscape processes on Mars identified from recent rover imagery, and possible Earth analogues. *Aust. J. Earth Sci. 52*, 365–378.

Tomasko, M. G., *et al.* (2005). Rain, winds and haze during the Huygens probe's descent to Titan's surface. *Nature 438*, 765–778.

Tsoar, H., R. Greeley, and A. R. Peterfreund (1979). Mars: The north polar sand sea and related wind patterns. *J. Geophys. Res. 84*, 8167–8180.

Tsoar, H. (1983). Dynamic processes acting on a longitudinal (seif) sand dune. *Sedimentology 30*, 567–578.

Tsoar, H. (1984). The formation of seif dunes from barchans — a discussion. *Z. Geomorph. N. F. 28*, 99–103.

Tsoar, H. (1985). Profiles Analysis of Sand Dunes and Their Steady State Signification. *Geografiska Annaler 67A*, 47–59.

Tsoar, H. (1986). Two-dimensional analysis of dune profile and the effect of grain size on sand dune morphology. In F. El-Baz and M. H. A. Hassan (Eds.), *Physics of Desertification*, pp. 94–108. Martinus Nyhoff, Dordrecht.

Tsoar, H. and K. Pye (1987). Dust transport and the question of desert loess formation. *Sedimentology 34*, 139–153.

Tsoar, H. (1989). Linear dunes — Forms and formation. *Progr. Physical Geogr. 13*, 507–528.

Tsoar, H. and D. G. Blumberg (2002). Formation of parabolic dunes from barchan and transverse dunes along Israel's Mediterranean Coast. *Earth Surface Processes and Landforms 27*, 1147–1161.

Tsoar, H. (2005). Sand dunes mobility and stability in relation to climate. *Physica A 357*, 59 – 56.

Ungar, J. E. and P. K. Haff (1987). Steady state saltation in air. *Sedimentology 34*, 289–299.

Walker, I. J. and W. G. Nickling (2002). Dynamics of secondary airflow and sediment transport over and in the lee of transverse dunes. *Progress in Physical Geography 26*, 47–75.

Walker, I. J. and W. G. Nickling (2003). Simulation and Measurement of Surface Shear Stress over Isolated and Closely Spaced Transverse Dunes in a Wind Tunnel. *Earth Surface Processes and Landforms 28*, 1111–1124.

Wang, X., Z. Dong, J. Qu, J. Zhang, and A. Zhao (1993). Dynamic processes of a simple linear dune — a study in the Taklimakan Sand Sea, China. *Geomorphology 52*, 233–241.

Warren, A. (1972). Observations on Dunes and Bi-Modal Sands in the Ténéré Desert. *Sedimentology 19*, 37–44.

Wasson, R. J. and R. Hyde (1983). Factors determining desert dune types. *Nature 304*, 337–339.

Wechsler, A. E. and P. E. Glaser (1965). Pressure effects on postulated lunar materials. *Icarus 4*, 435–352.

Weitz, C., J. J. Plaut, R. Greeley, and R. Steven Saunders (1994). Dunes and Microdunes on Venus: Why Were So Few Found in the Magellan Data? *Icarus 112*, 282–295.

Weng, W. S., J. C. R. Hunt, D. J. Carruthers, A. Warren, G. F. S. Wiggs, I. Livingstone, and I. Castro (1991). Air flow and sand transport over sand-dunes. *Acta Mechanica (Suppl.) 2*, 1–22.

Werner, B. T. and G. Kocurek (1999). Bedform spacing from defect dynamics. *Geology 27*, 727–730.

White, B. R., R. Greeley, J. D. Iversen, and J. B. Pollack (1976). Estimated Grain Saltation in a Martian Atmosphere. *Journal of Geophysical Research 81*, 5643–5650.

White, B. R. (1979). Soil transport by Winds on Mars. *Journal of Geophysical Research 84*, 4643–4651.

White, B. R. (1981). Venusian Saltation. *Icarus 46*, 226–232.

White, B. R. and H. Mounla (1991). An experimental study of Froud number effect on wind-tunnel saltation. *Acta Mechanica Suppl 1*, 145–157.

Wiggs, G. F. S. (2001). Desert dune processes and dynamics. *Progress in Physical Geography 25*, 53–79.

Williams, S. H. and R. Greeley (1980). Wind Erosion on Mars: An Estimate of the Rate of Abrasion. Lunar and Planetary Institute report 1980LPI...11. pp. 1254–1256.

Zhang, R., M. Kan, and T. Kawamura (2005). Numerical Study of the Formation of Transverse Dunes and Linear Dunes. *Journal of the Physical Society of Japan 74*, 599–604.

Acknowledgements

This work has been supported by CAPES, Coordenação de Aperfeiçoamento de Pessoal de Nível Superior - Brasília, Brasil. I thank Prof. Dr. Hans Herrmann who gave me the opportunity to work at ICP on an interesting subject, and who supervised this Thesis. I am also indebted to Prof. Dr. Günter Wunner who accepted to referee this Thesis. Finally, I acknowledge Prof. Dr. Ulrich Weiss and Prof. Dr. Jörg Wrachtrup with whom I took the exams for the “Zulassung zur Promotion”.

I thank Orencio Durán and Volker Schatz for the numerous discussions. I thank Dr. Mary Bourke from the Lunar and Planetary Science Institute for her interest in my work and stimulating discussions about dunes on Mars. I also thank Dr. Kenneth Edgett from Malin Space Science Systems and Prof. Dr. Haim Tsoar for informations about Mars, dunes on Mars and on Earth, and for comments and suggestions. Finally, I thank Prof. Dr. Keld Rasmussen for suggesting me to look at the smallest dunes and Prof. Dr. Dietrich Wolf for encouraging comments at the Powders and Grains 2005 Meeting.

I thank Martin Hecht, Frank Raischel and Jens Harting for the several computational hints, and Sean McNamara for the critical reading of many of the papers related to this work. André Souza and Daniela Maionchi are acknowledged for providing the brazilian condiment for an animated working atmosphere. I also acknowledge Adriano Sousa and Jason Gallas for stimulating conversations and comments. I thank Thomas Arul and Hansjörg Seybold for valuable discussions that helped me to prepare for the admission exams.

I am grateful to Raul Cruz-Hidalgo, Jorge Garibay and Fernando Alonso-Marroquin for the assistance they rendered me in my first weeks in Stuttgart. I acknowledge Henriette Patzelt and Marlies Parsons for the assistance with many administrative issues. I thank Frank Huber in a special manner for the impeccable maintenance of the ICP computer system, which allowed successful realization of the calculations. I thank Prof. Dr. Marcelo Gomes for encouragement and collaboration during my PhD studies. I acknowledge Prof. Dr. Luís P. Maia and Prof. Dr. José S. Andrade Jr. for discussions and Juliana Cristina Fukuda from IBAMA, São Luís, for useful informations about the Lençóis Maranhenses and for assistance during the field trip at the dunes in Barreirinhas and Atins, Maranhão.

Finally, I dedicate this work to my fiancée Yvonne, to my parents in Brazil and to my brother Johannes. I acknowledge them for the tireless understanding, support and incentivation. I also dedicate my Thesis to Regina, Ali and Nicole who represent my family in Germany. I thank Dona Maria and Abel for stimulating remarks, and Yvonne for the interest in the calculations of Martian dunes, and for many discussions, comments, and suggestions.